UNIVERSITY OF SOUTHAMPTON

FACULTY OF ENGINEERING AND THE ENVIRONMENT

Institute of Sound and Vibration Research

Investigation of ultrasonic properties of MAGIC gels for pulse-echo gel dosimetry

by

Timothy John Atkins

Thesis for the degree of Doctor of Philosophy

August 2014

UNIVERSITY OF SOUTHAMPTON

ABSTRACT

FACULTY OF ENGINEERING AND THE ENVIRONMENT

Sound and Vibration Studies

Thesis for the degree of Doctor of Philosophy

INVESTIGATION OF ULTRASONIC PROPERTIES OF MAGIC GELS FOR PULSE-ECHO GEL DOSIMETRY

Timothy John Atkins

This thesis describes investigations into the design and evaluation of novel ultrasonic methods for 3-dimensional ionising radiation dose verification. Pulse-echo ultrasound methods were investigated for the measurement and analysis of complex radiation therapy dose delivery.

The physical properties of MAGIC (Methacrylic and Ascorbic acid in Gelatin Initiated by Copper) polymer gel dosimeters have been characterized. The variations of speed of sound, ultrasonic attenuation coefficient and density of MAGIC gel with radiation dose and temperature have been quantified. This extends work that has previously been reported for the properties of this gel to the effect of measurement temperature on the results. The facilities to perform these measurements were specified, constructed and evaluated as part of the project.

The measurement of radiation dose using ultrasound back scatter from an interface between the polymer gel dosimeter and an inert reflector is demonstrated. To enable the measurement of radiation dose using pulse-echo ultrasound methods a novel inert material has been specified, manufactured and characterised. This material is matched to the acoustic impedance of MAGIC gel to produce the most dose-sensitive reflections.

The reflections from the interface between the inert reflector and dose-dependent MAGIC gel have been analysed using both a single element transducer and a commercial ultrasound scanner. Both measurement systems demonstrate the same dose and temperature dependence of the ultrasonic reflection. A methodology has been developed to relate pixel values from the ultrasound scanner to the amplitude of the reflected ultrasound signal. A phantom consisting of an array of threads formed from the inert backscattering material has been designed and constructed and a method of extracting pixel data from images of the array acquired using a commercial ultrasound scanner has been developed, so that multiple imaging positions could be used to perform a 3-dimensional assessment of radiation dose distributions.

It has been demonstrated that a pulse-echo technique using a commercial ultrasound scanner shows promise for radiation gel dosimetry. Further investigation and alternative polymer gel and inert reflector combinations may improve these techniques.

Contents

Contents

List of symbols and abbreviations

a	Radius of ultrasound transducer
a_1	Radius of ultrasound transducer 1
a_2	Radius of ultrasound transducer 2
c	Speed of sound of a wave
$\mathbf{c}$	Complex wave velocity
c_{25}	Speed of sound of MAGIC gel at 25°C
$c_{AP}(T)$	Speed of sound in acoustic polymers material parameterised by temperature T
$c_{MAGIC}(T, D)$	Speed of sound of MAGIC gel parameterised by temperature T and dose D
c_{ref}	Speed of sound of a wave in a reference medium
c_s	Speed of sound of a shear wave
c_{sample}	Speed of sound of a wave in a sample material
c_w	Speed of sound of a wave in a sample window material
$c(x, y)$	Speed of sound of a wave in a sample at coordinates (x, y).
e	Strain induced in a material
f	Frequency of a wave
h	Thickness of a sample window material
k	Real part of wavenumber
$\mathbf{k}$	Complex wavenumber
$n(x, y)$	Refractive index of the sample at coordinates (x, y) compared to the reference material
p	Complex sound pressure of a wave
p_1	Complex sound pressure produced by transducer 1
$p_1(r, z_1)$	Complex sound pressure produced by transducer 1 at a radial distance r in a plane at a distance z_1 from the source
$p_2(r, z_2)$	Complex sound pressure produced by transducer 2 at radial distance r in a plane at a distance z_2 from the source
$p(r)$	Sound pressure of focusing source in focal plane at radial distance r
p_{rec}	Sound pressure averaged over the active surface area of the receiver

$p_{rec,s}(z_T)$	Sound pressure averaged over the active surface area of the receiver for transducer separation z_T where the wave has passed through a sample
$p_{rec,s}(z_T,s)$	Estimate of the sound pressure averaged over the active surface area of the receiver for transducer separation z_T calculated by performing a restricted integration over the sample radius s where the wave has passed through a sample
$p_{rec}(z_T)$	Sound pressure averaged over the active surface area of the receiver for transducer separation z_T
$p_{rec}(z_T, R)$	Estimate of the sound pressure averaged over the active surface area of the receiver for transducer separation z_T calculated by performing a restricted integration to a radial distance R
$p_{rec}(z_T, s)$	Estimate of the sound pressure averaged over the active surface area of the receiver for transducer separation z_T calculated by performing a restricted integration over the sample radius s
$p(r, z)$	Sound pressure of focusing source at radial distance r in a plane at a distance z from the source
r	Radial distance in cylindrical coordinate system
s	Sample radius
t	Time of flight of a wave
td	Time delay between triggering and emission of first pulse
t_d	Time of flight of a directly transmitted wave through a sample
t_{delay}	Time delay/phase shift caused by introducing a sample into an ultrasonic path
t_f	Time taken for a signal to pass through a fluid-only path
t_r	Time of flight for a first reverberant wave through a sample
x, y, z	Parameters used for distance (see text for specific definitions at each stage)
z_1	Distance of integration plane from transducer 1
z_2	Distance of integration plane from transducer 2
z_T	Transducer separation for opposed transducers
A	Amplitude of a wave after passing through a medium
A_0	Initial amplitude of a wave

$Area_{bath}$	Area of a fluid bath at the surface of the fluid
$Area_{sh}$	Area of a sample holder at the surface of the fluid
$A_S(f, z)$	Amplitude spectrum (frequency f) of the received waveform after propagating through a distance z in a water-sample-water path
$A_W(f, z)$	Amplitude spectrum (frequency f) of the received waveform after propagating through a distance z in a water-only path
C_D	Increase in speed of sound with increasing dose at a temperature of 25°C
C_{DT}	Increase in the dose dependent increase of the speed of sound with increasing temperature above 25°C
C_T	Rate of increase of speed of sound with increasing temperature above 25°C
CT	Computed Tomography
D	Absorbed Radiation Dose
$D_d^S(f, z)$	Frequency (f) dependent reduction in amplitude of the ultrasound pulse as a result of diffraction for the water-sample-water path
$D_d^W(f, z)$	Frequency (f) dependent reduction in amplitude of the ultrasound pulse as a result of diffraction for a water-only path
E	Young's Modulus
EPID	Electronic Portal Imaging Device
F	Focal length of transducer
F_1	Radius of curvature of transducer 1
F_2	Radius of curvature of transducer 2
FFT	Fast Fourier Transform
G	Buoyancy of a material when placed in a fluid medium rather than air
IMRT	Intensity Modulate Radiation Therapy
K	Correction factor for measurement of buoyancy due to effect of sample holder
L	Signal path along which an ultrasound wave travels
MAGIC	Normoxic gel formulation used in radiation dosimetry (Methacrylic and Ascorbic acid in Gelatin Initiated by Copper)
MRI	Magnetic Resonance Imaging
N	Number of pulses in a pulse train

List of symbols and abbreviations

P	Pressure amplitude of a wave after propagating through a medium
P_0	Initial pressure amplitude of a wave
P_2	Average pressure amplitude across transducer 2
PAG	Anoxic gel formulation used in radiation dosimetry (Poly-Acrylamide Gel)
PNG	Portable Network Graphics format for image file saving
PTV	Planning target volume
R	Distance over which radial integration has been performed
R_{lim}	The minimum integration limit required to ensure that the ratio of $\lvert p_{\text{rec}}(z_T, R)\rvert$ / $\lvert p_{\text{rec}}(z_T)\rvert$ is greater than the specified value for all $R > R_{\text{lim}}$
RMS	Route Mean Square
S	External stress applied to a material
T	Temperature
TLD	Thermoluminescent detectors
THP	Bis[tetrakis(hydroxymethyl)phosphonium]sulphate, an alternative antioxidant material
THPC	Tetrakis (hydroxymethyl) phosphonium chloride, an alternative antioxidant material
U_0	Velocity amplitude of transducer surface
UCT	Ultrasound computed tomography
V_{c}	Compressional wave velocity
$V(f)$	Frequency (f) dependent amplitude spectrum of an input signal
$Vol.$	Volume of a sample
V_{s}	Shear wave velocity
W_{air}	Weight of a sample in air
W_{fl}	Weight of a sample in a fluid
Z	Characteristic acoustic impedance of a material
Z_1	Characteristic acoustic impedance of material 1
Z_2	Characteristic acoustic impedance of material 2
α	Acoustic attenuation coefficient
$\alpha(f)$	Frequency (f) dependent acoustic attenuation coefficient
$\alpha(x, y)$	Acoustic attenuation coefficient at coordinates (x, y)

ν	Poisson's ratio for a material
ρ	Density of a material
ρ_{air}	Density of air
$\rho_{AP}(T)$	Density of acoustic polymers material parameterised by temperature T
ρ_D	Rate of increase of MAGIC gel density with dose
ρ_{fl}	Density of a fluid medium
$\rho_{MAGIC}(T, D)$	Density of MAGIC gel parameterised by temperature T and dose D
ρ_{sample}	Density of a sample material
ρ_T	Rate of density increase of MAGIC gel with increasing temperature above 25°C
τ	Time period between pulses
φ	Angle in cylindrical coordinate system
ω	Angular frequency of a wave
$\Gamma(f)$	Frequency (f) dependent reduction in acoustic amplitude due to attenuation in a sample
Λ	Total transmission coefficient of an infinite sample including attenuation and transmission losses at interfaces
Λ'	Measured transmission coefficient of a finite sample including attenuation and transmission losses at interfaces
$\Xi_R(f)$	Frequency (f) dependent receiver response function
$\Xi_T(f)$	Frequency (f) dependent transmitter response function
$\Pi_l(f)$	Frequency (f) dependent transfer function due to interface losses

List of symbols and abbreviations

Declaration of authorship

I, ...

declare that this thesis and the work presented in it are my own and has been generated by me as the result of my own original research.

.....

.....

I confirm that:

1. This work was done wholly or mainly while in candidature for a research degree at this University;
2. Where any part of this thesis has previously been submitted for a degree or any other qualification at this University or any other institution, this has been clearly stated;
3. Where I have consulted the published work of others, this is always clearly attributed;
4. Where I have quoted from the work of others, the source is always given. With the exception of such quotations, this thesis is entirely my own work;
5. I have acknowledged all main sources of help;
6. Where the thesis is based on work done by myself jointly with others, I have made clear exactly what was done by others and what I have contributed myself;
7. Parts of this work have been published as:

Atkins, T.J. Humphrey, V.F. Duck, F.A. Tooley, M.A., 2011. The effects of focused transducer geometry and sample size on the measurement of ultrasonic transmission properties, J. Phys.: Conf. Ser., 279, 012024.

Atkins, T.J. Humphrey, V.F. Duck, F.A. Tooley, M.A., 2010. Investigation of ultrasonic properties of MAGIC gels for pulse-echo gel dosimetry, J. Phys.: Conf. Ser., 250, 012075.

Declaration of authorship

Atkins, T.J. Humphrey, V.F. Duck, F.A., 2009. Measurements of Ultrasonic Properties of Dosimetric Gels, The Physics and Technology of Medical Ultrasound, IPEM, March 2009.

Atkins, T.J. Humphrey, V.F. Duck, F.A., 2006. The effects of focused transducer geometry and sample size on the measurement of ultrasonic transmission properties. The Physics and Technology of Medical Ultrasound, IPEM, February 2007.

Signed: .....

Date: .....

Acknowledgements

During the course of producing this thesis I have been supported, challenged and encouraged by many people, without whom this thesis would be much the poorer.

Special thanks are due to Professor Francis Duck, without whom this would never have happened and who has always been available with a listening ear, a decisive word, a clear explanation of the ways of ultrasound and continual calls to ensure the words I have been writing contribute to the story.

Professor Victor Humphrey has shown amazing diligence in helping direct the path of investigation and has provided numerous insights into the interpretation of experimental results. He has also been a great help in ensuring that the thesis is clearly written, any failings are due to my input not his!

Thanks to everyone from the Department of Medical Physics and Bioengineering for all your help and assistance along the way, especially to Professor Mark Tooley and Dr Helen Morgan for enabling me to have time to perform the investigations. For my friends and colleagues in both the Department of Medical Physics and Bioengineering and the Department of Radiotherapy at the Royal United Hospital who have had to put up with my part time work and smelly gels, many thanks.

Part of this work has been funded by the Department of Health New and Emerging Technologies Fund under grant J008. Thank you for the support and money that has given me the time and equipment required for the experiments.

For those that have turned my dreams of equipment into reality and helped fabricate so many parts that have been essential to the experimental process, especially Mr Peter Laidler, Dr Mike Hillman, Mr Martin Rouse and Dr Sui Man Lee, I am forever grateful.

To my family, Rachel, my amazing wife, and our lovely girls, I could not have done this without your love and support. Thank you for putting up with me when I was tired and grumpy – you are all amazing, beautiful people.

And finally, to the one who is “before all things, and in him all things hold together” (Colossian 1v17), to you be glory and honour in Christ Jesus.

Acknowledgements

1. Introduction

1.1. Project outline

Radiation therapy is an important form of treatment for cancer. Successful radiation therapy depends on delivering accurate radiation dose to the tumour site with minimal exposure of the surrounding tissue. As modern radiotherapy devices can produce complex radiation dose distributions it is important to have accurate methods of measuring the radiation dose distributions created to ensure that the delivered dose distribution matches that planned.

Chemical dosimeters, in which radiation produces a chemical change, offer great potential to obtain three dimensional dosimetry information in Radiotherapy. A significant drawback of current techniques relates to the readout procedure – current research utilises MRI or optical techniques requiring dedicated systems, which are often not readily available in radiotherapy centres. In contrast, ultrasound is a very accessible medical imaging technique and the focus of this project is on utilising ultrasound imaging to obtain dose information from chemical dosimeters. One class of chemical dosimeters is based on radiation induced polymerisation initiated by incident radiation. The polymerisation that occurs creates changes to the structure of the dosimeter material, affecting its physical and mechanical properties, including ultrasonic relevant parameters such as speed of sound, density and attenuation coefficient.

To create a dosimeter that can be used with available ultrasound scanners the dosimeter must produce dose dependent acoustic reflections or backscatter levels that can be imaged using a B-Mode scan. To create these dose dependent acoustic reflections requires a contrast between a dose dependent and an inert material, or two differing dose dependent materials. The geometrical arrangement of the dosimeter could take a number of forms. Alternating layers of inert and dose dependent materials, or other geometric structures (threads, spheres) in known locations, would create specific dose dependent reflections throughout the material. Alternatively, multiple small fragments of one material within another would create a dose dependent incoherent backscatter (grey level) within an image. This project aims to develop

materials and methodologies based on MAGIC gels (Fong et al 2001) to produce dose dependent ultrasound images which can be developed into a three dimensional dosimetry technique.

1.2. Project specification

The aim of this project is to develop a clinically useful system for measuring 3D radiation dose distributions by utilising ultrasonic methods to analyse the polymerisation of MAGIC gels and hence measure radiation dose. Initial work will develop measurement methods and investigate the fundamental ultrasonic properties of the MAGIC gels which are required to produce a usable dosimetry technique. Building on the outcomes of these investigations of the ultrasonic properties of the MAGIC gels different dosimetry phantoms will be developed and tested.

1.3. Radiation therapy

In the UK in 2010 there were over 324,500 new cases of cancer diagnosed (Cancer Research UK 2013a), and cancer accounts for over a quarter of all deaths in the UK (Cancer Research UK 2013b). The overall cancer death rate has fallen by 10% over the last decade although the incidence rate has risen slightly over the same time period, indicating better diagnosis and treatment of cancer.

Radiation therapy is one of the three mainstream methods of treating cancer, alongside Chemotherapy and Surgery. The National Radiotherapy Implementation Group state that it is an essential treatment for the cure of cancer, being utilised in 40% of the cases that resulted in a cure of the cancer (National Cancer Action Team, 2009).

The intention of radiation therapy treatment is to deliver a homogeneous high energy radiation dose to the tumour target (planning target volume – PTV) without irradiating a large volume of normal tissue. Conventional techniques deliver a few rectangular or simply shaped fields to cover the planning target volume. However, this often leads to the irradiation of significant volumes of normal tissue or radiosensitive organs (see Figure 1.2a). Intensity Modulated Radiation Therapy (IMRT), and other

modern treatment techniques, promise to provide improved treatments compared to standard radiotherapy techniques by conforming the dose distribution tightly to the intended target (Nutting et al., 2000) and subsequently reducing dose to adjacent normal tissue. IMRT relies on the creation of high energy radiation exposures that have a non-uniform dose profile from each beam direction. The most commonly implemented method of constructing these non-uniform dose profiles is via superposition of multiple radiation exposures (segments) from each beam direction to deliver the intended radiation dose to the patient (see Figure 1.2b). These segments are usually shaped by multi-leaf collimators. The modulation of the radiation beam caused by the superposition of the various segments allows tight conformation of the dose distribution to the target volume and can be utilised to ensure that minimal dose is delivered to radiation sensitive normal tissue.

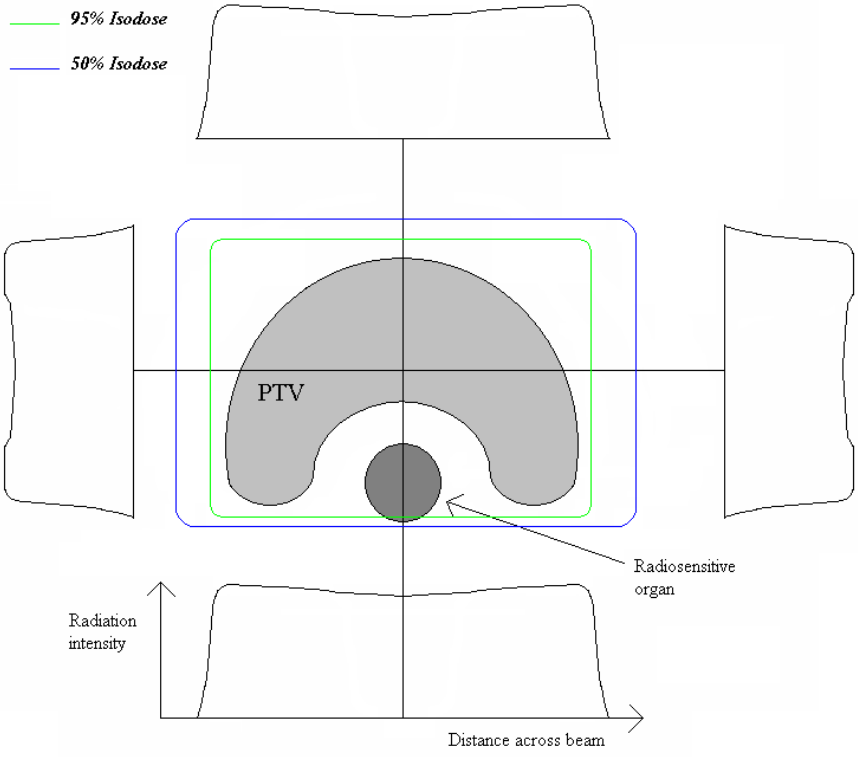

Figure 1.2. (a) Conventional Radiotherapy where simply shaped fields overlay to produce the dose distribution. Here PTV is the planning target volume. The green and blue lines indicate the high and low dose regions respectively. Adapted from Nutting et al. (2000).

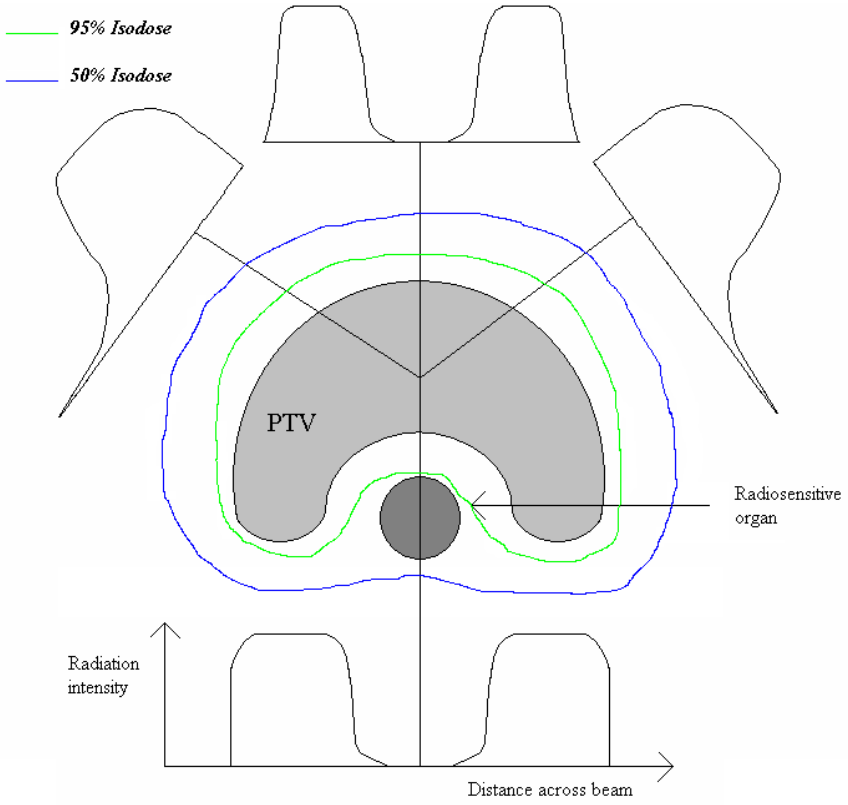

Figure 1.2. (b) IMRT where fields with varying intensity produce a highly shaped dose distribution. The green and blue lines indicate the high and low dose regions respectively. Adapted from Nutting et al. (2000).

The National Radiotherapy Implementation Group estimates that a third of all radiotherapy fractions in the UK should be delivered using IMRT as these patients would be likely to benefit from the use of IMRT in their treatment (National Cancer Action Team 2009, Williams et al. 2010) while the actual delivery of IMRT fractions is significantly below this, at about 12% (Jefferies et al. 2009). In 2012, the Cancer Radiotherapy Innovations Fund was announced to increase the use of Intensity Modulated Radiotherapy and other advanced radiotherapy techniques by April 2013, aiming to treat 8,000 patients per annum with these techniques (Department of Health, 2012) to achieve the level set out by the National Radiotherapy Implementation Group. A recent survey demonstrated a steady growth in the percentage of radical treatments treated with inverse-planned IMRT from 5.6% in 2010 to 15.3% in 2012 (Mayles et al. 2012).

Radiotherapy centres in the UK are well equipped to deliver IMRT treatments, with 97% of UK linear accelerators being equipped with multi-leaf collimators and capable of delivering IMRT (National Cancer Action Team, 2009). The multiple small

exposures may not be intuitively related to the intended dose distribution, and may have unintended consequences such as increased dose due to leakage radiation and scatter. Therefore accurate assessment of the 3-dimensional radiation dose distributions produced by these techniques is essential for their correct utilisation and implementation. There has been slow implementation of these techniques beyond large research centres due to the lack of suitable techniques to verify that the radiation distributions are being produced correctly and the cost of training and staff time to outline, plan and quality assure the treatments.

1.4. Established dosimetry techniques

There are a number of techniques which are currently used to determine the dose delivered during radiation therapy. These include the use of ionisation chambers, semi-conductor diode detectors, film (both radiographic and radiochromic), thermoluminescent detectors (TLDs) and electronic portal imaging devices (EPIDs).

1.4.1. Ionisation chambers

When ionising radiation passes through a gas filled chamber, if the radiation is energetic enough, it causes ionisation of the gas. Applying a potential difference across the chamber between two electrodes causes the charges to separate and move towards the electrodes. The charge created by the ionisation can be used to measure the radiation dose received by the chamber.

Ionisation chambers are the gold-standard device for measuring radiation dose at a single position in a radiation field. The amount of charge created in an ionisation chamber is relatively small, and therefore a large volume is required to produce a sensitive device. This limits the positional accuracy of the device, and their suitability for measuring in regions of steep dose gradients due to the partial volume effect. 2D and 3D measurements are possible for time invariant radiation fields by translating a single chamber through the field, or through the use of multiple ionsiation chambers.

1.4.2. Semi-conductor diodes

When certain semi-conductor junctions are irradiated, the radiation creates electron-hole pairs. The charge created in the junction can be used to measure the dose received by the diode, since the number of electron-hole pairs created is proportional to the dose of radiation received by the junction.

The sensitivity of a semi-conductor diode junction to radiation is greater than an ionisation chamber, due to the density of Silicon and the low average energy required to form a carrier pair, and therefore small junctions of approximately $10^{-2} – 10^{-1}$ mm^{-3} (AAPM, 2005) can be utilised in radiation dosimetry systems. Diodes can be used to measure steep dose grandients due to their more accurate spatial positioning. Arrays of diodes are available for measuring static and dynamic fields, and in multiple positions could measure 3D dose distributions of static or repeated dynamic fields.

1.4.3. Thermoluminescent dosimeters

When energy is imparted to certain crystalline materials, some of the energy is stored by the material by trapping electrons in raised, metastable states. When the material is gently heated, the electrons in these raised states are released. The transition energy between the raised and ground states can be released as visible radiation. The amount of light released is proportional to the energy stored in the crystal. Energy from ionising radiation can be stored in this way, with the amount of light emitted on heating being related to the dose received by the crystal.

Thermoluminescent materials are available in a variety of forms (chips, rods, powder) for use in radiation dosimetry. A single TLD can be used to make a point measurement, or multiple TLDs can be arranged to provide a 2D or 3D array of measurement points.

1.4.4. Radiographic film

When silver bromide crystals are irradiated the crystals ionise, with silver ions being produced. Producing a film with trapped silver bromide crystals, and after irradiation treating the film with appropriate chemical processes to atomise the silver ions and remove remaining bromine, reveals an image of the radiation distribution

made up of clusters of silver atoms. The optical density of the film is a function of the radiation dose received by the film.

Radiographic film provides two-dimensional dose information if scanned by an appropriate optical densitometer. However, due to the move towards digital systems in x-ray imaging the use and availability of radiographic films and appropriate processors is declining.

1.4.5. Chemical dosimeters

When certain chemical compounds are irradiated, they undergo chemical reactions such as reduction or polymerisation which are initiated by the energy imparted to the system by the ionising radiation. If the chemical changes that occur can be determined then this can be used as a method of dosimetry. If such a chemical system can be supported in an environment which limits the diffusion of the chemicals then a system for measuring spatial dose information can be formed. A number of different procedures exist for measuring the chemical changes that have occurred. Some chemical systems undergo a colour change when irradiated. The most famous such system is the Fricke solution (Fricke and Morse, 1927), in which ferrous ions (Fe^{2+}) are oxidised by the radiation into ferric ions (Fe^{3+}). Ferric ions strongly absorb ultraviolet radiation, with absorption peaks at 224 and 304 nm (Greening, 1981). The optical density of the solution measured at one of these wavelengths can therefore be used to determine dose. Other chemical systems undergo polymerisation, cross-linking or photo-reduction, and a variety of read-out methods exist.

1.4.6. Radiochromic film

When radiochromic materials are irradiated with ionising radiation a colour change occurs in the material. If such a material can be trapped in between transparent laminar sheets, a colour change of the resultant film on irradiation can be observed. A number of different processes can be utilised to form such radiochromic films (Niroomand-Rad et al., 1998). Commercially available radiochromic films are replacing the usage of radiographic films in many radiation therapy centres.

1.4.7. Portal dosimetry

The exiting radiation (port) from a radiotherapy treatment can be captured to produce an image of the treatment field. Traditionally this has been performed to assess the geometric positioning of the patient in relation to the treatment field and can be captured using either film based systems or electronic devices. For a review of electronic portal imaging devices see Kirby and Glendinning (2006). A calibration of these systems is possible to transform the image data captured into the radiation fluence incident on the device. The measured radiation fluence can be compare with predicted fluence maps (e.g. McCurdy et al. 2001) or by recalculating the fluence into a dose plan that can be compared with calculated dose from the treatment plan (e.g. Varatharaj et al. 2010). Portal dosimetry relies on a additional calculations, either of the expected fluence or the transformation of measured fluence into dose, and is also particularly dependent on the day to day variation of the patient anatomy.

1.4.8. Gel dosimeters

When chemical dosimeters are trapped within a 3-dimensional gel matrix and irradiated, the chemical changes that occur can be trapped at the location of dose deposition. If the readout method of the chemical changes is 3-dimensional, then the geometric location of the dose deposition can be determined. Many gel formulations have been proposed using systems based either on radiation-induced polymerisation or radiochromic reactions and a number of readout procedures are available, with the most well documented being MRI and optical computed tomography.

1.4.9. Comparison of established dosimetry techniques

Izewska and Rajan (2005) compare the different types of radiation dosimeters. Their conclusions are summarised in Table 1.1. Portal dosimetry is not discussed by Izewsk and Rajan and so comparable conclusions were taken from van Elmpt et al. (2008).

Dosimeter Type	Advantages	Disadvantages	Accuracy	Resolution
Ionisation chamber	Accurate Precise Instant reading Well-understood corrections	High Voltage Connecting cables required Corrections required	<1%	~1mm
Semiconductor diodes	Small size High sensitivity Instant readout Can be placed in arrays	Requires connecting cable Variable sensitivity and calibration Changes sensitivity with accumulated dose	~1%	Sub-millimeter
Radiographic film	High 2D spatial resolution Thin, non peturbing	Processing required Not an absolute measurement Energy dependent Not necessarily linear with dose	Requires absolute calibration by other method	Sub-millimeter
TLD	Point dose possible Can use multiple TLD to measure distribution	Processing required Calibration of batch required	~5%	~0.5mm
Radiochromic film	High 2D spatial resolution Thin, non peturbing	Not an absolute measurement Energy dependent Not necessarily linear with dose	Requires absolute calibration by other method	Sub-millimeter
Portal dosimetry (van Elmpt et al. 2008)	Pre-treatment or transmission dosimetry available Point calculation and distribution comparison available	Imager characterisation required Image processing required Complex calculations to compare with dose distributions	~2%	~1mm
Gel dosimeters	True 3D dosimeter Nearly water-equivalent No dose-rate effects	Absolute calibration required Read-out required Readout techniques still being developed Post-irradiation effects lead to distortion	Requires absolute calibration	~1mm depending on readout technique

Table 1.1. Comparison of radiation dosimeters stating advantages and disadvantages and comparative accuracy and resolution. Taken from Izewska and Rajan (2005) and van Elmpt et al. (2008).

1.5. Introduction to 3D dosimetry

De Wagter (2004) has outlined the need for a 3D dosimeter and has reviewed the essential characteristics of such a dosimeter. To summarise, the accurate measurement of IMRT doses requires an integrating 3D dosimeter to measure all the radiation exposures that compose an IMRT treatment. The following aspects are outlined:

- Absolute dose determination via a calibration curve
- Full 3D volumetric data should be available
- Tissue Equivalent so free from perturbation
- Reliable and reproducible
- Insensitive to energy spectrum and dose rate of radiation
- Non-toxic
- Reasonable in cost

1.5.1. Multiple 2D plane measurements

A number of techniques exist where (multiple) 2D planes are used for evaluation of 3D dose distributions. There are a number of commercially available devices and software products to provide 3D dose evaluation from 2D measurements. 2D ionisation chamber arrays, such as the PTW seven29 (PTW-Freiburg, Freiburg, Germany) and IBA MatriXX (IBA Dosimetry GmbH, Schwarzenbruck, Germany) can be mounted in phantoms (Octavius and MultiCube respectively) and used to measure multiple 2D planes and provide comparisons with calculated dose distributions at various positions in the 3D volume. Similarly, arrays of diodes are used in commercially available systems such as the Sun Nuclear MapCHECK series and ArcCHECK device (Sun Nuclear Corporation, Melbourne, FL) and the ScandiDos Delta4 (ScandiDos AB, Uppsala, Sweden). The ArcCHECK device uses a cylindrical array of diodes, and the Delta4 uses two 2D arrays of diodes mounted at an angle to each other, to produce interpolated 3D images. Software (for example FilmQA, 3cognition LLC, Wayne, NJ) and phantoms (for example Cube Phantom, Computerized Imaging Reference Systems, Inc., Norfolk, VA) are available for

exposing and interpreting multiple film measurements of a 3D dose distribution. Electronic portal imaging devices can be used to measure the fluence delivered by the linear accelerator and compare this to either the predicted fluence map (for example in the Varian Portal Dosimetry system, Varian Medical Systems, Inc., Palo Alto, CA), or by calculating the local dose to water at a plane within the patient that can then be compared to the treatment planning system calculated dose at same plane as carried out by the EPIdose ™ software (Sun Nuclear Corp., Melbourne, FL), or by reprojecting the fluence through a CT dataset to create a prediction of the delivered dose as carried out by the Dosimetry Check ™ system (MathResolutions, LLC., Columbia, MD).

These solutions are commercially available and in routine use in many radiotherapy centres. However, they are reliant on 2D measurements of a 3D dose distribution and interpretation of the data to be able to compare to the true 3D distribution.

1.5.2. 3D volumetric measurements

3D volumetric methods of dosimetry that are currently available are based on 3D chemical dosimeters. Chemical dosimeters based on radiation-induced polymerisation have been integrated into gel structures which maintain the positional location of polymers that have been formed by radiation. Alternatively, radiochromic materials have been integrated into gel structures, or more recently solid plastic materials. A number of types of gel have been produced with current readout procedures focused on the use of MRI methods, although computed tomography (CT) and optical tomography methods have also been used. Although significant progress in the formulations and readout methodologies has been made, and a number of commercial systems have been developed to produce 3D volumetric measurements, these methods have not been accepted into routine practice, with the main drawback being the type of readout methods on which these solutions are reliant.

1.6. Gel and plastic dosimeters

A number of different techniques exist for 3D dosimetry based on the constraining of a chemical dosimeter within a 3D structure so that the geometric

location of chemical changes generated by the irradiation is preserved. Different chemical systems have been proposed, along with different methods of retaining the spatial distribution of the information. The different chemical schemes utilised by the dosimeters can be interrogated by a number of different techniques to produce a measure of the 3D dose information.

1.6.1. Polymer gel dosimeters

Chemical dosimeters that undergo radiation-induced polymerisation have been incorporated into gel structures to produce a 3D dosimetry technique. Maryanski et al. (1993) first introduced a 3D polymer gel dosimeter consisting of acrylamide and N,N'-methylene-bisacrylamide monomers dispersed in an agarose gel. These and subsequent variation, including those based on a gelatine gel, had to be produced in an oxygen-free atmosphere as oxygen inhibits any radiation-induced polymerisation.

Fong et al. (2001) introduced a formulation that could be manufactured without the requirement of an oxygen-free atmosphere. This formulation, known as MAGIC gel, consists of methacrylic acid, ascorbic acid, hydroquinone and copper sulphate in a gelatine substrate.

A number of different types of polymer gels suitable for radiation dosimetry have been proposed, investigated and compared (e.g. De Deene et al. 2002a, Senden et al. 2006, Lepage et al. 2001a).

1.6.2. Radiochromic dosimeters

Radiochromic chemical dosimeters have been incorporated both into gel systems and into solid plastic materials. A number of different radiochromic systems have been investigated, from a system based on the standard Fricke solution (Gore et al. 1984a), to formulations with additional chelating agents such as xylenol-orange to reduce diffusion of Fe^{3+} ions and improve sensitivity (Kelly et al. 1998, Babic et al. 2008). Radiochromic plastic systems are available commercially as Presage® (Heuris Inc., Skillman, NJ.) and have been investigated by a number of authors (e.g. Guo et al. 2006, Sakhalkar et al., 2009)

1.6.3. Mechanical properties leading to alternative readout methods

Radiation also results in changes in the mechanical properties of the gel. As a result of irradiation of MAGIC gel it is conceivable that the real and imaginary parts of the dynamic bulk and shear moduli of the gel change. These changes will in turn result in changes to the compressional and shear wave velocities (V_c and V_s) in the material and the corresponding wave attenuation coefficients (α).

In order to resolve the dose distribution it will be necessary to resolve these changes on a small scale throughout a suitably sized gel sample (typically of dimensions 10 cm × 10 cm × 10 cm). There are a large number of potential methods, but not all will be suitable, convenient or have the required resolution or sensitivity.

For example the following might be considered for a uniform gel:

- Slice the gel and measure the velocity or attenuation directly;
- Ultrasonic velocity tomography;
- Ultrasonic attenuation tomography.

Alternatively it is possible to consider making the gel as a two phase material with interfaces or inhomogeneties. In this case the changes can be inferred by:

- Ultrasonic backscatter imaging of interfaces and inhomogeneities.

Finally ultrasound imaging may be used to infer the elastic moduli at lower dynamic frequencies using:

- Backscatter elastography to measure shear/Young's modulus;
- Shear wave elastography to measure shear modulus.

Whichever readout procedure is adopted it will be necessary to initially develop and characterise suitable gel materials. This will require accurate measurements of the desired readout property (modulus, velocity or attenuation) on uniform samples as a function of dose. Given the small changes expected it will also be necessary to study other factors that may affect the parameters. These include:

- Frequency of ultrasound;

- Temperature of measurement;
- Aging of the gels;
- Gel autopolymerisation by ambient light.

1.6.4. Ultrasonic methods

Although radiation results in changes in the mechanical properties of the gel including both density and elastic moduli, which in turn affect ultrasonic propagation through the gel, investigation of these changes has been sparse. Mather et al. (2002), has investigated dose-dependence of ultrasound attenuation and sound speed in two gel formulations known as PAG (PolyAcrylamide Gel) and MAGIC (Methacrylic and Ascorbic acid in Gelatine Initiated by Copper), and obtained preliminary images of dose distributions using transmission methods. Bamber et al. (2004) suggested using ultrasound elastography in the study of dose-dependent changes, and Crescenti (2009) has presented the results of elastographic measurements on MAGIC gels.

1.7. Developing an ultrasonic backscatter method of gel dosimetry

An ultrasonic pulse-echo dosimetry system will rely on the creation of a phantom that creates dose dependent reflections. This implies that a two-phase material is required, one which has ultrasonic properties that are invariant with dose, and one which has ultrasonic properties which alter once irradiated.

Large scale reflectors, such as layered plane surfaces or threads, would produce reflections that can be localised in an ultrasound image and the reflection amplitude measured. The position of the reflectors could be determined in the design of the phantom to ensure sufficient geometric sampling of the irradiated volume. However, the size and positioning of the reflectors would have to be carefully designed to ensure that they do not interfere with the propagation of the ultrasound field through the phantom and produce artefacts in the image and subsequent dose measurements.

A distribution of small scale reflectors, for example microspheres or fragments, would produce a dose dependent change in backscatter of the ultrasound, producing a

change in the image grey level. An appropriate proportion of reflectors to base material would need to be identified to ensure sufficient backscattered signal and observable dose dependent changes. A reproducible change in grey level with dose throughout such a system would be dependent on creating a uniform distribution of the reflectors in the phantom without agglomerating or coalescing.

To develop an ultrasonic method of gel dosimetry using backscatter or reflections from the gel dosimetry system entails the measurement of a number of ultrasonic and physical properties of the polymer gels, the development and characterisation of suitable ultrasonic reflectors and the development of a scanning system capable of acquiring 3-dimensional images and analysing the images to produce dose information.

The ultrasonic and physical properties of the polymer gels that have been identified for characterisation are the ultrasonic speed of sound, ultrasonic attenuation and density of the gels. Knowledge of the ultrasonic speed of sound and density is fundamental to the understanding of reflections from the interfaces between two materials, and so measurements of these two properties are important in the project to help identify and develop materials suitable for use as the backscattering medium. The ultrasonic attenuation is important to understand as it affects the passage of ultrasound through the gel both before and after reflection, and so will change the ultrasonic signal received after reflection.

The characterisation of suitable ultrasonic reflectors is an important aspect of the project. The reflection level must be suitably tailored to produce enough reflected signal to be measured but also be sensitive to the changes in signal reflection caused by the irradiation of the sample.

The development of a suitable measurement and analysis system is an important aspect of the project. The system needs to be able to acquire images using an ultrasound scanner in a format which can then be imported into an analysis programme. The analysis programme should take the ultrasound images and analyse the backscatter information contained within it to characterise the dose that is deposited within the phantom. This dose can then be related to the intended irradiation for further analysis.

1.8. Original contributions to science

The work described in this thesis contains a number of novel contributions to science as outlined in the following sections.

1.8.1. Measurement of radiation dose

This thesis shows that it is possible to detect radiation dose using ultrasound back scatter from an interface between a polymer gel dosimeter and an inert reflector. Figure 6.12 shows the reflection coefficient with irradiated dose, with the reflection coefficient decreasing approximately linearly with irradiated dose. Figure 6.13 shows the measurement of reflection amplitude across a dose profile. The reflection amplitude decreases rapidly across the dose discontinuity. To enable this measurement of radiation dose from ultrasound backscatter, the physical properties of the MAGIC gel were characterised, along with significant measurements of the properties with temperature and an inert reflector has been specified and characterised.

1.8.1.1. Physical and ultrasonic properties of MAGIC gels

A significantly enhanced knowledge of the physical properties of MAGIC gel and how these properties alter as a result of irradiation has been obtained. Many of these properties have previously been measured and reported in the literature at only a single temperature. This thesis has shown that these properties are significantly temperature dependent; the properties of MAGIC gel have been quantified at a number of temperatures to demonstrate the temperature dependence of these properties.

The temperature dependence of ultrasound attenuation coefficient has been quantified in Chapter 3, indicating that the attenuation coefficient decreases as temperature of the MAGIC gel is increased.

In Chapter 4 the temperature dependence of the speed of sound has been quantified, indicating that the speed of sound decreases as the temperature of the MAGIC gel decreases.

The density of MAGIC gel has been quantified, including the temperature dependence, as demonstrated in Chapter 5. These show how the density decreases with increasing temperature of the MAGIC gel.

1.8.1.2. Specification and characterisation of an inert reflector

To produce an ultrasonic reflection with a suitable sensitivity to radiation dose a reflector was required which had invariant properties when exposed to radiation. The specification for such a material has been determined, a supplier identified and the material produced. The physical and ultrasonic properties, including temperature dependence, of the material have been quantified to characterise the material, as shown in Chapter 6.

1.8.1.3. Investigations into reflection characteristics of MAGIC gel with inert reflector

The ultrasonic reflection characteristics of a radiation sensitive interface between MAGIC gel and an inert reflector have been investigated for the first time as demonstrated in Chapter 6.

A minimum in reflection coefficient as the temperature of the phantom was increased was predicted and this has been demonstrated by measurements of the reflection amplitude.

The temperature at which this minimum occurred was found to increase with radiation dose.

The variation of the reflection coefficient with radiation dose has been shown to be highly dependent on measurement temperature. At low temperatures the reflection coefficient decreases with dose while at high temperatures the reflection coefficient increases with dose. Near the temperature at which the minimum reflection occurs initially the reflection coefficient decreases with dose until it reaches a minimum, and then increases for further irradiation.

The temperature dependence of the reflection characteristics of the system can be utilised to select the temperature of measurement to give the most sensitive measurement of radiation dose distribution.

1.8.2. Gel manufacture and stability

It has been shown that there are significant challenges in the manufacture and use of gel dosimeters for ultrasound backscatter dosimetry purposes. The properties of the MAGIC gel dosimeters that are fundamental to the usage in gel dosimetry purposes are dependent on the rate of cooling of the gel dosimeters, see Figure 7.1 and Table 7.1. The measurements reported in Chapters 4, 5 and 6 demonstrate that there were significant differences in measurements made using the same setup indicating there are significant batch to batch variations in gel manufacture. The reproducibility and uniformity of the gel production has been a significant contributory factor to the uncertainties within the measurements made during this project and remains a significant challenge in developing this project further.

1.8.3. Usage of a commercial ultrasound scanner

In this thesis it is shown that it is possible to utilise an ultrasound backscatter imager to obtain quantitative backscatter information from the interface between MAGIC gel dosimeters and inert reflector material. Figures 10.10 – 10.13 show the measured pixel values compared to expected dose distribution across an image. Figures 10.14-10.18 show the variation in pixel value with irradiated dose. The backscatter information contained in ultrasonic images acquired by the scanner is altered by the image acquisition processes used by the scanner. Therefore a system has been demonstrated that would make it possible to relate pixel information from different positions within the image and between images acquired using different scanner settings.

1.8.3.1. Imaging reflection from interface between MAGIC gel and reflector

A processing system has been developed to identify and quantify the reflections from interfaces between MAGIC gel and the inert reflector obtained using a standard ultrasound scanner. Systems have been developed to identify the reflections from both an array of threads (Chapter 9) and a planar interface (Chapter 10). The reflections

from the planar interface analysed using the imaging system show the same changes with temperature and dose as previously identified. Maps of the reflection from a planar interface within a phantom that has received a complex irradiation pattern has been created and compared to the delivered dose distribution, for example see Figures 10.10 – 10.18.

1.8.3.2. Development of system capable of quantitative backscatter imaging

A system has been developed to identify the relationship between pixel values at different depths in an ultrasound image and between images acquired using different scanner settings as described in Chapter 11. A full calibration of the system using these techniques would enable quantitative backscatter imaging. The ability to relate pixel values in different positions and with different scanner settings is fundamental to the development of a dosimetry system based on a pulse echo ultrasound imaging system.

1.9. Publications and presentations

A number of publications and presentations have been prepared and delivered during the course of this research. Other aspects of the work are undergoing preparation for publication and presentation. Appendix A identifies the publications and presentations of this material that have been produced during the course of this research.

1.10. Thesis structure

Chapter 2 of the thesis reviews the existing literature on gel dosimeters and the work that has been performed on ultrasonic dosimeters. The measurement of fundamental ultrasonic properties of MAGIC gel are then considered in Chapters 3, 4 and 5 which consider in turn attenuation, speed of sound and density. Chapter 6 presents work on identifying and characterising a material to create dose dependent reflections, and Chapter 7 develops the measurement of gel properties at different temperatures. Chapter 8 identifies different phantom configurations that could be

considered, and records the development of a phantom based on threads of inert reflectors. Chapters 9 and 10 consider the imaging of phantoms based on threads or flat slabs of inert material using a commercial ultrasound scanner. Chapter 11 describes initial work performed on calibrating the scanner for quantitative backscatter imaging that could be used to determine reflection coefficient from pixel value.

2. Background

2.1. Polymer gel dosimetry

Considerable work on polymer gel dosimetry and the role of polymer gels in radiation therapy verification has been undertaken and reviewed by many authors, including McJury et al (2000) and Baldock et al (2010) and at the DosGel and IC3Ddose conferences, the proceedings of which are available in the Journal of Physics Conference series publications (Volumes 3, 56, 164 and 250).

Baldock et al (2010) trace a three stage process in the usage of polymer gels for dosimtery. Firstly, the process of fabrication of the polymer gel and creation of the phantom and calibration vials. Secondly, the irradiation of the phantom and calibration vials, and finally the scanning of the polymerised gel using an optimised imaging technique.

A number of different formulations of polymer gels have been used for dosimetry. Table 2.1 shows some of the formulations that have been used and references to their usage. The table does not show a comprehensive literature search of all formulations that have been used but is indicative of some of the main formulations and components. Many of these formulations have been used in other publications but for each formulation the first appearance in the literature has been selected as the reference where possible. The remainder of the gel formulations are made up of deionised water.

	PAG	**MAGIC**	**MAGAS**	**MAGAT**	**PAGAS**	**PAGAT**	**nMAG**	**nPAG**
Reference	Maryanski et al 1994	Fong et al 2001	De Deene et al 2002b	Venning et al 2005	De Deene et al 2002b	Brindha et al 2004	De Deene et al 2006	De Deene et al 2006
Gelatine	5%	8%	8%	8%	8%	5%	4-12%	3-9%
Acrylamide	3%				4.5%	4.5%		1-8%
BIS	3%				4.5%	4.5%	0-6%	0-8%
Methacrylic Acid		9%	9%	9%			2-8%	
Ascorbic Acid		2mM	5mM		5mM			
Copper Sulphate		0.08mM						
Hydroquinone		16mM				0.01mM		
THPC				10mM		5mM		
THP							2mM	5mM

Table 2.1. Selected published formulations of Polymer Gel dosimetry systems including content quantities. Where an absolute quantity is specified this is for a 1 litre batch of gel. BIS = N,N-methylene-bis-acrylamide, THPC = Tetrakis (hydroxymethyl) phosphonium chloride, THP = Bis[tetrakis(hydroxymethyl)phosphonium]sulphate.

There are a number of different classifications that can be applied to the polymer gel systems. The first is dependent on the gelling agent, the second on the monomer/cross-linker type and the third on whether there are oxygen scavengers present.

The first radiation sensitive gel systems were radiochromic systems based on the Fricke ferrous sulphate chemical system described by Gore et al. (1984a). These were incorporated into gelatine (Gore et al. 1984b) and agarose based gel systems (Appleby et al., 1987). Further refinements were made to the systems, for example by Ollson et al. (1989) and Schulz et al. (1990). When polymer systems were introduced these were initially based on agarose gels (Maryanski et al., 1993) and later developed with gelatine based systems (Maryanski et al., 1994). A third gelling agent polyvinyl alcohol (PVA) has been used with the Fricke radiochromic system (Chu et al. 2000, Hill et al. 2002) but has not undergone much investigation.

Two main monomer systems have been utilised within polymer gel dosimetry. Initial gel systems were based on Acrylamide monomers with some authors utilising N,N-methylene-bis-acrylamide (BIS) as a cross-linker. Subsequently other authors have utilised methacrylic acid as a less-toxic monomer. Data for the acute toxicity of acrylamide suggest an LD50 in rats of between 159mg/kg and 300mg/kg (http://www.epa.gov/chemfact/s_acryla.txt, downloaded 31 Oct 2012), for BIS is 390mg/kg (www.sigmaaldrich.com, Materials Safety Data Sheet Product M7279, accessed 31 Oct 2012) and for Methacrylic Acid is between 1320-2260 mg/kg (UNEP Publications, http://www.inchem.org/documents/sids/sids/79414.pdf, downloaded 31 Oct 2012). Senden et al (2006) introduce a number of other possible monomers with similar chemical structures to Acrylamide but reduced toxicity, however they still use the cross-linker BIS in their dosimeters.

Oxygen within polymer gel systems inhibits radiation induced polymerisation by the formation of peroxides. Gel systems such as PAG are manufactured in an oxygen free environment (nitrogen glove box or sealed nitrogen-filled reaction vessels) and use de-oxygenated water for making the gel solution. Other gel systems are ‘normoxic’ gels and do not require such specialised manufacturing equipment because they include an oxygen scavenger within the formulation. A number of different oxygen scavengers have been employed in an effort to optimise the ‘normoxic’ gels for

different readout procedures, such as Ascorbic Acid (with or without Copper Sulphate), Tetrakis (hydroxymethyl) phosphonium chloride (THPC) and Bis[tetrakis(hydroxymethyl)phosphonium]sulphate (THP).

A number of authors discuss the radiation induced polymerisation reactions that occur in various formulations, including De Deene et al (2002a). Baldock et al (2010) discuss the radiochemical yield of reactive intermediates from the radiolysis of pure water, and the reaction rate constants of various monomers and cross-linkers used in polymer gel formulations. The polymers gel formulations undergo a standard polymer chain and cross-linking process of initiation, propagation and termination and a number of processes for each of these steps are discussed by De Deene et al (2002a) for both Acrylamide and Methacrylic Acid based gel systems.

Baldock et al (2010) discuss in detail three methods of image acquisition and mention a fourth. The three main methods discussed are: Magnetic Resonance Imaging (MRI), optical CT and x-ray CT.

When considering the measurement of radiation dose by magnetic resonance imaging, three groups of proton pools can be considered, each of which affects magnetic resonance rate (Lepage 2001b). These groups are: (1) free and quasi-free protons from free water and unreacted monomers, (2) protons associated with the polymer network and (3) protons associated with the gel matrix. When a gel is irradiated, the number of protons in the first pool decreases and the number of protons in pool two increases. The relaxation rates of protons within each pool and the exchange of protons between each pool determine the characteristics of the relaxation curve that the polymer gel exhibits. Careful selection of imaging parameters and appropriate image processing enable the creation of quantitative R_2 (transverse relaxation rate) maps which can then be converted into a dose image by appropriate calibration.

The second imaging method discussed by Baldock et al. (2010) is optical CT. This method is based on the observation that the transparent unirradiated gel becomes increasingly opaque as it is irradiated due to scattering of light by the polymer particles. The measured light intensity along a ray-path is related to the line integral of the optical attenuation coefficient (μ) along that ray path. Measurements of light intensity along different ray paths at different rotation angles through the sample can be recombined

through the process of filtered back-projection to reconstruct the spatial variation of the attenuation coefficient. The attenuation coefficient map can be converted to dose by appropriate calibration. Two basic types of optical CT systems are discussed by Baldock et al (2010). The first is a scanning laser system first introduced by Gore et al (1996) where the laser is scanned across the sample to obtain a 1-D projection, and then the sample is rotated to sample another projection. After a full set of projections are acquired another slice can be acquired by repositioning the sample or resetting the laser scan height. The second type of device utilises broad beam light sources in either a fan-beam (Wolodzko et al 1999) or parallel beam (Doran et al 2001) configuration utilising CCD or CMOS detectors. This geometry enables faster image acquisition than a single laser beam, but due to the nature of the optical attenuation being caused by scattering rather than absorption they have limited use in polymer gel dosimetry. When an area detector is used, scattered light is also collected by the detector and so straight ray-path geometry cannot be assumed from the source, and hence the reconstruction of the position at which the attenuation occurs cannot be calculated. Other dosimeter types, which attenuate the light by absorption alone have been successfully imaged on these systems. The optical systems suffer in particular from reflection and refraction of light from the walls of the dosimeter, and several correction and minimisation techniques are discussed by Baldock et al. (2010) and the references therin.

The third imaging mechanism identified by Baldock et al. (2010) is X-ray CT, where small changes in linear attenuation coefficient can be observed in the CT number in the derived image. It has been shown that the linear attenuation coefficient and CT number are directly proportional to mass density (Trapp et al 2001). Measurements of mass density of various polymer gel systems indicate that density increases with radiation dose. These changes in density with dose are small and therefore produce low contrast images when imaged using X-ray CT. Various methods of increasing contrast-to-noise ratio are discussed by Baldock et al. (2010) as well as the radiation polymerisation from the X-ray CT procedure itself.

Ultrasound imaging is also mentioned by Baldock et al. (2010), based on Ultrasound tomography of transmission and time of flight measurements, although this is not described in detail.

Baldock et al. (2010) also discuss various aspects of Polymer Gel dosimetry affecting the accuracy and precision of measurements. Each step in the gel dosimetry experiment is analysed for potential sources of error. The response of the gel dosimeter is dependent on the gel composition and also on thermal effects during the manufacturing and storage process, as shown by De Deene (2006) and Dumas et al. (2006). There are potential sources of error from the radiation output and positioning of the phantom and calibration phantoms during the irradiations. The stochastic nature of the radiation induced chemical reactions will also introduce sources of error. Errors in the scanning process may come from thermal noise in the imaging equipment, from processing of the data or from imaging artefacts. Finally the conversion from measured data to dose involves a calibration pathway similar to that of the 3D phantom and will itself by subject to similar error sources.

Baldock et al. (2010) review two parameters that can be used to analyse the results of polymer gel dosimetry. The first is the gamma index introduced by Low et al. (1998) which gives an overall parameter at each measurement position of the dosimetric and spatial accuracy by combining a distance-to-agreement and dose difference between an experimental and reference dose distribution. Baldock et al (2010) argue that gamma analysis must be applied in polymer gel dosimetry only where clinically appropriate and as an additional analysis alongside dose difference and distance-to-agreement maps. They also review the concept of dose resolution (Baldock et al. 2001) which is defined as the minimum detectable dose difference for a given confidence level.

Finally Baldock et al. (2010) discuss the areas to which polymer gel dosimetry has been applied. They pay particular attention to the role of polymer gel dosimetry in external beam radiotherapy, both as a way of verifying the full 3D dose distributions from IMRT class solutions, in routine quality assurance of IMRT treatments where 1D or 2D detectors may not always be able to resolve machine failure or drifts, and in the assessment of set-up errors in the whole radiotherapy pathway. They also discuss the applications and review the literature regarding the use of polymer gel dosimetry in the measurement of the dose distribution from brachytherapy sources, the measurement of proton and heavy ion beams, the dose from Boron-neutron capture therapy using a PAG gel doped with boron, and usage in radionuclide and diagnostic dosimetry.

2.2. Ultrasound gel dosimetry

Two ultrasonic methods of imaging polymer gel dosimeters have been discussed in the literature. The first method proposed and investigated by Mather and Baldock (2003) utilises ultrasound computed tomography, where transmission measurements through a cylindrical polymer gel phantom are made and back-projection methods are used to reconstruct an image of attenuation or speed of sound at each voxel. The second method utilises ultrasound elastographic methods to image elastic moduli of the gel (Crescenti 2009, Crescenti et al 2010).

2.2.1. Ultrasound computed tomography

Similarly to optical CT and X-ray CT, ultrasound computed tomography (UCT) is based on the measurement of the energy propagated through an object from a source. In UCT the slower speed of sound (compared to the electromagnetic radiation used in optical and x-ray systems) enables not only the attenuation but also the time of flight to be measured through the object. Hence, using reconstruction techniques it is possible to map both the attenuation coefficient and refractive index of the object (Kak and Slaney, 1988).

An ultrasound source is directed at the sample and measurements of the ultrasonic signal are made using a transducer located on the far side of the object. Beer's Law states that the change in amplitude of a signal passing through an infinitesimally small length of attenuating material is accounted for by the attenuation coefficient α at that point. Integrating Beer's law along the signal path S from point z_1 to point z_2 gives

$$ln\ \frac{A}{A_0} = -\int_{z_1}^{z_2} \alpha(x, y)\, dS \qquad (2.1)$$

where A_o is the initial amplitude at point z_1 and A is the measured amplitude at point z_2. Here $\alpha(x, y)$ is the attenuation coefficient of the sample at coordinates (x, y).

Similarly, following Kak and Slaney (1988), the time shift t_{delay} introduced by the presence of the sample is given by the line integral along the signal path L

$$t_d = \frac{1}{c_{ref}} \int_{z_1}^{z_2} [n(x, y) - 1]\, dL. \qquad (2.2)$$

where c_{ref} is the speed of sound in the reference medium (usually water) and $n(x, y)$ is the refractive index of the sample at coordinates (x, y) compared to the reference material

$$n(x,y) = \frac{c_{ref}}{c(x,y)}. \tag{2.3}$$

Here $c(x, y)$ is the phase velocity of sound in the sample at coordinates (x, y).

The amplitude A and phase shift t_{delay} can be measured for multiple ray paths through the object by translating and rotating the object and/or transducer and receiver. With data from sufficient numbers of ray paths then it is possible to reconstruct the data for attenuation or refractive index for all coordinates on plane (x, y).

Two methods of reconstructing the data exist; filtered back-projection and iterative reconstruction. Due to the effects of refraction, scattering and diffraction a straight ray path cannot be assumed in ultrasound CT, leading to errors when utilising a filtered back-projection reconstruction technique. However, Mather and Baldock (2003) state that for a non-scattering material with minimal changes in acoustic impedance then the errors in assuming straight ray propagation are small.

Both the ultrasonic speed of sound (Mather et al. 2002) and the ultrasonic attenuation coefficient (Mather et al. 2002, Mather et al. 2003, Crescenti et al. 2007) have been shown to vary with radiation dose. Therefore the use of ultrasound computed tomography to measure attenuation and phase shift related data should result in an image that can be correlated to radiation dose.

Mather and Baldock (2003) used ultrasound computed tomography to produce images of a square 4 cm x 4 cm irradiation of a PAG polymer gel dosimeter. They collected 80 scan lines at 1mm spacing for 180 projections around a phantom using a single element transducer to produce an ultrasound pulse and collected data with a needle hydrophone. They used a filtered back-projection method to produce two images, one of transmission properties and one of time of flight.

2.2.2. Measurement of elasticity using ultrasound

A number of techniques aimed at assess shear elastic modulus in a medium from ultrasound images exist. When an external stress (S) is applied to a material it induces a strain (e). The Young's Modulus (E) of the tissue is defined as

$$E = \frac{\sigma}{e}. \qquad (2.4)$$

If different parts of the imaged medium have different Young's moduli, then they react to the applied stress in different ways. For example, a stiff lesion within a softer surrounding will deform less (have a smaller strain) than the surrounding material. Ophir et al. (1991) identify two techniques for producing maps of elastic properties from ultrasound images. They identify "Sonoelasticity" as the measurement of the velocity of propagation of low frequency shear waves using Doppler velocity measurements and they define a second methodology based on cross-correlation between images to identify the displacement of tissues under stress.

There are a number of ways of generating the force to generate the stress in the medium. In discussion *in-vivo* imaging Ophir et al. (1996) identify internal excitation as motion generated in the subject for example by arterial motion. Other methods involve the deformation of the tissue using the ultrasound transducer itself or with some other external mechanical stimulator. A third method of applying force using ultrasonic radiation force has been described by Nightingale et al. (2000). Unless the magnitude of the applied force is known, then the resultant images are qualitative only and the tissue elasticity cannot be determined.

For a shear wave passing through a material the elasticity can be determined from the shear wave speed, since Young's modulus

$$E = 2(1+\upsilon)\rho c_s^2, \qquad (2.5)$$

where υ is Poisson's ratio, ρ is the material density and c_s is the shear wave speed (Bayón et al. 2005). This enables a direct measurement of the elasticity if the shear wave speed can be measured and Poisson's ratio and the material density is known. Shear waves propagate more slowly than compressional waves and therefore the measurement of the shear wave speed by ultrasonic imaging of the wave front is possible.

Recently a commercially available scanner based on shear-wave propagation has been made available by Supersonic Imagine S.A (Aix en Provence, France). This system utilises a ultrasonic pulse to generate a shear wave in the medium and then images at high frame rates (thousands of frames per second) to measure the propagation of the shear wave front and produce a map of elasticity in the medium (ShearWave™

Elastography White Paper, Supersonic Imagine). One fundamental assumption in the system is that the imaged material is approximately incompressible, having a Poisson's ratio of 0.5, so that shear wave speed can be related directly to Young's Modulus.

Crescenti et al (2009a) demonstrated that Young's Modulus was dose dependent by mechanically measuring the Young's Modulus of irradiated polymer gels.

Elastographic measurement based on statically applied external forces Crescenti (2009b, Crescenti 2009) and ShearWave^{TM} Elastography (Crescenti 2009) have been used to measure simple radiation dose distributions. Crescenti et al. (2009b) demonstrate images of a 10 mm × 10 mm irradiation of a MAGIC polymer gel dosimeter using a statically applied force and an inverse reconstruction method was used to calculated Young's modulus. Crescenti (2009) uses the same image acquisition setup to produce images of more complex dose distributions, and also demonstrates the usage of the ShearWave^{TM} Elastography in the measurement of radiation sensitive polymer gels on the assumption that polymer gels are approximately incompressible.

2.3. Criteria for analysing project outcomes

De Wagter (2004) outlined the essential characteristics of a 3D dosimetry system, as summarised in Section 1.5. The work reported in this thesis focuses on demonstrating a system that can determine the full 3D volumetric data in terms of both absolute dose and positional accuracy so that it can be compared to a calculated dose distribution. It also discusses the reliability and reproducibility of such a dosimetry system. The choice of ultrasonic readout method and the usage of MAGIC gel dosimeters aim to ensure that the system is reasonable in cost and low in toxicity compared to alternatives.

To be able to use a dosimetry technique clinically it should be able to determine the magnitude and location of the radiation dose distribution. This is so that an independent system (from the calculation and delivery system) can be used to identify errors in either or both the geometrical accuracy of the radiation delivery and the absolute dose level delivered. There are two aspects of measurement of dose that are important in a dosimetry system, the ability to measure a known radiation dose accurately (absolute accuracy), and the ability to distinguish between different dose

levels in a distribution (precision). In radiation dosimetry gamma analysis (Low et al., 1998) is often used to determine either the distance-to-agreement or the level of agreement between dose distributions (measurements or calculations). The gamma value is calculated at each point within the dose distribution, where the distance-to-agreement is the shortest distance between corresponding dose levels in the two distributions and the level of agreement is the dose difference between the two distributions at that point. In this case a precise system is required to ensure that the different dose levels can be distinguished. It is helpful if the system is also absolutely accurate otherwise a cross-calibration or alternative absolute measurement is also required. When comparing dose distributions, gamma criteria of 3 mm and 3% respectively are often used to determine whether the two dose distributions are similar (Nelms and Simon, 2007), although many different criteria have been applied in different clinical situations (for example see James et al., 2008, Both et al., 2007) and the actual criteria that are used should be selected according to the clinical situation. For the purposes of this study since most clinical criteria will require 3% and 3 mm or better, an excellent outcome would be to produce a system that could determine radiation dose distributions to a precision of 3% and a distance of 3 mm or better. A good outcome for this project would be to produce a system that would be to be able to determine dose distributions with a precision of 10% and a distance of 10 mm as this would show that the system, with further development, may be able to be clinically useful. A system that falls short of the 10% and 10 mm level would require significant development to produce a system that may be clinically usable, and therefore consideration should be made as to whether other systems may be more worthy of the investigative effort.

3. Measurement of ultrasonic attenuation coefficient

3.1. Introduction

Ultrasonic backscatter imaging is based on reception of low amplitude ultrasound signals that are reflected from inhomogeneities in the sample from an initial ultrasound signal, usually produced by the same transducer. The amplitude of the received signal is dependent on both the strength of the reflection and also losses to both the outgoing and reflected signal. The losses of an ultrasound wave passing through a homogeneous medium are characterised by the attenuation coefficient of that medium.

Therefore it is important to understand how the ultrasonic attenuation of MAGIC gels is affected by radiation dose if a pulse echo method is to be used for measuring radiation dose. Any measurement system based on a pulse echo method will require signals to be corrected for any attenuation that they have been subjected to by their passage through the gel, otherwise the dose may be incorrectly calculated, especially if the attenuation is dose dependant.

3.2. Theory

For sound waves travelling through real materials the wave undergoes scattering and absorption processes. For uniform media this means that the amplitude of a wave that has travelled a distance x through a material is reduced from its initial amplitude by a constant factor per unit path length. For a wave with initial pressure amplitude P_0 and pressure amplitude P after propagating a distance x cm the amplitude attenuation coefficient can be expressed as

$$\alpha = -\frac{20}{x}\log_{10}\frac{P}{P_0} \qquad (3.1)$$

with units of dB cm^{-1}. The relaxation processes that contribute to the absorption of the wave are frequency dependent, therefore α is also frequency dependent.

A wave produced by a focusing transducer and passing through a water path and a sample, as used in our measurement for attenuation, also undergoes diffraction and interface losses. Following the notation of Xu and Kaufman (1993), the amplitude spectrum of the received waveform after propagating through a distance z (the transducer separation) is given by

$$A_S(f, z) = \Gamma(f) D_d^S(f, z) \Xi_T(f)\, \Xi_R(f) \Pi_I(f) V(f) \tag{3.2}$$

where $\Gamma(f)$ is the reduction in acoustic amplitude due to attenuation in the sample, $D_d^S(f, z)$ characterizes the reduction in amplitude of the ultrasound pulse as a result of diffraction for the water-sample-water path, $\Xi_T(f)$ is the transmitter response function, $\Xi_R(f)$ is the receiver response function, $\Pi_I(f)$ is the transfer function due to interface losses and $V(f)$ is the amplitude spectrum of the input signal.

For a water path only the amplitude spectrum of the received waveform is given by

$$A_W(f, z) = D_d^W(f, z) \Xi_T(f)\, \Xi_R(f) V(f) \tag{3.3}$$

where $D_d^W(f, z)$ characterizes the diffraction of the ultrasound pulse by the water-only path.

An estimation of $\Gamma(f)$, the reduction in amplitude spectrum due to the sample attenuation, can be obtained from the ratio of $A_S(f, z)$ to $A_W(f, z)$ giving

$$\frac{A_S(f,z)}{A_W(f,z)} = \frac{\Gamma\ f) D_d^{\,s}(f,z) \Pi\ \ f)}{D_d^{\,w}(f,z)}. \tag{3.4}$$

The interface losses can be dealt with in two ways. Either samples of differing thickness can be measured and $\Gamma(f)$ calculated from the slope of a plot of the ratio of $A_S(f, z)$ to $A_W(f, z)$ against sample thickness, or by measuring $A_W(f, z)$ with a sample holder filled with water in the position of a sample. In this project samples of differing

thickness were used as this also accounts for any surface effects of the samples in a similar way to the interface losses.

The difference in the diffraction effects for the sample and water paths can also be dealt with in two ways. Firstly, diffraction patterns can be modelled and theoretical corrections applied. There are a number of reports of these methods in the literature (Xu & Kaufman, 1993; Seki et al., 1956; Zequiri, 1996). Secondly, the change in diffraction can be minimized by minimizing the effect of the difference in path lengths for the reference and attenuated measurements using a buffered insertion technique. For fixed frequency systems this can be achieved by placing the two transducers at a position of diffraction maxima or minima, thereby reducing any change in diffraction loss (Bamber, 2004a; Penttinen & Luukkala, 1977). This second method is the one selected in this project to reduce the diffraction errors associated with attenuation measurement due to its simplicity.

To calculate $\Gamma(f)$, the reduction in signal amplitude due to attenuation in the sample, either the Fourier transform of an impulse signal can be used, or multiple measurements using single frequency 'tone bursts' can be used. In this project multiple measurements of single frequency 'tone burst' excitations were used as this enabled a larger frequency range to be investigated while maintaining adequate signal to noise ratio at frequencies other than the transducer resonance; this approach also enabled low amplitude signals to be used thus ensuring quasi-linear conditions were maintained through the entire path length between transducers.

Finally, the frequency dependant attenuation coefficient $\alpha(f)$ of the sample media can be calculated from the measured reduction in signal amplitude and the sample thickness, x, according to equation 3.1.

3.4. Materials and methods

3.4.1. Gel manufacture

Gels were manufactured as described by Fong et al. (2001). To make a 1 litre batch of dosimetric gel, 80.0g of 300 bloom gelatine (Sigma Aldrich, Poole) was dissolved in 700ml distilled water. The solution was heated to 50ºC using a

thermostatically controlled heater and a magnetic stir bar was used to continuously stir the solution. The solution was kept at 50ºC until the gelatine had dissolved and the solution was clear. Then 2.0g Hydroquinone (Sigma Aldrich, Poole) in 48ml distilled water was added. The mixture was then allowed to cool to 37ºC, at which point 0.352g Ascorbic Acid (Sigma Aldrich, Poole) in 50ml distilled water, 0.020g Copper Sulphate pentahydrate (Sigma Aldrich, Poole) in 30ml distilled water and 90g Methacrylic Acid (Sigma Aldrich, Poole) were added. The gels were manufactured in a fume cupboard.

3.4.2. Gel holders

The results reported in Appendix B were used guide the design of a measurement system to measure gel attenuation. Sample holders of three different nominal thicknesses were designed and constructed. The sample holders were made of 3 perpex blocks as shown in Figure 3.1. Each block had a hole of radius 19mm cut in the centre. This size was selected so the small sample size estimate of the receiver response would be greater than 0.98. (In Appendix B this is calculated as ensuring the ratio $|p_{\mathrm{rec}}(z_T, R)| / |p_{\mathrm{rec}}(z_T)|$ is greater than 0.98). The centre blocks were manufactured in three different thicknesses to give the different nominal thickness of the samples and were to contain the gel itself. A piece of 0.18mm thick Mylar film was used either side of the central block to create the outer surface of the mould and the two thin outer blocks held the films in place. The elements were held together using Nylon nuts and bolts. In the centre element a hole was drilled to enable the holders to be filled with the gel solution after the holders were assembled. Once filled with gel the holes were covered with two layers of PVC insulation tape to seal the hole and to reduce the potential for oxygen contamination of the gels. The filling hole had the additional benefit that any small gas bubbles in the gel rose to the top of the holder and into the filling hole prior to the gel setting and therefore did not cause any attenuation or scattering of the ultrasound signal. The gel holders were designed in conjunction with, and constructed by, Dr Michael Hillman and Mr Martin Rouse of Designability (Bath Institute of Medical Engineering).

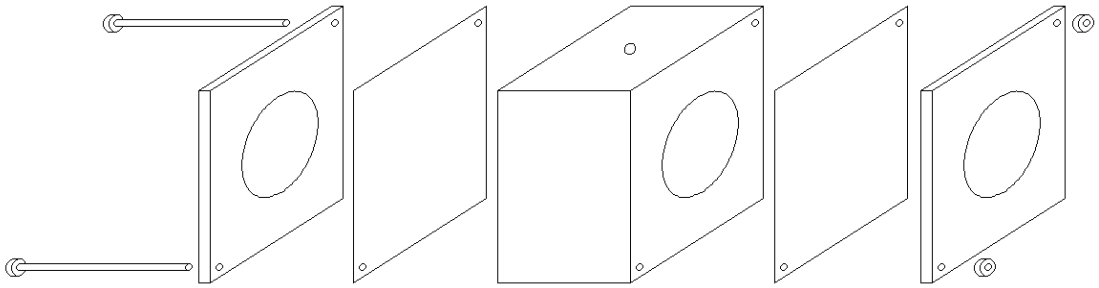

Figure 3.1. Diagram showing the construction of the gel holders. The central element was filled with gel through the filling hole, with acoustic windows provided by Mylar film. The film was held in place by the outer plates and the entire structure held together by two Nylon nuts and bolts.

3.4.3. Gel handling and irradiations

For each batch of MAGIC gels produced, once the gels had been poured into the containers they were cooled to room temperature and then refrigerated for approximately twenty-four hours. The samples were then irradiated using a Siemens Primus 6MV linear accelerator (Siemens AG, Erlangen, Federal Republic of Germany). The gel samples were placed in turn in a water tank, which provided build up and scattering so that a uniform dose was received by each sample. After irradiation the gel samples were returned to the refrigerator for approximately forty-eight hours prior to measurement.

3.4.4. Measurement system

Two weakly focused single element ultrasound transducers with a centre frequency of 3.5MHz were used with a temperature controlled water tank to measure attenuation. One transducer was coupled to the outside of the tank at a fixed position on an acoustic window, with ultrasound coupling gel used to ensure good ultrasonic transmission into the tank (see Figure 3.2). The second transducer, within the water tank, was attached to a micromanipulation stage so that the transducers could be correctly aligned and the separation adjusted to ensure that the transducers were at a diffraction maximum. The temperature of the water tank was maintained at a constant temperature using a Grant GD100 digital immersion thermostat (Grant Instruments Ltd, Cambridge, UK). All measurements were made at 25.0 ± 0.1°C, with the water tank

being filled with distilled water. The gel samples were mounted in turn in a re-locatable frame in the water tank. The micromanipulation stage, transducer holders and sample mounting frame were designed in conjunction with, and constructed by, Dr Michael Hillman and Mr Martin Rouse of Designability (Bath Institute of Medical Engineering).

A tone burst signal generated by an Agilent 33220A signal generator (Agilent Technologies, Inc., Santa Clara, CA) was amplified using an ENI 240L RF Power Amplifier (ENI, Inc., Rochester, NY) and applied to the transmitting transducer. The received signal from the ultrasound attenuation measurement system was digitized using a PicoScope 3206 digital PC Oscilloscope (Pico Technology Ltd, St Neots, Cambridgeshire, UK). The frequency of the tone burst was varied from 2 MHz to 5.5 MHz with the length of pulse being varied with frequency as well. Data from 100 ultrasound pulses were recorded for each sample.

The amplitude of each tone burst frequency was selected to ensure that quasi-linear conditions still existed in accordance with the published recommendations (International Electrotechnical Commission (IEC), 2007; Duck, 2002). Measurements of the transducer characteristics with different amplitude toneburst signals were made with an Ultrasound Beam Calibrator (Preston, 1998). Measurements of acoustic pressure (peak rarefactional and peak-compressional) for different drive amplitudes, as well as acoustic working frequency and local area factor were made according to IEC 2007 and used to calculate the local distortion parameter at the focus. The maximum drive amplitude consistent with a focal distortion parameter of less than 0.5 was then chosen as the drive amplitude for subsequent measurements.

The signals were analysed in Matlab R12.1 (The Mathworks, Inc., Natick, MA), where a steady state region of the toneburst was selected and an FFT performed to compute the amplitude of the signal at the frequency of the tone burst. An example of the Matlab code used for analysing the signals is contained in Appendix C1.

Later, the PicoScope 3206 digital PC Oscilloscope was replaced by a National Instruments NI-5133 USB Oscilloscope (National Instruments Corporation, Austin, Texas) and analysis was also performed using National Instruments Labview Signal Express 3.0.

A photograph of the experimental setup is shown in Figure 3.3.

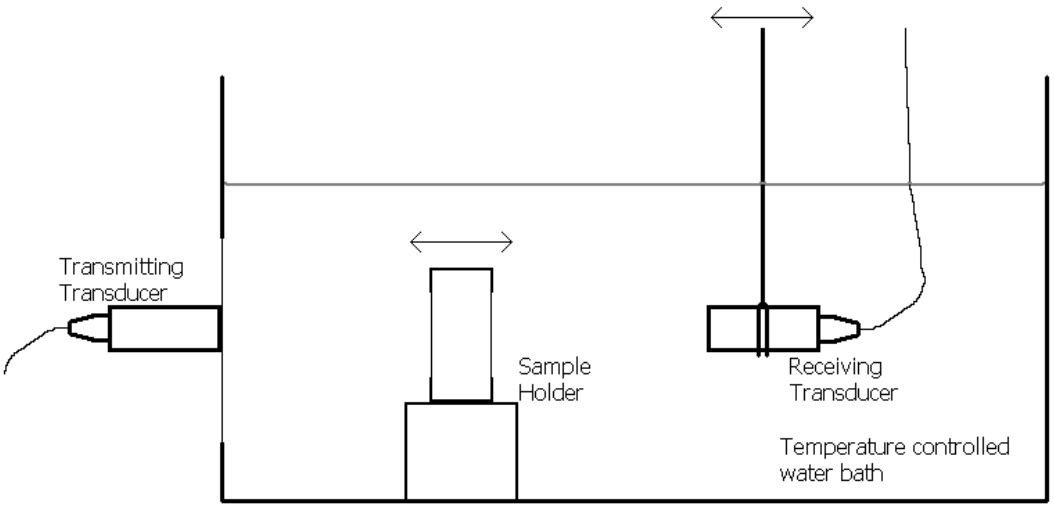

Figure 3.2. Diagram of the measurement apparatus for attenuation measurements. The transmitting transducer was clamped to the outside of the water tank and acoustically coupled using ultrasound gel. The samples were placed in turn in a re-locatable frame in the tank. The receiving transducer was mounted on a micromanipulation stage.

Figure 3.3. Photo of the measurement apparatus for attenuation measurements. The water tank containing the samples is shown on the right of the photograph. The pulse generating system is in the centre, with the laptop used to store the received signals is shown on the left.

3.4.5. Temperature dependence of attenuation coefficient

As the project progressed, it became apparent that the physical properties of MAGIC gels exhibit significant temperature dependence. Therefore measurements of

ultrasonic attenuation coefficient were made at different temperatures and doses. Temperature was controlled using a Grant GD 100 Immersion Thermostat (Grant Instruments Ltd, Cambridge, UK) and a Grant C1G Refrigerated Immersion Cooler attached to the water tank.

3.5. Results

Figures 3.4, 3.5 and 3.6 show the results of measurement of attenuation coefficient for 3 different batches of gels. The attenuation coefficient appears to increase with both irradiated dose and ultrasound frequency. The error bars shown are one standard error in the mean of the attenuation coefficient for each dose-frequency combination calculated from regression analysis of the results for the three thicknesses of gel sample that were irradiated to that dose.

Figures 3.7, 3.8 and 3.9 show the measured variation of attenuation coefficient with temperature for gels irradiated to 3 different dose levels. The attenuation coefficient decreases with increasing temperature. The increase in attenuation coefficient with ultrasound frequency is also demonstrated at each temperature.

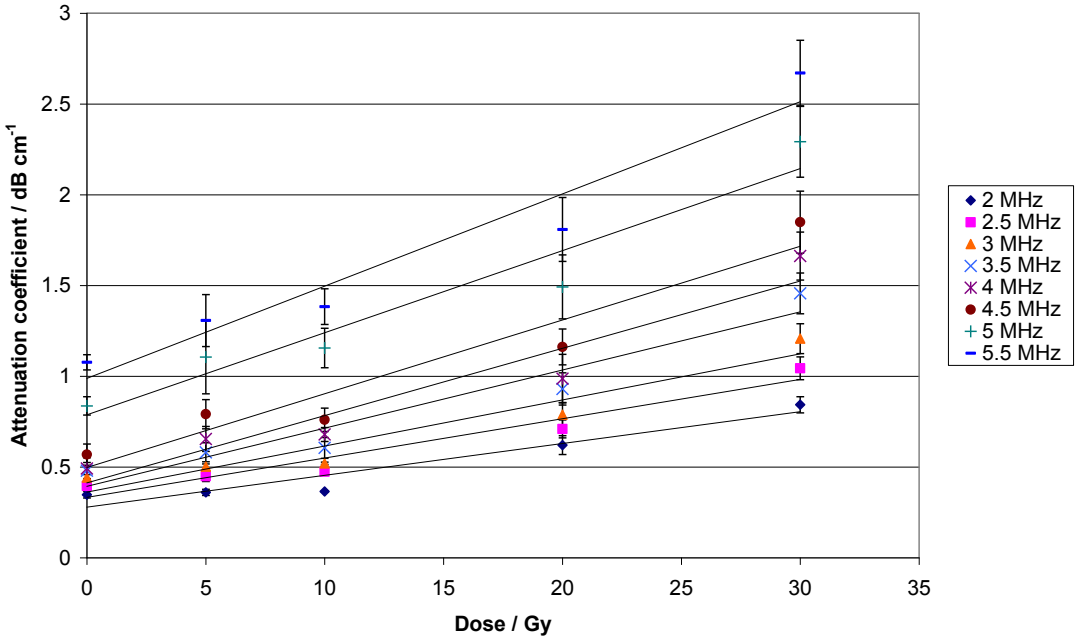

Figure 3.4. Attenuation coefficient measured at discrete frequencies (see key) for Batch 1 MAGIC gel irradiated to different doses at 25°C. Error bars are one standard error on the mean attenuation coefficient from three gel samples.

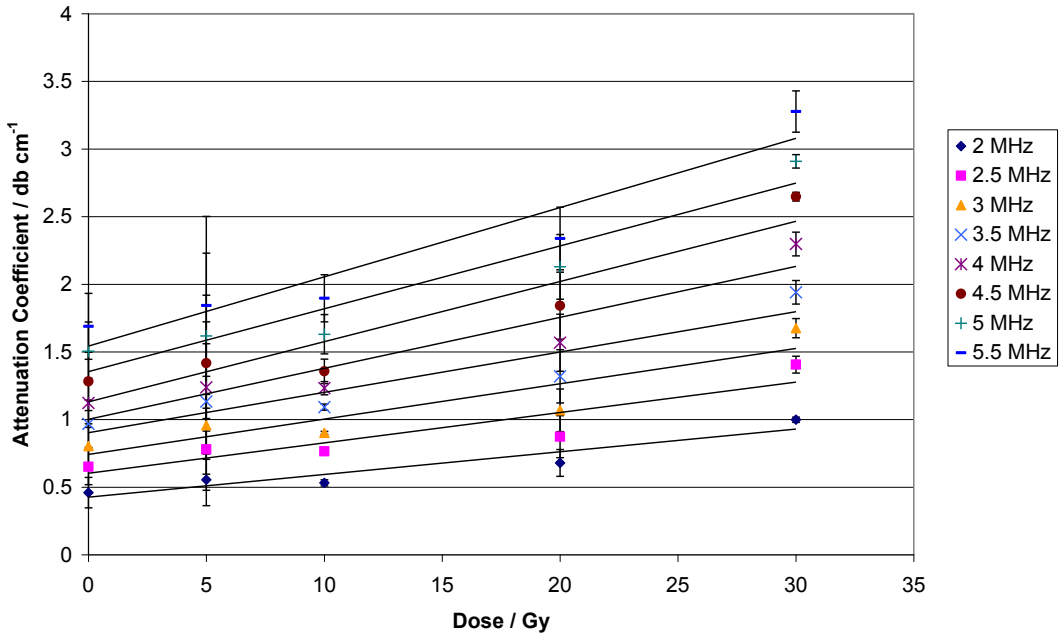

Figure 3.5. Attenuation coefficient measured at discrete frequencies (see key) for Batch 2 MAGIC gel irradiated to different doses at 25°C. Error bars are one standard error on the mean attenuation coefficient from three gel samples.

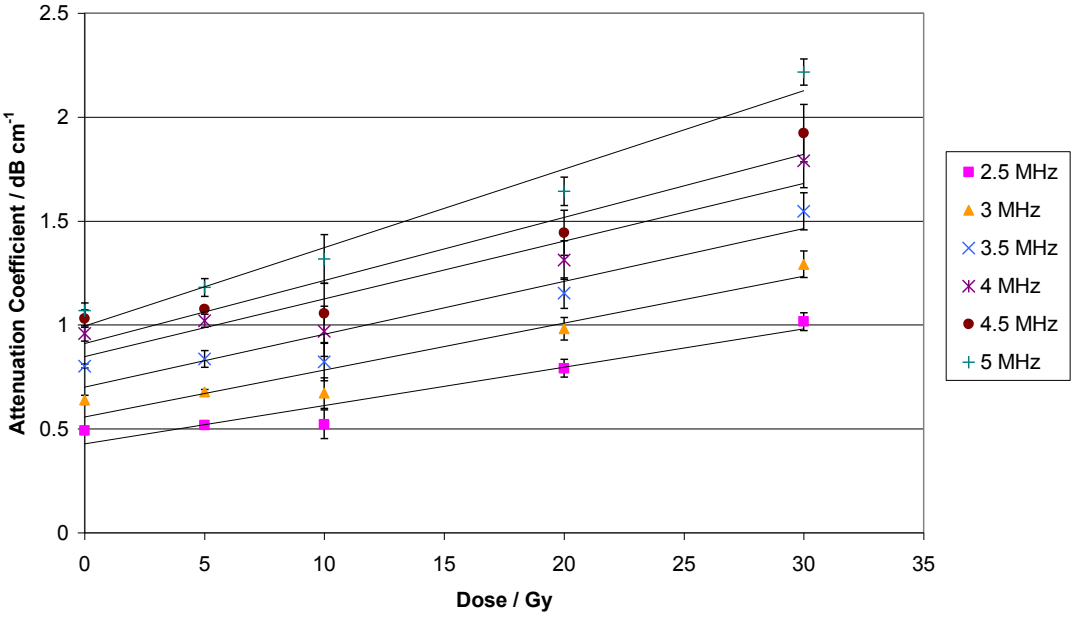

Figure 3.6. Attenuation coefficient measured at discrete frequencies (see key) for Batch 3 MAGIC gel irradiated to different doses at 25°C. Error bars are one standard error on the mean attenuation coefficient from three gel samples.

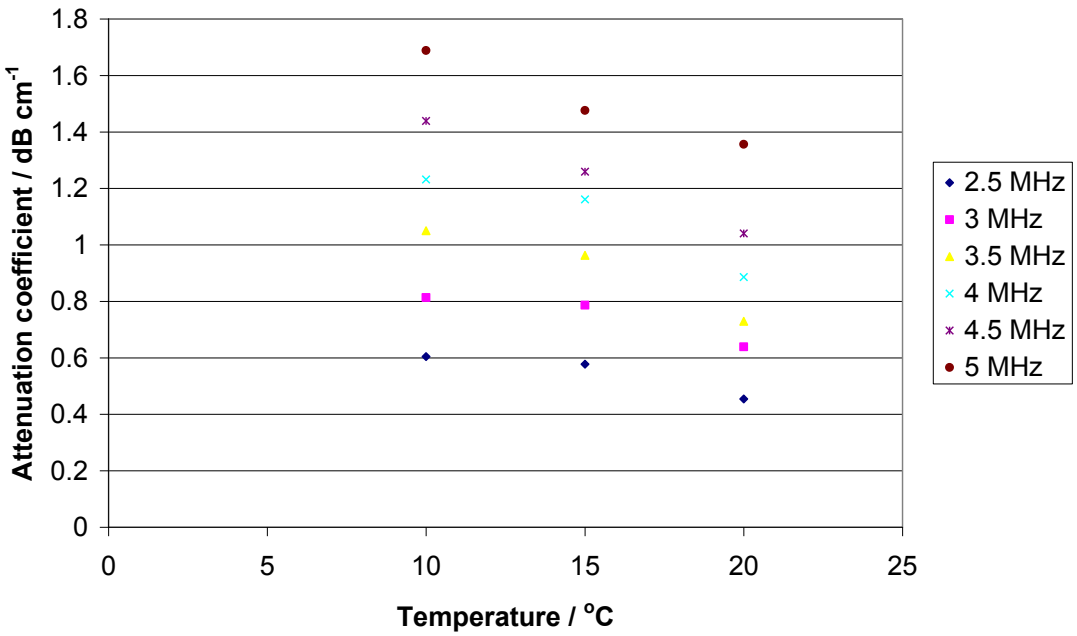

Figure 3.7. Variation in attenuation coefficient with temperature for selected frequencies (see key) for unirradiated MAGIC gel.

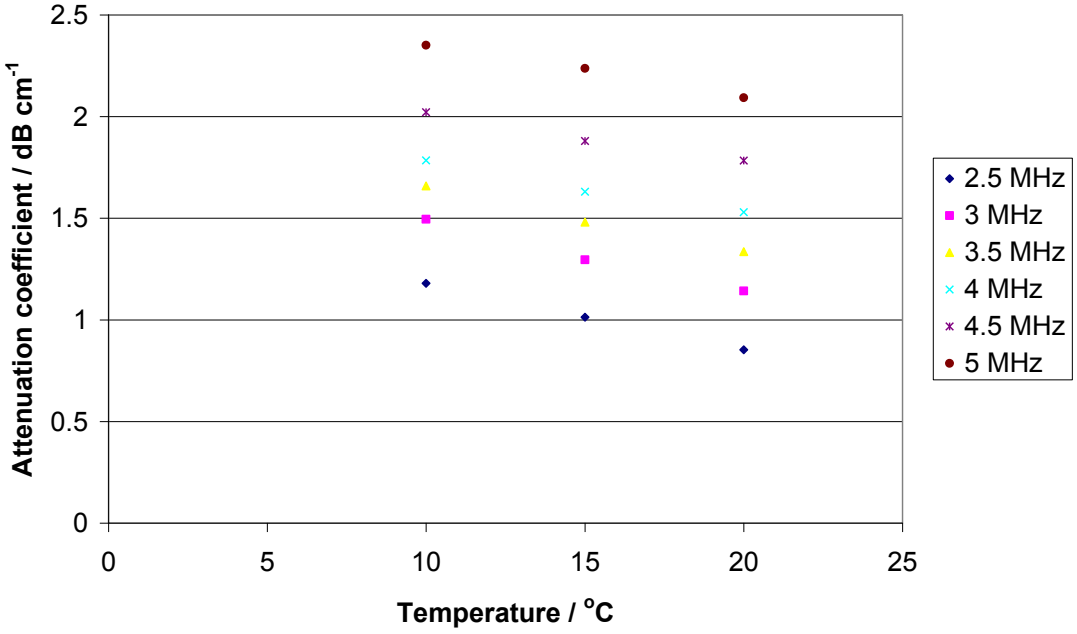

Figure 3.8. Variation in attenuation coefficient with temperature for selected frequencies (see key) for MAGIC gel irradiated to 10 Gy.

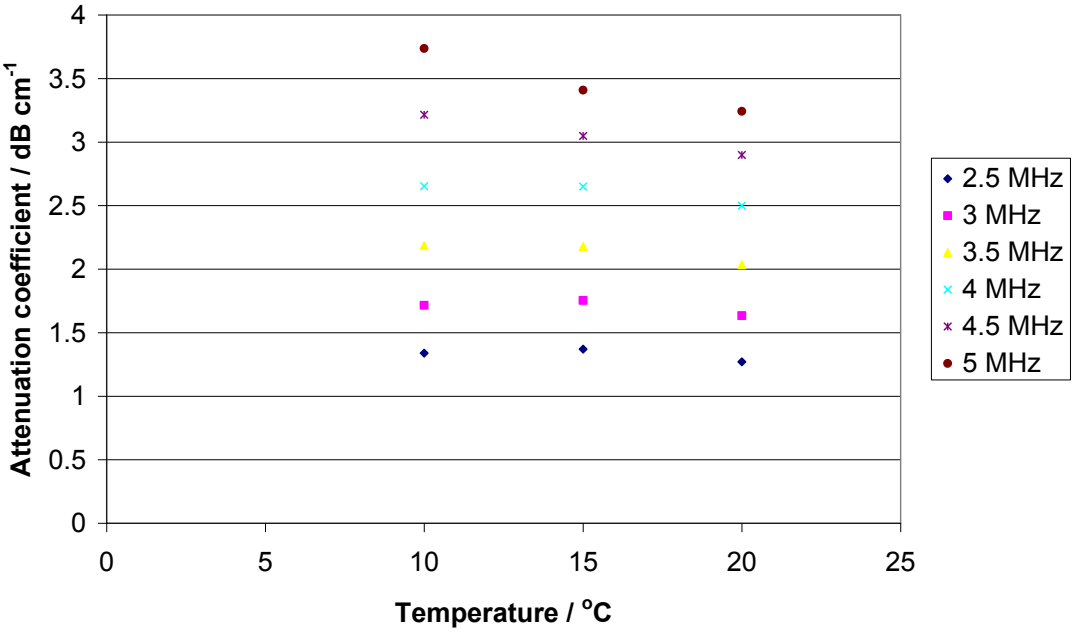

Figure 3.9. Variation in attenuation coefficient with temperature for selected frequencies (see key) for MAGIC gel irradiated to 30 Gy.

3.6. *Discussion*

Following Mather et al. (2002, 2003) and Crescenti et al. (2007) a linear fit has been applied to the graphs of attenuation coefficient as a function of dose.

Mather et al. (2002, 2003) found the attenuation coefficient of unirradiated gels to be 0.6 dB cm^{-1} and 1.25 dB cm^{-1} at 4MHz in their two papers respectively, while Crescenti et al. (2007) showed the attenuation coefficient of unirradiated gels to be between 1.0 and 1.4 dB cm^{-1} at 4.1 MHz. The three batches of gels here show an attenuation coefficient of unirradiated samples to be between 0.49 dB cm^{-1} and 1.12 dB cm^{-1} at 4MHz.

Slopes of 0.047 ± 0.003 dB cm^{-1} Gy^{-1} and 0.042 ± 0.003 dB cm^{-1} Gy^{-1} were reported by Mather et al. (2002, 2003) at 4MHz respectively. Crescenti et al. (2007) demonstrated a slope of between 0.045 dB cm^{-1} Gy^{-1} and 0.061 dB cm^{-1} Gy^{-1} at 4.1 MHz. Data collected in these experiments show a slope of between 0.028 dB cm^{-1} Gy^{-1} and 0.038 dB cm^{-1} Gy^{-1} at 4 MHz. The data from the three groups discussed here are summarised in Table 3.1.

Reference	Batch	Attenuation Coefficient Dose sensitivity / dB cm^{-1} Gy^{-1}	Error on Attenuation Coefficient Dose Sensitivity / dB cm^{-1} Gy^{-1}
Mather 2002		0.047	0.003
Mather 2003		0.042	0.003
Crescenti 2007	1	0.0530	
	2	0.0454	
	3	0.0608	
	4	0.0447	
This work	1	0.037	0.006
	2	0.038	0.008
	3	0.028	0.006

Table 3.1. Comparison of the dose sensitivity of attenuation coefficient for MAGIC gels measured at 4 MHz in literature and in the current work

It is observed that a linear fit may not be the most suitable for this data, or the data presented in the literature. At doses below 10 Gy the attenuation is low and does not change significantly with dose. Initially this was thought to be a problem with the measurement system and a number of possible sources of error were investigated. A potential problem with the PICOScope PC Oscilloscope was thought to be a cause of error, and so as a replacement the National Instruments NI-5133 was obtained and used on an independent set of measurements (Batch 3) which gave similar results to the previous two batches.

Further consideration of the data presented by Crescenti et al in the literature shows that only one Batch (Batch 1) of his data shows a significant change to the attenuation below 10 Gy. The other three batches presented show little change with attenuation at low dose. Such a non-linear behaviour of attenuation could be explained by the existence of two independent attenuation mechanisms, one of which is invariant with dose and the other being dose dependent.

If the attenuation of ultrasound by the MAGIC gels below 10 Gy can be characterized by a non dose-dependent parameter then this will significantly simplify the processing of the measurement of backscattered ultrasound data for dose dependence.

The results presented here show considerable batch variability, both in the attenuation of the unirradiated gel and the dose sensitivity of the attenuation. As part of

future development of ultrasonic gel dosimeters this will have to be considered and potentially a more stable and reproducible formulation for the dose dependent gel will have to be formulated.

For each dose level, it was observed that the attenuation coefficient decreased with increasing temperature. Combined with the observation that the attenuation increases with increasing frequency, this indicates that in the temperature and frequency range considered here the frequencies being used are below the relaxation frequency for the relaxation process dominating the absorption and attenuation in this temperature and frequency range.

There are a number of possible factors affecting the dose sensitivity of attenuation measurements reported here. These include the presence of bubbles in some samples, the thermal cycle undergone by the samples and the presence of oxygen within the samples.

If the samples contained small bubbles within the MAGIC gel, the presence of the bubbles will create additional scattering centres compared to a homogeneous sample. The additional scattering centres will increase attenuation compared to the expected attenuation from a homogenous sample. During the filling of each container, the elimination of bubbles from the sample was attempted, but may not have been completely successful. The presence of bubbles in some samples and not others will have contributed to random errors in the measured attenuation.

The thermal cycle undergone by the samples may have affected the measured attenuation. As each holder was filled with MAGIC gel, the gel in the holder will have started to cool at a higher rate than the bulk gel remaining in the manufacturing container. The three different thicknesses of sample holders will also have different thermal capacities, and therefore will also have affected the cooling rates. The ambient temperature of the room during the process of filling the holders will have affected the cooling rates as well. The temperature of the gels during the irradiation will be dependent on the ambient temperature at the time of irradiation. It is well known that temperature affects reaction rates, and the thermal cycle affects the physical properties of gelatine (for example, te Nijenhuis, 1981). Therefore the thermal cycle that the samples will have undergone will affect the attenuation of the samples due to the physical properties of the gelatine framework and the reaction rates during the

polymerisation process. Differences in the thermal cycle can introduce both systematic and random errors into the measured attenuation.

The presence of oxygen within the samples is know to inhibit polymerisation. Although the use of oxygen scavengers within the MAGIC gel preparation is made to reduce the affect of oxygen contamination, it is observable that significant surface effects still remain, where the available oxygen scavengers are overwhelmed by the amount of oxygen present in the sample. Therefore it is important to remove the oxygen from the sample. Although this was attempted by fully filling the samples and sealing them with multiple layers of tape, it was not always successful, and some oxygen contamination may have occurred in some samples. This will have contributed to random errors in the measured attenuation.

3.7. Conclusion

There is a wide variation in measured attenuation coefficients for MAGIC gel samples. Both measurements reported here and in the literature present wide inter-batch variability. The measurements presented here suggest that the attenuation coefficient may change non-linearly with dose and also has a strong temperature dependence. This suggests that when using large 3D phantoms that the attenuation of the ultrasound by the phantom itself will need to be carefully considered in the analysis. More investigation into the dose and temperature dependence of the MAGIC gel may need to be performed to ensure that corrections for ultrasound attenuation by the gel can be applied.

4. Measurement of ultrasonic speed of sound

4.1. Introduction

The sound power reflection coefficient for the reflection of ultrasound from an interface between two fluid materials is dependent on the characteristic acoustic impedences of the two materials. For a plane wave incident normally on a planar surface the Sound Power reflection coefficient is given by Kinsler and Frey (1962) as

$$\text{Sound power reflection} = \left(\frac{Z_2 - Z_1}{Z_2 + Z_1} \right)^{\wedge} \tag{4.1}$$

where Z_1 is the characteristic acoustic impedance of the material through which the ultrasound is passing and Z_2 is the characteristic acoustic impedance of the reflecting material.

The characteristic acoustic impedance of a material is the product of the density and the speed of sound of the material. Therefore, to be able to understand the reflections between MAGIC gel and another material it is important to understand how the speed of sound and density of the MAGIC gel is affected by radiation dose and other environmental properties.

A convenient way for measuring the speed of sound of a material is to use the time of flight of a sound pulse. This simplification ignores the complexities of dispersive effects which give rise to the need to consider both group and phase speeds. The complexities in such measurements arise from the difficulty of defining the pulse arrival time. If the pulse shape changes due to dispersion in the measurement medium, due to frequency dependence of speed of sound or attenuation, then the definition of a single point of reference is difficult. The definition of first arrival as the time that the signal can be distinguished from the background noise, and the time of the first zero crossing have both been utilized (Bamber, 2004b). In this work the first zero crossing was used as the definition of first arrival time as this was more reproducible when considering the different signal attenuation from the various samples. Different sample doses and thicknesses would cause different attenuation of the signal, and therefore the time at which the signal becomes distinguishable from background would be dependent on the attenuation of the signal. To illustrate this, in Figure 4.1, two signals are shown

based on a single sinusoidal pulse of duration 225 time units, one with amplitude of 1, and the other with amplitude 0.4. Randomly generated noise of amplitude 0.05 has been superimposed on the signals, and is shown in the figure. If the time of flight is based on the time that the signal is first distinguishable from the noise then the difference between the two arrival times is 2.5 time units compared to no difference using the first zero crossing.

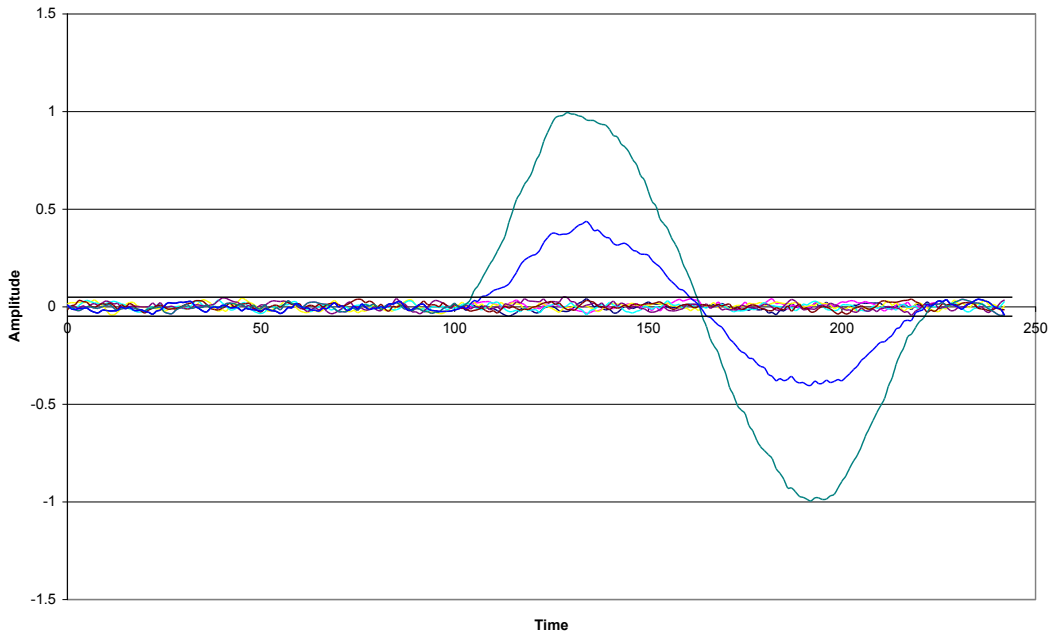

Figure 4.1. Illustration of the effect of noise and signal amplitude on the estimation of pulse arrival time. Maximum noise level is shown in black.

Diffraction effects also are important in measurement of ultrasonic speed, however when insertion measurements are carried out in biological tissues with the reference medium being water then diffraction effects are so small they can safely be ignored (Kaufman et al., 1995). A similar argument can be utilised for the small samples used in this project.

4.2. Theory

Measurements of sound velocity on gel samples are potentially sensitive to bowing of the gel windows and resulting uncertainty in the sample thickness. The first reverberation (multiple reflection) from within the gel sample can be used, along with

the direct path time of flight, to obtain a measurement of the speed of sound independent of the thickness of the sample.

Figure 4.2 shows a schematic diagram of the insertion method arrangement with two transducers immersed in a fluid bath and illustrates the quantities used in this note. The time taken for the ultrasound to travel from the source to receiver through the fluid alone, t_f is given by

$$t_f = \frac{x}{c_{ref}} \tag{4.2}$$

where x is the distance between the transducers and c_{ref} is the speed of sound in the reference fluid.

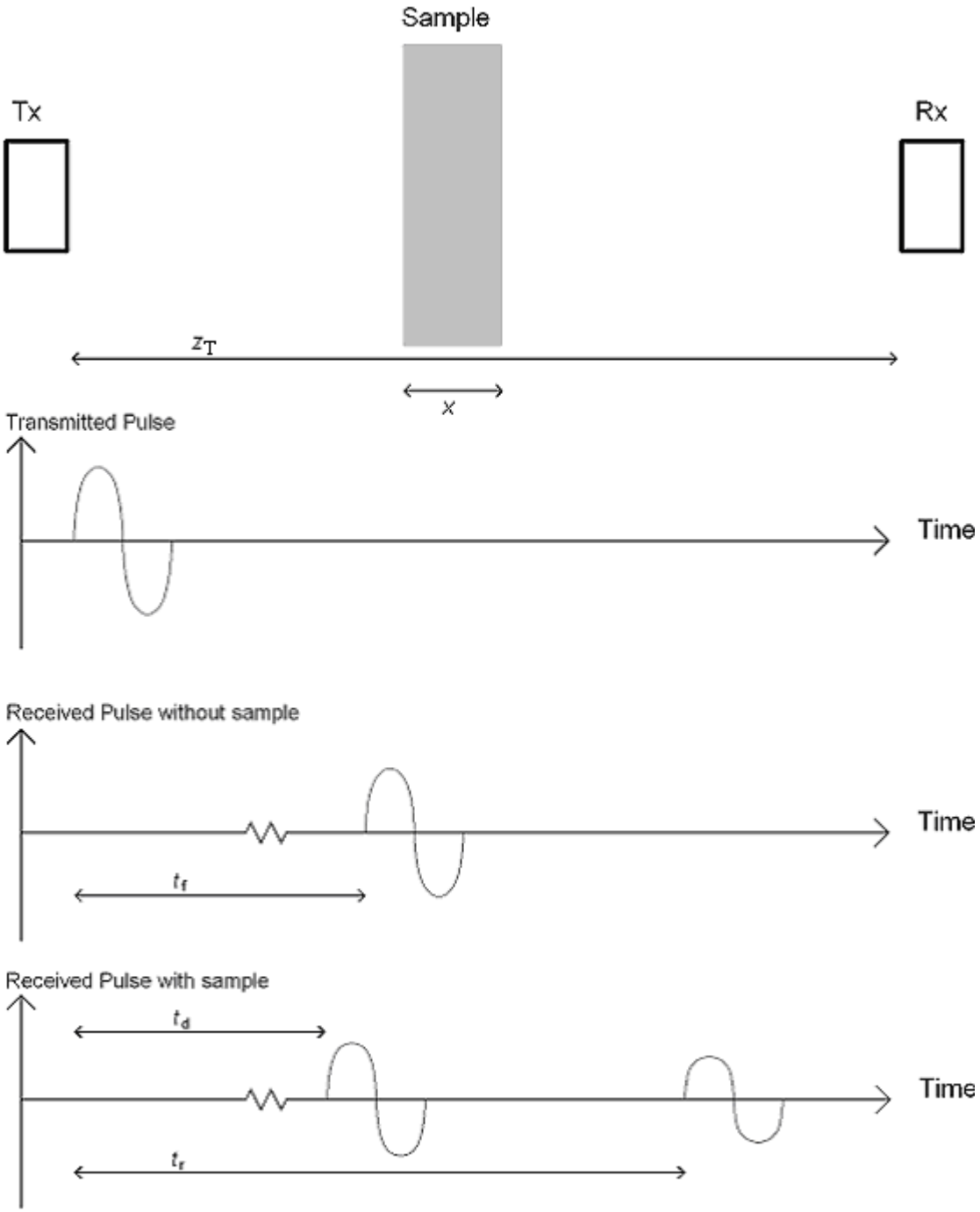

Figure 4.2. Definition of quantities used in the determination of sample thickness from first internal reverberation. Transducer separation (z_T), sample thickness (x), time of flight through fluid path (t_f), direct time of flight through sample (t_d) and first reverberant echo (t_r) are as described in the text. Tx is the transmitting transducer and Rx is the receiving transducer.

When a sample of thickness x is introduced the arrival time of both the directly transmitted wave, t_d, and the first multiple reflection within the sample, t_r,can be measured. These times of flight are given by

$$t_{\mathrm{d}} = \frac{z - x}{c_{\mathrm{ref}}} + \frac{x}{c_{\mathrm{sample}}} \tag{4.3}$$

and

$$t_{\mathrm{r}} = \frac{z - x}{c_{\mathrm{ref}}} + \frac{3x}{c_{\mathrm{sample}}}, \tag{4.4}$$

where c_{sample} is the speed of sound in the sample.

Eliminating z and x and writing c_{s} in terms of the arrival times gives

$$c_{\mathrm{sample}} = c_{\mathrm{ref}}\left(\frac{t_{\mathrm{r}} + 2t_{\mathrm{f}} - 3t_{\mathrm{d}}}{t_{\mathrm{r}} - t_{\mathrm{d}}}\right). \tag{4.5}$$

The sample thickness can be calculated by writing x in terms of the arrival times and c_{f} and eliminating c_{sample} and z:

$$x = c_{\mathrm{ref}}\left(\frac{t_{\mathrm{r}} + 2t_{\mathrm{f}} - 3t_{\mathrm{d}}}{2}\right). \tag{4.6}$$

These calculations require knowledge of the speed of sound in the fluid medium. This can either be calculated from an accurate measurement of the transducer separation or from published data relating to the chosen fluid medium.

Bamber (2004b) notes that a number of choices of pulse arrival time are possible, the choice of which may give rise to uncertainties in the measurement of time of flight due to non-linear propagation and pulse stretching from ultrasonic attenuation. The uncertainties introduced by these factors will affect the sound velocity and sample thickness estimated by these methods.

These formulae apply to the case of a sample without any window material to contain the sample. Clearly the presence of a widow will have an influence on the arrival times. The transmission effects can be allowed for by adding a term $2h\left(\frac{1}{c_{\mathrm{w}}} - \frac{1}{c_{\mathrm{ref}}}\right)$ to both t_{d} and t_{r}, where h is the window thickness and c_{w} is the speed of sound in the window material. This assumes the reflection comes from the interface

between the sample and the window, not the window and fluid medium. The resulting formulae become

$$c_{\text{sample}} = c_{\text{ref}} \left(\frac{t_{\text{r}} + 2t_{\text{f}} - 3t_{\text{d}} - 4h\left(\frac{1}{c_{\text{w}}} - \frac{1}{c_{\text{ref}}}\right)}{t_{\text{r}} - t_{\text{d}}} \right) \tag{4.7}$$

and

$$x = c_{\text{ref}} \left(\frac{t_{\text{r}} + 2t_{\text{f}} - 3t_{\text{d}} - 4h\left(\frac{1}{c_{\text{w}}} - \frac{1}{c_{\text{ref}}}\right)}{2} \right). \tag{4.8}$$

This method requires the unique identification of the arrival of the first internal reflection. This is an important consideration when designing the experimental setup. Three aspects are identified here. Firstly, there should be no surfaces close to the direct path which could produce reflections at the receiving transducer which could be misinterpreted as the first internal reflection. Any unwanted reflections can be identified by observing the received pulse on an extended timebase without the sample present. Secondly, the attenuation in the sample and the strength of the reflection at the interface between the fluid and sample should be considered to ensure that the amplitude of the first internal reflection is sufficient to be detected by the signal acquisition system. Thirdly, the samples should be carefully prepared and aligned with the beam path so that all surfaces are normal to the beam path. This will provide the largest signal amplitude for the internal reflection.

All of the calculations require knowledge of the speed of sound in water. Speed of sound in water was calculated according to Marczak (1997) based on the measured temperature of the water.

4.3. Materials and methods

Two unfocused single element ultrasound transducers with a centre frequency of 10MHz were used in a temperature controlled water tank. The higher frequency transducers were selected to improve temporal resolution of measurements. The

transducers were mounted opposite each other in a custom designed frame as shown in Figure 4.3. The frame was designed in conjunction with, and constructed by, Mr Peter Laidler of the Department of Medical Physics and Bioengineering at the Royal United Hospital NHS Trust, Bath. Adjustable positioning of the transducers was not considered to be important as for the attenuation measurements. The frame ensured that the transducers were held with their radiating surfaces parallel. All measurements were made at 25.0 ± 0.1°C, with the water tank being filled with distilled water.

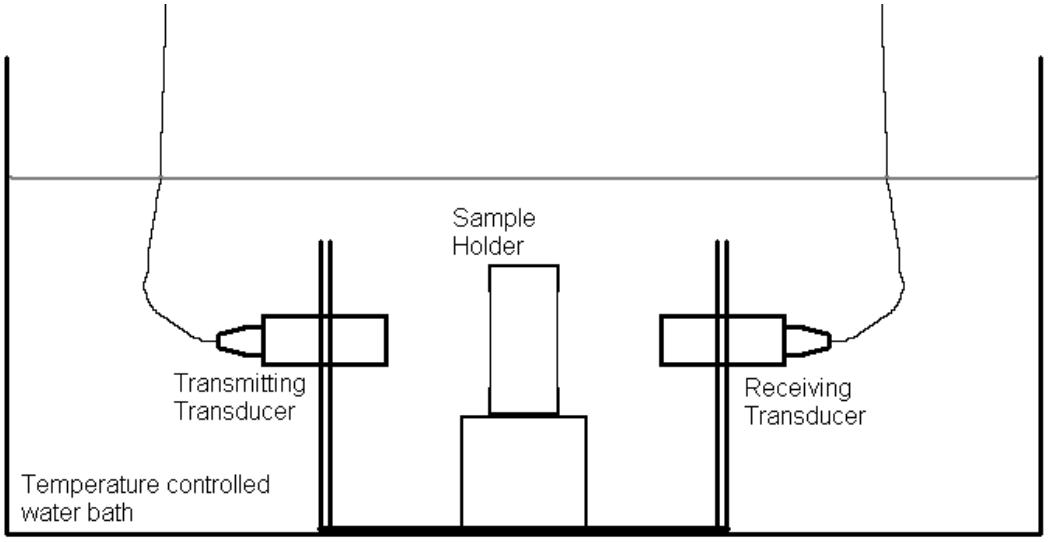

Figure 4.3. Measurement setup for Speed of Sound measurements.

A signal was generated by an Agilent 33220A signal generator (Agilent Technologies, Inc., Santa Clara, CA) and amplified using an ENI 240L RF Power Amplifier (ENI, Inc., Rochester, NY). The signal was then passed through the ultrasound speed of sound measurement system and digitized using a PicoScope 3206 digital PC Oscilloscope (Pico Technology Ltd, St Neots, Cambridgeshire, UK). The signals were analysed in Matlab R12.1 (The Mathworks, Inc., Natick, MA), for time of arrival. An example of the Matlab code used for analysing the signals is contained in Appendix C1. Later, the PicoScope 3206 digital PC Oscilloscope was replaced by a National Instruments NI-5133 USB Oscilloscope (National Instruments Corporation, Austin, Texas) and analysis was also performed using National Instruments Labview Signal Express 3.0. Data from 100 ultrasound pulses were recorded for each sample.

A pulse of 30ns duration was utilised as an impulse to drive the transducers and enabled the determination of the first rise time and first zero crossing of the resulting

received signal. This enabled the calculation of both speed of sound and sample thickness. For batch 3 and 4 a tone burst signal of frequency 8 MHz was also used to determine the phase of the signal and, when compared to the phase of a direct water path and the calculated sample thickness, to calculate the speed of sound from phase information. To measure the phase velocity a time window within the toneburst section of the received signal was selected. A fast fourier transform of the received signal was used to calculate the phase of the signal within the selected time window. The difference between the measured phase of a direct water path and through the sample was used to calculate the phase velocity within the sample.

To measure the speed of sound the same gel samples were used as were prepared for the attenuation measurements (see sections 3.3.1 and 3.3.3).

According to Kaye and Laby (http://www.kayelaby.npl.co.uk/, v1.0, accessed 25th October 2007) the speed of sound in Mylar is 2400 ms^{-1}. This was used along with the average thickness of the Mylar windows (0.108mm) measured using a micrometer from 20 readings to correct for the effects of the windows.

4.3.1. Temperature dependence of speed of sound

As the project progressed, it became apparent that the physical properties of MAGIC gels exhibit significant temperature dependence. Therefore measurements of speed of sound were made at different temperatures and doses. Temperature was controlled using a Grant GD 100 Immersion Thermostat (Grant Instruments Ltd, Cambridge, UK) and a Grant C1G Refrigerated Immersion Cooler attached to the water tank.

4.4. Results

It was found that to calculate the thickness of the sample that the best definition for the time of flight (t) came from the first zero crossing. This was the most reproducible quantity that could be determined for both the direct path through the gel and the first reverberation.

Figures 4.4, 4.5 and 4.6 show the speed of sound measured for 3 different gel batches calculated from the time of first zero crossing. The speed of sound appears to increase approximately linearly with dose. Error bars are standard deviations on the value of the speed of sound calculated from estimates of the error in determining the three time periods used in the calculation (t_d, t_r and t_f). Estimates of the error in determining the time period were calculated from the standard deviation of the first zero crossing calculated for the 100 pulse sequences acquired. Figure 4.7 shows the phase speed calculated for Batch 3 gel. The speed of sound appears to increase approximately linearly with dose. Error bars are standard deviations on the value of the speed of sound calculated from estimates of the error in determining the phase of the signal and estimates of the error on the calculated sample thickness. Estimates of the error in determining the time period were calculated from the standard deviation of the phase of the 100 pulse sequences acquired. Estimates of the error in the sample thickness were calculated from the standard deviation of the first zero crossing calculated for the 100 pulse sequences acquired.

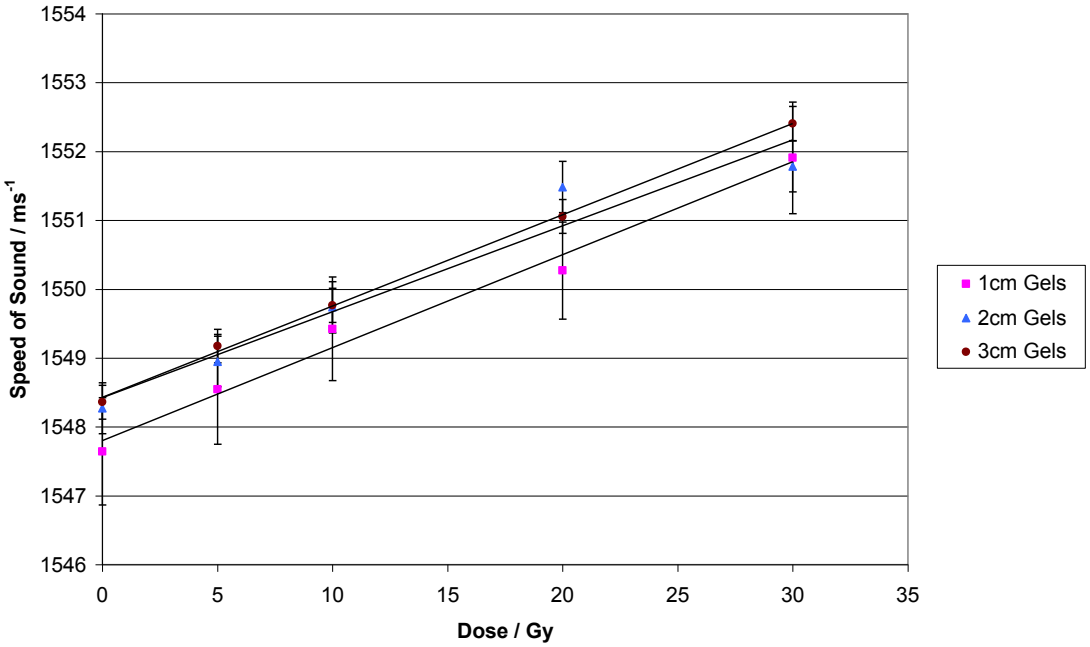

Figure 4.4. Variation in speed of sound measured using time of flight for batch 1 MAGIC gels of different thicknesses (see key). Error bars are standard deviations on the value of the speed of sound calculated from the error in determining the three time periods used in the calculation from 100 repeated measurements. Temperature of measurement was 25°C.

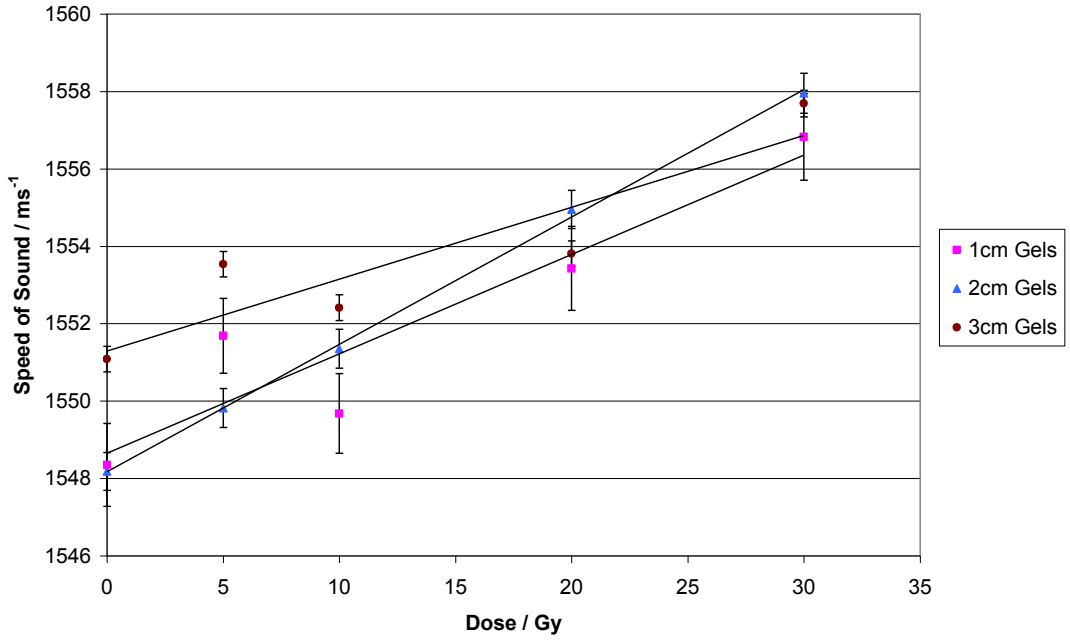

Figure 4.5. Variation in speed of sound measured using time of flight for batch 2 MAGIC gels of different thicknesses (see key). Error bars are standard deviations on the value of the speed of sound calculated from the error in determining the three time periods used in the calculation from 100 repeated measurements. Temperature of measurement was 25°C.

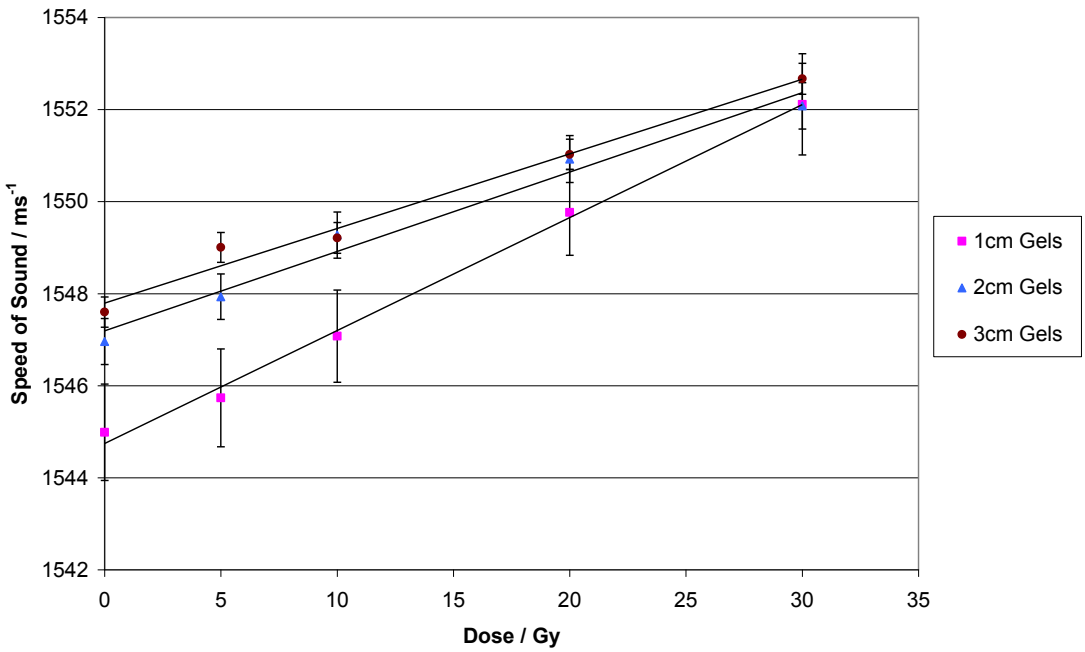

Figure 4.6. Variation in speed of sound measured using time of flight for batch 3 MAGIC gels of different thicknesses (see key). Error bars are standard deviations on the value of the speed of sound calculated from the error in determining the three time periods used in the calculation from 100 repeated measurements. Temperature of measurement was 25°C.

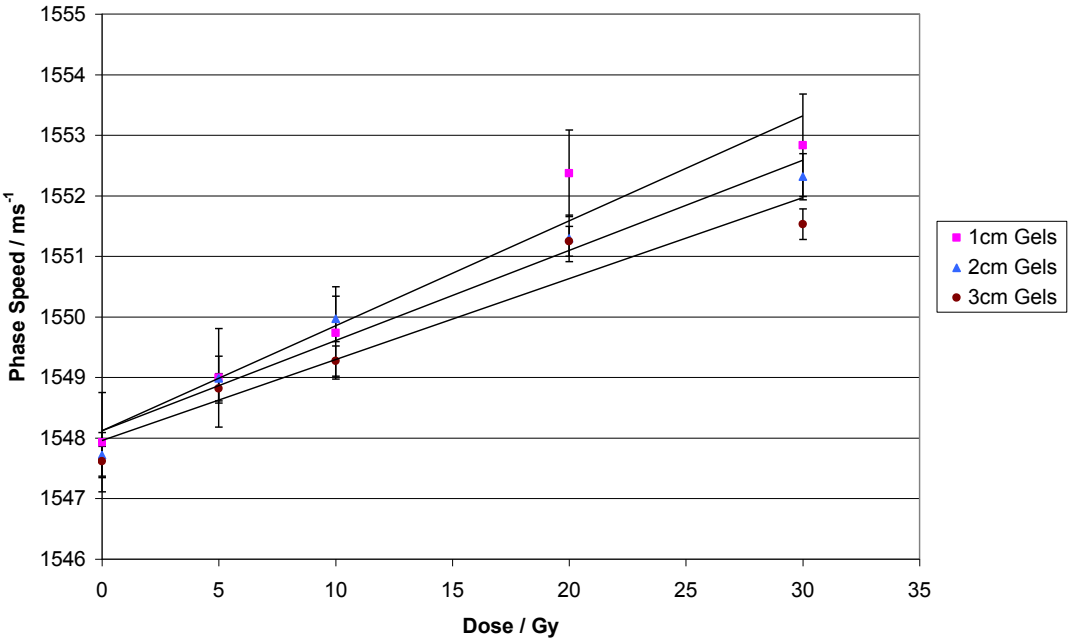

Figure 4.7. Variation in speed of sound measured using phase speed for batch 3 MAGIC gels of different thicknesses (see key) at 8 MHz. Error bars are standard deviations on the value of the phase speed calculated from the error in determining the phase speed from 100 repeated measurements. Temperature of measurement was 25°C.

Figures 4.8 and 4.9 show the speed of sound variation with temperature. The speed of sound appears to increase approximately linearly with dose at 20°C but decreases with dose at lower temperatures. Error bars are standard deviations on the value of the speed of sound calculated from three different samples at each dose level. Figure 4.8 shows the speed of sound from a time of flight calculation and Figure 4.9 shows the speed of sound from the phase method.

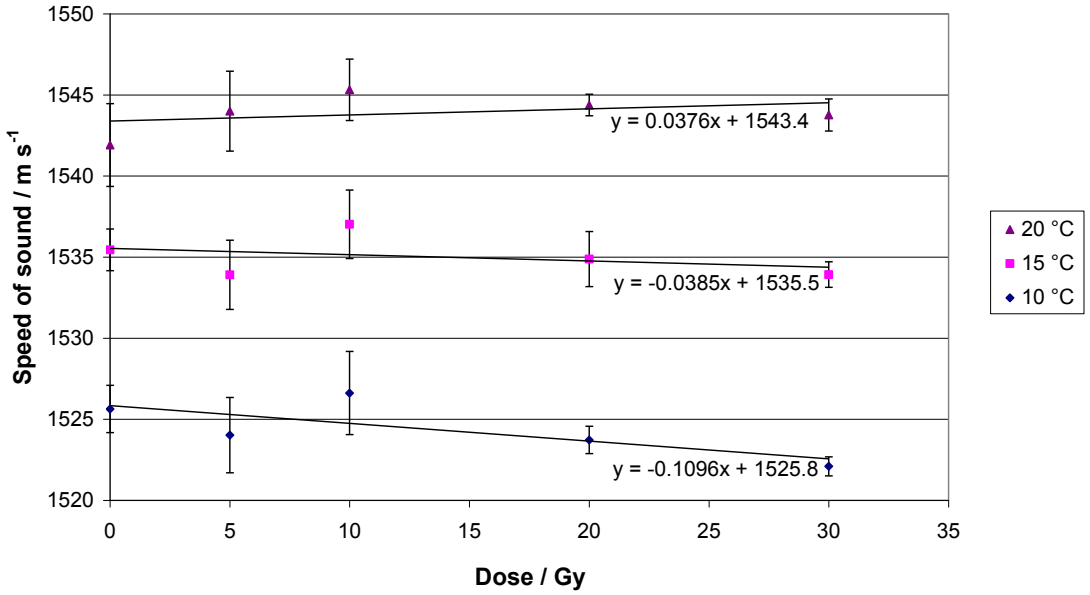

Figure 4.8. Variation in speed of sound measured using time of flight for batch 4 MAGIC gels at different temperatures (see key). Error bars are the standard deviation of the speed of sound for the three samples of gel thickness 1cm, 2cm and 3cm at each dose level.

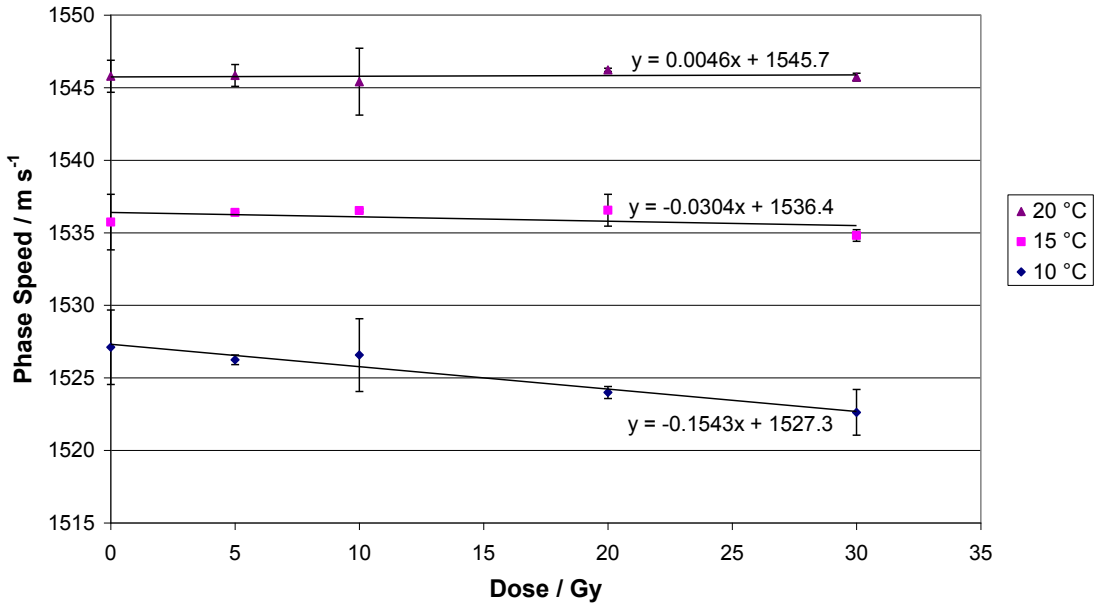

Figure 4.9. Variation in speed of sound measured using phase speed for batch 4 MAGIC gels at different temperatures (see key) at 8 MHz. Error bars are the standard deviation of the phase speed for the three samples of gel thickness 1cm, 2cm and 3cm at each dose level.

4.5. Discussion

For the selection of the time of flight (t) to use to calculate the sample thickness the use of the first zero crossing is the most logical selection. The other two options, the time that the signal can be distinguished from background, and the phase of the signal, both have disadvantages for determining the first reverberation time. The time that the signal can be first distinguished from background can be used successfully for the determination of t_f and t_d as the signal amplitudes are similar and so the signal arises out of the background at similar positions in the signal. However, due to the weakness of the reverberation signal, the background noise is comparatively greater, and therefore the position within the signal that it can be distinguished from the background is different. The phase of the signal, depending on the strength of the reverberant signal, can only sometimes be determined and it is possible that this is a factor of 2π different from what is required, due to it being difficult to determine accurately the beginning and end of the signal.

When determining the speed of sound in the sample, c_s, it is important to accurately know the sample thickness. Since the sample holders were deliberately made with thin windows to provide low attenuation from the window itself, the inherent flexibility provided a means by which each sample could be a different thickness from the nominal size defined by the holder dimensions. The irradiation and subsequent polymerization of the gel samples increases the density of the gel, implying the gel shrinks with increasing radiation dose. The flexibility of the sample holder windows will cause the path length of the ultrasound through the gel to decrease with dose. Therefore it is important to determine the actual path length through which the ultrasound passes. Therefore the calculation shown above of c_s from the first reverberation is a more robust method of determining the speed of sound in this case.

For the fixed temperature (25°C) experiments, each set of measurements of speed of sound through the samples shows an increase in speed of sound with radiation dose. There is some variability in the speed of sound of unirradiated gel, and some evidence of batch variability in the speed of sound.

Mather et al. (2002) showed the ultrasonic speed of unirradiated gels to be approximately 1540 m s^{-1} with a dose sensitivity of 0.178±0.006 m s^{-1} Gy^{-1}. The data from the three batches of gels reported here show a similar speed of sound in

unirradiated gel and similar dose sensitivity, although there is batch variability in the determined speed of sound.

The measured speed of sound varied significantly with temperature. As the temperature was reduced the speed of sound for unirradiated gel was found to be slower. Also, the speed of sound of the irradiated gel was seen to decrease with dose at lower temperatures, rather than the increase in speed of sound with dose initially observed and also reported by Mather et al. (2002).

5. Density of MAGIC gel

5.1. Introduction

The density of a material affects its ultrasonic properties and interfaces between materials of different density will cause reflection and refraction of the ultrasound. The characteristic acoustic impedance of a material is the product of the density and speed of sound of the material, and is fundamental to calculating the reflection coefficient between two materials. It is therefore important to understand how density of the gels is affected by the radiation dose as this may provide a dose dependent reflection which can subsequently be measured by ultrasound.

Work has been carried out to develop a system capable of measuring the density of gels. A calculation of the density of a sample requires measurement of its mass and volume. Measurement of mass is easily and accurately performed using an analytical balance. Three possible methods of volume measurement have been identified.

One technique is based on the filling of a known volume with the material and then measuring its' mass. This would not work in our case as it will not tell us the volume change that will occur upon irradiation.

Another method is to use gas pycnometry, which uses gas pressures to measure volumes accurately, based on Boyle's law. However, this method requires access to specialised equipment. Also, if the gels are not sealed they will exchange moisture content with the gas used in the pycnometer, so the properties of the gels will be continuously changing during the measurement process.

A third method was investigated, based on the Archimedean principle. A balance is used to weigh the sample in air. Then the material is submerged in a fluid, which displaces an amount of fluid equal to the volume of the material. This subjects the material to a buoyancy force, which can be measured as a change in weight. If the density of the fluid is known, the volume of fluid displaced can be calculated from the measured buoyancy force.

5.2. Theory

Initially the sample is weighed in air (W_{air}). Then a sample holder is placed on the balance and the fluid bath is put in place. When the sample is placed on the holder, the weight of the sample in fluid (W_{fl}) will be the weight in air reduced by the buoyancy (G), so

$$W_{fl} = W_{air} - G. \tag{5.1}$$

The weight of a sample in different fluid mediums can be calculated from the sample density, the fluid medium density and the sample volume, *Vol.*. Calculations of weight from density and volume measurements with a fluid medium of air often assume that the density of air has a negligible effect on the weight of the sample. It is however correct to write

$$W_{air}=Vol.(\rho_{sample} - \rho_{air}) \tag{5.2}$$

Where ρ_{sample} is the density of the sample and ρ_{air} is the density of air.

The buoyancy G is the weight of fluid displaced, and similarly can be written as

$$G=Vol.(\rho_{fl} - \rho_{air}) \tag{5.3}$$

Where ρ_{fl} is the density of the fluid.

Hence by eliminating the sample volume *Vol.*, the density of the sample can be calculated as

$$\rho_{sample}= \frac{W_{air}\rho_{fl}}{W_{air} - V_{fl}} + \rho_{air} \tag{5.4}$$

if the density of the fluid is known. This assumes that the sample does not float in the fluid. This can be achieved either by using a fluid that is less dense than the sample or if the fluid is more dense than the sample, by securing the sample to the holder, in which case the weight of the sample in fluid (W_{fl}) will be negative. Mather et. al. (2002) suggest that the density of MAGIC gels ranges from 1047 – 1054 kg m^{-3} and therefore MAGIC gel is more dense than water, so water would be a suitable choice of fluid medium.

When the sample is introduced into the water there is a change in buoyancy of the sample holder caused by the increased water height. The change in sample holder buoyancy requires a correction factor K to be applied to the measurement of buoyancy

unless the balance is tared when the sample is in the water tank but not on the sample holder. The full calculation is then

$$\rho_{sample} = \frac{W_{air}(\rho_{fl} - \rho_{air})}{(W_{air} - V_{fl})K} + \rho_{air} \qquad (5.5)$$

where K is given by 1 - $\frac{Area_{sh}}{Area_{bath}}$ where $Area_{sh}$ is the area of the sample holder at the surface of the fluid and $Area_{bath}$ is the area of the fluid bath at the surface of the fluid. A value of $K = 1$ is used when the balance is tared with the sample in the water bath but not on the sample holder.

Figure 5.1 illustrates the process. In stage 1 sample is placed on the balance. This provides the measurement of W_{air}. In stage 2 the frame and the fluid bath is introduced. This bath is held independently of the balance by a stand and the hanging part of the frame should be free to move within the bath. At this stage the balance is tared. In stage 3 the sample is placed on the frame and all air bubbles are removed from the sample surface. This provides the measurement of the sample in fluid W_{fl}.

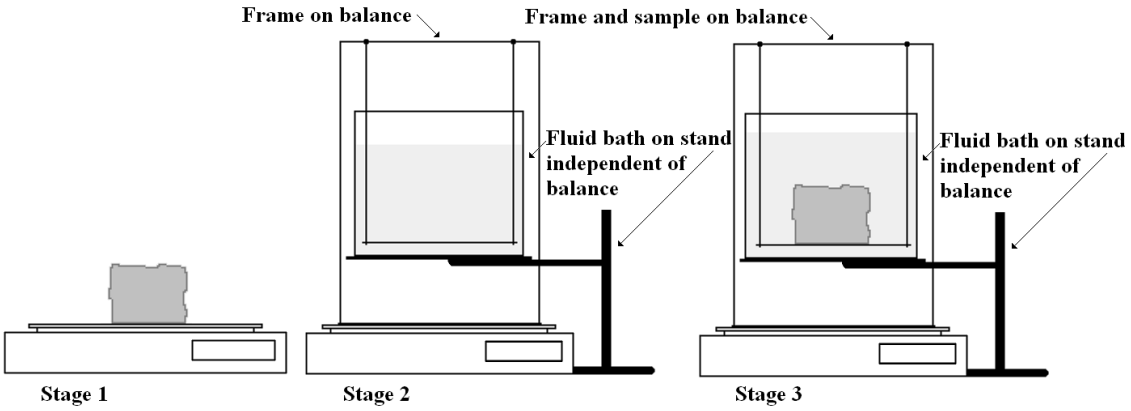

Figure 5.1. Stages of measurement of sample density. See text for details.

5.3. Analysis of uncertainty and an estimation of requirements

Since essentially a ratio of the weight of the sample to the weight of fluid displaced by the sample is being used in the calculation, an estimate of the uncertainty

in the calculation of density can be obtained from standard application of error tracking, assuming that the fluid used is well characterised.

For known densities ρ_{fl} and ρ_{air} with a fixed value of K, then calculation is $\rho_{sample} \propto \frac{W_{air}}{W_{fl}}$ and uncertainties ΔW_{fl} and ΔW_{air} lead to uncertainties in ρ which can be written as

$$\frac{\Delta\rho}{\rho} = \sqrt{\left(\frac{\Delta W_{air}}{W_{air}}\right)^2 + \left(\frac{\Delta W_{fl}}{W_{fl}}\right)^2} \quad . \tag{5.6}$$

Mather et. al. (2002) suggest that the density of MAGIC gels ranges from 1047 – 1054 kg m^{-3} as a function of dose from 0 – 50 Gy (from Figure 2 of the paper). Therefore density measurements with a precision of ±0.5 kg m^{-3} would be required to determine the density change caused by the irradiation of MAGIC gels.

The balance available for these measurements is a Mettler-Toledo AT 400 Electronic Analytical Balance (Leicester, UK). This has a maximum weight of 400g and reads to 0.0001g.

The maximum allowed weight and the geometry of the balance dictates that the sample will be of the order of 50ml size. This should translate to a weight of both sample and fluid displacement of ~50g since density of MAGIC gels are ~1g cm^{-3}. If reproducible measurements are made to within 0.001g then the fractional error on the density will be 0.00003. This is a precision about an order of magnitude greater than the requirement suggested above. An increase in the weight/volume of the sample, and a decrease in the uncertainty of the measurement of weight/volume will increase the precision of the measurement. A set of measurements were performed on a sample to calculate the measurement reproducibility of this system. From five repeated measurements of a single sample it was determined that it was possible to measure sample weight to within a standard deviation of 0.001g. The measurement of sample volume was found to be less reproducible, giving a standard deviation of 0.02g from a sample of eight repeated measurements. This gives a measurement uncertainty for this method of measuring density to be 0.4 kg m^{-3} assuming 50g samples with a density of 1, which is sufficiently small to be able to resolve the expected density variation.

5.4. Materials and methods

5.4.1. Gel manufacture and irradiation

Gels were manufactured as described by Fong et. al. (2001) and summarized in Chapter 3.4.3. Once manufactured, the gel was used to fill small plastic bags which were then sealed. The plastic bags were chosen as sample containers as the gel had to be sealed because they are hydroscopic, but flexible containers were required to allow the volume of the samples to change without restriction. The use of bags to contain the Gel will introduce uncertainties into the measured gel densities. 14 bags were used in this experiment. Once manufactured the gels were allowed to cool for 6 hours until the gels had set. The density of the gels was then measured to obtain their 'unirradiated' density. The gels were then refrigerated for approximately twenty-four hours.

Subsequently the gels were irradiated. A 6 MV photon beam from a calibrated Primus linear accelerator (Siemens Medical Solutions, Concorde, CA) was used to irradiate the gels. The gels were irradiated in pairs to the following doses – 0, 2, 5, 10, 15, 20 and 30 Gy. After irradiation the gels were refrigerated prior to density measurements.

5.4.2. Density measurement

The density of the gels was measured 18 hours and 4 days post-irradiation. For measurements "A" the balance was tared with the sample in the water bath but not on the holder so a correction factor of $K = 1$ was used. For measurements "B" the balance was tared before the sample was introduced into the water bath. Distilled water was used in the water bath and the temperature of the water was measured so that the water density could be calculated. Water density was calculated using the formula of Bigg (1967), a fifth-order polynomial based on the temperature of the water.

Further measurements were obtained with the samples held in a temperature controlled environment. To do this, a second water bath was used held at the same temperature as the fluid bath. The temperature of the two baths was maintained at 14.5, 21 and 26 °C for each set of experiments. Therefore measurements using the "A" procedure, where the balance was tared with the sample in the water bath but not on the frame, was used to ensure that the samples were at thermal equilibrium with the water

bath at all times. The samples were left in the temperature controlled water bath for 2 hours prior to measurement of their density. In this second set of experiments the density measurements were made 18 hours post-irradiation.

5.5. Results

Figure 5.2 shows how the density varied with dose. The density of the gel samples appears to increase linearly with dose within the range measured, from 0 to 30 Gy. The density increases by 0.19 ± 0.007 kg m^{-3} / Gy. The increasing density with radiation dose is consistent with the gels undergoing radiation induced polymerisation. The error bars on the measurements are the standard deviation of observed density calculated from repeated measurements of the same gel sample used to estimate the uncertainties ΔW_{fl} and ΔW_{air}. Regression analysis was performed on the four sets of measurements. The measured gradients (density increase with dose) all fell within ±2 standard errors of the mean gradient. This suggests that the measurements of the increase in density with dose are the same, within the measurement uncertainty, for both the different methods of measurement and the different time at which the measurements were made. The intercepts show greater variation and the calculated intercept from the measurement set 4 days post-irradiation method B is greater than 2 standard errors smaller than the other 3 measurements. This indicates that there are either systematic differences between the two methods of volume measurement or physical changes that have occurred in the gels between the sets of measurements or a combination of both.

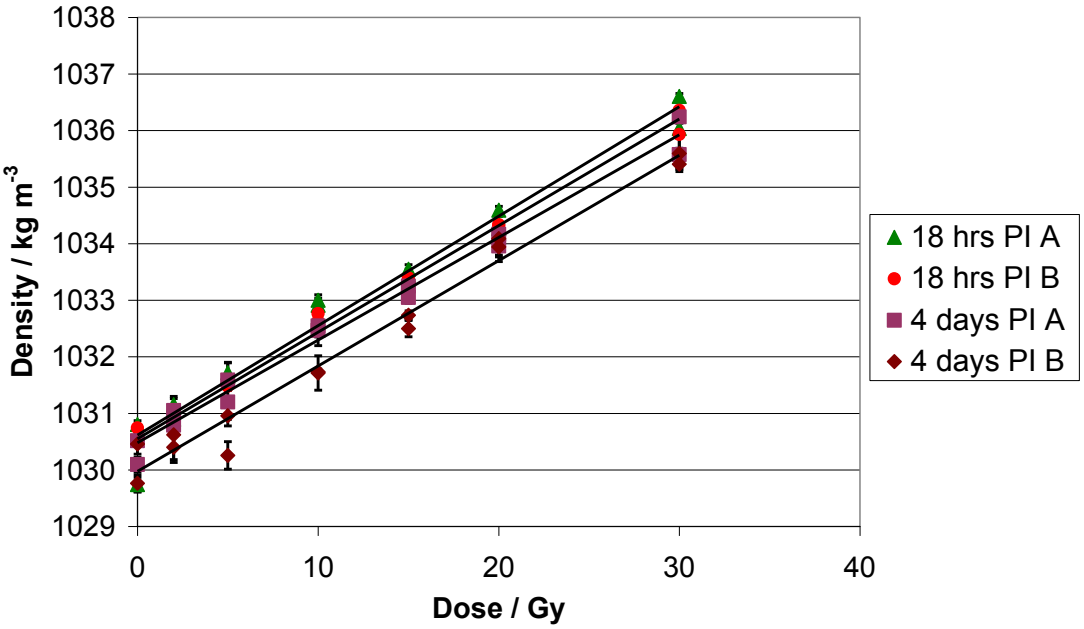

Figure 5.2. Variation in density of gel with irradiated dose, 18 hours (triangle and circle) and 4 days (square and diamond) post-irradiation (PI). Error bars are standard deviations for five measurements of density for each sample.

Figure 5.3 shows the measured variation of density of MAGIC gels with temperature. Error bars are the standard deviation of 8 repeated measurements on each sample. The density of MAGIC gel increased from 1028.9 ± 0.3 kg m^{-3} at 26 °C to 1033.3 ± 0.3 kg m^{-3} at 14.5 °C. The density appears to increase linearly with dose over the range measured with a dose sensitivity of 0.178 ± 0.004 kg m^{-3} Gy^{-1}.

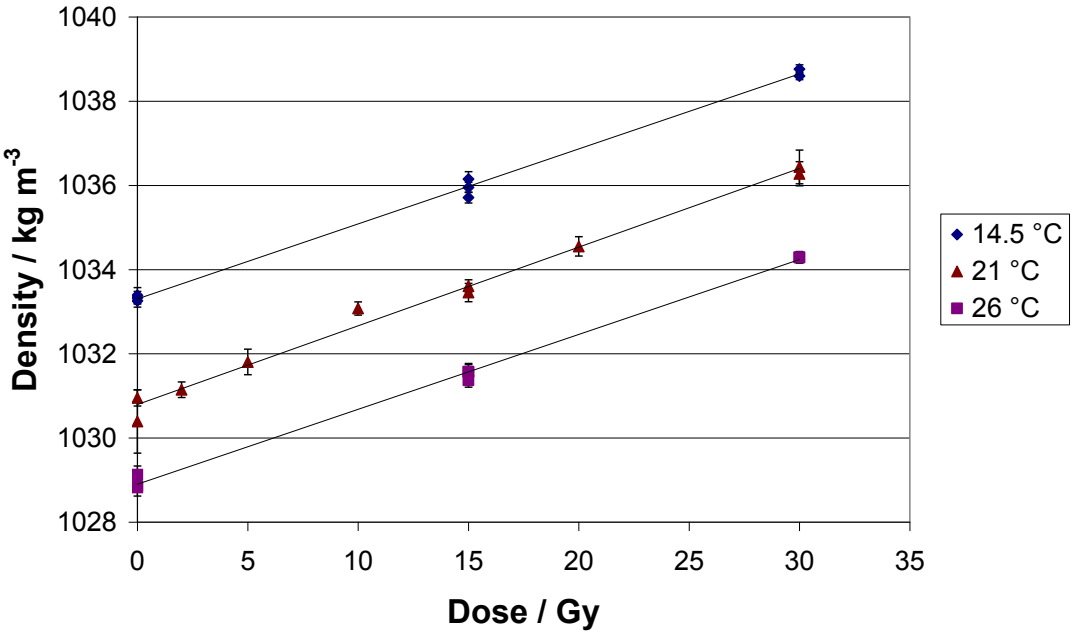

Figure 5.3. Variation of density of MAGIC gels with dose at selected temperatures (see key) measured using method 'A'. Error bars are standard deviations for five measurements of density for each sample.

5.6. Discussion

The change in density with dose is similar to that measured by Mather et. al. (2005), although the absolute measurement of density is different. The measurements reported here are more comprehensive than in Mather's paper, and no other reports of the change in density with dose are believed to have been published. There are a number of systematic errors that may be found both in Mather's technique and in the technique described here, which may account for the differences in absolute density reported.

Approximate comparisons can be made with data from x-ray CT based measurements of polymer gel dosimeters. The CT numbers (HU) from a calibrated CT scanner are related to the linear attenuation coefficient of the material being scanned. The CT number can be converted to relative electron density or physical density by scanning phantoms containing section of known radiological parameters (Saw et al., 2005). Dose responses measured using x-ray CT usually only report CT number to dose comparison and do not contain a calibration of CT number to density (e.g. Hill et

al., 2005). As Saw et al. (2005) note, the CT number to density conversion curve is dependent on individual scanner parameters such as kV/p, filtration and reconstruction algorithm therefore a detailed comparison cannot be made. Hill et al. (2005) measured a CT number-dose sensitivity of 0.37 HU Gy^{-1} and the CT number of unirradiated gel to be 22 HU. This approximately equates to a density of 1031 kg m^{-3} and a dose sensitivity of 0.23 kg m^{-3} Gy^{-1} based on the CT number to density conversion used locally at the Royal United Hospital in Bath. These values for density and dose sensitivity are similar to the values measured in this research.

There are systematic differences between method "A" and method "B" of measuring density. The main difference between the two methods may come from the correction factor *K*, which has been calculated as 0.991 for the equipment used in the experiments, but has not been verified. Also, differences between the two techniques could be caused by splashing or removal of water from the water bath as the gel samples are manipulated. Also, in these initial experiments, the gels were not maintained at a known temperature, and although the temperature of the water bath was known, no effort was made to control the temperature of the gels.

There are also differences between the density measured 18 hours post-irradiation and that measured at 4 days post-irradiation. These differences could be due to aging of the gel or the temperature of the gels at the time of measurement. Insufficient data is presented here to conclude whether there is a difference in the results obtained using the different measurement methodologies or whether a longer period post-irradiation affects the measured density.

Another source of uncertainty in these results was due to the containment of the gels in polythene bags. The gels had to be sealed during the experiment as if left open in room atmosphere they evaporated water, or if left unsealed in water they absorb water. Each polythene bag weighed approximately 0.6g prior to being filled with gel. Polythene has a density of between 940 and 965 kg m^{-3} (http://www.kayelaby.npl.co.uk/). This will affect the measurements made here as the density calculated in these experiments is that of the whole sample, including the polythene bag used as an enclosure. This will have the effect of systematically reducing the measured gel density from the actual gel density. To estimate the effect of the polythene bag on the measured density the reduction in density due to a bag of weight 0.6g and an assumed

density of either 940 or 965 kg m^{-3} was calculated for 14 samples. The average decrease in sample density due to the effect of the bag was 0.38 kg m^{-3} or 0.13 kg m^{-3} respectively dependent on the assumed density of the bag.

Another source of uncertainty in these measurements is the presence of air bubbles in the samples. Small air bubbles were introduced in the manufacturing process due to the continuous stirring of the mixture. Care was taken to remove any air bubbles prior to sealing the bags, although from observation this was not completely successful. The presence of air bubbles in the bags will have the effect of reducing the observed gel density from the actual gel density, but will depend on the amount of air in each individual bag.

The absolute density may also change between different batches of gels due to small variations in the manufacturing procedure.

The measurements reported of the variation of density with temperature show that the gel density decreases as the temperature increases. The change in density with dose was shown to be independent of the measurement temperature over the range of temperatures investigated.

5.7. Conclusion

The density of the gel appeared to increase linearly with radiation dose over the range measured, consistent with the gels undergoing radiation-induced polymerisation. There are a number of uncertainties in the method used to measure gel density which have been identified. The density change with radiation dose is consistent with the previous report of changing density with radiation dose (Mather, 2005), although it appears that the study performed here is more comprehensive than anything that appears in the literature, including the change in density with temperature, which has not been previously reported.

6. Acoustically matched reflector – reflection from planar interface

6.1. Introduction

To be successful, ultrasound pulse-echo methods will depend on the dose-sensitivity of echoes from interfaces between two materials. This depends in turn on changes in characteristic acoustic impedance, and hence on density and sound speed, both of which have been shown to be dose-dependent in dosimetric gels (Chapters 4 and 5). A simple dose-dependent system could be designed using, for example, material 1 being dose-dependent and material 2 not. The acoustic properties of potential inert reflectors can be compared to the acoustic properties of the MAGIC gel and the dose sensitivity of these properties, to determine if the inert reflector will be suitable. Once some suitable reflective materials have been determined, a series of measurements of the dose dependency of reflections from a plane interface between MAGIC gel and the reflector will be made using a single element transducer. Different areas of the system will be irradiated to different doses so that a comparison of reflection amplitude with dose can be made. The material producing a reproducible and significant the change in reflection amplitude with dose will show the most promise for further investigation into its use in producing an pulse-echo ultrasonic dosimetry system.

6.2. Theory

Reflection of ultrasound from the interface of two materials is dependent on the differences in characteristic acoustic impedance of the two materials. Using the properties of MAGIC gels determined from the mean of the measurements detailed above, the characteristic acoustic impedance (given by $Z = \rho c$) is

$Z \approx 1.598 \times 10^6$ kg m^2 s^{-1} at 0 Gy and 25 °C

$Z \approx 1.613 \times 10^6$ kg m^2 s^{-1} at 30 Gy and 25 °C.

The sound power reflection coefficient for the reflection at the interface between two fluid materials is given by Kinsler and Frey (1962) as

$$\text{Sound power reflection} = \left(\frac{Z_2 - Z_1}{Z_2 + Z_1} \right)^{\wedge} \qquad (6.1)$$

where Z_1 is the characteristic acoustic impedance of the material through which the ultrasound is passing and Z_2 is the characteristic acoustic impedance of the reflecting material.

The dose sensitivity of the acoustic impedance is small and appears to be linear with dose over the range measured (approximately 500 kg m^{-2} s^{-1} Gy^{-1}). Therefore to achieve a sensitive system, with a significant change in reflection amplitude, requires a reflector that has a similar acoustic impedance to the dose dependant gel, since the reflection amplitude is dependent on the difference between the acoustic impedances of the two materials.

Material	***c* / m s^{-1}**	**ρ / kg m^{-3}**	***Z* / kg m^{-2} s^{-1}**	**Sound power reflection at 30 Gy (relative to 0 Gy)**
Polyethylene	2100-2400	940-965	2.15×10^6	0.94
Polystyrene	2350	1040-1090	2.50×10^6	0.96
Natural Rubber	1600	906-913	1.45×10^6	0.82
Hard Rubber	1680	1130-1180	1.94×10^6	0.90
Neopene	1510	1240	1.87×10^6	0.88
Castor Oil	1490	950	1.42×10^6	0.86

Table 6.1. Speed of sound and density of materials with potential for use as a matched reflector to MAGIC gel. Source: http://www.kayelaby.npl.co.uk/

According to the data presented in Table 6.1, the most suitable materials to produce a reflection of the ultrasound are Natural Rubber, Neoprene or Castor Oil. A simple gelatine solution, which will have very similar properties to MAGIC gels, could also be used. These all have similar acoustic impedances to MAGIC gels, and therefore the reflected sound power will be small. The change in reflected sound power as the gels are irradiated will be greater with these materials.

Other materials that were identified as being suitable for investigation are solid polymers based on anechoic acoustic tank lining materials. These materials are designed to have a minimal reflection of ultrasound, and will therefore be of similar acoustic impedance to water (and hence MAGIC gels). They may also be designed as acoustic absorbers, and this property may make them unsuitable to use as a backscattering material. However, the surface of these materials is flat and so may be useful in creating a uniform reflecting surface.

After some initial investigation into some of the materials identified in Table 6.1, a bespoke matched material was specified and a supplier was identified and three samples were ordered. The material was specified to have a characteristic impedance of 1.58×10^6 kg m^2 s^{-1}. This characteristic acoustic impedance was chosen to be just below that of unirradiated MAGIC gel, and any irradiation of the MAGIC gel would further increase the difference between the inert reflector and the MAGIC gel. The material was produced by Acoustic Polymers Ltd (Mitcheldean, Gloucestershire, UK) from a polymeric material with a known speed of sound (1535 ± 3 ms^{-1}). The required acoustic impedance was created by introducing a filler material into the polymer to increase the density. Barium Sulphate, with a density of 4500 kg m^{-3} (http://www.kayelaby.npl.co.uk/), was used as the filler. This high density filler was chosen so that the volumetric addition will be low.

Formula 6.1 describes reflection that occurs at normal incidence. At other angles of incidence, the angle of reflection equals the angle of incidence. Therefore, if the angle of incidence changes, either because the surface is not flat, and so the angle of incidence changes, or the mechanical mounting of the transducer means that the beam direction changes, this can have a significant impact on the measurement of reflected sound power. Also, if the ultrasound beam is refracted before it reaches the reflector, then this will change the angle of incidence. Therefore it is important to ensure that the reflective surface is flat and that the mechanical mounting of the transducer means that no change to the angle of incidence occurs.

An alternative method would be to use spheres of reflective material embedded in the MAGIC gel, where normal incidence will occur at the position of maximum reflection. This would cause its own difficulties in positioning the spheres and

ensuring that the position of maximum reflection was accurately and consistently located.

6.3. Materials and methods

6.3.1. Reflections from plane interfaces

MAGIC gel samples were made using according to Fong et al. (2001) and combined with a number of different inert materials to produce interfaces from which ultrasound reflections could be obtained. A number of standard materials were identified and tested, including vegetable oil, 5% w/w gelatine, rubber, polyethylene, and some specialist materials including Precision Acoustics Aptflex F28 acoustic absorber tile (Precision Acoustics Ltd, Dorchester, UK) and a bespoke solid polymer from Acoustic Polymers (Acoustic Polymers Ltd, Mitcheldean, Gloucestershire, UK) were used as reflectors that has similar acoustic impedances to MAGIC gel.

The method for layering the inert material with MAGIC gel depended on the properties of the material. Figure 6.1 shows the various geometrical arrangements that were used. For inert materials in liquid form, such as vegetable oil or weak gelatine solution, MAGIC gels layers were created and then a layer of inert material was formed on top of the MAGIC gel. For inert materials in solid form, such as rubber or acoustic absorber tile, the inert material was placed at the bottom of a container and the MAGIC gel poured over the top. To ensure that the surface of the MAGIC gel was not subject to oxygen contamination and to provide a method of consistent acoustic coupling, a layer of vegetable oil was poured over the top of the MAGIC gel as soon as the gel layer had been created. Vegetable oil was chosen as it has a low density and therefore floated above the MAGIC gel, and if another material needed to be poured in to create a layer, such as a weak gelatine solution, then the oil would float above this layer without mixing with the layer. A lipid based product was chosen for this layer so that it would not mix with the MAGIC gel solution while it solidified.

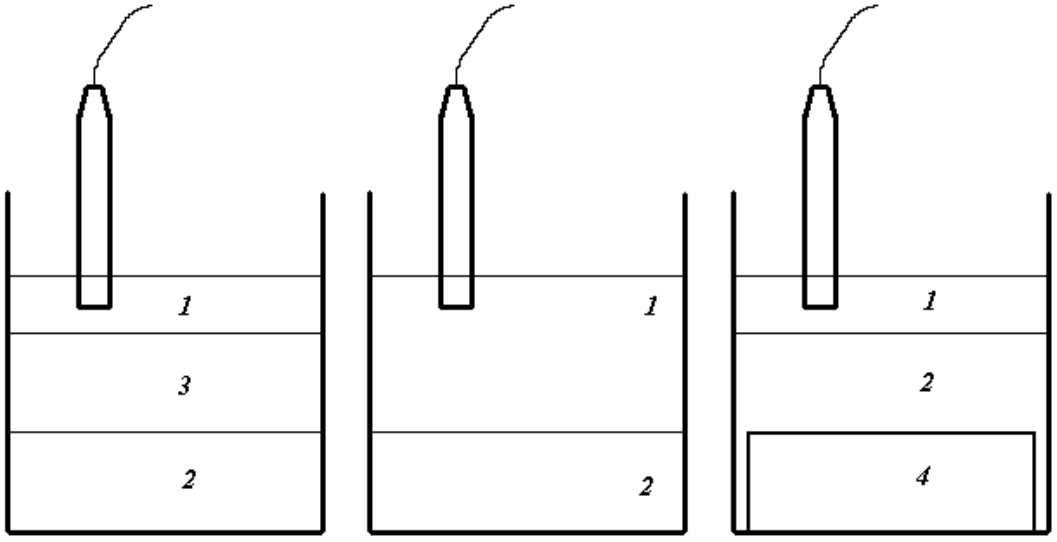

Figure 6.1. Geometries used in measurement of dose dependent reflection from the interface between MAGIC gel and various inert materials.

Once formed the gels were irradiated using a Siemens Primus 6MV linear accelerator (Siemens AG, Erlangen, Federal Republic of Germany). Three quadrants were irradiated to increasing dose levels (10, 20 and 30 Gy) with the fourth quadrant being unirradiated.

A single element transducer of centre frequency 3.5 MHz was used in pulse-echo mode to measure reflections from interfaces. The transducer had a -6dB width of 3mm at the focal depth of 55mm, measured using an NPL Beam Calibrator (Preston, 1988). A Panametrics 5077PR pulser-receiver (Olympus-NDT, Waltham, MA) was used to apply a square-wave pulse to the transducer which was clamped in a micromanipulator above the sample. The Panametrics 5077PR then amplified the reflected waveform produced by the transducer which was digitized using a National Instruments NI-5133 USB Oscilloscope (National Instruments Corporation, Austin, Texas). The received signal was analysed using National Instruments Labview Signal Express 3.0 and Matlab R12.1 (The MathWorks, Inc., Natick, MA). An example of the Matlab code used for analysing the signals is contained in Appendix C2.

The most promising material tested was the custom made solid polymer from Acoustic Polymers Ltd. This custom made polymer had a customised density so that its acoustic impedance was closely matched to that of MAGIC gel.

Initially the variation in reflected amplitude from the interface between the MAGIC gel and the inert material with temperature was measured at a single position

in the sample. A sample consisting of unirradiated MAGIC gel with an inert reflector was cooled to 5 °C. The sample was then placed in a water bath and the temperature was slowly increased. The temperature of the gel/inert material interface was measured with a digital thermometer. As the temperature increased repeated measurements of the reflection amplitude were made. The average reflected ultrasound signal from 100 transmitted pulses was recorded at each temperature and analysed for RMS amplitude and an FFT was taken and the phase of the fundamental mode was recorded.

The reflection amplitude from the interface between the MAGIC gel and inert material was mapped over a 15 x 15 square grid of 4mm spacing for a number of batches of MAGIC gel, which were irradiated in different geometrical arrangements. Gels were manufactured as described by Fong et. al. (2001) and summarized in Chapter 3.4.3. Once manufactured, the gel was poured onto the top of the inert reflector, taking care not to introduce any bubbles into the mixture. Once the MAGIC gel was poured into the phantom, a vacuum system (Island Scientific cylindrical chamber (Island scientific Ltd, Isle of Wight, UK) with Edwards E2M8 vacuum pump (Edwards High Vacuum International, Crawley, UK)) was used to ensure any bubbles introduced during the creation of the phantom were removed. Once all the bubbles in the gel had been removed a layer of vegetable oil was poured over the MAGIC gel to provide ultrasonic coupling between the transducer and the gel, and to seal the MAGIC gel and to help prevent oxygen contamination. The gels were then left for 6 hours to cool before being placed into a refrigerator for approximately 24 hours prior to irradiation. After irradiation the phantoms were returned to the refrigerator for approximately 48 hours prior to measurement,

The mapping of reflected amplitude was performed at a number of temperatures and 1 ½ hours was left between changing temperature of the water bath for the gel material to reach thermal equilibrium. At each position the reflected ultrasound signal from 100 transmitted pulses was recorded and the RMS amplitude was calculated.

Two batches of MAGIC gel were made and used to create an interface with the acoustic polymers material. They were irradiated using a 6 MV photon beam from a calibrated Primus linear accelerator (Siemens Medical Solutions, Concorde, CA) to create four different dose levels. One quadrant remained unirradiated while the other three received 10 Gy, 20 Gy and 30 Gy respectively. For the second batch an estimate

of the reflection coefficient and an estimate of the noise floor were made. The reflection coefficient was estimated by comparing the RMS reflection amplitude received from the acoustic polymer material with the RMS reflection amplitude received when the acoustic polymer material was replaced by a pure reflector. To do this, another set of measurements were performed with the acoustic polymer reflector material being replaced by a material of very high acoustic impedance (stainless steel), to simulate pure reflection at this interface. All other geometrical aspects of the experiment remained the same. To assess the noise floor, a second measurement window was created immediately prior to the reflected pulse being received and the maximum RMS amplitude was measured.

A third batch of gel was made and used to create an interface with the acoustic polymers material. A 6 MV photon beam from a calibrated Primus linear accelerator (Siemens Medical Solutions, Concorde, CA) was used to irradiate one half of the phantom to 30Gy, with the other half remaining unirradiated.

For each of the irradiation patterns the delivered dose was calculated in Nucletron Oncentra MasterPlan (Nucletron B.V., Veenendaal, The Netherlands). The sample geometry was entered into the treatment planning system and the commissioned beam model of the Siemens Linear Accelerator was used to calculated the delivered dose distribution.

6.3.2. Temperature dependence of properties

During the process of measuring reflections from various materials it was determined that the temperature at which measurements were made significantly affected the results. To aid understanding of the temperature and dose dependence of the reflection coefficient $\left|\frac{Z_2 - Z_1}{Z_2 + Z_1}\right|$, a parameterisation of Z_1 and Z_2 in terms of the temperature and dose dependence of density and speed of sound was used to create a model of the reflection coefficient. Measurements of the temperature and dose dependent acoustic properties of the MAGIC gel described in previous chapters, and similar measurements of the temperature dependence of acoustic properties of the inert reflectors were used in the parameterisation. The parameterisation was coded in

Matlab R12.1 where the reflected pressure amplitude was calculated for the interface between MAGIC gels and selected inert materials at different doses and temperatures.

The speed of sound of unirradiated MAGIC gel is temperature dependent, and the dose dependency of the speed of sound also varies with temperature. Therefore taking 25°C as our baseline temperature, the speed of sound of MAGIC gel can be parameterised by

$$c_{\mathrm{MAGIC}}(T, D) = c_{25} + C_T(T\text{-}25) + (C_D + C_{DT}(T\text{-}25))D \qquad (6.2)$$

where c_{25} is the speed of sound of MAGIC gel at 25°C. C_T is the rate of increase of speed of sound with increasing temperature above 25°C. C_D is the increase in speed of sound with increasing dose at a temperature of 25°C. C_{DT} is the increase in the dose dependent increase of the speed of sound with increasing temperature above 25°C.

Similarly the density of MAGIC gel can be parameterised by

$$\rho_{\mathrm{MAGIC}}(T, D) = \rho_{25} + \rho_T(T\text{-}25) + (\rho_D)D \qquad (6.3)$$

where ρ_{25} is the density of MAGIC gel at 25°C. ρ_T is the rate of density increase of MAGIC gel with increasing temperature above 25°C. ρ_D is the rate of increase of density with dose.

Similar equations (without the dose dependency) can be formed for the speed of sound and density of the acoustic polymer material, $c_{\mathrm{AP}}(T)$ and $\rho_{\mathrm{AP}}(T)$. These parameterised values for density and speed of sound of the two materials can be used in the formula to calculate reflection coefficient from the acoustic impedances of the two materials.

This parameterisation of the reflection coefficient is a simplification due to the use of a real number as the speed of sound. Speed of sound is a complex property in a dispersive medium. Following Kinsler and Frey (1962) it is possible to introduce dissipation into the wave equation by replacing the real velocity c with a complex velocity $\mathbf{c}$. The complex velocity $\mathbf{c}$ can be written in terms of the complex wavenumber $\mathbf{k}$. The angular frequency ω remains real and therefore

$$\mathbf{c} = \frac{\omega}{\mathbf{k}}. \qquad (6.4)$$

The complex wavenumber can be written as

$$\mathbf{k} = k + i\alpha. \qquad (6.5)$$

where k is the wavenumber derived from the real part of the speed of sound (as measured in the previous sections) and α is the attenuation coefficient.

An extension to the parametric model to include the complex speed of sound was created using measured data of attenuation coefficient. Due to the uncertainties in the measurement of the attenuation coefficient the robustness of this extension to the model is unknown.

Measurements of the temperature dependence of the speed of sound of the acoustic polymer material was performed in a similar method to the measurements of the speed of sound of MAGIC gel (Section 3), but without the need for Mylar sheets to provide the outer surface of the mould. The temperature dependence of the density of the acoustic polymer material was determined in a similar way to that of MAGIC gel (Section 4), but without the need for the polythene bags to hold the gel material in.

6.4. Results

6.4.1. Temperature dependence of properties of acoustic polymers inert reflector

The speed of sound of the acoustic polymer material was measured at four different temperatures. It was found that the speed of sound decreased with temperature by approximately 3.5 ms^{-1} $°C^{-1}$. The results are plotted in Figure 6.2. Error bars shown are the standard deviations of the measured speed of sound through 3 different samples at each temperature.

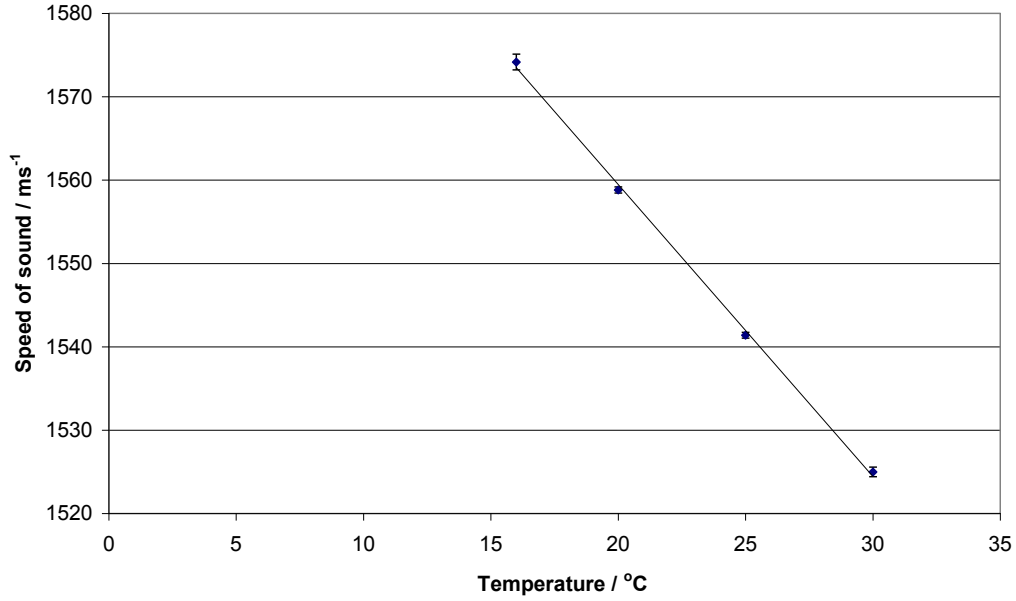

Figure 6.2. Temperature dependence of the speed of sound of the acoustic polymer reflector. Error bars are the standard deviations for three different samples of material.

The density of the acoustic polymer reflector was observed to change with temperature by -0.63 kg m^{-3} $°C^{-1}$. This change in density with temperature is shown in Figure 6.3.

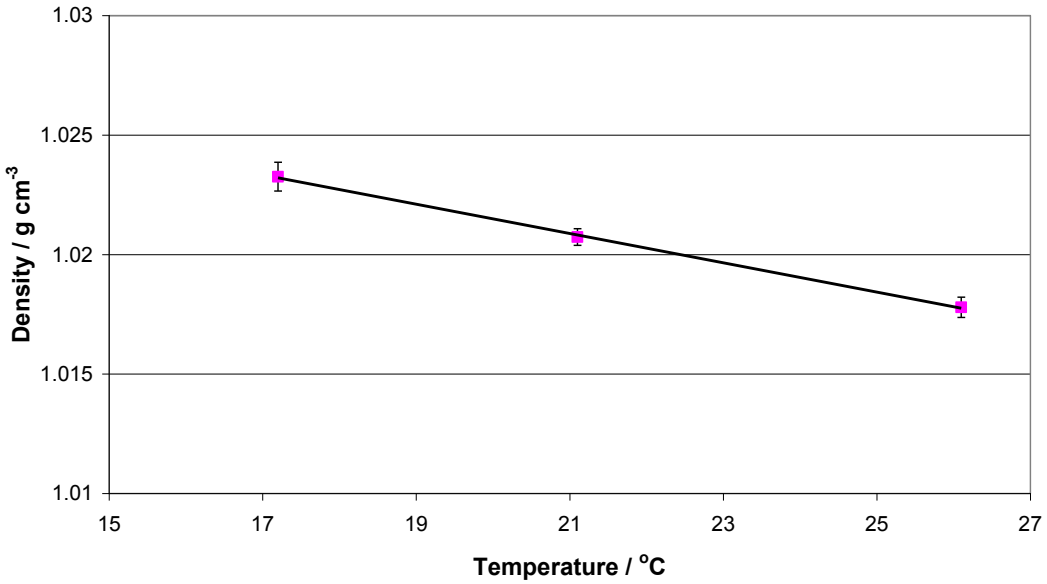

Figure 6.3. Temperature dependence of the density of the acoustic polymer reflector. Error bars are the standard deviations for three different samples of material.

6.4.2. Parametric model of temperature dependence of reflection from plane surface

The parametric model of the temperature and dose dependence of the reflection amplitude from the interface between MAGIC gel and acoustic polymers plane reflector is exemplified in Figure 6.4. The model contains the measured dependence of density and speed of sound of MAGIC gel with dose and temperature. It includes the temperature dependence of density for the acoustic polymer reflector. For unirradiated gel this shows an expected decrease in reflection coefficient as temperature increases, reaching zero reflection coefficient at a temperature of 21°C, above which the reflection coefficient increases with temperature. For irradiated gel this shows a steeper change in reflection coefficient with temperature following a similar pattern, with the zero occurring at 19°C. The extension of the model to utilise the complex speed of sound is shown in Figure 6.5. This shows a similar pattern to Figure 6.4, although the reflection coefficient does not reach zero, but instead goes through a minimum at approximately 22°C for unirradiated gel and 20°C for gel irradiated to 30 Gy.

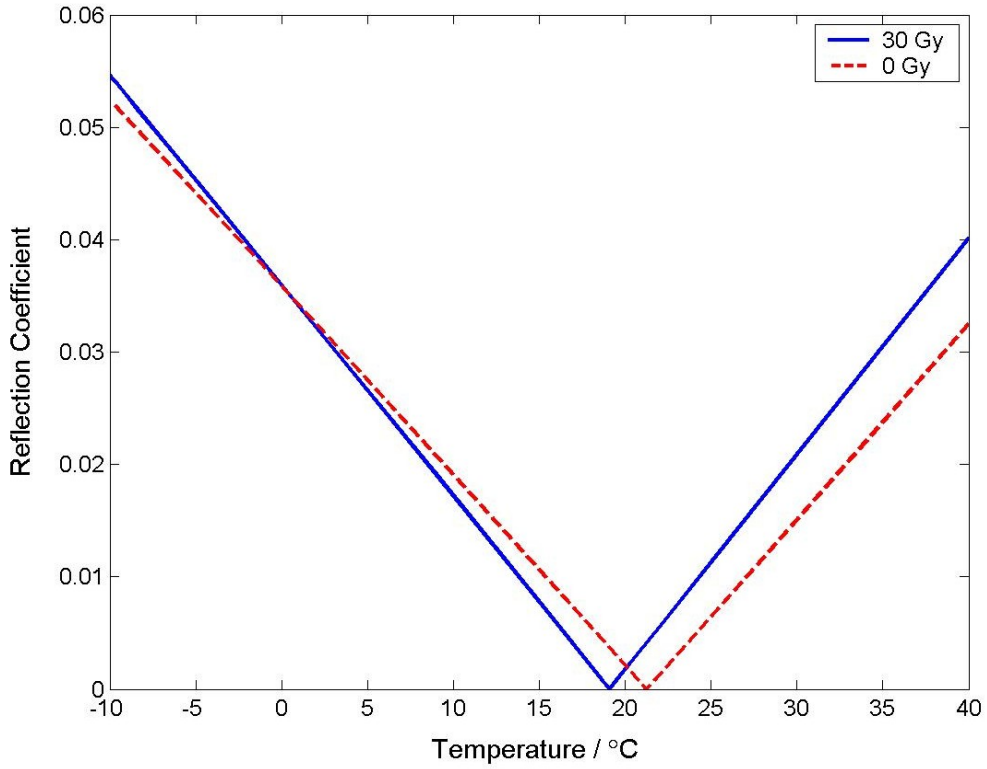

Figure 6.4. Model of temperature dependence of reflection from interface between MAGIC gel and acoustic polymers plane reflector for unirradiated (- - - -) and irradiated (—)regions using real speed of sound.

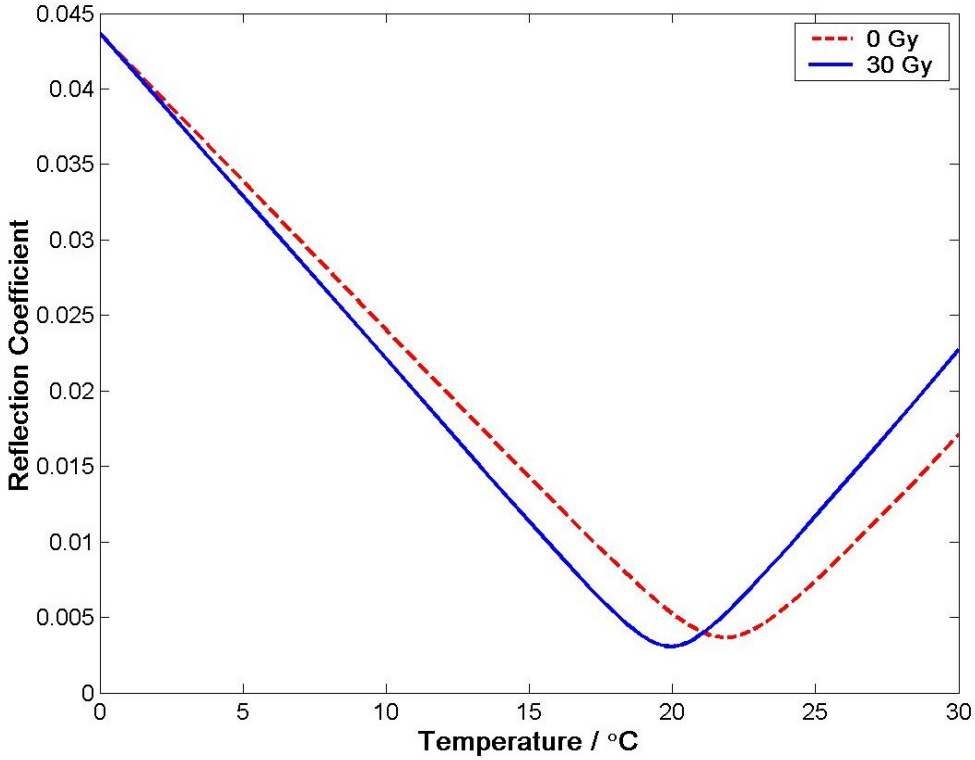

Figure 6.5. Model of temperature dependence of reflection from interface between MAGIC gel and acoustic polymers plane reflector for unirradiated (- - - -) and irradiated (—) regions using estimates of the complex speed of sound.

6.4.3. Measurement of temperature dependence of reflections from a plane surface

For an unirradiated sample, the temperature dependence of the reflection amplitude at a single position is shown in Figure 6.6. The RMS amplitude of the signal initially decreases with increasing temperature. The RMS amplitude reaches a minimum at approximately 11 °C, above which the RMS amplitude increases. The FFT of the reflected signal was used to analyse the phase at each temperature, as shown in Figure 6.7. The phase decreases slowly with increasing temperature until a phase change of approximately π occurs at approximately 11°C.

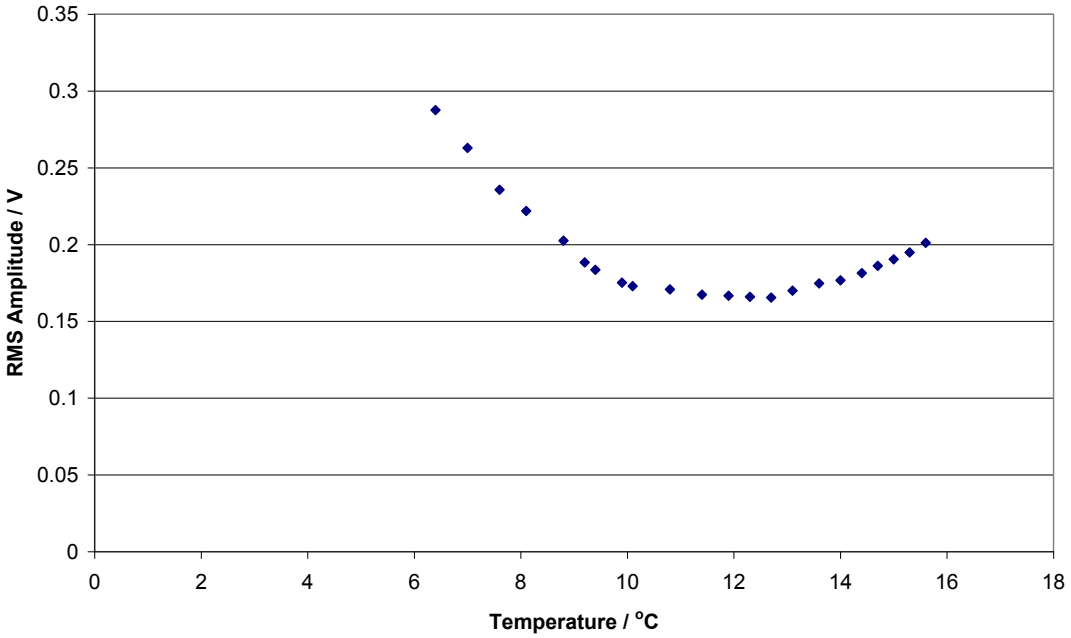

Figure 6.6. Reflection amplitude as a function of temperature for unirradiated gel sample

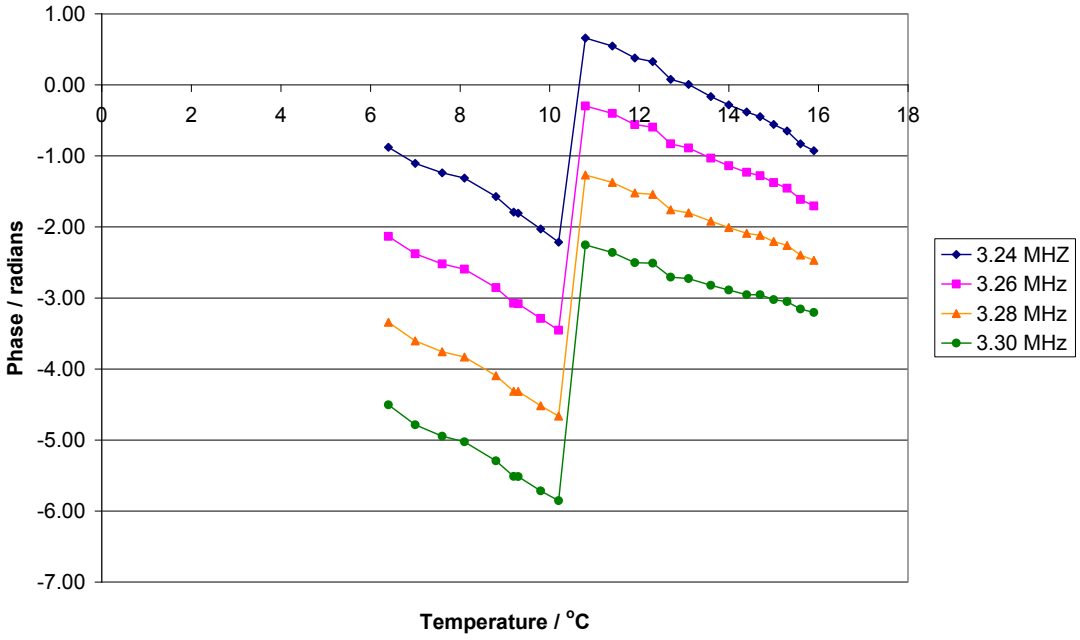

Figure 6.7. Phase of reflected signal as a function of temperature for unirradiated gel sample

For each of the four quadrants the average RMS amplitude from a 6 × 6 region in the quadrant was calculated. This average RMS amplitude for each quadrant is plotted against temperature in Figures 6.8 and 6.9. For Batch 2 (Figure 6.9) the reflection coefficient was calculated by comparison to the RMS amplitude from a pure

reflector and the noise floor (cyan) is indicated as the maximum RMS amplitude received in a time gate immediately prior to the receiver window. The error bars plotted are the standard errors of the received signals in the 6 × 6 region – 36 data points. Both figures show a similar pattern with the RMS amplitude/reflection coefficient decreasing as temperature increased to a minimum, after which the RMS amplitude/reflection coefficient increases. The temperature at which the minimum in RMS amplitude/reflection coefficient occurs increases with irradiated dose. Figure 6.10 shows the data reconfigured to show how the reflection amplitude varies with dose for three selected temperatures, one of which (13.4 °C) is below the temperature at which the minimum reflection occurs, one (17 °C) around the temperature of minimum reflection and one (23 °C) above the temperature of minimum reflection. At the lowest temperature the reflection coefficient increases with nominal dose, whereas at the highest temperature the reflection coefficient decreases with dose.

Figure 6.11 shows the data for Batch 2 where the RMS amplitude was averaged over a 2 × 2 region from each quadrant rather than using the whole quadrant. The error bars plotted are the standard errors of the received signals from the 4 data points from each quadrant. The variation in reflection coefficient with temperature and dose is the same as the plots for the 6 × 6 regions.

Figure 6.12 shows the data for Batch 2 where the RMS amplitude was averaged for each 2 × 2 region over the sample at 27 °C. The dose was calculated as the average dose received by the same region of the sample as calculated by the Nucletron Oncentra treatment planning system. The reflection coefficient decreases approximately linearly with irradiated dose, although there is significant variation around this general trend.

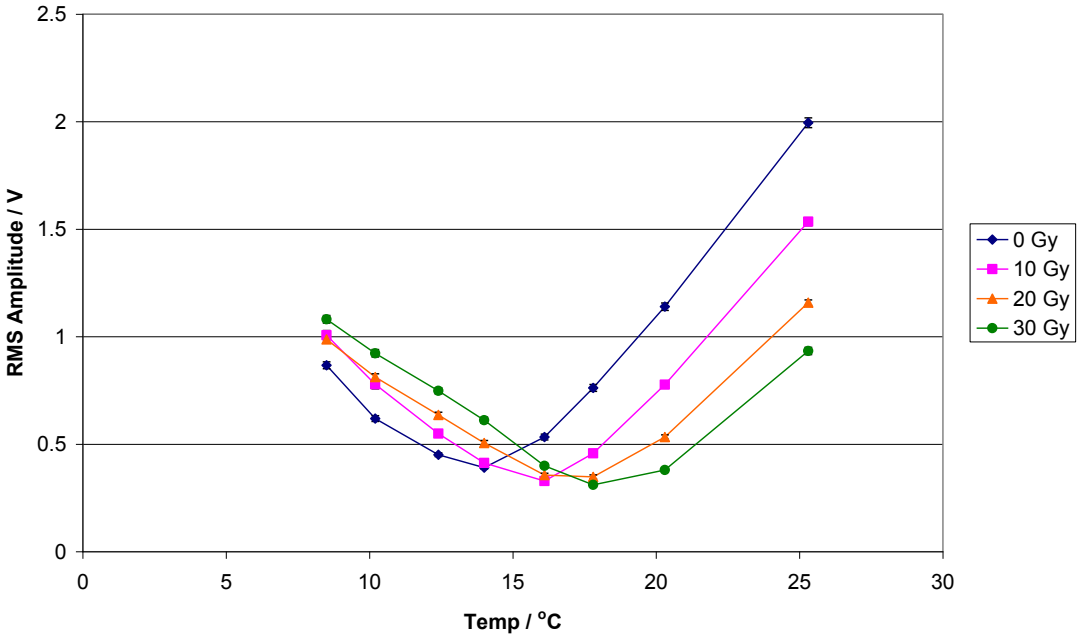

Figure 6.8. Batch 1 averaged reflection amplitude as a function of temperature for the different quadrants of the gel samples. The dose levels are the nominal dose received by each quadrant.

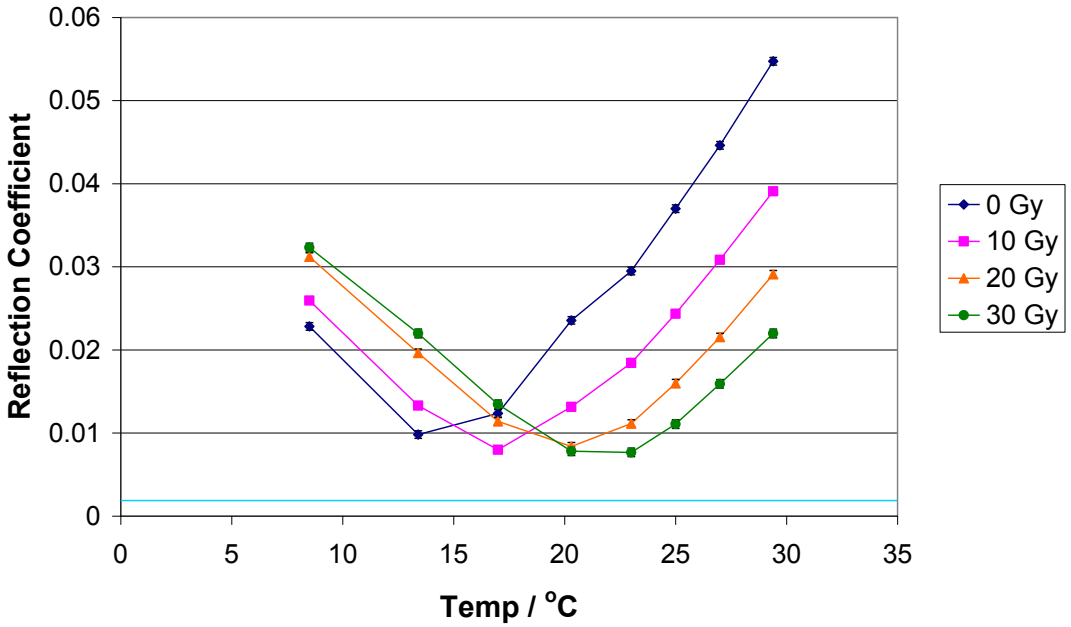

Figure 6.9. Batch 2 averaged reflection ceofficient as a function of temperature for the different quadrants of the gel samples. The dose levels are the nominal dose received by each quadrant. Noise floor is indicated in cyan.

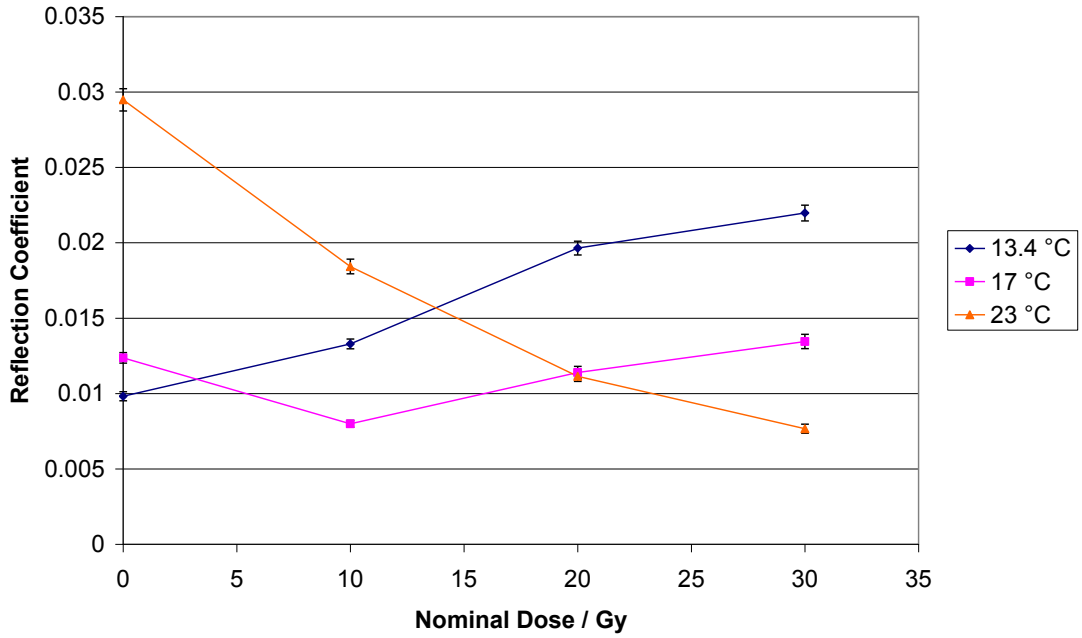

Figure 6.10. Batch 2 averaged reflection coefficient as a function of nominal dose for the different quadrants of the gel samples at 3 selected temperatures.

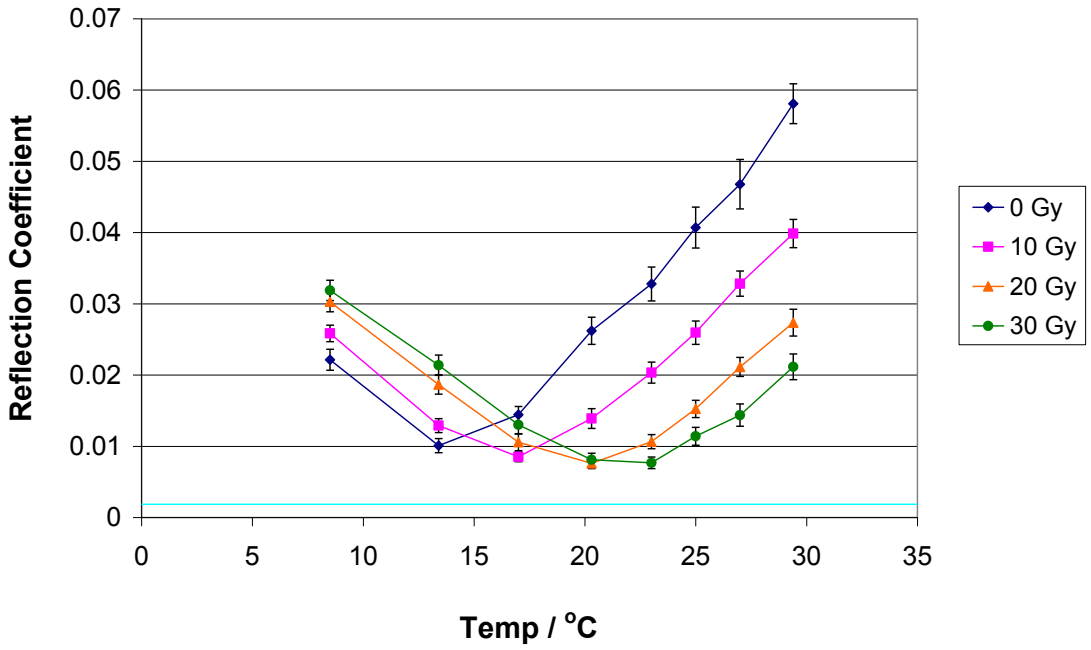

Figure 6.11. Batch 2 averaged reflection coefficient as a function of temperature for a 2 x 2 square in each quadrant. The dose levels are the nominal dose received by each quadrant. Noise floor is indicated in cyan.

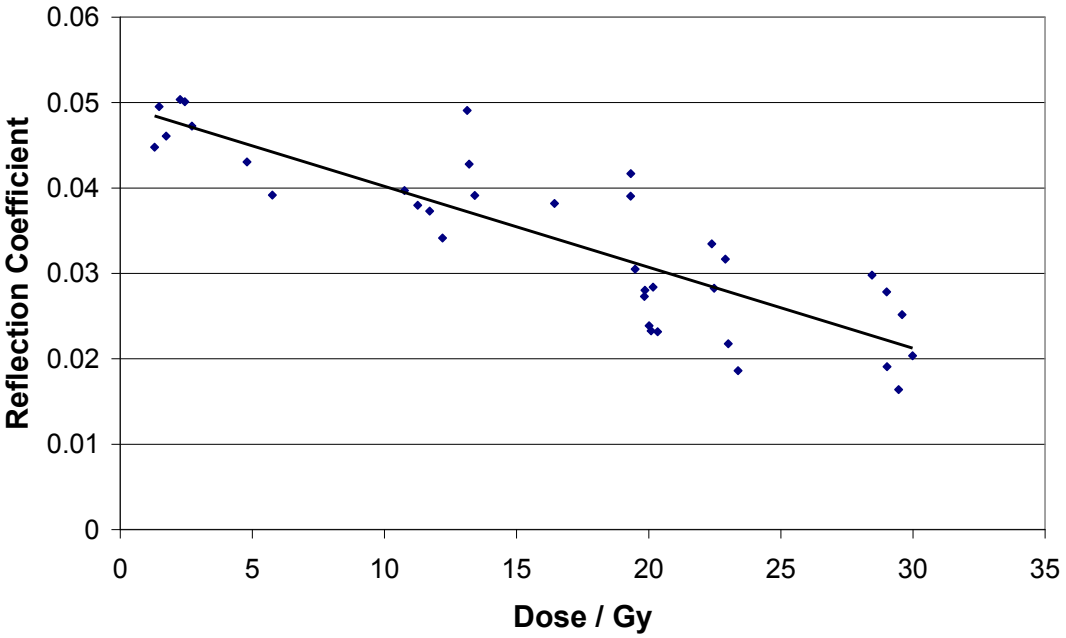

Figure 6.12. Batch 2 averaged reflection coefficient as a function of dose for all 2 x 2 squares in the sample irradiated as a quadrant. The temperature at which the measurements were made was 27 °C.

6.4.4. Measurement of profiles across a dose discontinuity

Figure 6.13 shows the RMS amplitude of the reflected signal across the sample. Five rows of data from the grid are displayed. The left hand side of the sample was unirradiated while the right hand side was irradiated to 30 Gy. The measurements were made at a temperature of 21°C. The average dose profile created by the irradiation is represented by the solid line. This demonstrates that the reflection amplitude decreases as the dose increases. The change in signal amplitude occurs within four measurement positions (approximately 12 mm), similar to the change in irradiated dose which occurs over approximately 10 mm. Figure 6.14 shows the RMS amplitude of the reflected signal against dose, showing the reduced signal amplitude for the irradiated region.

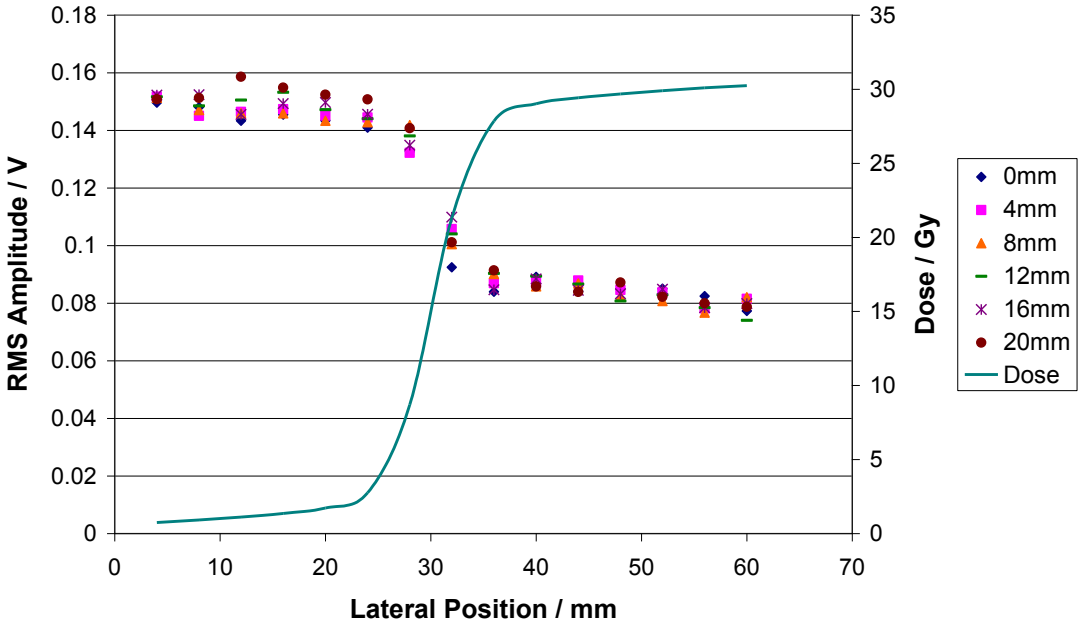

Figure 6.13. RMS amplitude of reflected signal with position across the sample. The left hand side was unirradiated while the right hand side was irradiated to 30 Gy. The solid line represents the dose profile created by the irradiation. The different series represent different longitudinal positions.

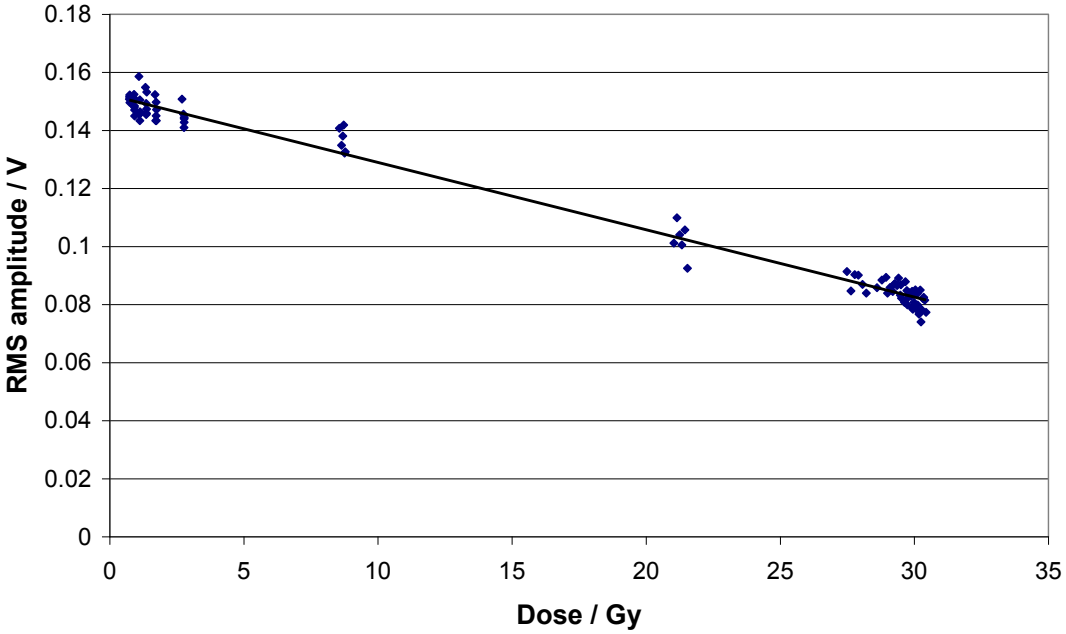

Figure 6.14. RMS amplitude of reflected signal with dose for a sample with half irradiated to approximately 30 Gy.

6.5. Discussion

The reflection of an ultrasound pulse from a plane interface between the dose dependent MAGIC gel and an inert reflector has shown that dose dependent reflections can be measured.

A novel material has been developed that matches the acoustic impedance of unirradiated MAGIC gel. This material is a polymer, manufactured by Acoustic Polymers Ltd (Mitcheldean, Gloucestershire, UK) and along with the MAGIC gel itself shows thermal variation of its physical and ultrasonic properties. The acoustic polymers material shows a reduction in its speed of sound and density as temperature increases. Over the range of temperatures tested the changes in speed of sound (Figure 6.2) and density (Figure 6.3) appear to be linear with temperature.

The parameterised model of the temperature variation of reflection for an unirradiated plane interface (——) shows an approximately linear decrease with temperature until zero reflection is reached (Figure 6.4). Then the reflection amplitude increases again approximately linearly. The temperature changes the characteristic acoustic impedance of the two materials. As temperature increases, the speed of sound of the MAGIC gel increases, indicating that the characteristic acoustic impedance will increase. As temperature increases, the speed of sound of the acoustic polymers material decreases, indicating that its characteristic acoustic impedance decreases. Therefore, at low temperatures (below 22°C) the parameterisation suggests that the characteristic acoustic impedance of MAGIC gel is lower than that of the acoustic polymers material. As the temperature increases, the difference in the acoustic impedances reduces, until they are exactly matched and no reflection occurs. Then as the temperature increases further, the acoustic impedance of the MAGIC gel now becomes higher than that of the acoustic polymers material, and the difference increases as the temperature rises. The change between which material has the higher/lower characteristic acoustic impedance will be associated in a change in sign of the reflected signal, associated with a change in phase of the frequency components.

For the irradiated region (- - - -), the irradiation increases the characteristic acoustic impedance of the MAGIC gel and therefore the temperature at which the zero reflection amplitude occurs changes. The parameterisation suggests that the temperature at which the zero occurs is lower for irradiated gel than for unirradiated

gel. It also suggests that the gradient of change in reflection coefficient with temperature is greater for irradiated regions than for unirradiated regions, because of the change in speed of sound variation with temperature for irradiated MAGIC gel.

The extension of the parameterised model to include the complex speed of sound due to the dispersive medium shows that the reflection coefficient does not go to zero, but goes through a minimum. This is due to the characteristic acoustic impedances of the two materials now not exactly matching at any temperature due to the differences in the complex velocity. It also shows that the value of the reflection coefficient at the minimum is smaller in the irradiated region than in the unirradiated region. This is due to the increased attenuation of the irradiated MAGIC gel more closely matching that of the higher attenuating acoustic polymers material.

Measurement from a plane unirradiated interface shows that, starting at the lowest temperature, the amplitude falls as the temperature increases, until a minima is reached at approximately 11°C, at which point the amplitude begins to increase again (Figure 6.6). Figure 6.7 shows the phase changes slowly until close to the temperature at which the minima in amplitude occurred, at which point (approx 10.5°C) the phase changes rapidly by approximately π. Thereafter the phase changes slowly as the temperature increases further. The change from decreasing to increasing amplitude of reflection coefficient, along with the π change in phase at the same temperature, are both consistent with the change in acoustic impedance predicted for the two materials. The temperature at which the change in reflection coefficient goes from negative to positive with increasing temperature and the π change in phase will occur at the temperature where the real parts of the acoustic impedances for the two materials are the same.

Figures 6.8 and 6.9 show the averaged amplitude of reflection from each of the four quadrants of the samples with variation in temperature. Each quadrant was irriadiated to a different dose level. For each dose level, the averaged amplitude falls as the temperature increases, until a minima is reached, at which point the amplitude begins to increase again. The overall shape of each individual curve is similar to that predicted by the parameterise model. The temperatures at which these minima occur increases with dose, which is the opposite of what the model predicted. The model predicts that due to the unirradiated MAGIC gel being less dense than the irradiated

MAGIC gel the unirradiated MAGIC gel has an acoustic impedance that is more different to the acoustic polymers material than the irradiated MAGIC gel. Therefore a higher temperature is required to match the acoustic impedance of the unirradiated gel to that of the acoustic polymers material than that required for the irradiated gel due to the known changes in acoustic impedance with temperature. However, the measurements indicate that the match occurs at a higher temperature for irradiated materials than unirradiated materials, in contradiction to the model. A number of reasons for the discrepancy between the model and the measurements can be postulated. The first is that the model is based on the measurements of speed of sound and density, and experimental errors during the course of these measurements could cause inconsistencies between the model and the way in which the actual materials behave. The second is that these measurements have been made of bulk properties of the materials, whereas the reflection occurs at the interface of the materials. Any change in the surface properties will cause the physical properties of the surface to be different from the bulk properties of the materials, again causing inconsistencies in the model. Thirdly, the model is based on a simple parameterisation of the acoustic properties based on the observations made and known parameters that affect the acoustic properties. Any other parameters, or a more complex relationship between the parameters and the acoustic properties of the material will also cause there to be inconsistencies between the model and the way in which the actual materials behave.

The value of the reflection coefficient at the minimum is smaller in the irradiated region than in the unirradiated region, as predicted by the extension of the model to include the dispersive effects of the materials. The model predicts that the increase in attenuation that occurs as the MAGIC gel is irradiated makes the imaginary (dispersive) part of the complex impedance of the MAGIC gel closer to that of the acoustic polymers material. Hence the imaginary parts of the acoustic impedance are more closely matched when the real parts of the acoustic impedances are the same, and so the reflection coefficient is closer to zero.

Figure 6.9 also has a noise floor indicated, calculated from the RMS noise in the time window immediately prior to the received signal. This shows that the minimum reflection amplitude is approximately four times the background noise signal.

Figure 6.10 shows the data for three selected temperatures. For the series at 13.4 °C the temperature is below that for which the minimum reflection occurs for unirradiated gel, and irradiating the MAGIC gel increases the reflection amplitude, indicating that the irradiation changes the acoustic impedance of the gel so that it is less closely matched to the acoustic polymers reflector. The series at 17 °C is at a temperature around the minimum reflection coefficient. An irradiation of 10 Gy decreases the reflection coefficient, indicating at this dose that the MAGIC gel and acoustic polymers reflector are more closely matched, whereas for the sections of the gel irradiated to higher doses the reflection coefficient increased again, indicating that at these higher doses the match in acoustic impedance between the acoustic polymers material was less close. For the highest temperature, the irradiation of the gel decreased the reflection coefficient, indicating that the irradiation of the MAGIC gel made the acoustic impedances of the two materials become more closely matched.

Figure 6.11 shows that the same shape and trends are visible when a 2 × 2 region in each quadrant is used for the analysis as Figure 6.9. A 2 × 2 region equates to data spacing of 8 mm, which is below the 10 mm suggested in Section 2.3 as producing a good outcome for the project, as this suggests that future developments may enable a clinically usable system to be produced.

Figure 6.12 shows the data for the average reflection coefficient for each 2 × 2 region in the sample as a function of dose received by that region at 27 °C. The data shows correlation between the irradiated dose and the reflection coefficient, even in the regions between the quadrants where the dose gradient is steep. However the level of scatter on the plot would indicate that the dose resolution of the system is not sufficient to resolve dose difference of less than 10% of the total irradiated dose.

Figure 6.13 shows the amplitude profile across a change in the irradiated dose. In each of the dose regions the reflected amplitude is approximately constant. The change in reflected amplitude occurs over a distance of about 12mm, consistent with the penumbra width of the radiation field creating the dose change, as shown by the dose profile. Figure 6.14 shows the reflection amplitude compared to the calculated dose at each measurement position.

There are a number of possible causes for the difference between the model and the measured reflections from a plane surface. The cause of the observation of the

temperature of minimum reflection increasing for an irradiated region could be due to a difference between the properties of the bulk material which have been entered into the model, and the surface of the material which creates the reflection. A difference between bulk and surface properties could be caused by oxidation of the polymer by the MAGIC gel at the interface, causing the polymer to become harder and more brittle. This will potentially change both the speed of sound and density of the surface material and how these properties vary with temperature. Due to the superficial nature of these changes, measurements of these properties is likely to be difficult and contain significant errors. A second possible cause of differences between the parametric model and the observed behaviour of the materials could be due to inaccuracies in the parameteristaion that was used in the model. Any uncertainties in the measurements of the acoustic properties will lead to uncertainties in the behaviour of the parametric model. Systematic errors in the measurements could also lead to significant differences in the model behaviour. If the parametric model of the acoustic properties is to simple or misses out some important factors then the model will be incorrect. Another possible cause of the difference between the parametric model of the reflection coefficient and the measured reflection coefficient is that the parametric model assumes a single frequency is being used, whereas the measurements were made using a broadband source. The reason for using the broadband source in these measurements was that the Panametrics 5077PR pulser-receiver was the only available instrument for driving a single element transducer in pulse-echo mode available, and only had a broadband pulse setting and not a tone-burst setting.

7. Investigation into effect of cooling rates on acoustic properties

7.1. Introduction

After attendance of the 6th International Conference on 3D Radiation Dosimetry, at which material on the current work on the ultrasonic properties of MAGIC gels for pulse-echo gel dosimetry (Atkins et al., 2010) was presented, discussions with other conference attendees indicated that different cooling rates affected gel properties. It was therefore postulated that some of the inconsistencies in the temperature dependence of the reflection from a plane surface, and also the measurements of attenuation, speed of sound and density, may be due to the cooling rate of the material. In the original experiments in Chapters 3, 4, 5 and 6 the MAGIC gel was poured when at a temperature of approximately 35°C. The phantoms (acoustic polymer material, base plate and container) or containers into which the MAGIC gel was poured were at room temperature (approximately 20°C). It is postulated that the resulting temperature difference between the MAGIC gel and the reflector surface created different cooling rates within the MAGIC gel depending on the proximity to the acoustic polymer reflector material. The MAGIC gel closest to the acoustic polymer reflector will have cooled quickest, whereas material at the centre of the gel will have cooled slowest. If the different cooling rates cause the MAGIC gel to have different acoustic properties at different areas of the gel, then the varying acoustic properties within the MAGIC gel could cause the minimum in the temperature variation of the reflection amplitude from a plane interface to be non-zero. The effect of cooling rates on material properties could also explain the batch-to-batch variations observed in other measurements (particularly attenuation and speed of sound), as during these measurements the cooling rate was not controlled, and certainly would be different for the different sample thicknesses that were used in the experiment.

7.2. Literature review

A number of authors have discussed thermal issues regarding polymer gel dosimeters.

De Deene et al. (2006) suggest that for some types of polymer gel dosimeters the dose sensitivity is dependent on the temperature of irradiation, and demonstrate a clear dependence of dose sensitivity of a number of types of polymer gel dosimeters on temperature during scanning.

Salomons et al. (2002) showed that the exothermic polymerisation reaction in polymer gels could lead to a temperature rise of up to 12°C under their experimental conditions, with the temperature rise being dependent on thermal boundary conditions and irradiated dose. They suggest that such temperature rises could have a significant effect on the polymerisation process as they will affect reaction rates, thermal motion of radicals and monomers and resulting gel structure.

Dumas et al. (2006) observed that normoxic PAG dosimeters in containers fabricated from the same Plexiglas plates but with different cross-sectional areas but irradiated to the same dose had different MR responses (larger T_2 and hence less polymer for larger cross-sectional areas). They suggest the difference is due to the different cross-sectional areas of their samples changing the thermal boundary conditions causing different temperature rises in the different samples.

Crescenti (2009) argues that the responses of the gels in the containers can be alternatively explained by the different cooling and setting rates of the gels in the different containers due to their different total heat capacities, and therefore the different responses are due to the differences in the gel prior to irradiation.

Another aspect of thermal effects that is not covered specifically in the literature on polymer gel dosimeters is the effect the thermal cycle has on the physical properties of gelatine (te Nijenhuis, 1981). The mechanical properties of the gelatine matrix are highly dependent on the thermal cycle which it has experienced. Since MAGIC gels are essentially gelatine gels, the physical properties of the gelatine matrix will have a significant effect on the properties of the full gel.

7.3. Materials and methods

To identify whether the cooling rates is affecting the acoustic impedance of the MAGIC gel, a measurement was made of the temperature dependence of the acoustic reflection amplitude from a plane interface. Two phantoms were created from the same batch of gel, one had a controlled cooling rate and the second was handled as previously. To manage the cooling rate, the plane surface was warmed prior to pouring the MAGIC gel and the cooling rate was controlled by inserting the phantom into a temperature controlled water bath and slowly letting the temperature decrease from the pouring temperature (35°C) to room temperature, at which point the gel had solidified. This management of the cooling rate should mean that the temperature within the phantom should have been as uniform as possible during the cooling process. The second phantom was not warmed and the cooling rate was not controlled in any way, so that a comparison could be made between the two methods. After 6 hours both phantoms were at room temperature and they were placed in the refrigerator for approximately 48 hours prior to measurement.

The variation in reflection coefficient with temperature was measured at a single position in both phantoms, along with a measurement of the variation in reflection coefficient with position at a fixed temperature (close to the temperature of minimum reflection coefficient). A single element transducer was used in pulse-echo mode to measure reflections from interfaces. A Panametrics 5077PR pulser-receiver (Olympus-NDT, Waltham, MA) was used to apply a square-wave pulse to the transducer which was clamped in a micromanipulator above the sample. The received waveform of the transducer was digitized using a National Instruments NI-5133 USB Oscilloscope (National Instruments Corporation, Austin, Texas) and analysis of the signal was performed using National Instruments Labview Signal Express 3.0 and Matlab R12.1 (The MathWorks, Inc., Natick, MA). An example of the Matlab code used for analysing the signals is contained in Appendix C2.

7.4. Results

Figure 7.1 shows the temperature variation of the reflection coefficient between MAGIC gel and acoustic polymers reflector for an unirradiated sample with uncontrolled cooling conditions compared to controlled cooling conditions. The samples were made from the same batch of gel but with different cooling conditions. In the uncontrolled cooling conditions the gel was poured onto the reflector and left to cool at ambient conditions. For the controlled cooling samples after pouring the gel onto the reflector and the container was placed into a water bath where the temperature was slowly reduced from the pouring temperature of the gels (35 °C) to room temperature, by which time the gel had set. This shows that controlled cooling with a slower cooling rate results in both a lower minimum reflection coefficient and a lower temperature at which this minimum occurs.

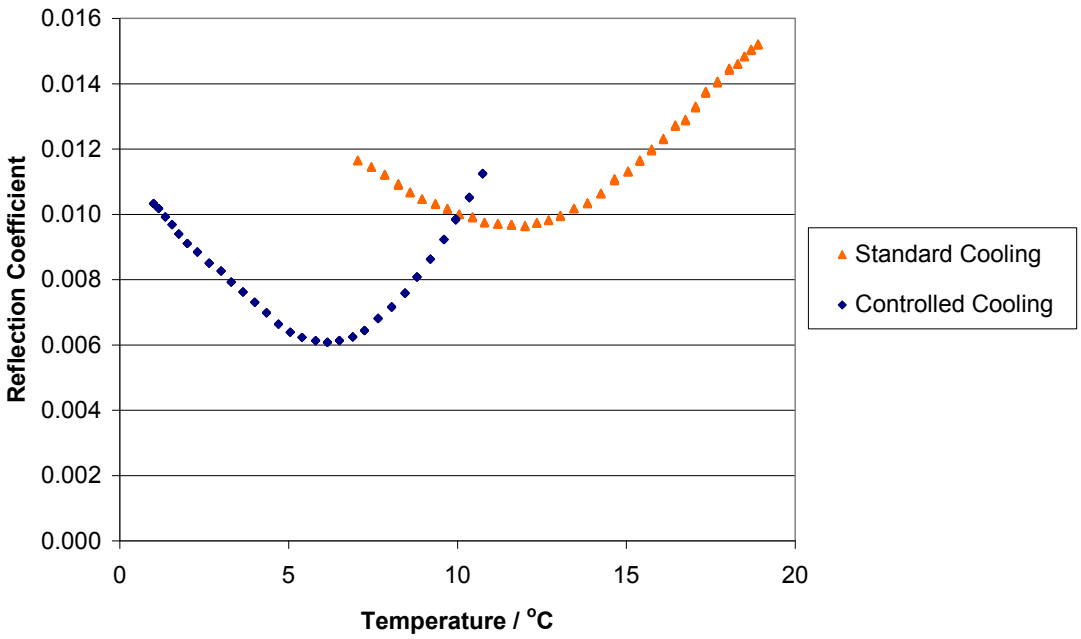

Figure 7.1. Variation in reflection coefficient with temperature between MAGIC gel and acoustic polymer reflector for standard and controlled cooling conditions.

Table 7.1 shows the results of the measurement of the variation in reflection coefficient with position for the two samples at a fixed temperature close to the temperature at which minimum reflection amplitude was observed. The original data

from an unirradiated sample is also show to compare the reflection coefficients of two batches of gels to show the batch to batch variation.

Sample	No. of measurement positions	Temperature of measurement / °C	Mean reflection coefficient
Controlled cooling	15	6.0	0.0056 ± 0.0008
Uncontrolled cooling	11	11.2	0.0097 ± 0.0014
Original unirradiated data	45	13.4	0.0098 ± 0.0005

Table 7.1. Measured reflection coefficient between MAGIC gel and acoustic polymer reflector for a number of measurement conditions comparing different cooling conditions.

7.5. Discussion

There are two differences to note between the two temperature profiles shown in Figures 7.1 comparing the temperature dependence of the reflection coefficient between MAGIC gel and acoustic polymer reflector for different cooling regimes.

The first difference between the two cooling regimes is that the temperature at which the minimum reflection coefficient is observed is lower for the controlled cooling conditions compared to the uncontrolled cooling conditions. The temperature at which the minimum reflection coefficient is observed is approximately 6°C for the controlled cooling conditions while it is approximately 12°C for the uncontrolled cooling conditions.

The second difference between the two cooling regimes is the minimum reflection coefficient itself. For the uncontrolled cooling regime the minimum reflection coefficient was observed to be approximately 0.0095, while for the controlled cooling conditions this was observed to be approximately 0.006.

Table 7.1 summarises the measurements of the reflection coefficient at different positions for the two cooling regimes. Measurements were acquired at 6°C for the controlled cooling conditions and 11.2°C for the uncontrolled cooling conditions. The mean reflection coefficient was observed to be 0.0097 ± 0.0014 from 11 measurement positions for the uncontrolled cooling conditions and 0.0056 ± 0.0008 from 15 measurement positions for the controlled cooling conditions. Using this data the hypothesis that there is a difference in the reflection coefficient between these two

samples can be tested. The difference between the means is significant at the 0.5% level when using a one tailed paired t-test, indicating that the minimum reflection coefficient for this measurement of controlled cooling conditions is significantly lower than the minimum reflection coefficient for this measurement of uncontrolled cooling conditions. To prove that controlling the cooling rate results in a statistically significant difference in measured reflection coefficient, further measurements of the reflection coefficients with different batches of gel are required to determine the population variation in the measured reflection coefficients for controlled and uncontrolled cooling.

The reduction in temperature at which the minimum reflection amplitude is observed between the uncontrolled and controlled cooling regimes respectively indicates that the physical properties (speed of sound, density) of the MAGIC gel are altered by the change in cooling conditions. The dependence of the physical properties of MAGIC gel on cooling rate could be a contributory factor in the batch variation observed in previous experiments, and also could contribute to difference between measurements on different thickness samples, since in all previous experiments cooling rates will have been uncontrolled and will have depended on ambient temperature at the time of MAGIC gel formulation, and size/volume of container into which the gel was placed.

The reduction in the observed minimum reflection coefficient between the uncontrolled and controlled cooling regimes respectively indicates that the impedance match between the MAGIC gel and acoustic polymer reflector is better with the controlled cooling rate. This will be due to the acoustic properties of the MAGIC gel being more uniform near the interface with the acoustic polymer material for the controlled cooling rate than for the uncontrolled cooling rate.

Crescenti (2009) discusses temperature effects on polymer gel dosimeters, but concentrates on minimising any effects that temperature will have on results by trying to control the thermal conditions and make them reproducible between experiments. In contrast this thesis aims to characterise the thermal effects and utilises the thermal conditions to produce more favourable results.

8. Acoustically matched reflector – reflection from an array of threads

8.1. Introduction

Gel dosimetry is unique in being able to measure the entire three-dimensional dose distribution of a radiotherapy treatment delivery, therefore it is important to determine if it is possible to design a phantom that would introduce the possibility of measuring 3 dimensional dose dependent reflections. In Chapter 6 it has been shown that it was possible to measure dose dependent reflections across a plane surface, and so different methods of producing 3 dimensional dose dependent reflections were considered. Three possibilities were considered: interleaved layers of dose dependent material and inert reflectors, threads of inert reflectors in a dose dependent gel and fragments of inert reflectors in a dose dependent gel.

8.2. Gedankenexperiment

8.2.1. Layered phantoms

One method of producing a 3 dimensional phantom would involve the layering of dose dependent and inert materials. There are two problems with this design that led to it being dismissed. The first is the introduction of multiple reverberations between parallel reflectors, and the second is the attenuation caused by the acoustic polymers reflector being used in the design.

To produce the same reflection conditions at different depths, a layered phantom would need to consist of parallel layers of the inert reflector and dose dependent material, otherwise the angular dependency of reflection would cause different proportions of the reflected beam to be intercepted by the transducer. However, multiple parallel layers would produce multiple reverberations in the phantom, preventing suitable time gating of signals to produce depth determination of echo position.

The attenuation coefficient of the acoustic polymers material is approximately 18 dB cm^{-1}. Even thin layers of the material would therefore cause significant

attenuation in a layered phantom, leading to only small depths being able to be investigated.

8.2.2. Fragments of inert reflector

If the inert reflector could be fragmented and mixed homogeneously throughout the dose dependent gel, then the multiple small reflections from the fragments would be seen as grey level on a conventional ultrasound scanner. The dose dependency of grey level of such a phantom could then be investigated. However, after discussion with Acoustic Polymers, Ltd, it was decided not to pursue this line of investigation since efforts to produce granules or fragments of the material that could be subsequently incorporated into such a phantom would be hampered by agglomeration of the fragments without the addition of an additive to prevent this occurring. Such an additive would then be present when mixing the fragments with the dose dependent gel, and would alter the properties of the phantom in an unknown manner.

8.2.3. Matrix of inert threads

The third method to be considered was a matrix of inert threads in a dose dependent gel. Although the threads will cause shadowing behind them, the matrix can be designed in such a way to prevent the shadows affecting other threads. Cylindrical threads will not cause multiple reflections and will reduce the angular dependence of reflection amplitude.

8.3. Thread phantom

A set of 150 mm long, 1 mm diameter threads was manufactured by Acoustic Polymers, Ltd. with a target density of 1030 kg m^{-3}. The diameter of the threads was specified as 1 mm so that they were thin with respect to the wavelength of the ultrasound (approximately 0.5mm at 3 MHz), but strong enough to withstand handling.

A frame was constructed from which the threads were suspended. The frame consisted of 2 pieces of veroboard with 4 fixing spacers to maintain the geometry. An

array of 23 holes was drilled in the board in four rows. Each row was 10 mm apart, and the holes were 10 mm apart in each row. The holes in consecutive rows were displaced by 2.5mm laterally. There were five holes on the top row and six in each of the subsequent three rows. The diameter of the holes in the veroboard were 1mm, through which the threads could be passed. The holes were positioned so that when imaged from a direction perpendicular to the rows each thread should not interfere with the ultrasound path to threads in the rows below, and is shown in Figure 8.1. The overall width of the thread array was 57.5mm, which fits within the 60mm imaging width of the Ultrasonix MDP ultrasound scanner (Ultrasonix Medical Corporation, Richmond, BC, Canada) used in this thesis. Each thread was held in place by glue before being encased in an epoxy housing. The threads were placed under slight tension between the frame to reduce any sag that occurred. The tension was created by hanging a weight from each thread as it was glued in place. Figure 8.2 shows a diagram of the construction of the thread holder. Figure 8.3 and 8.4 show the partly constructed and completed thread phantom respectively. The array of threads was designed in conjunction with, and manufactured by, Dr Sui Man Lee and Mr Peter Laidler of the Department of Medical Physics and Bioengineering, Royal United Hospital NHS Trust, Bath.

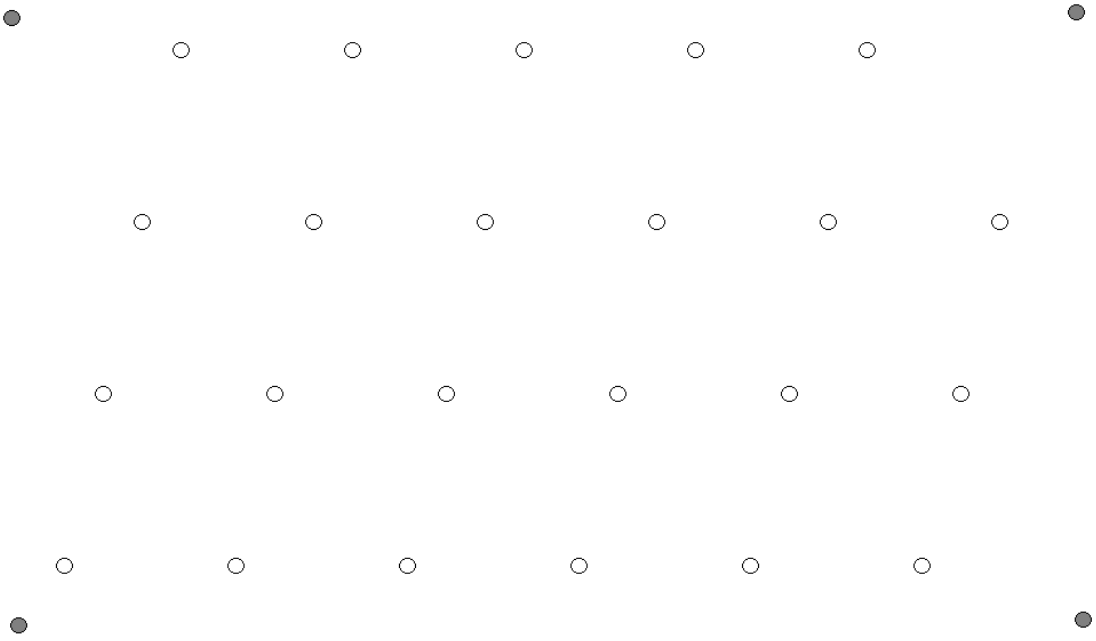

Figure 8.1. Schematic diagram showing the positioning of the threads (open circles) in the array. The filled circles indicate the positions of the spacers.

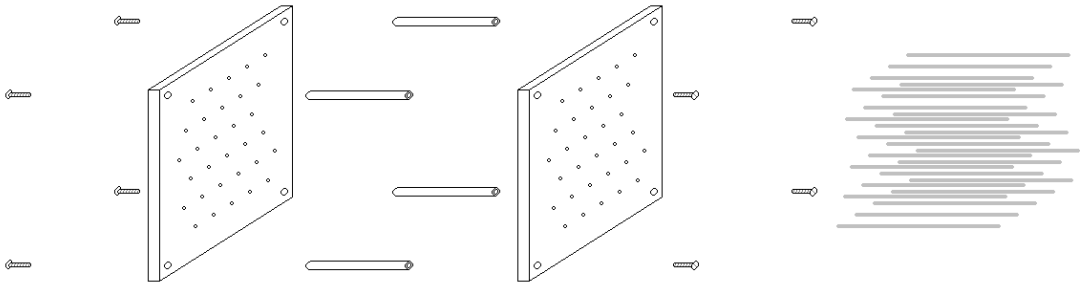

Figure 8.2. Diagram showing the construction of the thread holders. The plates are spaced by four Nylon spacers held in place by Nylon bolts. The acoustic polymers threads are pushed through the matrix of holes in the plates and secured each side by glue and an epoxy moulding (not shown).

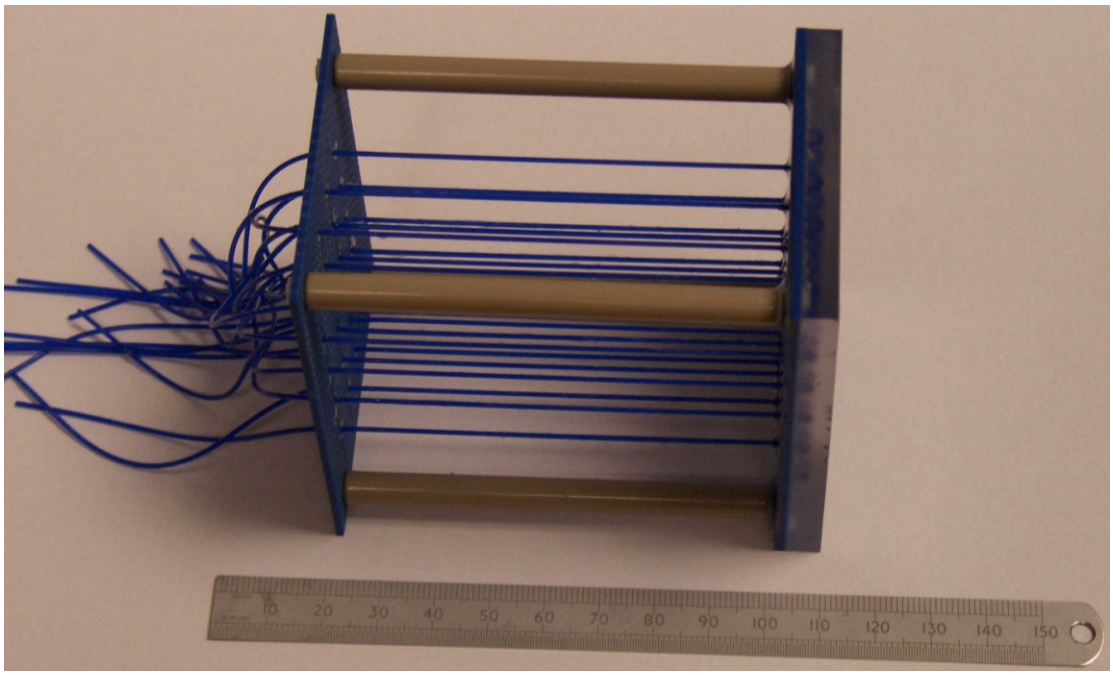

Figure 8.3. Photo showing the construction of the thread holders. The plates are spaced by four Nylon spacers held in place by Nylon bolts. The acoustic polymers threads are pushed through the matrix of holes in the plates and secured each side by glue and an epoxy moulding on the right hand side. The threads on the left hand side are free prior to them being glued and set in epoxy.

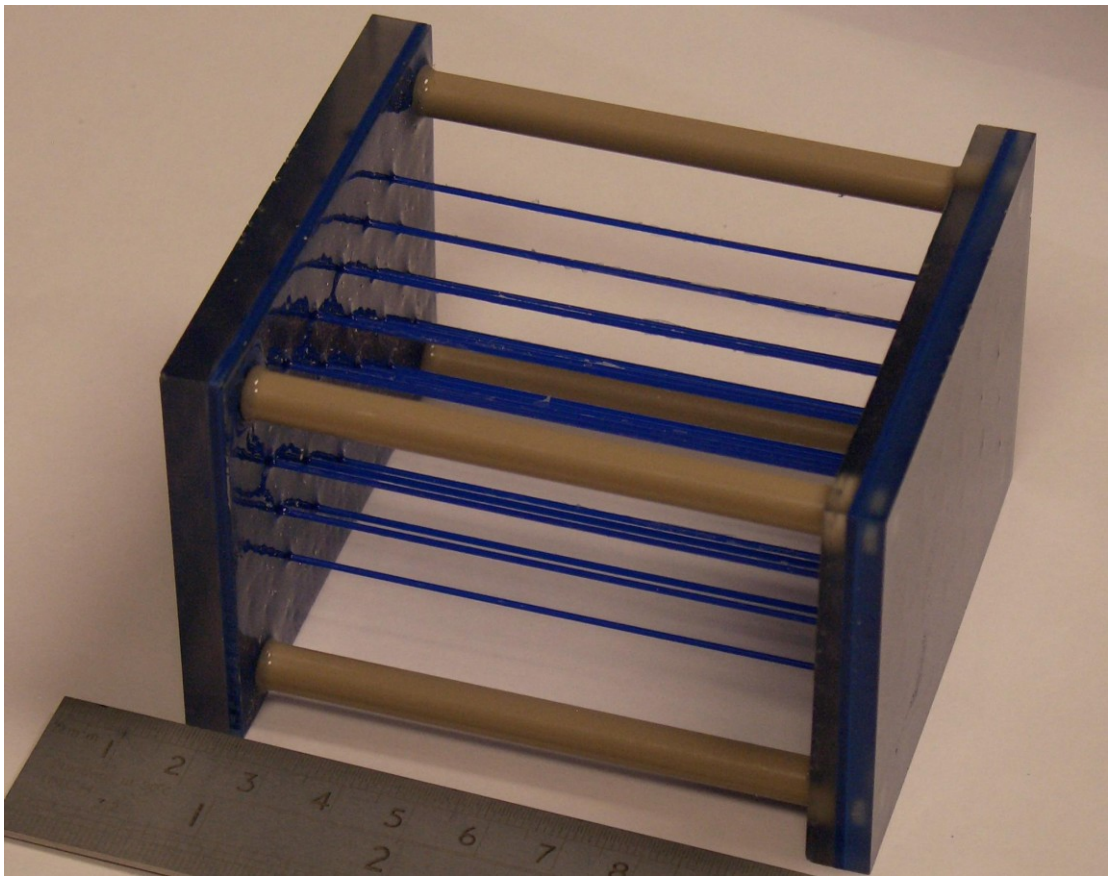

Figure 8.4. Photo showing the completed thread holder with both ends of the threads glued and encased in epoxy.

9. Imaging of thread phantom

9.1. Introduction

The use of an ultrasound scanner to acquire the ultrasonic data is an important part of this project. Using an ultrasound scanner to acquire the data will provide faster data acquisition compared to the use of the single element transducer in Chapter 6 and should lead to the applicability of this system to many hospitals beyond teaching and research institutes which currently use gel dosimetry for radiotherapy verification. Experiments were performed to identify if the ultrasound scanner could be used to acquire images of the thread phantom proposed and developed in Chapter 8.

9.2. Materials and methods

9.2.1. Image acquisition

An Ultrasonix MDP scanner (Ultrasonix Medical Corporation, Richmond, BC, Canada) with Research Package was used to scan the phantom, using a 60mm linear transducer operating in the range 5-14 MHz. Images were acquired in Portable Network Graphics (PNG) format, with lossless compression, utilising the print functionality of the scanner. These images were transferred from the scanner to a computer for subsequent image analysis using Matlab R12.1 (The Mathworks, Inc., Natick, MA). The ultrasound transducer was held in a custom frame with micromanipulator controls of positioning. Images were acquired either at a static position while the other properties such as temperature and salinity were varied, or were acquired at 4mm intervals across the entire phantom at fixed temperature settings. While images were acquired the temperature of the phantom was controlled using a Grant GD 100 Immersion Thermostat (Grant Instruments Ltd, Cambridge, UK) and a Grant C1G Refrigerated Immersion Cooler attached to the water tank.

The scanner configuration will be adjusted to ensure that the most suitable settings were used in the image acquisition. Settings such as swept gain, dynamic

range and focussing were all adjusted. From section 2, the measured attenuation coefficient of MAGIC gels is in the range 0.5 – 3.5 dB cm^{-1} (Figures 3.4 – 3.6), compared to 0.54 dB cm^{-1} MHz^{-1} as the average soft tissue attenuation (Culjat et al. 2010). Therefore, the swept gain was reduced to ensure a greater dynamic range was available. For the rho-c matched polymer the reflection amplitude will be small, although the relative change in reflection coefficient (unirradiated to irradiated) will be significant. Therefore the overall gain was set high, with an appropriate selection of the dynamic range made to ensure the expected changes were observed within the available dynamic range while reducing any quantisation that may occur due to digitisation into the 8-bit images produced by the system.

The image acquisition system of the Ultrasonix MDP Scanner includes a pre-image formation logarithmic gain compression. This logarithmic compression aids the display of the ultrasound images but no user control of this gain compression is available. When performing quantitative image analysis this pre-display logarithmic compression needs to be accounted for in subsequent analysis and image comparison.

9.2.2. Temperature and dose dependence of reflections from simple thread phantom

A simple three-thread phantom was utilised to measure the temperature and dose dependence of reflection from the threads when the phantom was placed into MAGIC gel. The thread phantom was placed in a Polyethylene box and held in place using silicone. MAGIC gel was manufactured and poured into the container, taking care not to introduce any bubbles into the mixture. Once the MAGIC gel was poured a vacuum system (Island Scientific cylindrical chamber (Island scientific Ltd, Isle of Wight, UK) with Edwards E2M8 vacuum pump (Edwards High Vacuum International, Crawley, UK)) was used to ensure any bubbles introduced during the creation of the phantom were removed. Once all the bubbles in the gel had been removed a layer of vegetable oil was poured over the MAGIC gel to provide ultrasonic coupling between the transducer and the gel, and to seal the MAGIC gel and to help prevent oxygen contamination. Then the entire system was allowed to cool slowly until the MAGIC

gel had set. Once the MAGIC gel had set the system was placed into a refrigerator prior for approximately 24 hours.

Ultrasonic images of the thread phantom were acquired at four positions across the phantom as the temperature of the phantom was increased up to room temperature. Each image was acquired using a single focal zone on the scanner set at 31mm deep, with a Power Setting of -10, Gain of 65% and Dynamic Range of 80dB.

The images acquired by the scanner were exported to a PC running Matlab R12.1 (The Mathworks, Inc., Natick, MA). The PNG format images were imported into Matlab and pixel data for the scan area was selected. The approximate location of the acoustic polymers threads was known and the analysis routine searched a 20 by 30 pixel region around the initialisation position for each thread to identify the strongest echo for each thread. The average value of a 61 pixel region was also calculated as a surrogate for the reflected power from the thread, taking the greatest value from a search of a 20 by 30 pixel region centred on the initialisation position. The 61 pixel mask used to calculate the average pixel value was an oval eleven pixels wide and seven pixels deep. Seven pixels is approximately 1 mm and equates to the thread diameter in the scan direction. The mask was larger across the thread width as the lateral resolution of the ultrasound image is governed by the image focusing. An example of the Matlab code used for analysing the signals is contained in Appendix C3.

Then the phantom was irradiated using a Siemens Primus linear accelerator (Siemens AG, Erlangen, Federal Republic of Germany). A dose of 10 Gy was delivered to half of the phantom. Two of the measurement positions were therefore irradiated and two of the measurement positions remained unirradiated. After returning the phantom to the refrigerator for approximately 48 hours, ultrasound images were acquired of the irradiated phantom at each of the four measurement positions at two temperatures, 5°C and 16.5°C, the minimum and maximum temperatures at which the unirradiated phantom was imaged. One and a half hours was left between temperature changes to allow the phantom to thermally equilibrate. The same imaging parameters were used as the pre-irradiation images. Two sets of images were acquired post-irradiation with independent positioning of the scan plane.

The pixel values measured from the scans acquired post-irradiation were normalised to the pre-irradiation values by subtracting the pre-irradiation values. This

subtraction of pre-irradiation images was used to correct for variation in imager performance, the variation in the interface itself and inhomogeneities in the acoustic path between the scanner and the interface. The use of subtraction rather than division for this method is based on the scanner performing logarithmic gain compression on the ultrasound images prior to any subsequent processing.

9.2.3. Measurement of acoustic impedance

A measurement of the acoustic impedance of the acoustic polymers material was made both as a verification of the process of using the Ultrasonix scanner for image acquisition of the thread phantom and to verify that the formation of the acoustic polymers material into threads had not affected the acoustic impedance of the material.

A phantom consisting of three acoustic polymers threads was immersed in saline solution. The images acquired by the scanner were exported to a PC running Matlab R12.1 (The Mathworks, Inc., Natick, MA). The PNG format images were imported into Matlab and pixel data for the scan area was selected. The approximate location of the acoustic polymers threads was known and the analysis routine searched a 20 by 30 pixel region around the initialisation position for each thread to identify the strongest echo for each thread. The average value of a 61 pixel region was also calculated as a surrogate for the reflected power from the thread, taking the greatest value from a search of a 20 by 30 pixel region centred on the initialisation position. The 61 pixel mask used to calculate the average pixel value was an oval eleven pixels wide and seven pixels deep. Seven pixels is approximately 1 mm and equates to the thread diameter in the scan direction. The mask was larger across the thread width as the lateral resolution of the ultrasound image is governed by the image focusing. An example of the Matlab code used for analysing the signals is contained in Appendix C3.

Initially the three thread phantom was immersed in a strong saline solution. The saline solution was gradually diluted, changing the acoustic impedance of the saline solution. At each dilution five images of the threads were acquired and the pixel value for each thread was determined for each image. Each image was acquired using a single focal zone on the scanner set at 21mm deep, with a Power Setting of -14, Gain of 55% and Dynamic Range of 40dB.

As the saline solution was diluted the reflection amplitude from the threads was altered and the pixel value associated with each thread changed. A minimum in reflection amplitude or pixel value would indicate the position at which the real part of the acoustic impedance was matched between the acoustic polymers material and the saline solution.

The speed of sound in saline solution was calculated from the corrections Wong and Zhu (1995) made to the equations of Del Grosso (1974). The density of the saline solution was calculated from the UNESCO report of Fofonoff and Millard (1983). Knowledge of the speed of sound and density of the saline solution allowed calculation of the acoustic impedance of the solution at each salinity level where images of the thread phantom were acquired.

To extend the range of acoustic impedances that could be measured further a similar experiment was performed using an ethanol and water mixture instead of a saline solution. The thread phantom was initially immersed in a strong ethanol/water solution which had a low acoustic impedance. The solution was gradually diluted, increasing the acoustic impedance of the solution. The speed of sound and density of the ethanol-water mixture was calculated from 6^{th} and 4^{th} order polynomial fits respectively to the data from D'Arrigo and Paparelli (1988) at the measurement temperature of 20°C. The mixing of ethanol and water is an endothermic reaction (Boyne and Williamson, 1967) and the temperature of the mixture decreased at each dilution and gas bubbles were released. Any gas bubbles that attached to the threads or the transducer surface were released by gentle brushing and the temperature of the solution was allowed to return to 20 °C before the images were acquired. To try and reduce the potential for errors due to the presence of gas bubbles, two sets of five images were acquired, with the threads and transducer surface being brushed in between each set of five images. Each image was acquired using a single focal zone on the scanner set at 21mm deep, with a Power Setting of -10, Gain of 65% and Dynamic Range of 40dB.

9.2.4. Image analysis of thread phantom

Work was also performed on code to identify all twenty-three threads in the phantom designed in Chapter 8. This work was performed using images acquired of

the phantom immersed in water. The images acquired by the scanner were exported to a PC running Matlab R12.1 (The Mathworks, Inc., Natick, MA). The PNG format images were imported into Matlab and pixel data for the scan area was selected. The location of the acoustic polymers threads were identified by the user on the first image in any analysis series by locating the positions of the bottom left and top right thread in the image. A mask was then formed to show the user an array of twenty-four points consisting of four rows of six points. Twenty-four points were used as the phantom could be imaged from either the top or the bottom, with one of the array points falling outside the area imaged by the scanner. Once accepted by the user these locations were used as seed locations to identify the maximum pixel value produced by the reflection from each thread in each image in the image series. The twenty-fourth position returned a value of zero. The average value of a 61 pixel region close to the maximum pixel value was also calculated as a surrogate for the reflected power from the thread. The seed locations from the first image were stored by the analysis routine and used for subsequent images loaded by the user without requiring the input of the thread positions to speed up subsequent analysis. An example of the Matlab code used for analysing the signals is contained in Appendix C4.

9.3. Results

9.3.1. Measurement of temperature and dose dependence of reflections

Figure 9.1 shows a typical image acquired of the three acoustic polymers threads in the MAGIC gel phantom. The red circles indicate the position of maximum pixel value for the three threads as identified by the Matlab routine, and the threads are numbered to aid identification in further analysis.

Figure 9.1 Example of image of threads in MAGIC gel phantom. The red circle indicates the thread positions as identified by the Matlab analysis routine, and the threads are numbered to aid identification in further analysis

Figures 9.2, 9.3 and 9.4 show the average pixel value for a 61 pixel region for four imaging positions across the thread phantom with temperature for threads 1, 2 and 3 respectively. Each imaging position is shown as a separate plot on each figure, and shows a small increase in pixel value with temperature for each thread at each of the four imaging positions.

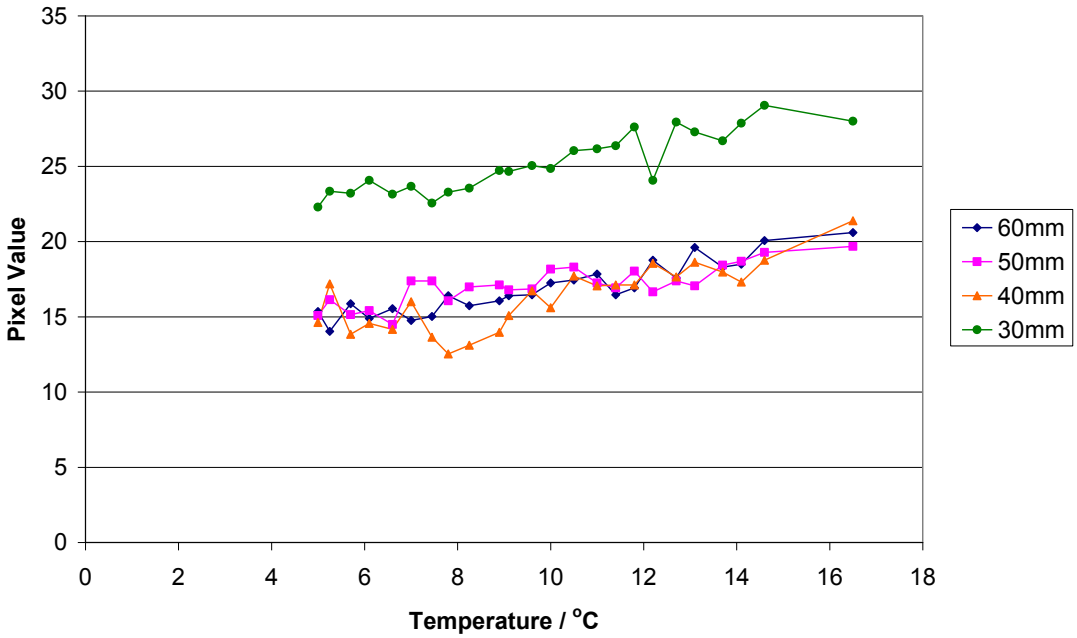

Figure 9.2 Variation of average pixel value for a 61 pixel region for four imaging positions across the thread phantom with temperature for thread 1. Each imaging position is shown as a separate plot. Lines are displayed to guide the reader and are not necessarily indicative of actual behaviour.

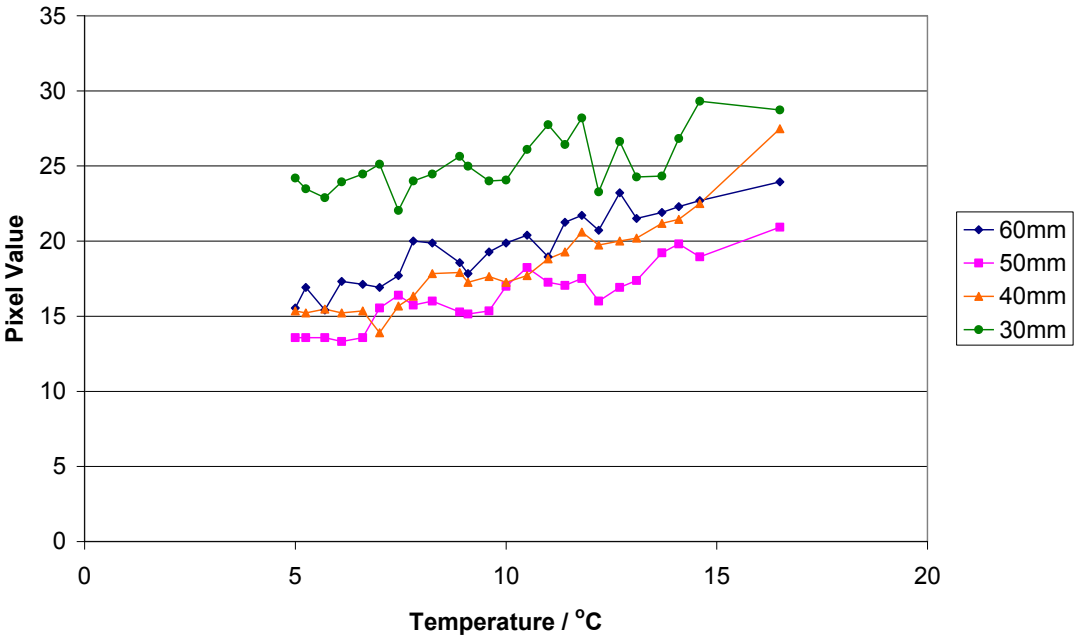

Figure 9.3 Variation of average pixel value for a 61 pixel region for four imaging positions across the thread phantom with temperature for thread 2. Each imaging position is shown as a separate plot. Lines are displayed to guide the reader and are not necessarily indicative of actual behaviour.

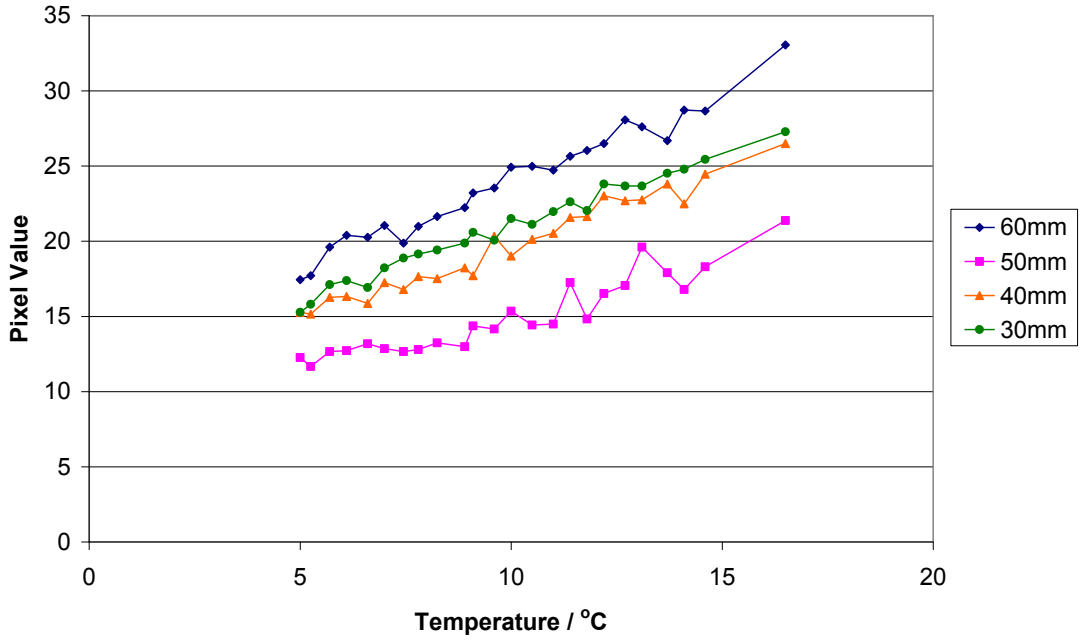

Figure 9.4 Variation of average pixel value for a 61 pixel region for four imaging positions across the thread phantom with temperature for thread 3. Each imaging position is shown as a separate plot. Lines are displayed to guide the reader and are not necessarily indicative of actual behaviour.

Figures 9.5, 9.6 and 9.7 show the post-irradiation normalised pixel values for a 61 pixel region for four imaging positions across thread phantom with temperature for threads 1, 2 and 3 respectively. Error bars are one standard deviation calculated from the repeated imaging series. The threads at 30mm and 40mm were irradiated to approximately 10 Gy. Figures 9.5 and 9.7 show that the pixel value for the irradaiated threads decreased as the temperature was changed from 5°C to 16.5°C. Figure 9.6 shows this decrease for the thread at 40mm but the thread at 30mm shows an increase in pixel value with temperature. Figures 9.5 and 9.7 also show that the pixel value for the irradaiated threads increased as the temperature was changed from 5°C to 16.5°C. Figure 9.6 shows this increase for the thread at 50mm but the thread at 60mm shows a decrease in pixel value with temperature.

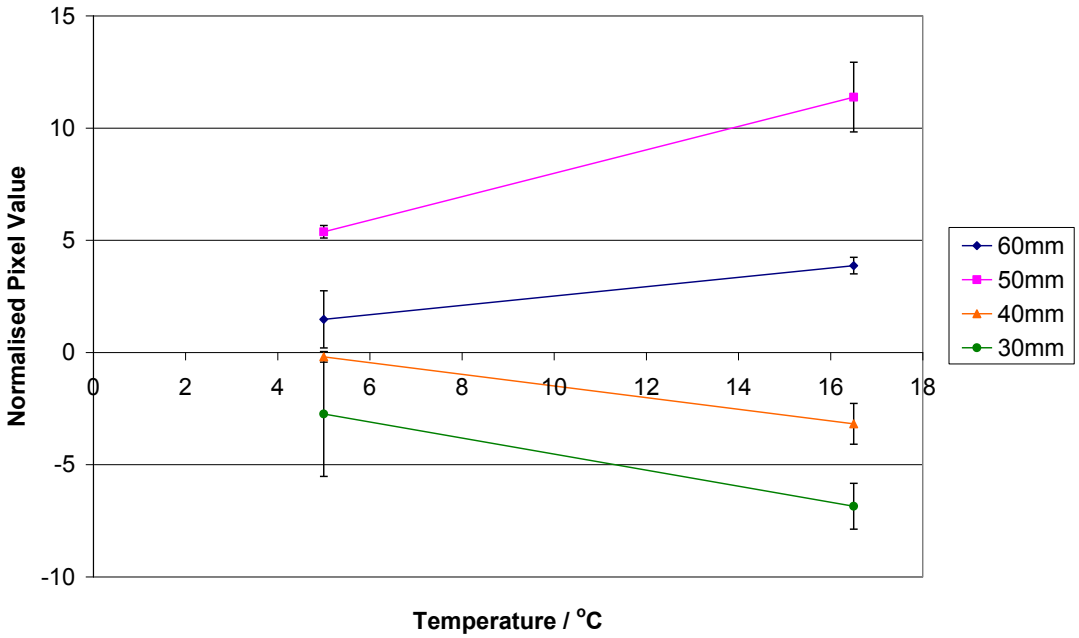

Figure 9.5 Normalised average pixel value for a 61 pixel region for four imaging positions across thread phantom at two selected temperatures for thread 1. Each imaging position is shown as a separate plot. Lines are displayed to guide the reader and are not necessarily indicative of actual behaviour.

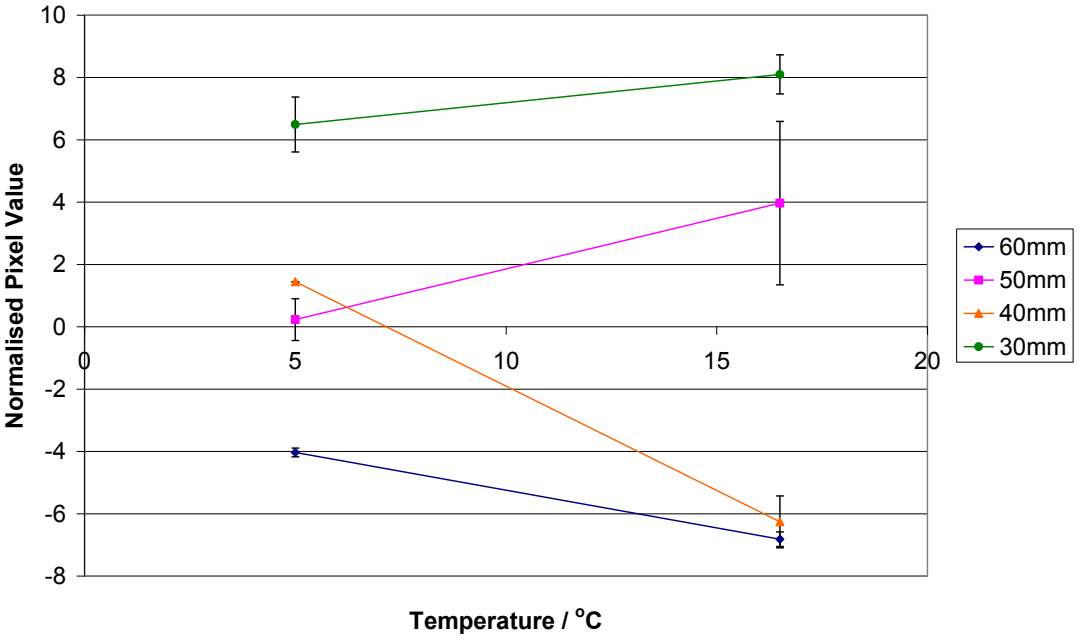

Figure 9.6 Normalised average pixel value for a 61 pixel region for four imaging positions across thread phantom at two selected temperatures for thread 2. Each imaging position is shown as a separate plot. Lines are displayed to guide the reader and are not necessarily indicative of actual behaviour.

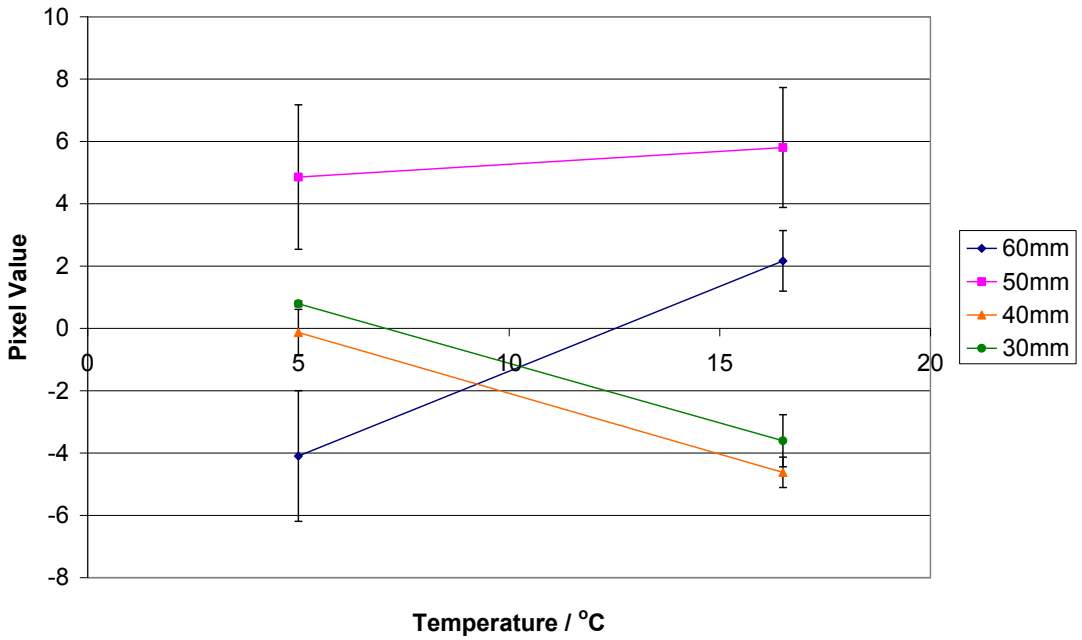

Figure 9.7 Normalised average pixel value for a 61 pixel region for four imaging positions across thread phantom at two selected temperatures for thread 3. Each imaging position is shown as a separate plot. Lines are displayed to guide the reader and are not necessarily indicative of actual behaviour.

9.3.2. Measurement of acoustic impedance

Figure 9.8 shows a typical image acquired of the three acoustic polymers threads in the saline solution. The red circles indicate the position of maximum pixel value for the three threads as identified by the Matlab routine, and the threads are numbered to aid identification in further analysis.

Figure 9.9 shows the average pixel value for a 61 pixel region around each acoustic polymers threads with the calculated acoustic impedance of the saline solution. Each thread is displayed as a separate plot and the average for all three threads is also displayed. Error bars are standard deviations on pixel value calculated from the 5 images acquired at each dilution. The pixel value for each thread appears to increase with increasing salinity. Figure 9.10 shows the pixel value for a 61 pixel region around each acoustic polymers threads with the calculated acoustic impedance of the ethanol/water mixture. Each thread is displayed as a separate plot. Error bars are standard deviations on pixel value calculated from the 10 images acquired at each dilution.

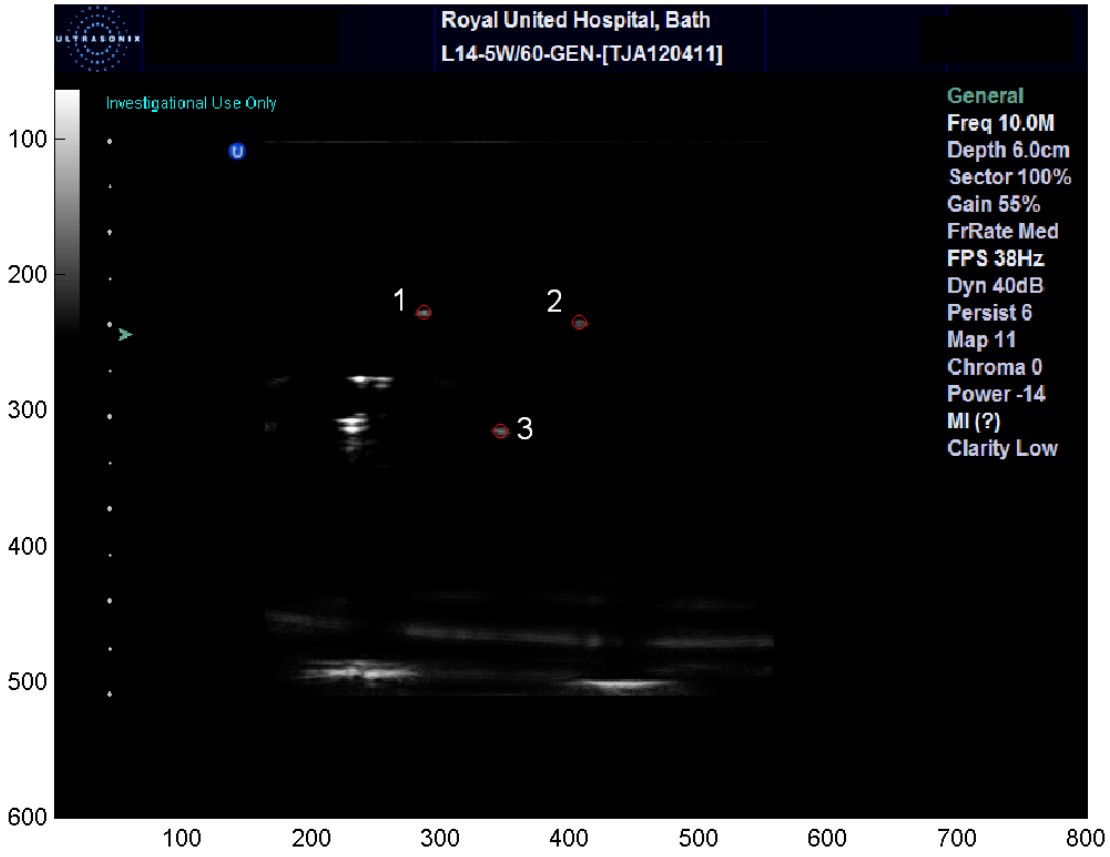

Figure 9.8 Example of image of threads in saline solution. The red circle indicates the thread positions as identified by the Matlab analysis routine, and the threads are numbered to aid identification in further analysis.

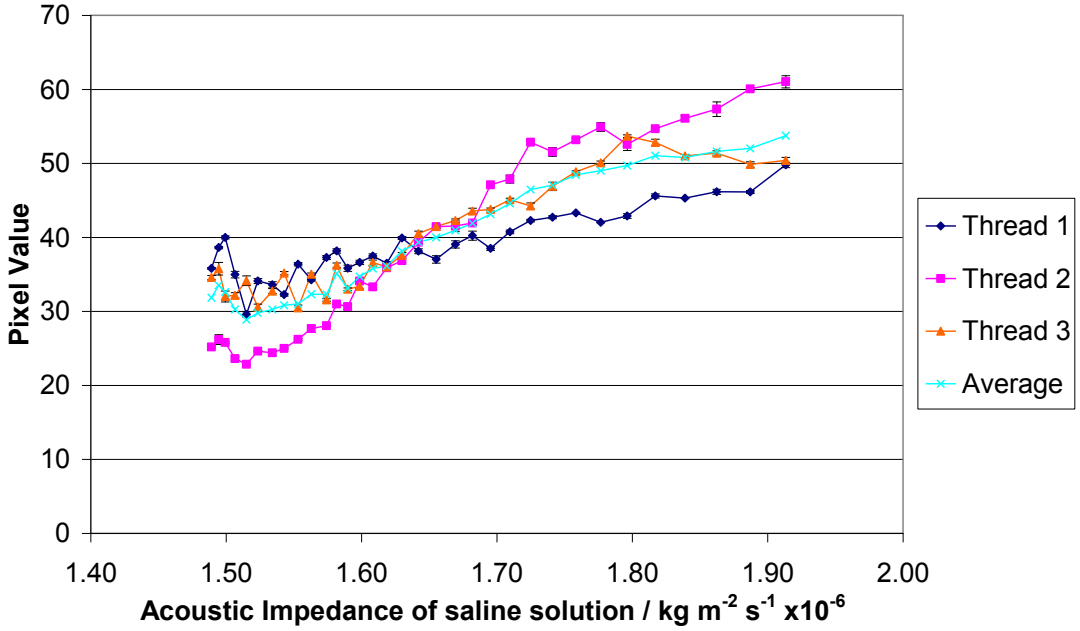

Figure 9.9 Variation of average pixel value for a 61 pixel region for three threads with acoustic impedance of saline solution. Temperature of measurement 20 °C.

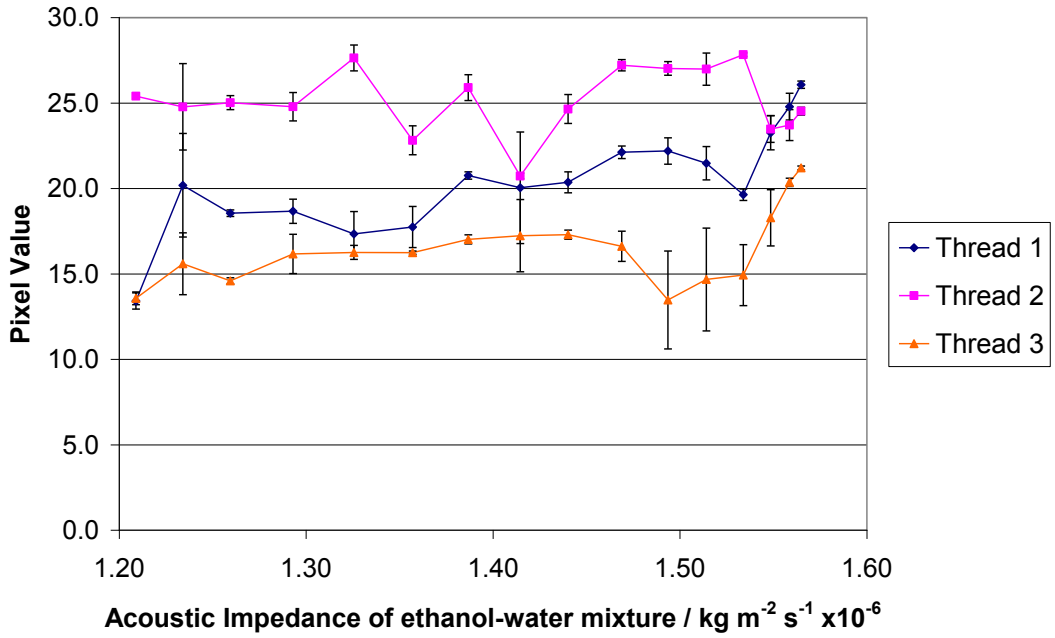

Figure 9.10 Variation of average pixel value for a 61 pixel region for three threads with acoustic impedance of ethanol-water mixture. Temperature of measurement 20 °C.

9.3.3. Image acquisition from 24 thread phantom

Figure 9.11 shows a typical image from the development of the analysis routine for images of the 24 thread phantom. The red circles indicate the position of maximum pixel value for the twenty three threads as identified by the Matlab routine. The top right red circle is outside the imaging area and is required if the phantom is imaged from the other direction. This returned a value of zero from the analysis routine.

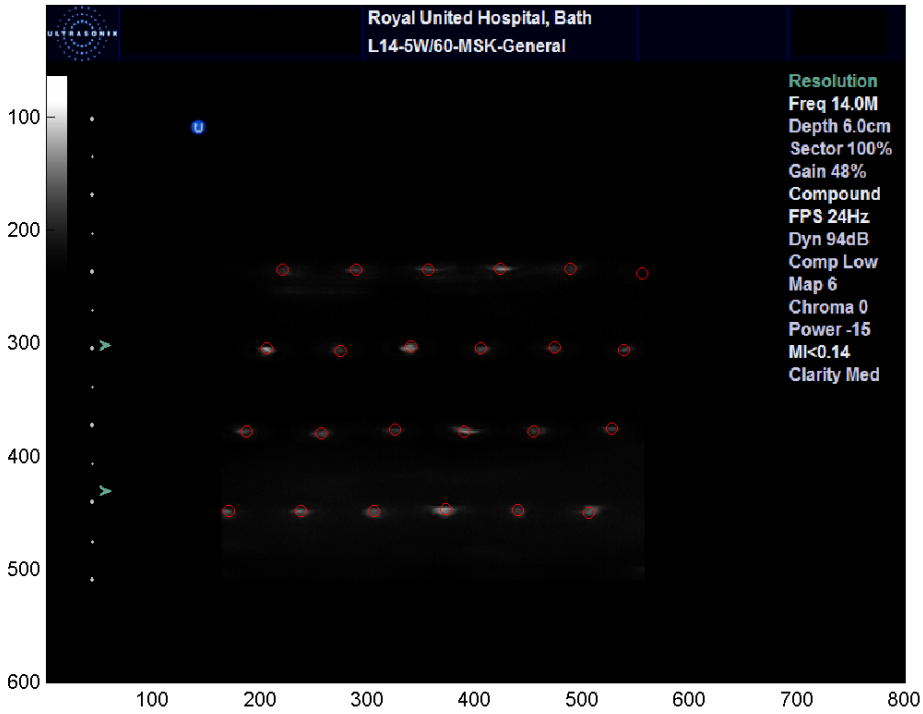

Figure 9.11 Example of image of 23 thread array in water. The red circles indicates the maximum pixel value at each thread positions as identified by the Matlab analysis routine.

9.4. Discussion

The measurement of the temperature dependence of the reflection of ultrasound from threads of acoustic polymers in MAGIC gel material did not produce a definitive minimum. Figures 9.2, 9.3 and 9.4 show an increase in the pixel value with increasing temperature in MAGIC gel. However, Figures 9.2, 9.3 and 9.4 do not show the minimum in reflection amplitude that is expected. However, if the temperature range had been extended below 5°C a definitive minimum may have been observed.

Figures 9.5 and 9.7 show the expected variation in pixel value with dose and temperature. The unirradiated threads (at 50 and 60mm) show the same increase in pixel value with temperature as was observed pre-irradiation. The irradiated threads (30 and 40mm) show a decrease in pixel value with temperature consistent with earlier observations implying that the temperature at which the minimum reflection coefficient occurs has been increased by the irradiation of the MAGIC gel.

However, only imaging Thread 2 at 40mm and 50mm follow the same trend, as shown in Figure 9.6. For the others two imaging positions the trend is reversed, where

the 60mm thread which was unirradiated shows an increase in pixel value with temperature, and the irradiated 30mm threads shows a decrease in pixel value with temperature.

The measurement of the acoustic impedance of the threads of acoustic polymers material did not produce a definitive minimum. Figure 9.9 shows a decrease in the pixel value when in the saline solution. Figure 9.9 also does not show a minimum in reflection amplitude that is expected.

One explanation for the absence of a minimum is that the formation of the acoustic polymers material into threads has caused the acoustic impedance to be different to the expected value, and hence the measurements may have been completed at too high an acoustic impedance. The change in acoustic impedance could potentially be due to the size of the threads (making them effectively all 'surface' and no 'bulk' material) or by the different batch having slightly different properties.

The attempt to extend the range of acoustic impedances of the fluid medium for the experiment by using and ethanol-water mixture did not produce the expected result. Figure 9.10 shows no discernable change in pixel value for all ethanol-water mixtures. This implies that either the reflection coefficient is not changing in the region of the acoustic impedances measured, or the errors in the experiment mean that any changes in reflection coefficient that may have been observed as a change in pixel value are not visible.

The size of the uncertainty at each data point in Figure 9.10 indicate that there were significant differences between the images that were acquired. This will either have been due to the presence of gas bubbles in one set of images or the brushing of the threads and transducer surfaces affecting the images that were acquired in some other way.

The endothermic reaction between ethanol and water caused some complications with the measurements of the pixel value in the ethanol-water mixture. The gas bubbles released at each successive dilution sometimes attached to either the transducer surface or the acoustic polymers threads. Any visible gas bubbles were dispersed using a fine brush, however it is not certain that every gas bubble was removed at each dilution from all threads or the transducer surface. Additionally, the endothermic reaction between ethanol and water caused the temperature of the solution

to drop at each dilution. Although the images were acquired when the temperature of the solution had returned to the measurement temperature of 20°C a measurement of the temperature of the acoustic polymer threads was not possible and the threads could have been at a lower temperature and not returned to the expected temperature. Since it has previously been determined that the acoustic impedance of the acoustic polymers material is strongly dependent on the temperature, any uncertainties in the temperature of the material may cause the reflection coefficient to be very different from expected.

Another potential explanation for not seeing the expected variation in pixel value of threads is that the change in acoustic impedance is not dominating the reflection from the threads. It has been assumed that the relationship between the acoustic impedance of the materials and the reflection coefficient (or its surrogate, pixel value of threads) is similar to that of a plane surface. The reflection coefficient of a rod-like structure will not be the same as an (infinite) planar surface due to the different geometries and the ability to induce surface waves around the rod. Another cause of differences from the planar slab situation is irregularities in the structure of the threads. Any small irregularities such as moulding lines from the way in which the threads were produced will cause different reflections of the ultrasonic waves to occur which would not necessarily have the same characteristics as other reflections. If these reflections dominate the reflection from the threads then any changes from the changing acoustic impedance may not be observable. Modelling of the reflection characteristics of these geometries may lead to further insights into why the pixel values did not vary as expected with changing acoustic impedance of the fluid.

Another source of error in the measurements reported in this chapter is the assumption of logarithmic gain compression within the scanner. This assumption was significant in the implementation of subtracting the pre-irradiation pixel values within the analysis routines. This assumption of logarithmic gain compression was taken from the scanner technical manual, however this was not independently verified. Any deviation from logarithmic gain compression will introduce non-linearities into the measured reflection coefficients. A method of characterising the gain compression applied to the images by the scanner would be needed to verify the validity of this analysis method.

Figure 9.11 shows that the analysis routine could be used to successfully apply a mask and identify the twenty four positions at which threads may be located and determine the maximum and average pixel value for the threads. The missing thread in the array returned a pixel value of zero.

10. Slab phantom imaged using the Ultrasonix Scanner

10.1. Introduction

The integration of a commercial ultrasound scanner into the data acquisition system is an important aspect of this project, as it will enable the applicability of the system to a larger set of radiotherapy centres than currently employ gel dosimetry techniques due to the lack of available analysis methods.

In Chapter 9 a description of the methodology for acquiring images of the thread phantom was described. Measurements of the acoustic properties of the threads and dose and temperature related changes in polymer gels was inconclusive using the system. Therefore images of phantoms based on a planar interface were acquired and used to measure and characterise the response from the system in comparison to the single element pulse-echo system used in Chapter 6.

10.2. Materials and methods

10.2.1. Image acquisition and analysis

Images were acquired using the Ultrasonix MDP scanner (Ultrasonix Medical Corporation, Richmond, BC, Canada) as described previously. The images acquired by the scanner were exported to a PC running Matlab R12.1 (The Mathworks, Inc., Natick, MA). The PNG format images were imported into Matlab and pixel data for the scan area was selected. The location of the upper surface of the acoustic polymers material was identified in each column of the image. Three values for the pixel value at the interface were produced. The first two values were indicative of the maximum pixel intensity at the interface for each column of the image. Both the point maximum and the value produced by averaging the three pixels in each image column closest to the interface were recorded. The third value was chosen to be indicative of the total reflected power in reflection from the interface. This value was produced by averaging the seven pixels closest to the interface, since this was found in most cases to include all of the pixels that had grey levels greater than the background image level. An

example of the Matlab code used for analysing the signals is contained in Appendix C5. Once the scan line in each image was analysed the data for each image set (which included repeated images taken in the same position and at the same temperature) was combined to produce average and standard deviations for the pixel value at the interface for each image position and temperature were produced. Further image analysis, such as spatial averaging across scan lines, was performed as required.

The image acquisition system of the Ultrasonix MDP Scanner includes a pre-image formation logarithmic gain compression. This logarithmic compression aids the display of the ultrasound images but no user control of this gain compression is available. When performing quantitative image analysis this pre-display logarithmic compression needs to be accounted for in subsequent analysis and image comparison.

10.2.2. Measurement of acoustic impedance

A measurement of the acoustic impedance of the acoustic polymers material was made both as a verification of the process of using the Ultrasonix scanner for image acquisition and analysis and to verify the measurement of the acoustic impedance of the material.

The acoustic polymers material was immersed in saline solution and the interface between the acoustic polymers material and the saline solution was imaged using the Ultrasonix scanner. At each salinity two images of the interface were acquired. Each image was acquired using a single focal zone on the scanner set at 21mm deep, with a Power Setting of -14, Gain of 30% and Dynamic Range of 45dB. The reflection amplitude was calculated by averaging the pixel value at the interface across each scan line in the image.

The saline solution was gradually diluted, changing the acoustic impedance of the saline solution. Therefore the reflection amplitude was altered. The minimum in reflection amplitude indicated the position at which the real part of the acoustic impedance was matched between the acoustic polymers material and the saline solution. The acoustic impedance of the saline solution at each dilution was calculated, and therefore the real part of the acoustic impedance of the acoustic polymers material could be inferred.

The speed of sound in saline solution was calculated from the corrections Wong and Zhu (1995) made to the equations of Del Grosso (1974). The density of the saline solution was calculated from the UNESCO report of Fofonoff and Millard (1983). Knowledge of the speed of sound and density of the saline solution allowed calculation of the acoustic impedance of the solution at each salinity level where images of the interface were acquired.

10.2.3. Phantom manufacture and irradiation

Pieces of the acoustic polymers inert reflector of approximately 8 cm × 8 cm were used to make the phantoms. The material was placed into a polyethylene container and held in place using silicone. MAGIC gel was manufactured and poured onto the acoustic polymer reflector, taking care not to introduce any bubbles into the mixture. The acoustic polymers reflector and container were held at 35 °C in a water bath as the MAGIC gel was poured. Once the MAGIC gel was poured a vacuum system (Island Scientific cylindrical chamber (Island scientific Ltd, Isle of Wight, UK) with Edwards E2M8 vacuum pump (Edwards High Vacuum International, Crawley, UK)) was used to ensure any bubbles introduced during the creation of the phantom were removed. Once all the bubbles in the gel had been removed a layer of vegetable oil was poured over the MAGIC gel to provide ultrasonic coupling between the transducer and the gel, and to seal the MAGIC gel and to help prevent oxygen contamination. Then the entire system was allowed to cool slowly until the MAGIC gel had set. The system was then refrigerated for approximately 24 hours prior to irradiation.

The phantoms were irradiated using a Siemens Primus linear accelerator (Siemens AG, Erlangen, Federal Republic of Germany). Two phantoms were created and irradiated on two separate occasions. The first phantom (Phantom A) left one side of the phantom unirradiated whereas the other side was irradiated to approximately 20 Gy, as shown in Figure 10.1. The second phantom (Phantom B) had a more complex dose distribution. The right hand side of the phantom was irradiated to a dose of approximately 20 Gy, with a 4 cm × 4 cm square in the centre of the phantom being irradiated to an additional dose of approximately 10 Gy, as shown in Figure 10.2. After

irradiation the phantoms were refrigerated for approximately 48 hours prior to ultrasound image acquisition.

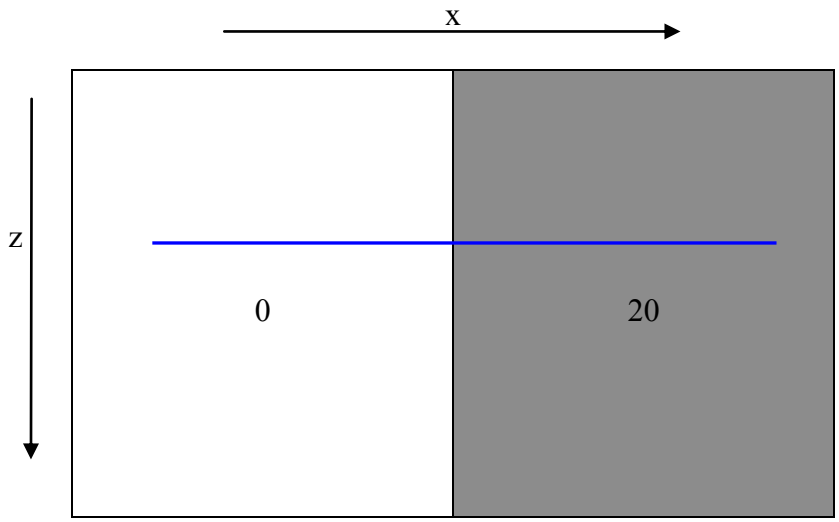

Figure 10.1 Plan view of the irradiation of Phantom A. The right hand side was irradiated to 20 Gy. The blue line indicates the scan plane.

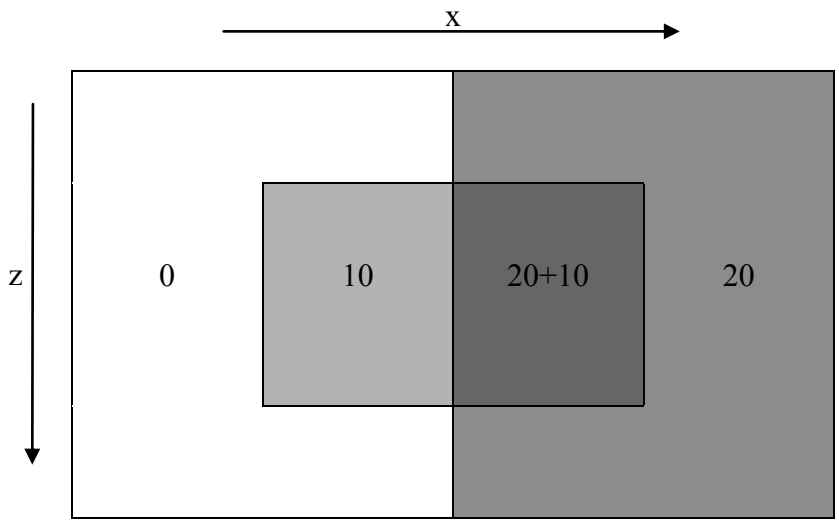

Figure 10.2 Plan view of the irradiation of Phantom B. The right hand side was irradiated to 20 Gy and the central 4 cm × 4 cm was irradiated to an additional 10 Gy.

For Phantom A no pre-irradiation images were acquired of the phantom. Post-irradiation the phantom was placed in a water bath at an initial temperature of 11°C. The temperature on the water bath was slowly increased while images of the

interface between the acoustic polymers material and the MAGIC gel were acquired at regular intervals. Each image acquired the reflection from the interface in the *x*-direction, as shown in Figure 10.1. As each image was acquired the temperature of the interface was measured and recorded. Each image was acquired using a single focal zone on the scanner set at 31mm deep, with a Power Setting of -14, Gain of 75% and Dynamic Range of 40dB.

For Phantom B, a set of images were acquired at temperatures of 10, 15, 20 and 25 °C prior to irradiation. Images were acquired at 3mm intervals in the z-direction (as shown in Figure 10.2) across the phantom surface. Each image acquired a 60mm scan of the phantom surface in the *x*-direction, so that a 60 × 60 mm area was imaged at each temperature. At each imaging position two sets of 5 images were acquired and averaged, with the position being reset between each set of images to correct for positioning uncertainties. The same imaging protocol was applied post-irradiation.

The ten images at each location were analysed to identify the averaged pixel value at the interface across each image. A seven pixel mask was used to measure the average pixel value at each scan line. Seven pixels corresponds to approximately 1mm. The pre-irradiation value at each location was subtracted from the post-irradiation value at each location to produce a 'normalised' pixel value. This subtraction of pre-irradiation images was used to correct for variation in imager performance, the variation in the interface itself and inhomogeneities in the acoustic path between the scanner and the interface. The use of subtraction rather than division for this method is based on the scanner performing logarithmic gain compression on the ultrasound images prior to any subsequent processing. Within each image the scan lines were averaged to produce data points at 3.5mm intervals. Pairs of scan planes were averaged to produce profiles at 6 mm intervals across the phantom.

10.3. Results

10.3.1. Measurement of acoustic impedance

Figure 10.3 shows the variation of averaged pixel value at the interface of between the saline solution and the acoustic polymers material with the calculated

acoustic impedance of the saline solution. Error bars show the standard deviation of pixel values along the interface for each image acquired. The pixel value decreases with decreasing salinity until the salinity of 0.036 g cm^{-3} was reached, which gives a calculated acoustic impedance of 1.57×10^6 kg m^{-2} s^{-1}. As this point the minimum pixel value is observed and then the pixel value increases as the salinity decreases further. Measurements were made at 22 °C.

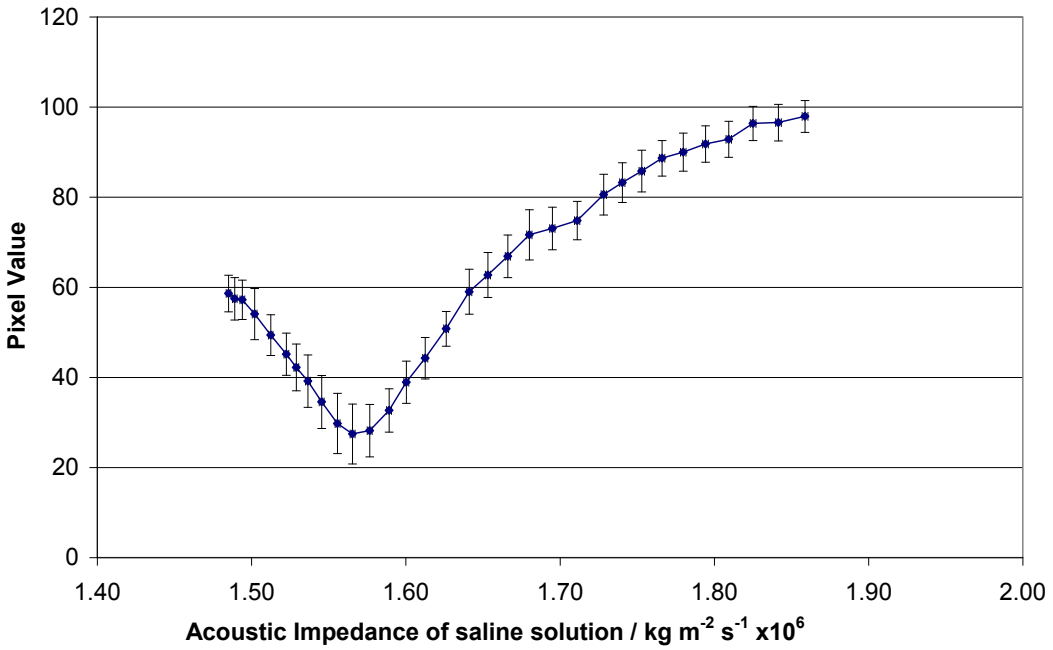

Figure 10.3 Variation of averaged pixel value across interface between saline solution and acoustic polymers material. The acoustic impedance was calculated from the temperature and salinity of the saline solution. Lines are displayed to guide the reader and are not necessarily indicative of actual behaviour.

10.3.2. Measurement of a temperature variation of pixel value (Phantom A)

Figure 10.4 shows and example of the image acquired using the Ultrasonix scanner of Phantom A. The interface between the MAGIC gel and the acoustic polymers inert reflector is close to the focal zone set on the scanner at 31 mm deep (indicated by the light blue arrow). The bright reflection at approximately 20mm deep is from the interface between the oil used as an acoustic coupler and the MAGIC gel layer. Figure 10.5 shows the left hand side of the interface zoomed to show the individual pixels. The brightest pixels are the second and third pixels in the scan line

across the interface, although non-zero pixel values can be observed from deeper within the acoustic polymers reflector material.

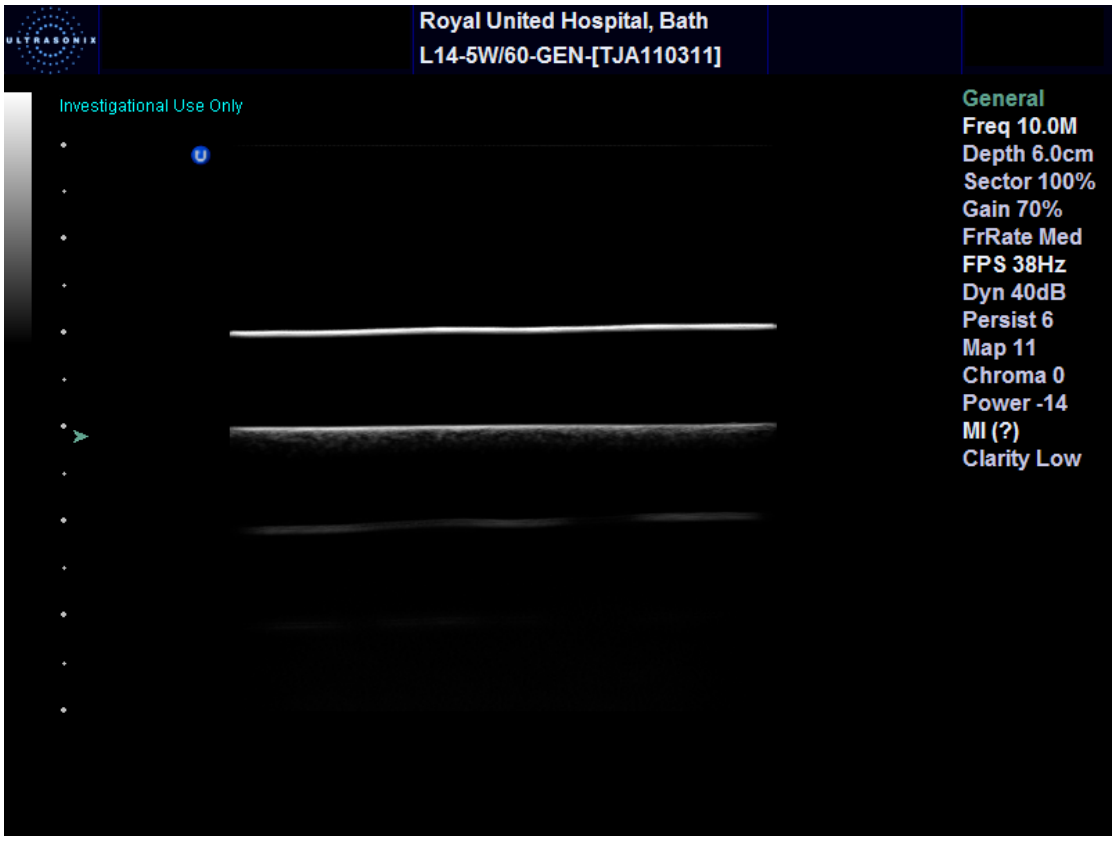

Figure 10.4 Example of image of acoustic polymer inert reflector in MAGIC gel phantom A. The interface between MAGIC gel and acoustic polymer inert reflector is at the level of the focal depth (31mm) as indicated by the blue arrow.

Figure 10.5 Example of image of acoustic polymer inert reflector in MAGIC gel phantom A zoomed on the interface between the MAGIC and acoustic polymer inert reflector.

Figure 10.6 shows how the pixel value varies across the image of Phantom A in the x-direction for two selected temperatures, 14.4°C and 23.5°C. At a temperature of 14.4°C the left hand side of the image (unirradiated) shows a lower pixel value than the

right hand side of the image. Conversely, at 23.5°C the left hand side is higher than the right hand side of the image.

Figure 10.7 shows how the averaged pixel value for each side of the phantom varies with temperature. Error bars are standard deviation across the selected region of image for each temperature. The blue diamonds are the averaged pixel values for the unirradiated region and the red squares are the averaged pixel values for the irradiated region. The irradiated region was irradiated to 20 Gy. The error bars show the standard deviation of pixel value for the 50 pixels within the region used for averaging. The pixel values show similar variation with temperature as observed with the single element transducer in Chapter 6. A minimum in pixel value is observed at approximately 19°C for the irradiated region and at approximately 16°C for the unirradiated region.

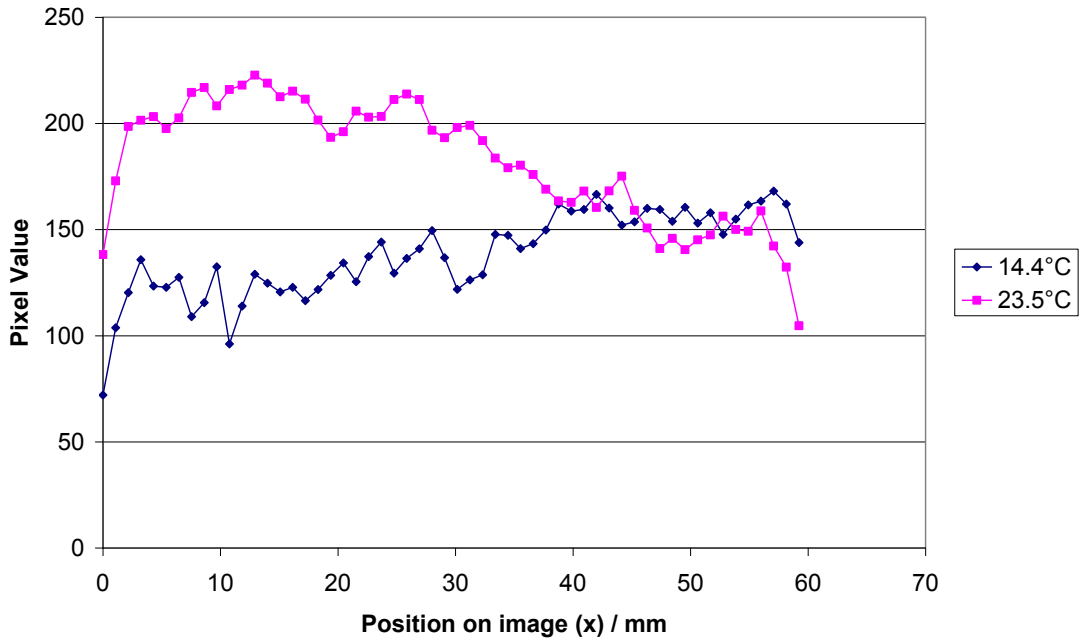

Figure 10.6 Variation of pixel value at interface of MAGIC gel and acoustic polymers inert reflector for Phantom A acquired using Ultrasonix scanner at selected temperatures with position across image in x-direction. Lines are displayed to guide the reader and are not necessarily indicative of actual behaviour.

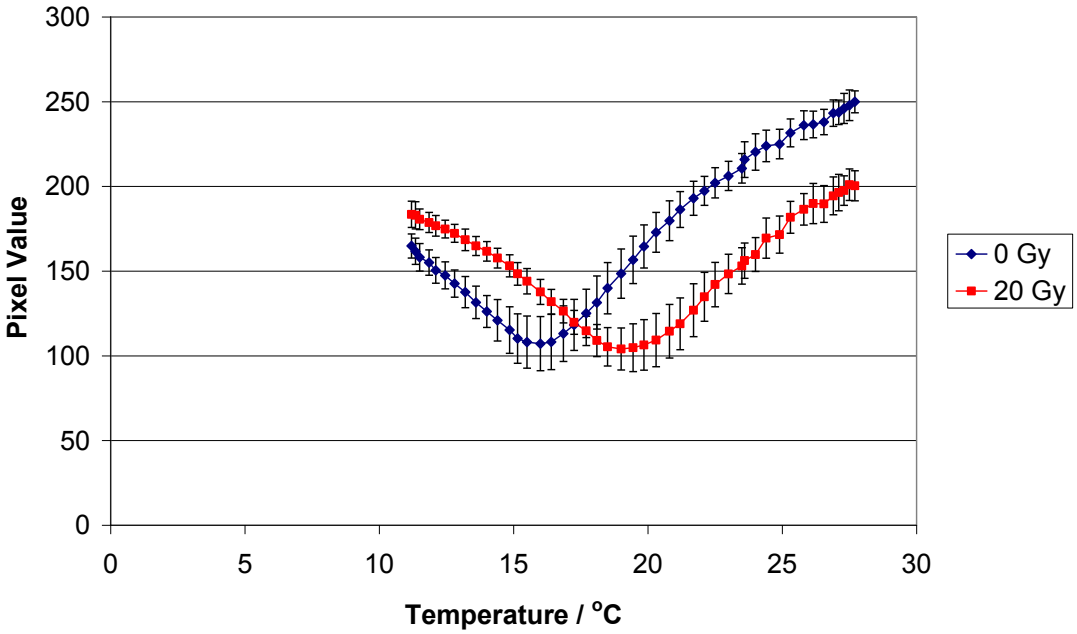

Figure 10.7 Variation of averaged pixel value for irradiated and unirradiated polymer gel acquired using Ultrasonix scanner as temperature is varied. Lines are displayed to guide the reader and are not necessarily indicative of actual behaviour.

10.3.3. Measurement of pixel value for complex radiation dose distribution (Phantom B)

Figure 10.8 shows the variation in pixel value that is observed across the image in the x-direction at the interface between the MAGIC gel and the acoustic polymer material in Phantom B prior to the irradiation for the different scan planes used. There seems to be some systematic variation across each image that is reproduced for each imaging position (z). Figure 10.9 shows the variation in pixel value that is observed across the scan planes (z-direction) at different positions across the image at the interface between the MAGIC gel and the acoustic polymer material prior to the irradiation. 18 positions at 3.5mm intervals across each image were selected to create representative profiles.

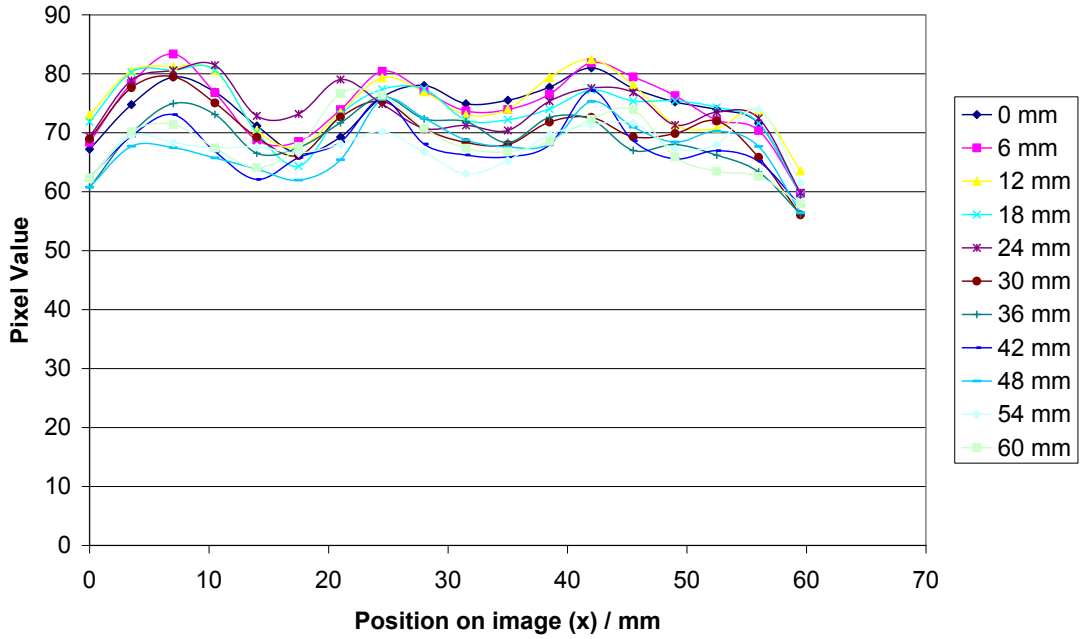

Figure 10.8 Example of pixel value variation across images in x-direction prior to irradiation. The eleven series correspond to the imaging planes (z) used. Temperature of measurement 15 °C. Lines are displayed to guide the reader and are not necessarily indicative of actual behaviour.

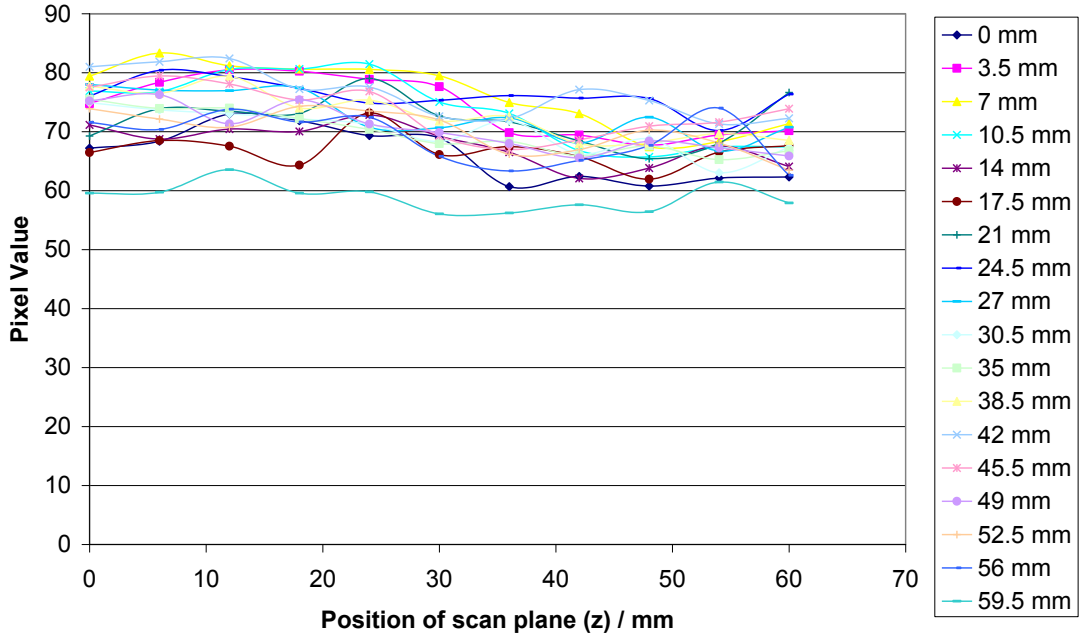

Figure 10.9 Example of pixel value variation across scan planes in z-direction prior to irradiation. The eighteen series correspond to selected positions across the images in the x-direction. Temperature of measurement 15 °C. Lines are displayed to guide the reader and are not necessarily indicative of actual behaviour.

Figure 10.10 shows the averaged 'normalised' pixel value data for four imaging positions (post-irradiation pixel value minus pre-irradiation pixel value) within the

peripheral region that contained dose levels of approximately 0 Gy and 20 Gy, with the corresponding dose distribution. Figure 10.11 shows the averaged 'normalised' pixel value data for five imaging positions within the central region with the complex profile showing irradiation levels of approximately 0, 10, 30 and 20 Gy across the figure from left to right. Both Figure 10.10 and 10.11 are from data acquired at 15°C. Figure 10.12 and 10.13 show the same data acquired at 25°C. Figures 10.10 to 10.13 all show the relationship where pixel value decreases as the irradiated dose increases.

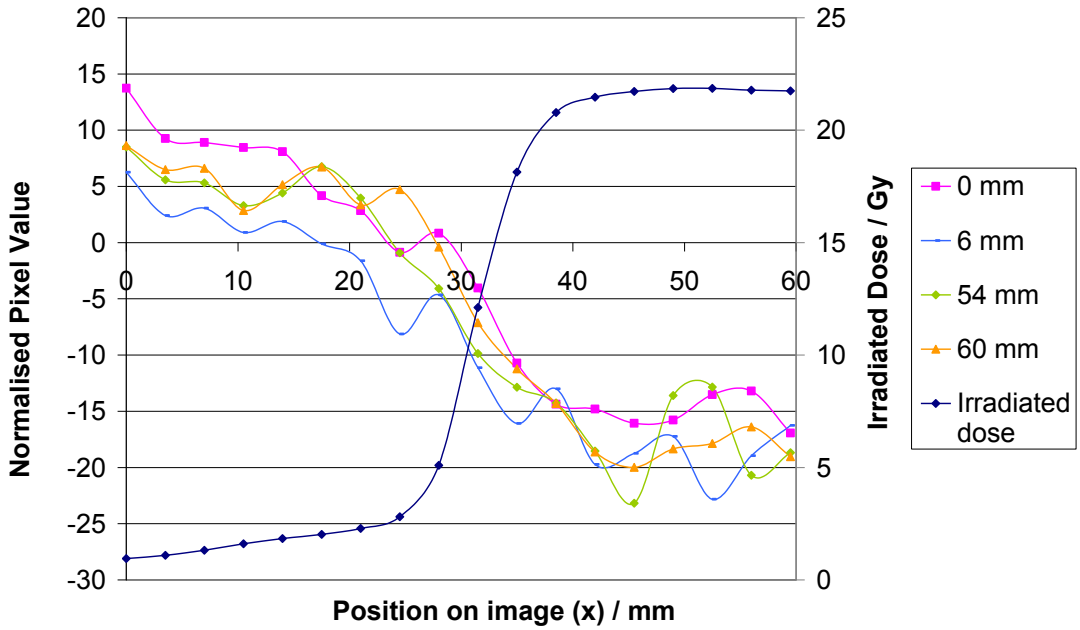

Figure 10.10 Variation of normalised pixel value across image in the x-direction for four scan positions (z-direction) within simple irraidation area of Phantom B acquired using Ultrasonix scanner. Calculated dose profile across the scan positions is also shown. Temperature of measurement was 15 °C. Lines are displayed to guide the reader and are not necessarily indicative of actual behaviour.

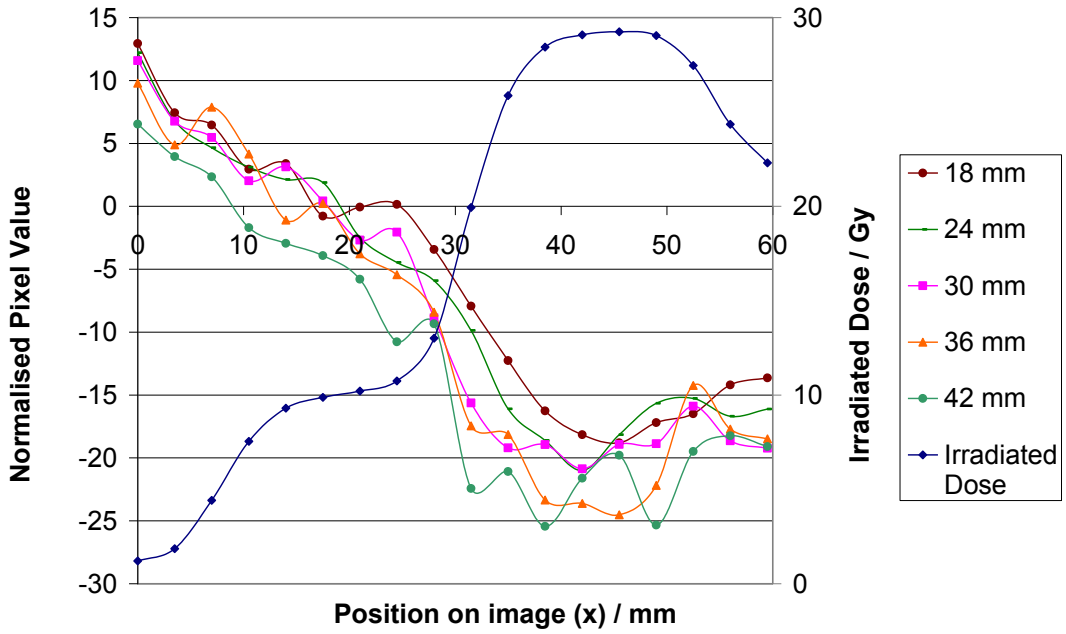

Figure 10.11 Variation of normalised pixel value across image in the x-direction for five scan positions (z-direction) within complex irraidation area of Phantom B acquired using Ultrasonix scanner. Calculated dose profile across the scan positions is also shown. Temperature of measurement was 15 °C. Lines are displayed to guide the reader and are not necessarily indicative of actual behaviour.

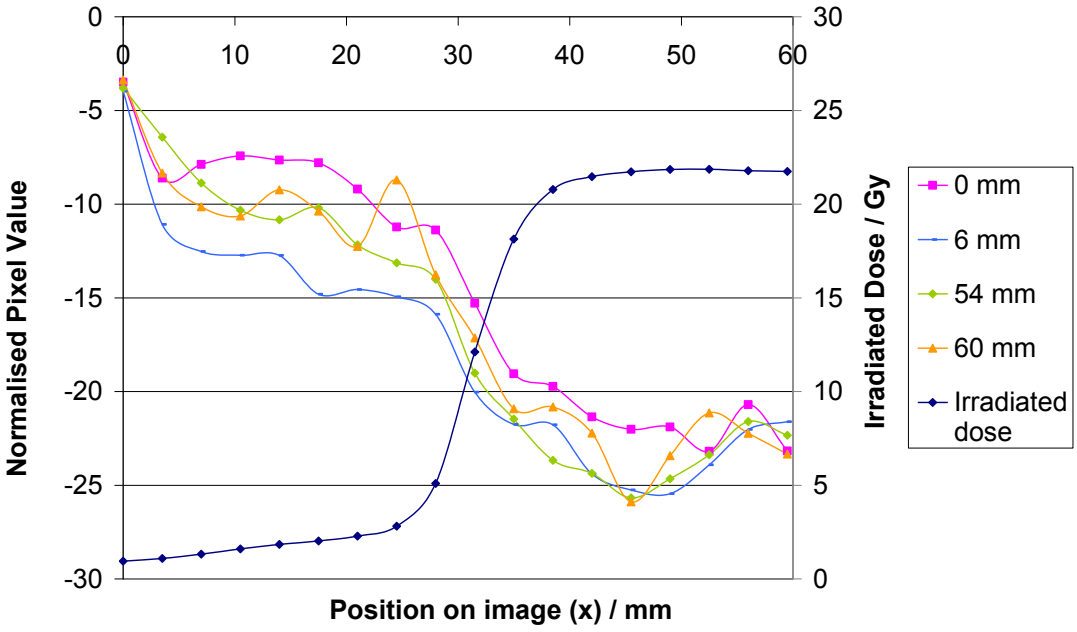

Figure 10.12 Variation of normalised pixel value across image in the x-direction for four scan positions (z-direction) within simple irraidation area acquired using Ultrasonix scanner. Calculated dose profile across the scan positions is also shown. Temperature of measurement was 25 °C. Lines are displayed to guide the reader and are not necessarily indicative of actual behaviour.

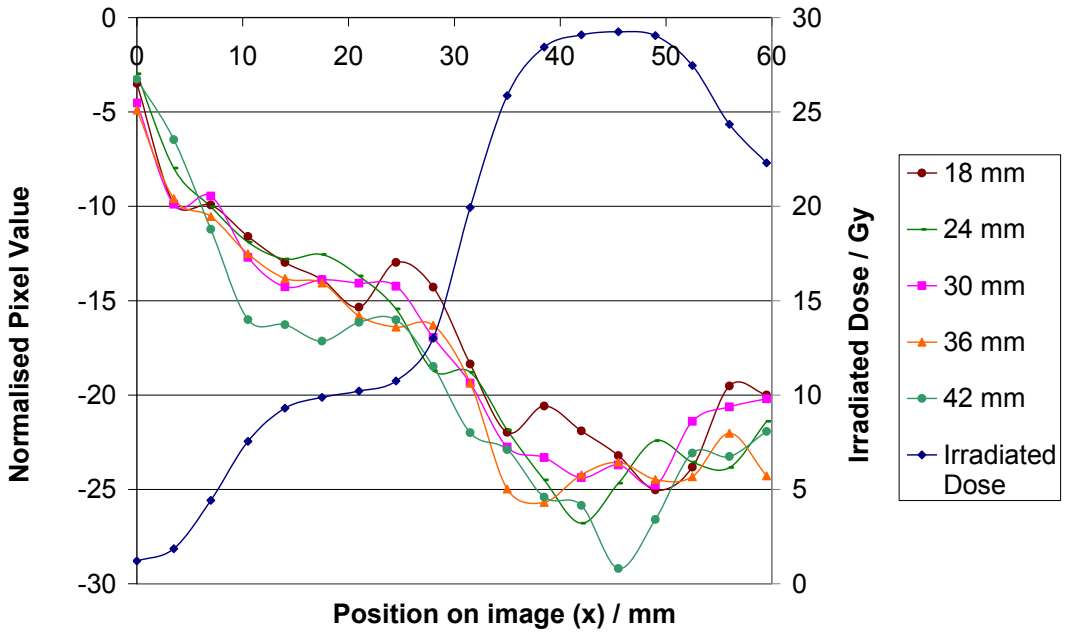

Figure 10.13 Variation of normalised pixel value across image in x-direction for five scan positions (z-direction) within complex irraidation area acquired using Ultrasonix scanner. Calculated dose profile across the scan positions is also shown. Temperature of measurement was 25 °C. Lines are displayed to guide the reader and are not necessarily indicative of actual behaviour.

Four areas from the total scan set were selected from the calculated dose distribution for having received a uniform irraidated dose. The 'normalised' pixel value for the positions within each area were then averaged. Figure 10.14 to 10.17 show the averaged 'normalised' pixel value for the four areas with the dose that the area received for the temperature of measurement of 10, 15, 20 and 25 °C respectively. Error bars are standard errors on pixel value within the selected region. For the nominal irradiation of 0 and 20 Gy areas of 35 (5x7) data points were selected and for the 10 and 30 Gy irradiations areas of 28 (4x7) data points were selected. Figure 10.4 shows an reduction in pixel value between the unirradiated region and the region irradiated to approx 10 Gy, and then the pixel value increases as the dose is increased further. This implies that the temperature of measurement is just above the temperature at which minimum reflection occurs for unirradiated MAGIC gel, but below the temperature at which minimum reflection occurs for the higher doses. Figures 10.15 to 10.17 show an approximately linear decrease in pixel value with dose with irradiated dose, in which case the measurement temperature is above the temperature at which minimum reflection occurs for the range of irradiated doses.

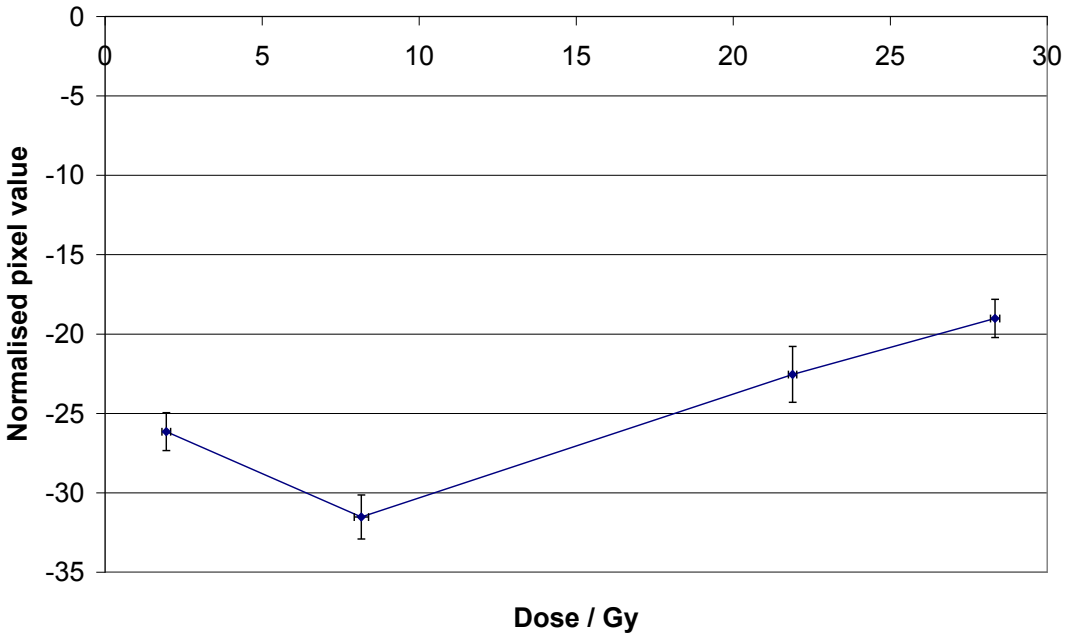

Figure 10.14 Average normalised pixel value for four uniform dose areas within the total scan set with dose. Temperature of measurement 10 °C. Lines are displayed to guide the reader and are not necessarily indicative of actual behaviour.

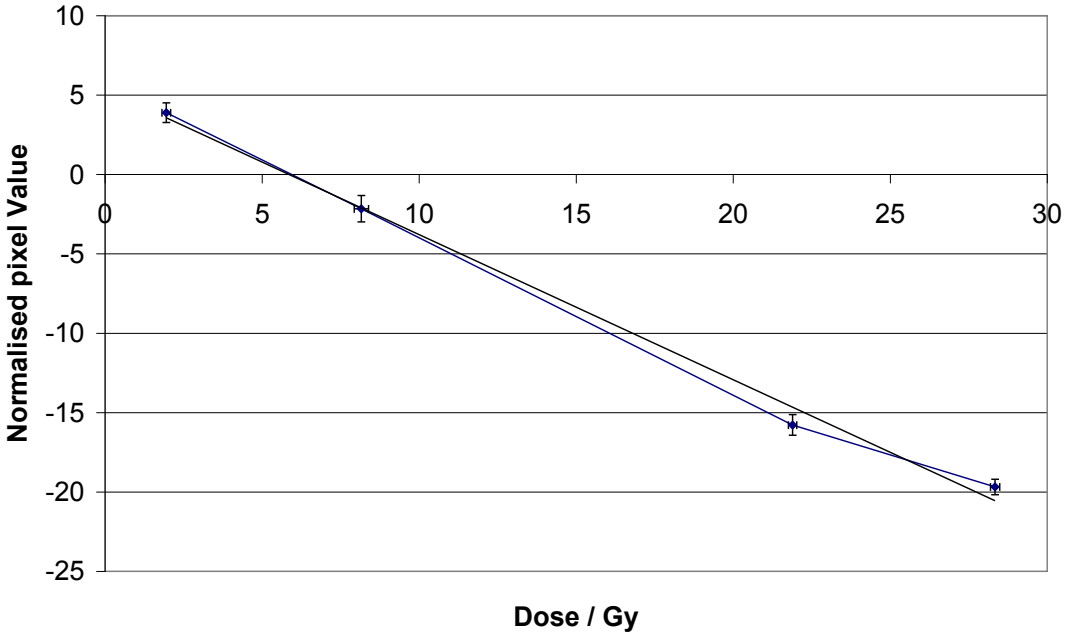

Figure 10.15 Average normalised pixel value for four uniform dose areas within the total scan set with dose. Temperature of measurement 15 °C. Lines are displayed to guide the reader and are not necessarily indicative of actual behaviour.

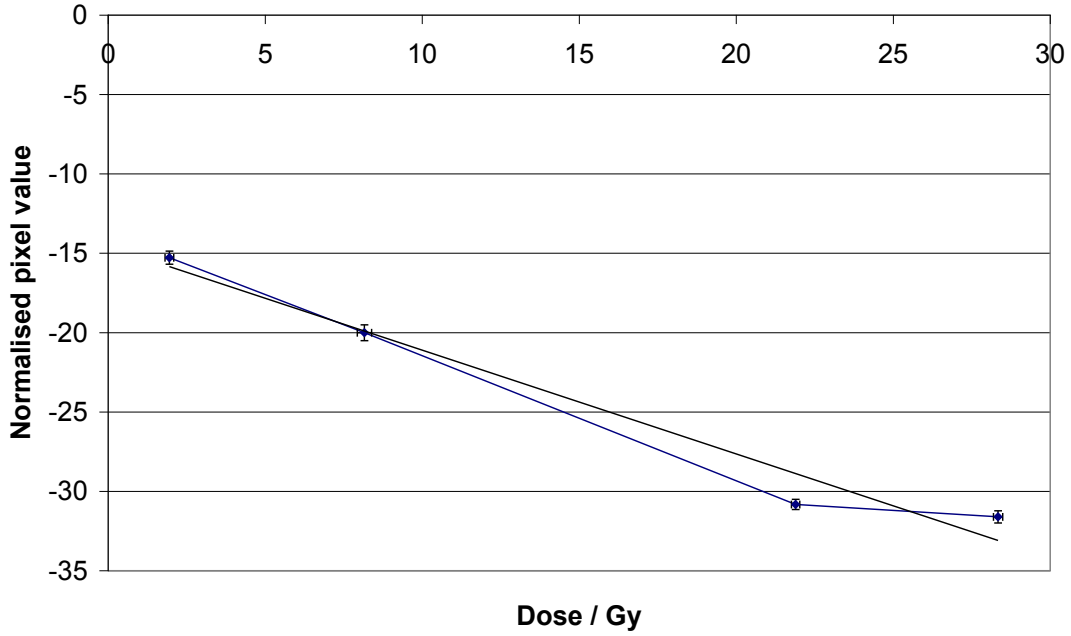

Figure 10.16 Average normalised pixel value for four uniform dose areas within the total scan set with dose. Temperature of measurement 20 °C. Lines are displayed to guide the reader and are not necessarily indicative of actual behaviour.

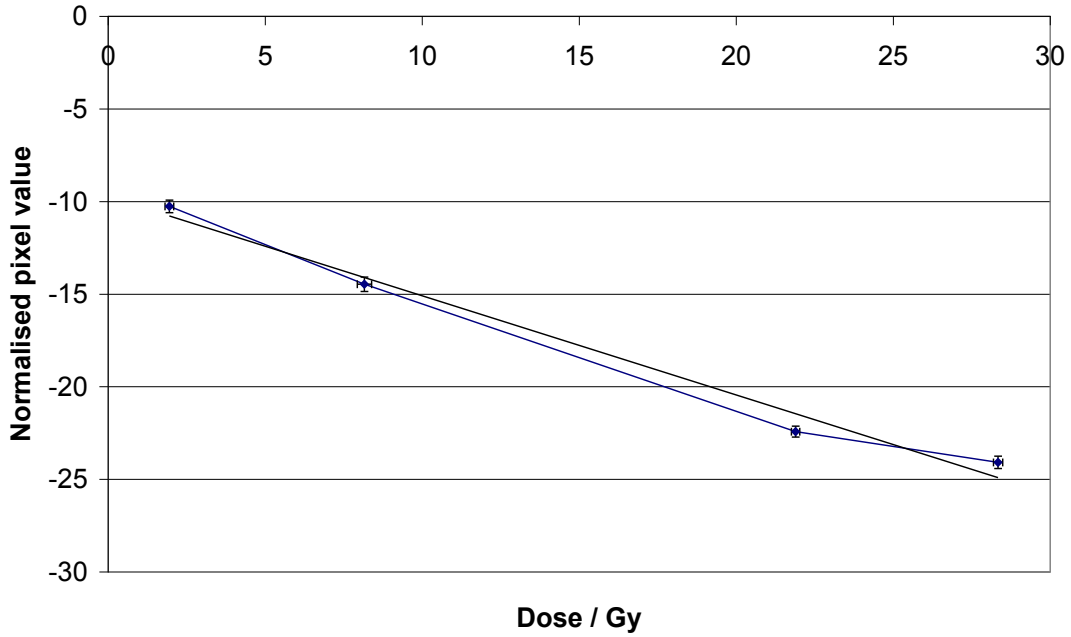

Figure 10.17 Average normalised pixel value for four uniform dose areas within the total scan set with dose. Temperature of measurement 25 °C. Lines are displayed to guide the reader and are not necessarily indicative of actual behaviour.

Figure 10.18 shows the averaged 'normalised' pixel value data for localised areas within the uniformly irradiated sections. Error bars are standard errors on pixel

value within the selected region. 12 areas of 6 data points were selected and averaged and presented against dose calculated for those 6 data points. The 6 data points relate to an area of 8mm by 10.5mm. This figure shows an approximately linear decrease in pixel value with dose.

Figure 10.18 Average normalised pixel value for twelve areas within the total scan set with dose. Each area contained 6 data points and relates to 8mm by 10.5mm. Temperature of measurement 15 °C.

10.4. Discussion

The acoustic impedance of the acoustic polymers tile was measured by identifying the minimum in the reflection coefficient between the tile and a saline solution of varying salinity. The minimum in the reflection coefficient will coincide with the best match between the real parts of the Acoustic Impedance of the tile and the saline solution. As shown in Figure 10.3 the minimum in the reflection coefficient occurs when the salinity was 0.036 g cm^{-3}, which gives a calculated acoustic impedance of 1.57×10^6 kg m^{-2} s^{-1} at 22 °C. This value of the acoustic impedance of the acoustic polymers tile corresponds well with the value from the parametric model of 1.59×10^6 kg m^{-2} s^{-1} at 22 °C. This serves both to provide an independent measurement of acoustic impedance of the acoustic polymers material compared to the values calculated from measurements of the speed of sound and density of the material, as

well as providing an initial validation that images from the Ultrasonix scanner can be acquired and analysed.

Figure 10.5 shows a typical image of the pixel values from the interface. The brightest pixels are the second and third pixels in the interface region, however structure can be observered from deeper in the reflector.

The simple irraidation of a MAGIC gel and acoustic polymer material phantom imaged using the Ultrasonix scanner utilised a step irradiation where one side was irradiated to 20 Gy and the other side left unirraidated. As shown in Figure 10.7 the two sides of the phantom produce very different reflections, as shown by the observed pixel values. The pixel value shows similar variation with temperature as was observed of the RMS amplitude with the single element transducer. A minimum in pixel value is observed at approximately 19°C for the irradiated region and at approximately 16°C for the unirradiated region. It was observed during these measurements that significant variation within the scan images was occurring even for the nominally uniformly irradiated regions. Subsequent measurements of the complex irradiation regime included pre-irradiation images to try and correct for some of these variations.

Figure 10.8 shows the pixel variation across the image prior to irradiation for the eleven scan planes. For each scan plane there is a systematic variation across the image. The reason for this variation is not known, although a number of possible causes have been identified. The variation across the images could be caused by variation on the surface of the interface between the acoustic polymer reflector and the MAGIC gel, variation at the interface between the MAGIC gel and the oil used as the transducer coupling agent, acoustic variation within the MAGIC gel or by the ultrasonic pulse formation/reception/image formation on the scanner itself. Further testing is required to identify which of these causes are contributory factors to the image variation across the unirradiated surface. Figure 10.9 shows corresponding data for each scan plan and how the pixel varies with position on the image. There is less systematic variation in this plane, indicating that the variation displayed in Figure 10.8 may be more likely to be caused by some property of the scanner or image formation rather than the MAGIC gel and acoustic polymer reflector phantom.

Figures 10.10 and 10.11 show the variation in pixel value at the interface between the acoustic polymers material and MAGIC gel for the complex irradiation

scheme at 15 °C. In both Figures 10.10 and 10.11 the central portion of the scan planes show the expected variation of the pixel value with irradiated dose. Towards the left hand edge of Figure 10.10 the pixel value increases as was expected for an unirradiated region. Towards the right-hand edge of Figure 10.11 it was expected that the pixel values should increase as the irradiation at the far right was to approximately 20 Gy rather than 30 Gy in the central right region. However, this is not clearly evident in the observed pixel values. Similar variations are observed for the 25 °C scans shown in Figures 10.12 and 10.13. There are a number of potential reasons for the pixel values not corresponding to the expected variation at the edges as observed in Figure 10.11 and 10.13. At these positions it was observed when removing the MAGIC gel from the phantom that during the manufacture and irradiation process the edges of the acoustic polymer material had become raised. This change in surface geometry, maybe caused by some absorption by the acoustic polymers material, may have affected the angle of reflection from the interface and altered the pixel value that is observed at the edges of the images. Alternatively, the number of elements that the transducer can use to form the beam and receive the signal is lower at the edges of the field than at the centre of the field, and so beam and image quality at the edges of the field may be poorer, leading to more noise and uncertainty in the pixel values produced. Additionally, small changes in phantom position between the pre- and post-irradiation images may cause these problems to be magnified.

In Figures 10.10, 10.11, 10.12 and 10.13 the ‘normalised’ pixel values still show significant variation across the uniform sections of irradiation, similar to Figure 10.7, and so the process of subtracting pre-irradiation pixel values has improved data quality but further work is required in this area to improve performance of the system.

The assumption that the scanner applies logarithmic gain compression to the images was significant in the implementation of subtracting the pre-irradiation pixel values within the analysis routines. This assumption of logarithmic gain compression was not independently verified. Any deviation from logarithmic gain compression will introduce non-linearities into the measured reflection coefficients. A method of characterising the gain compression applied to the images by the scanner would be needed to verify the validity of this analysis method.

By performing further averaging as shown in Figures 10.14 to 10.17 the data from the scanner is seen to resemble the data acquired using the single element transducer. At the lowest temperature measured (10 °C in Figure 10.14) as the irradiation dose is increased the pixel value decreases initially and then increases as the dose increases further. This corresponds to the temperature in Figure 6.10 where around the temperature of minimum reflection coefficient (17°C) the reflection coefficient first decreases and then increases with increasing dose. For the higher temperatures (Figures 10.15, 10.16 and 10.17) the trend is for the increasing dose to decrease the pixel value, as seen for the highest temperature in Figure 6.10, where the reflection coefficient decreased with increasing dose.

Figure 10.18 shows the data for 15°C averaging over a smaller spatial area. The relationship between the averaged 'normalised' pixel value and dose is still visible, but there is more scatter on the points. However, the spatial averaging over an area representing 8 mm by 10.5 mm indicates that dose can be resolved on the scale of 10mm as discussed previously. However the distinction between dose levels of 10% for an adequate system is still some way from being realised, as identified in Chapter 2.3 as having potential for development into a clinically usable dosimetry system.

Chapter 10: Slab phantom imaged using the Ultrasonix scanner

11. Ultrasonix system characterisation

11.1. Introduction

In Chapter 10 it has been shown that quantitative information on the effect of radiation dose on reflections can be obtained with an ultrasonic scanner. In order to maximise the ability to acquire the best possible images for further analysis, a full calibration of the scanner would be required. Manufacturers do not provide a method of calibrating the scanner settings. This chapter considers this issue of scanner calibration. Image acquisition is subject to swept gain so that ultrasound signals from deeper in the image are amplified by a greater amount to compensate for signal attenuation as the ultrasound pulse passes through tissue. Also, each change in image acquisition setting, such as Gain, Power, Dynamic Range and Focal depth setting will cause the displayed and captured pixel value to vary. Therefore a method was developed to calibrate the scanner so that pixel values can be compared between different depths in an image and between images. This characterisation would ultimately enable the conversion of a measured pixel value in the image into a change in reflection amplitude in dB. On the Ultrasonix MDP scanner (Ultrasonix Medical Corporation, Richmond, BC, Canada) used in this thesis, scanner settings can be stored as imaging 'templates' in the scanner, and so can be recalled when required for system characterisation.

11.2. Materials and methods

To characterise the pixel value a system was available to produce a rapid series of uniform amplitude ultrasound pulses incident upon the image transducer face for each scan line produced. This is known as an Impulse Triggering System and was developed by Mr Michael Perkins at the Department of Medical Physics and Bioengineering at the Royal United Hospital NHS Trust, Bath. A single element transducer was coupled to the face of the imaging transducer using ultrasound gel and held in place using a clamp. The ultrasound imaging field produced by the imaging transducer is received by the single element transducer. The system receives this as an

input signal and once the amplitude reaches the trigger level of the system it initiates the production of a series of impulses that are applied back to the single element transducer. These are converted by the transducer into a series of ultrasound pulses which are interpreted by the ultrasound imager as a series of planes in the image. A diagram of the system functionality and the controllable parameters are shown in Figure 11.1. The number of pulses, N, the delay between reception of the imaging and the first output impulse, td, the period between impulses τ, and the amplitude of each impulse A_0 can all be varied. By varying the amplitude of the impulses, a comparison between the pixel value in the image and the impulse amplitude can be made. The settings on the scanner such as overall gain can also be characterised by using this system to quantify the variation in pixel value with scanner settings for the same amplitude received signal.

A single element transducer of diameter 12mm and centre frequency 3.5MHz was connected to the Impulse Triggering System. A transducer with a large diameter was selected to ensure that the impulses generated by the Impulse Triggering System were converted into ultrasound pulses that were wide compared to the width of the elements in the imaging transducer selected to form the image lines.

The images produced by the system were saved as described previously. Images were analysed using Matlab R12.1 (The Mathworks, Inc., Natick, MA). The analysis routine selected the same scan line in each image and identified the depth in the image that each reinjected pulse was received and identified the maximum pixel value associated with each pulse for a 5 pixel width scan line. An example of the Matlab code used for analysing the signals is contained in Appendix C6.

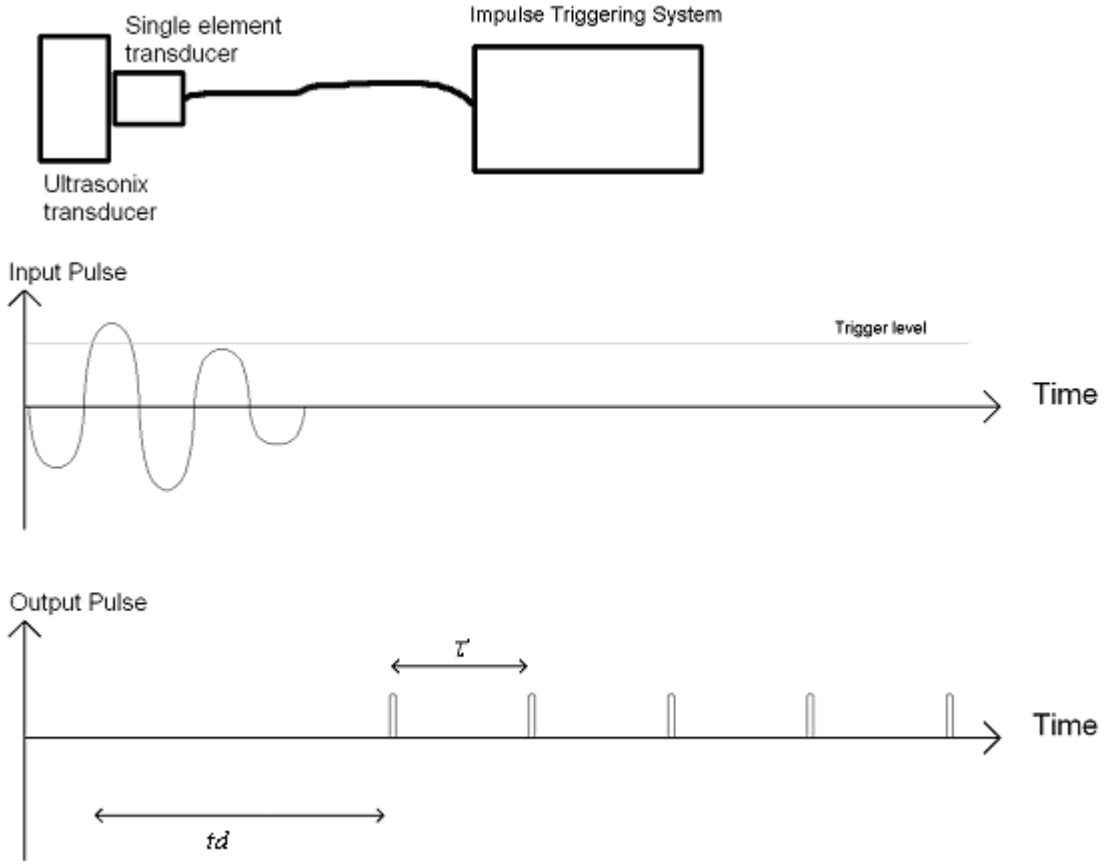

Figure 11.1 Schematic diagram of the Impulse Triggering System showing the Input and Output pulse sequences. Each output has a variable number of impulses. Each impulse is of the same amplitude A_0, which can be varied, as can the delay between the pulse train starting (td) and the period between impulses (τ).

11.3. Results

An example of the image produced by the Ultrasonix scanner when connected to the Impulse Triggering System is shown in Figure 11.2. The scan line analysed in each image is shown as a red line superimposed on the image.

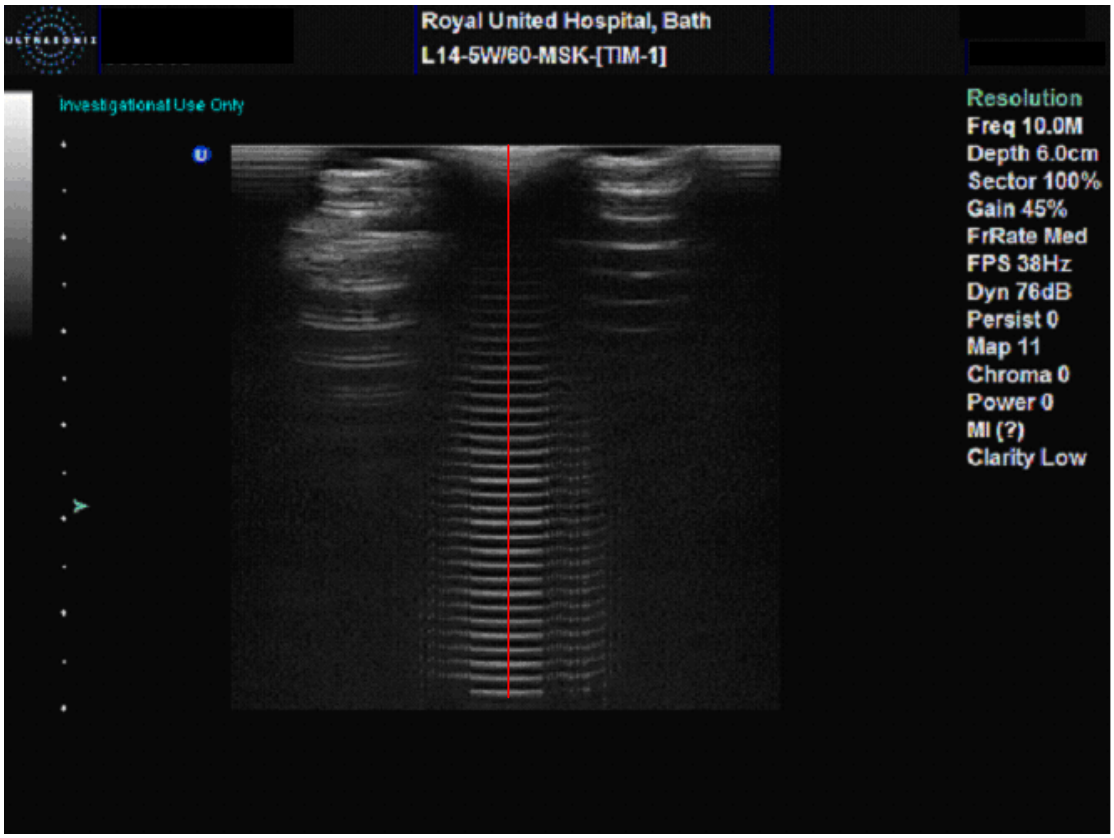

Figure 11.2 Image from the Ultrasonix scanner of the pulse train produced by Impulse Triggering System, showing lines of received pulses down the centre of the image. The red line on the image indicates the pixel line used for analysis

Figure 11.3 shows how the pixel values vary with depth as the Power on the scanner was varied. Error bars are the standard deviation of pixel values computed for each pulse from five separate images. A system gain of 55%, focal depth of 38mm and dynamic range of 76dB was used when acquiring these images. The pixel value increases with depth from 1.5 cm to 4 cm, showing the swept gain of the system. Beyond 4 cm the variation of pixel value with depth shows no systematic variation, although a drop in pixel value at approximately 4.5 cm is observed. There appears to be no change in pixel value for the four different acoustic power settings used.

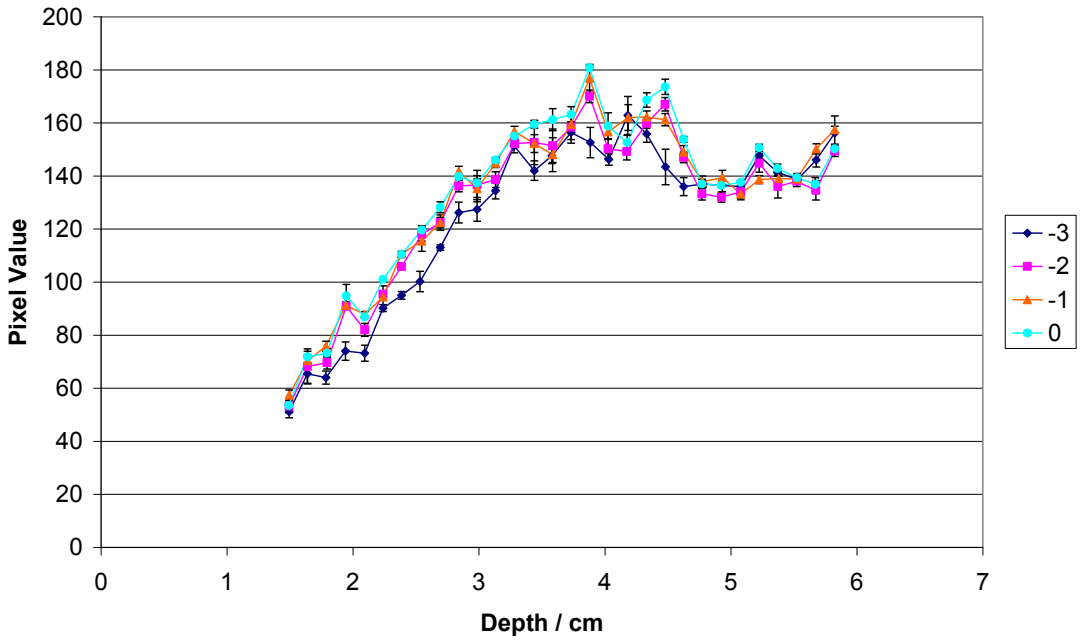

Figure 11.3 Variation of Pixel Value with imaging depth as the acoustic Power (see key) setting on the scanner was varied, generated using the Impulse Triggering System. Each Power setting is shown as a separate plot. Lines are displayed to guide the reader and are not necessarily indicative of actual behaviour.

Figure 11.4 shows the variation in pixel value with depth as the focal depth on the imager was varied. Error bars are the standard deviation of pixel values computed for each pulse from five separate images. A power of 0, system gain of 67%, and dynamic range of 76dB was used when acquiring these images. The pixel value increases with depth from 1 cm to 4 cm. Beyond 4 cm the variation of pixel value with depth shows no systematic variation, although a drop in pixel value at approximately 4.5 cm is observed. There appears to be no change in pixel value for the seven different focal depths used.

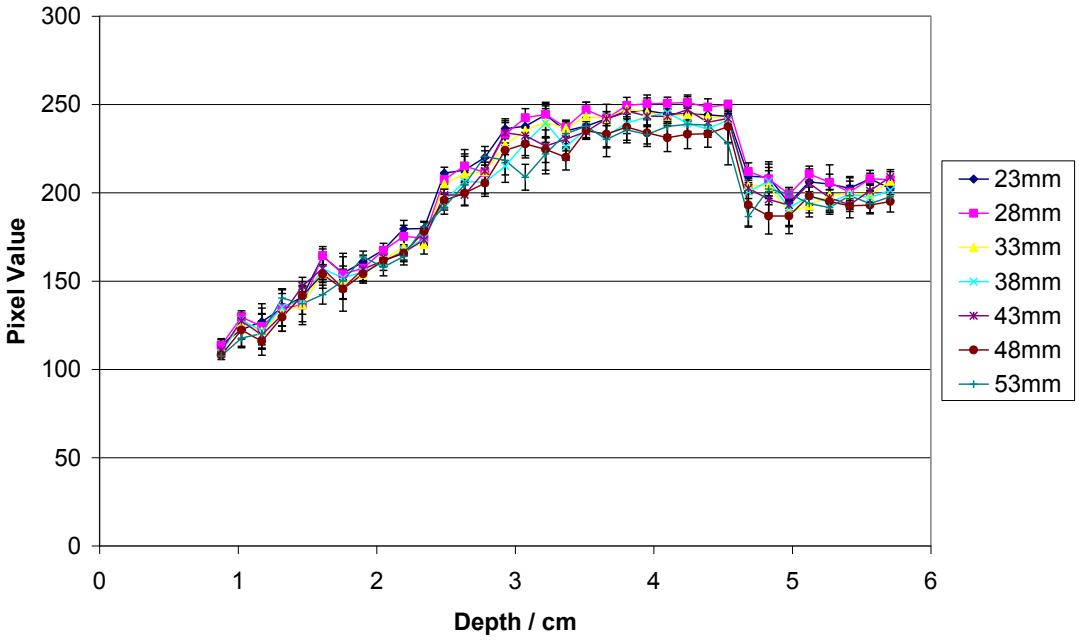

Figure 11.4 Pixel value with depth in the Ultrasonix image as the focal depth (see key) was varied, generated using the Impulse Triggering System. Each focal depth is shown as a separate plot. Lines are displayed to guide the reader and are not necessarily indicative of actual behaviour.

Figures 11.5 and 11.6 shows how the pixel value in the image varies with amplitude (A) of the triggered impulses. Error bars are the standard deviation of pixel values computed for each pulse from five separate images. The amplitude of the triggered impulses is modified from its nominal value (0dB) by applying attenuation to the output. The actual attenuation applied was calculated from measurements of the pulse amplitude made using a LeCroy 9310A oscilloscope (LeCroy, Teledyne LeCroy, Chestnut Ridge, NY). A power of 0, system gain of 67%, focal depth of 38mm and dynamic range of 76dB was used when acquiring these images. Figure 11.5 shows the same pattern of increasing pixel value with depth is observed up to 4 cm, with a drop in pixel value at approximately 4.5 cm. Figure 11.6 shows that the pixel value is approximately linear with applied attenuation at all depths.

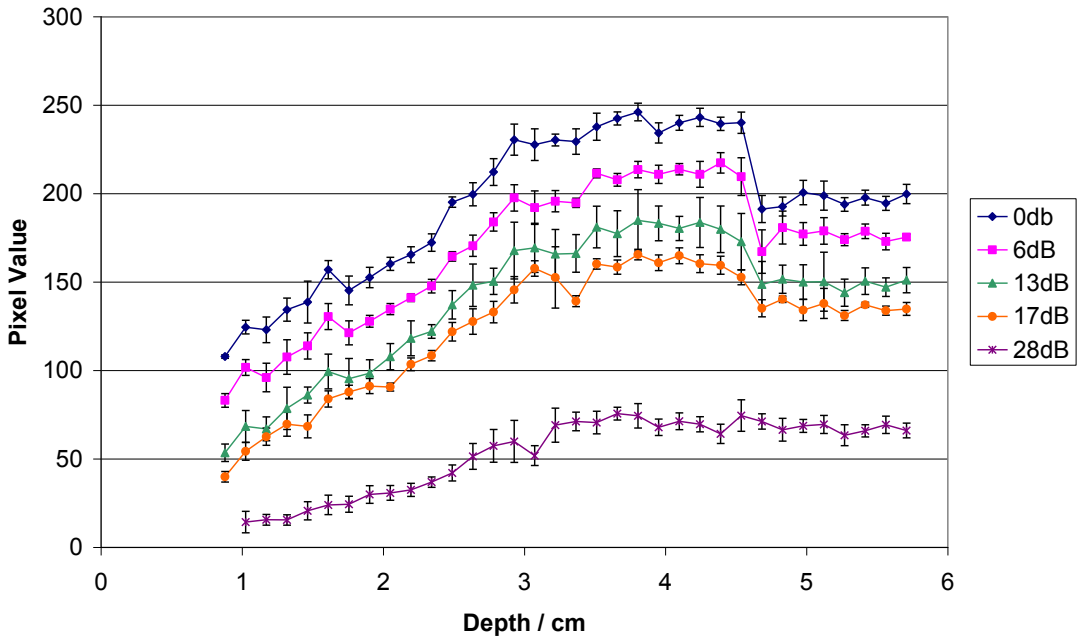

Figure 11.5 Pixel value on the Ultrasonix scanner with depth in image as the impulse amplitude (attenuation – see key) of the Impulse Triggering System was varied. Each pulse amplitude is shown as a separate plot. Lines are displayed to guide the reader and are not necessarily indicative of actual behaviour.

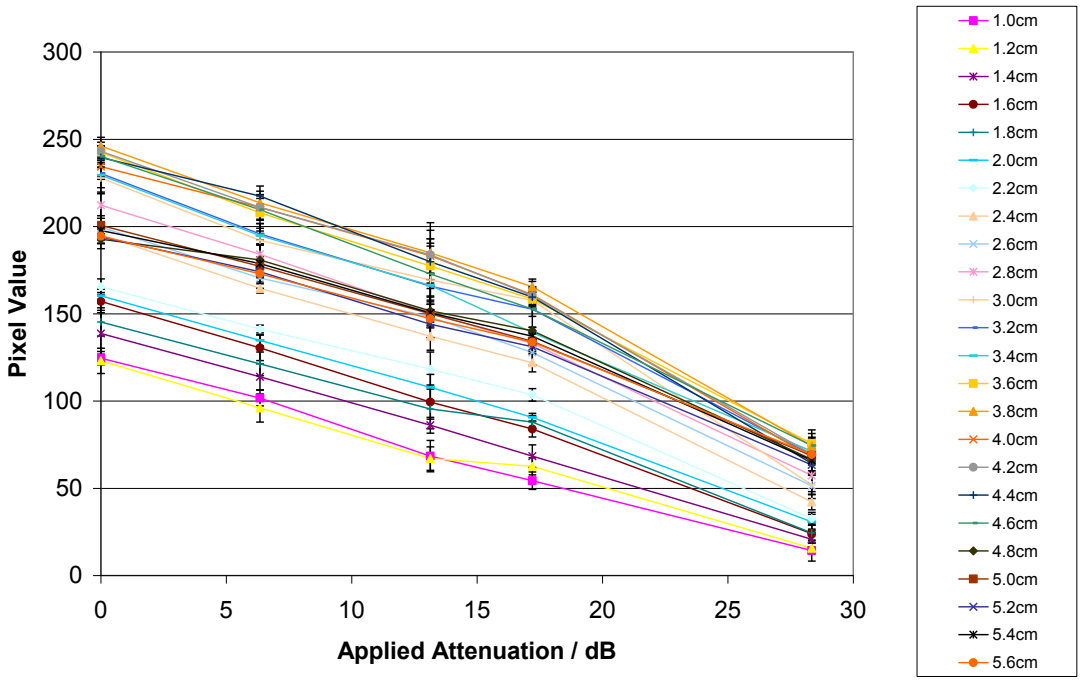

Figure 11.6 Pixel value on the Ultrasonix with attenuation applied to the impluses of the Impulse Triggering System at selected depths (see key). Each depth is shown as a separate plot. Lines are displayed to guide the reader and are not necessarily indicative of actual behaviour.

Figures 11.7 shows how the pixel value varies as the system gain of the Ultrasonix scanner is varied. The variation in pixel value with depth is as observed for the other settings. There appears to be compression of the pixel value range at the higher gain settings. Error bars are the standard deviation of pixel values computed for each pulse from five separate images. The system gain had two values, an internal system setting accessed by in the research setup and a value displayed on screen. The internal system value had more resolution than the on screen display. The internal system value is used here and varied from 0 (on screen value of 50%) to 2000 (on screen value of 83%). A power of 0, focal depth of 38mm and dynamic range of 76dB was used when acquiring these images. Figure 11.8 shows the difference in pixel value at each depth between pairs of gain settings. Combined standard deviations of the pixel value computed for each pair of gain images were calculated and an example of the combined error is shown on the plot of 250-0 gain settings.

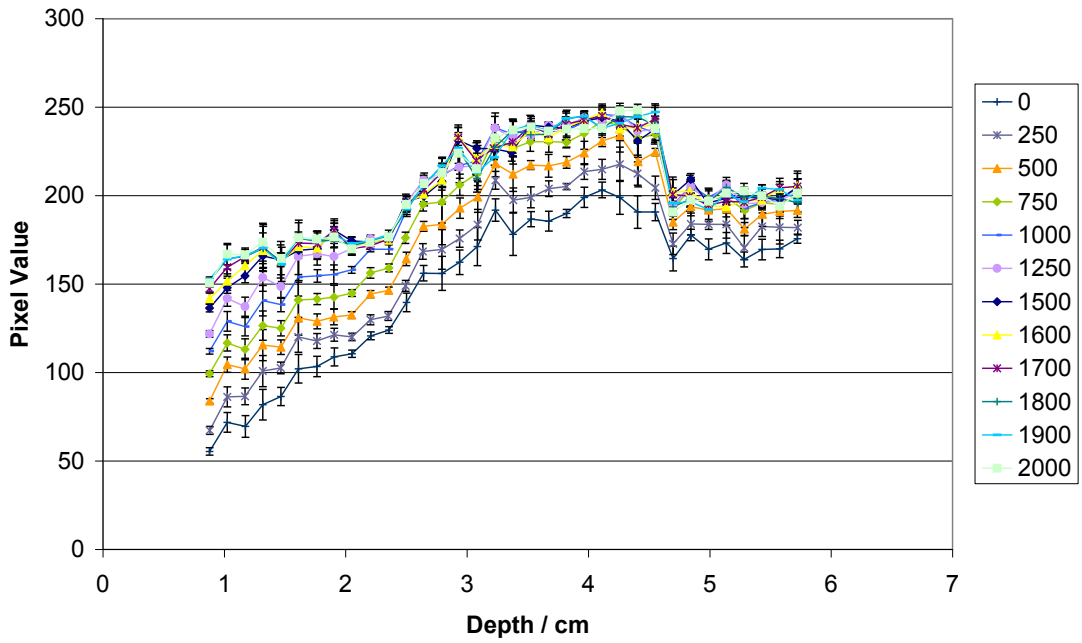

Figure 11.7 Pixel value with depth on the Ultrasonix scanner as the internal system gain (see key) was varied generated using the Impulse Triggering System. Each gain setting is shown as a separate plot. Lines are displayed to guide the reader and are not necessarily indicative of actual behaviour.

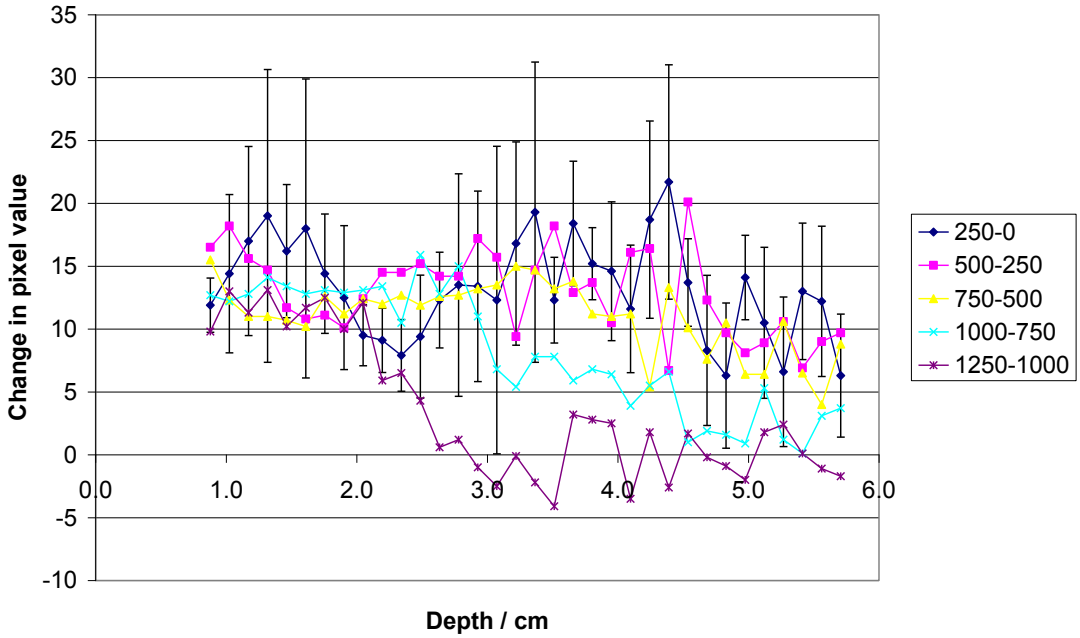

Figure 11.8 Change in pixel value between gain settings with depth for the pulse reinjection system as the internal system gain (see key) was varied. Each pair of gain setting is shown as a separate plot. Lines are displayed to guide the reader and are not necessarily indicative of actual behaviour.

11.4. Discussion

A small subset of the imaging parameters on the Ultrasonix scanner have been analysed using the Impulse Triggering System to develop an understanding of the performance of the scanner and how various settings affect the pixel value in the image.

Figure 11.3 shows that the pixel level in the image is not dependent on the output power set on the imager over the range measured and with the selected scanner settings. This implies that whatever output power is selected the same acquisition parameters are used. However, the Impulse Triggering System could only reliably pick up the imaging pulses for power settings of 0, -1, -2 and -3. For imaging the gel phantoms used in this project lower power setting of -15 to -10 have been used. Therefore to extend the use of the system the input to the Impulse Triggering System needs redesigning to enable the use of the system on lower power fields and the analysis repeated at these lower output powers.

Figure 11.4 shows pixel value is independent of the focal depth over the range measured and with the selected scanner settings. This implies that the focus is applied

by varying the output pulse waveform and not the receive function within the scanner, and that other imaging parameters are also independent of the focal depth.

The Impulse Triggering System was only able to function with acquisitions using a single focus. When multiple foci were used, the image produced by the impulses became unstable. The Impulse Triggering System produced a series of impulses whenever the imaging pulse reached the trigger level. The scanner produces separate image pulses for each focal depth with different phasing to produce the depth focus, and hence the point within the imaging cycle at which the trigger level was reached was different for each focal depth. This caused the depth at which the impulses appeared on the image to become unstable. A development of the system would be required to enable the analysis of imaging fields employing multiple foci. Such a development would require a complex control system to distinguish between the different image pulses used for each of the multiple focal depths.

Figures 11.5 and 11.6 show how the pixel values vary with the pulse amplitude of the impulses produced by the system. The pixel value appears to be approximately linear with impulse amplitude (measured by the attenuation applied to the impulses generated in dB) over the range measured and with the selected scanner settings. This implies that a logarithmic gain compression is applied to the input pulses. A slight sub-linearity at pulse amplitudes with an attenuation of 28dB is observable and may affect the measurements of very weak reflections in images.

Figures 11.7 and 11.8 show the variation of pixel value with gain setting on the scanner. At shallow depths (1-2cm) it appears that the pixel value is approximately linear with gain setting for the gains of 1250 (71%) or below with the selected scanner settings. At depths of 2-3cm it appears that the pixel value is approximately linear with gain settings of 1000 (67%) or below with the selected scanner settings. The gain settings of 750 (63%) and below appear to produce a linear change in pixel value with gain setting at all depths, although there is a step change in pixel value that occurs at approximately 4.6cm deep. At gain settings of 1500 (75%) and greater it appears that no change in pixel value with gain setting occurs at any depth with the selected scanner settings. These results imply that at high gain settings (>75%) on the scanner the combination of time-gain compensation and system gain implies that the gain is saturated for the amplitude of signals produced by the Impulse Triggering System and

so no change in pixel amplitude occurs for a change in gain. At small depths and reduced system gain, the linear change in pixel value with gain setting implies that the combination of time-gain compensation and overall gain is not saturated, but that the gain set relates to a linear, as opposed to logarithmic, amplification of the received signal. It also suggests that to avoid signal saturation a low gain setting should be utilised. However the measurements of pixel value with system gain were made with only one the highest amplitude impulses (0 dB attenuation) from the Impulse Triggering System, and the system may behave differently for lower amplitude signals.

Figures 11.3, 11.4, 11.5 and 11.7 show the same basic variation of pixel value with depth. Since the Impulse Triggering System is inputting the same pulse amplitude for all times after the imaging pulse, this behaviour is indicative of the swept gain (time-gain compensation) of the system. Between 1cm and 3cm deep the pixel value increases with depth. At 3cm to 4.5 cm the pixel value is approximately constant with depth. At approximately 4.6cm there is a drop in the pixel value, beyond which the pixel value is again approximately constant with depth. However, using a single element transducer to transmit the impulses to the imager implies that all the impulse signals received by the imager are of the same phase relationship. The imager will be compensating for the depth from which echos are likely to be generated by changing the phase association between transducer elements, based on the time after the imaging pulse was transmitted. This conflict between the phase-compensated imaging system and the single phase ultrasonic field generated by the single element transducer will interfere with the results obtained here, so the shape of pixel value with depth seen in Figures 11.3, 11.4, 11.5 and 11.7 is not only due to the swept gain of the system.

Only a limited subset of each imaging parameter available on the Ultrasonix scanner has been assessed, and other parameters such as dynamic range, Time Gain Compensation maps, image depth and reject levels have not been assessed. However, from the results of this initial investigation it would seem possible to identify a subset of parameter settings to be used in image acquisition for the analysis of dosimetric gels that could then be fully characterised using this system so that an absolute measure of reflection coefficient could be produced from pixel values at each point in the image.

This image characterisation has only been performed for a single scan line of the image. Repeated acquisition at different positions across the image are required to fully characterise the response of the system at all points within the image.

The Impluse Triggering System presented here is a simple system which has only limited functionality and limitations. Significant development of the system is required to enable a full characterisation of a complex imaging system. The limitations of the Impulse Triggering System include the inability of the system to respond to low amplitude imaging signals, the use of a single element transducer to receive the imaging signal and to transmit the impulses to the imaging transducer and the simple electronic controls used in the system.

The system input is set up so that only high amplitude imaging pulses trigger the production of an impulse train. This is useful in that the system only responds to the imaging fields of scan lines near where the single element transducer is located on the imaging transducer. This ensures that images produced on the scanner by the system are clean and stable. However, it does mean that the low power settings on the scanner used in the project were unable to be characterised using this system.

The use of a large single element transducer to receive and transmit signals to the system ensures that the array aperture used for imaging is smaller than the size of the transducer. Using a single element transducer implies that all the impulse signals received by the imager are of the same phase relationship. The conflict between the phase-compensated imaging system and the single phase ultrasonic field generated by the single element transducer will introduce errors into all the results obtained with the system.

The only large diameter transducers available were of centre frequency 3.5 MHz, much lower than the imaging frequency of 10 MHz. The mis-match between the imager frequency and the frequency of the single element transducer will affect the results obtained by the system as the signal processing chain on the imager will not be optimised for the lower frequency ultrasound produced by the single element transducer when it receives an impulse as generated by the Impulse Triggering System.

The simple electronic controls in the system meant that only imaging fields with a single focal depth could be characterised using the system, and only a few different controls of the impulse train were available. This affects the ability to fully

characterise the system by limiting, for example, the number of available amplitude impulses (5) or by limiting the system to use with only single focal depth imaging fields. A more sophisticated control system would enable a more detailed characterisation to be performed using this system.

This work will enable the development of a fully characterised ultrasonic back scatter imager. No manufacturer currently provides a method of characterising a system in this way. The only ultrasound systems currently capable of producing calibrated images are those which produce calibrated elastographic images such as those used by Crescenti (2009) to produce dose dependent elastograms.

12. Conclusions and further work

12.1. Introduction

This chapter summarises the main achievements of the research described in this thesis and introduces work which could be performed to further the research and optimise the solutions which have been developed in measuring radiation dose using backscatter ultrasound techniques.

12.2. Measurement of physical and ultrasonic properties of MAGIC gels

Techniques for the measurement of physical and ultrasonic properties of MAGIC gels have been developed and demonstrated within this thesis. The measurements reported in this thesis have developed the understanding of the physical and ultrasonic properties of MAGIC gels and how these properties vary with radiation dose. The temperature dependent variation of attenuation coefficient, speed of sound and density of MAGIC gel, have been demonstrated for the first time in this thesis. The dose dependent properties of MAGIC gels reported in this thesis have been used to determine the appropriate properties of materials that can be utilised to produce dose dependent backscatter reflections. The techniques demonstrated for measuring the physical and ultrasonic properties of MAGIC gel could be utilised to measure the same properties of alternative dosimetric gel formulations.

12.3. Measurement of dose dependent reflections

The ability to measure radiation dose dependent reflections from planar interfaces using ultrasonic pulse echo techniques has been demonstrated in this thesis. Non-uniform dose distributions have been imaged with changes in reflection amplitude corresponding to different dose levels being identified with a resolution of less than 10 mm. However the ability to resolve changes in dose remains at greater than 10%. To measure these dose dependent reflections an inert reflector material has been

specified, manufactured and characterised. The properties of this inert reflector material were matched to the measured properties of the MAGIC gel to ensure the greatest sensitivity to dose dependent changes in MAGIC gel properties could be observed. Further developments using alternative gel formulations or different inert reflector materials could increase the sensitivity of dose dependent reflections and enable better spatial and dosimetric resolution to be achieved.

12.4. Measurement reproducibility and repeatability

One of the major issues that has become apparent during the course of this research is the consistency and uniformity of the polymer gel which has led to uncertainties in the results of measurements of gel properties and the dose dependent reflections. Throughout the research efforts were made to improve the batch variation by introducing controlled cooling conditions and the usage of evacuation techniques to reduce the amount of air bubbles in the polymer gel. Work to improve the batch-to-batch reproducibility and sample uniformity of the MAGIC gels could be performed, as appears to be developed by Liney et al (2003, and personal communication) for MRI based measurement of MAGIC gels. Both batch-to-batch variability and sample uniformity may be improved by utilising a chemical batch reactor or other chemical engineering techniques. Reducing the batch-to-batch would require a more consistent preparation technique for the gel and improving on the cooling techniques to result in more consistent cooling conditions for all samples. Reduced batch-to-batch variability would result in more consistent reflection coefficient versus temperature profiles. Improving the sample uniformity would reduce the variation across images and the uncertainty in measurements at each position. This would reduce the variation in reflection coefficient with dose making the reflection coefficient a better measure of dose, and improve the dosimetric and positional accuracy of measurements.

A variety of techniques could be used to study the reproducibility and repeatability of improved gel production and ultrasound measurements on the gels. From repeated image acquisitions suitable error analysis techniques could be employed to determine reproducibility of measurements for the thread and the same batch of gel.

Measurements of the same irradiated dose but for different gel batches could be taken to produce an estimation of repeatability of the measurements.

12.5. Use of a commercial ultrasound scanner usage and scanner characterisation

Within this thesis it has been demonstrated that it is possible to utilise a commercial ultrasound scanner to obtain quantitative backscatter information from an interface between MAGIC gel and an inert reflector. Measurements of dose dependent reflections from planar interfaces obtained using a commercial ultrasound scanner are similar to those obtained using single element ultrasound transducers.

The scanner configuration could be further optimised to ensure that the most suitable settings are used in the image acquisition. Settings such as swept gain, dynamic range and focussing could all be optimised. The swept gain could be reduced to ensure the greatest dynamic range is available due to the low attenuation coefficient of MAGIC gel compared to soft tissue. The reflection amplitude is expected to be small, although the relative change in reflection coefficient (unirradiated to irradiated) would still be significant. Therefore the overall gain could be set high, with an appropriate selection of the dynamic range made to ensure the expected changes can be observed within the available dynamic range while reducing any quantisation that may occur due to digitisation into the 8-bit images produced by the system.

The Impulse Triggering System used in this research has demonstrated an ability to characterise the response of the ultrasound scanner. Improvements in the measurements of dose dependent reflections could be made by full characterisation of the scanner to enable greater utilisation of its capabilities. The Impulse Triggering System to characterise the scanner could be performed to enable the calculation of reflection coefficient from pixel value at each position in the image.

12.6. Investigation into thread phantom

A phantom consisting of threads of inert reflector material has been developed as part of this research. Further work is required to characterise the thread phantom as

the acoustic impedance of the threads could not be verified by the initial measurements of the acoustic polymers threads. Additional work is required, including modelling of thread materials, to determine why the initial investigations did not produce the expected output. Results of these investigations could then be used to develop an understanding of the way in which the thread phantom could be used to measure changes in reflection and how these can be related to the irradiated dose of a phantom containing MAGIC gel.

12.7. Alternative designs for pulse-echo ultrasound systems

A number of potential pulse-echo ultrasound systems have been identified and discussed in this thesis. These include the planar reflector and the thread phantom. Alternative designs of systems could be investigated, some of which may prove to be successful dosimetry systems. Two potential geometrical arrangements which could be investigated is the use of spheres of backscattering material and micro-spheres of MAGIC gel within an inert matrix.

The acoustic polymers material could potentially be manufactured not as slabs or threads, but as small spheres. Insertion of these spheres into a MAGIC gel dosimeter may produce a backscatter phantom from which changes in grey-level could be correlated with radiation dose. Challenges with such a system lie in the creation of individual spheres that can be dispersed uniformly throughout a MAGIC gel dosimeter without accumulation or agglomeration. The reflections from the spheres would need to be characterised to understand the relationship between the change in reflection amplitude and irradiated dose.

The work and discussion within this thesis has focused on the use of MAGIC gel as the prime ingredient to a dosimetry system, with inert materials added to create the reflection of the ultrasound. This was purposefully chosen as the MAGIC gel is nearly water-equivalent, and other materials may not be be water equivalent and would significantly perturb the radiation field. Alternatively, if an inert material that was water-equivalent were chosen, then the prime ingredient could be made inert, with small amounts of dose-dependent material added to create dose-dependent echos. In such a system the inert material would need to be able to retain the geometric

positioning of the dose-dependent reflectors, and hence would need to be a material that solidifies during the preparation process. Gelling materials such as gelatine, agar or poly-vinyl alcohol would be possibilities for the inert matrix. Methods would need to be developed to enable the creation of dose-dependent insertions into the inert matrix without mixing between the inert and dose-dependent materials. The inclusion of MAGIC gel within microspheres is a possibility for this, however, this introduces the possibility that the material of the microsphere itself would significantly affect the reflection of ultrasound, and would therefore need to be carefully developed and investigated.

Appendix A. List of publications and presentations arising from this project

Atkins, T.J. Humphrey, V.F. Duck, F.A. Tooley, M.A., 2011. The effects of focused transducer geometry and sample size on the measurement of ultrasonic transmission properties, *J. Phys.: Conf. Ser.*, 279, 012024.

Atkins, T.J. Humphrey, V.F. Duck, F.A. Tooley, M.A., 2010. Investigation of ultrasonic properties of MAGIC gels for pulse-echo gel dosimetry, *J. Phys.: Conf. Ser.*, 250, 012075.

Atkins, T.J. Humphrey, V.F. Duck, F.A., 2009. Measurements of Ultrasonic Properties of Dosimetric Gels, The Physics and Technology of Medical Ultrasound, IPEM, March 2009.

Atkins, T.J. Humphrey, V.F. Duck, F.A., 2006. The effects of focused transducer geometry and sample size on the measurement of ultrasonic transmission properties. The Physics and Technology of Medical Ultrasound, IPEM, February 2007.

Appendix A: :List of publications and presentations arising from this project

Appendix B. The effects of focused transducer geometry and sample size on the measurement of ultrasonic transmission properties

Work was performed concentrating on the development of a system to measure acoustic properties using coaxially aligned focused transducers. Confidence in the estimation of acoustic properties from such measurements is dependent on the geometrical positioning of transducers and homogeneous samples to reduce errors in the measurement. Geometry and sample size issues related to measurement of sample properties using coaxially aligned spherically focused transducers (with weak focusing) have been explored by measuring and modelling the interaction of three specific transducers.

B1. Theoretical expression for receiver response

Consider a spherically concave source with radius a_1 and radius of curvature F_1 producing sound at angular frequency ω in cylindrical coordinate system (z, r, φ) as shown in Figure B1. The radiation is generated by uniform radial motion of the transducer surface with velocity amplitude U_0.

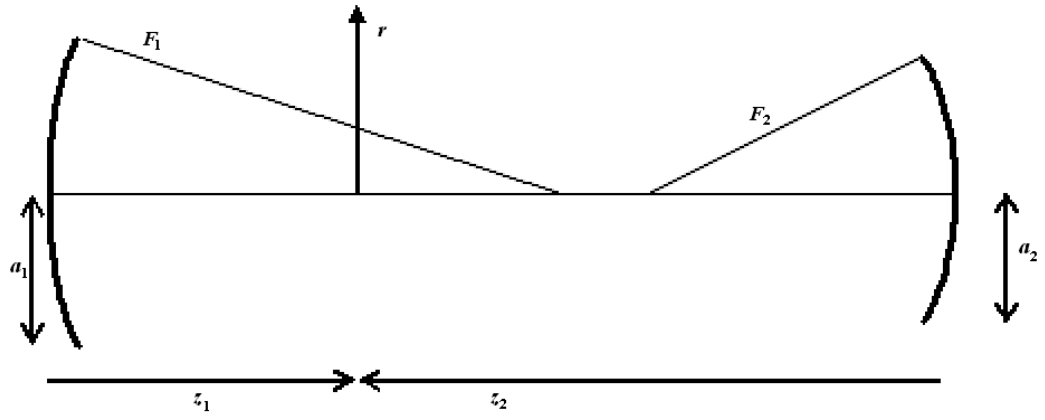

Figure B1. Cross section view of two coaxially aligned spherically symmetric concave transducers, showing coordinates and symbols used in the analysis.

Following Gavrilov *et. al.* (1988), a second transducer is located coaxially with the source at a separation $z_T = z_1 + z_2$. Application of the Huygens-Fresnel principle and reciprocity principle allows the sound pressure averaged over the active surface area of the receiver, $p_{rec}(z_T)$, to be given by the surface integral over an infinite plane between the two transducers

$$p_{rec}(z_T) = \frac{1}{P_2 \pi a_2^{\,2}} \int_{\sigma} p_1(r, z_1) p_2(r, z_2) d\sigma \qquad \text{(B1)}$$

where $p_1(r, z_1)$ is the complex sound pressure produced by the radiator at a distance r from the z axis in a plane at a distance z_1 from the source. Likewise $p_2(r, z_2)$ is the complex sound pressure produced by the second transducer operating in transmit mode at radial coordinate r in a plane at a distance z_2 from the source when P_2 is the average pressure amplitude across the surface of the second transducer. Here a_2 and F_2 are the radius and radius of curvature of the second transducer. For such a system the measured receiver response is assumed to be proportional to the calculated value $p_{rec}(z_T)$.

This solution is invariant over the choice of integration plane. For a given transducer separation z_T, z_1 and z_2 may be varied within the restriction that $z_T = z_1 + z_2$ without affecting the received sound pressure.

The use of cylindrical coordinates allows the transformation of the surface integration into a radial integral with $\sigma = \pi r^2$. The receiver response can be estimated by

$$p_{rec}(z_T, R) = \frac{1}{P_2 a_2^{\,2}} \int_{r=0}^{R} p_1(r, z_1) p_2(r, z_2) r dr \qquad \text{(B2)}$$

where $p_{rec}(z_T, R) = p_{rec}(z_T)$ when $R = \infty$.

Restricting the integration to a finite radial distance R introduces an error into the calculation of the $p_{rec}(z_T)$, and hence a measured receiver response. This allows the investigation of the effect of using finite size samples on the received sound pressure by analysis of the size of the restricted integral region required to accurately estimate the receiver response. It also allows investigation of the positioning of the sample by varying z_1 and z_2 for a fixed separation and determining the required integration limit to ensure an accurate estimate of the receiver response.

Gavrilov *et. al.* (1988), give a solution for the sound pressure of a focusing source of radius a and focal length F in the focal plane as

$$p(r) = \; - \; ?_0 \frac{a}{r} e^{ikF} J_1\left(\frac{kar}{F}\right) \qquad \text{(B3)}$$

where k is the wavenumber and P_0 is the average pressure amplitude at the surface of the transducer.

Lucas and Muir (1982) provide a more general solution for the sound pressure of a focusing source at a distance z from a source as

$$p(r,z) = -ik\frac{P_0}{z} e^{ikz} e^{\frac{ikr^2}{2z}} \int_0^a e^{\frac{ikx^2}{2}\left(\frac{1}{z}-\frac{1}{F}\right)} J_0\left(\frac{krx}{z}\right) x dx \qquad \text{(B4)}$$

which can be used in Equation (2) to estimate the receiver response $p_{rec}(z_T,R)$.

A significant feature of the model in Equation (B4) is the presence of the phase term $e^{\frac{ikr^2}{2z}}$. This phase term indicates that the phase is not constant across the field in the focal plane $z = F$. The phase term is not important when considering point measurements in a field, however, as a subsequent integration over r of the product of two of these functions is to be performed the phase needs to be carefully considered. It is omitted from (B3) as this is an approximation based on the geometrical optics work of Debye (1909). An alternative solution from O'Neil (1949) has the coordinate origin at the centre of the transducer. The distance of the field point from the co-ordinate origin is defined as $y = \sqrt{(z^2 + r^2)}$, and this solution includes a phase term e^{iky}. Using an Taylor series expansion around $r = 0$ this solution also contains a phase term $e^{\frac{ikr^2}{2z}}$ in agreement with Equation B4.

Introducing a sample into the measurement system during immersion measurements can be considered to split the integration used in this paper to calculate the receiver response, $p_{rec}(z_T)$, into two parts. The first part consists of an integration from the axis up to the sample radius s, for which there will be an attenuation introduced, and an integration beyond the sample radius s. The introduction of the sample may change the phase of the ultrasonic wave through the sample area.

Let the average receiver pressure without the sample be $p_{rec}(z_T)$ and the sample have a transmission coefficient Λ (allowing for attenuation and transmission at the

sample interfaces). The average receiver pressure with the sample is given by $p_{rec,s}(z_T)$ which can be approximated by

$$p_{rec,s}(z_T) = \Lambda\, p_{rec}(z_T,s) + [p_{rec}(z_T,\infty) - p_{rec}(z_T,s)]$$
$$= \Lambda\, p_{rec}(z_T,s) + [(p_{rec}(z_T,\infty) - p_{rec}(z_T,s)] + \Lambda[p_{rec}(z_T,\infty) - p_{rec}(z_T,s)]$$
$$- \Lambda[p_{rec}(z_T,\infty) - p_{rec}(z_T,s)]$$
$$= \Lambda p_{rec}(z_T,\infty) + (1-\Lambda).[p_{rec}(z_T,\infty) - p_{rec}(z_T,s)]. \quad \text{(B5)}$$

Hence the measured transmission coefficient Λ' is given by

$$\Lambda' = p_{rec,s}(z_T,\infty) / p_{rec}(z_T,\infty)$$
$$= \Lambda + (1-\Lambda)\,.\,[p_{rec}(z_T,\infty) - p_{rec}(z_T,s)]/\, p_{rec}(z_T,\infty) \quad \text{(B6)}$$

and the error in estimating Λ by Λ' is

$$\Lambda' - \Lambda = (1-\Lambda)\,.[1 - p_{rec}(z_T,s)/\, p_{rec}(z_T,\infty)]. \quad \text{(B7)}$$

The magnitude of the error in estimating Λ by Λ' is therefore minimised by ensuring $p_{rec}(z_T,s) / p_{rec}(z_T,\infty)$ is close to unity. When comparing the solutions it is therefore necessary to consider how close $p_{rec}(z_T, R)$ is to the infinite value $p_{rec}(z_T)$. Ratios $p_{rec}(z_T, R) / p_{rec}(z_T)$, for situation with no phase variation, and $|p_{rec}(z_T, R)| / |p_{rec}(z_T)|$, for situations with phase variation, are used to illustrate how close $p_{rec}(z_T, R)$ is to the infinite value $p_{rec}(z_T)$. To assist in the analysis R_{lim} is defined as the minimum integration limit required to ensure that the ratio of $|p_{rec}(z_T, R)| / |p_{rec}(z_T)|$ is greater than the specified value for all $R > R_{lim}$. Similar analysis is performed and integration limits used for the phase variation of $p_{rec}(z_T, R) / p_{rec}(z_T)$.

The maximum error that will be introduced by using a finite sized sample can be calculated from the ratio of $p_{rec}(z_T, R) / p_{rec}(z_T)$ and the sample transmission coefficient; alternatively the minimum sample size required to ensure that the diffraction errors are below a specified level can be calculated. This does not include errors from other effects such as higher diffraction effects due to the sample presence or sample inhomogeneity.

Three weakly-focused transducers of approximate centre frequency 3.5 MHz were selected for this investigation; Table B1 shows the properties of the transducers used. The properties are estimates of the actual values for three transducers calculated from measurements performed using an NPL Ultrasound Beam Calibrator (Preston, 1988). Each transducer was modelled using equation (B3) or by numerically

integrating equation (B4). The models for $p(z, r)$ were then used in equation (B2) to calculate the receiver response $p_{rec}(z_T)$ and the estimate for a restricted integration plane $p_{rec}(z_T, R)$.

Transducer	Radius of curvature (F) / cm	Transducer radius (a) / cm	Acoustic focal depth / cm	Beam width at acoustic focus / cm
A	7.6	0.608	5.0	0.27
B	11.6	0.621	6.0	0.39
C	13.5	0.914	9.5	0.35

Table B1. Measured transducer characteristics used in theoretical model.

B2. Results

B2.1 Debye approximation – identical transducers

Firstly consider a pair of matched transducers such that $a = a_1 = a_2$ and $F = F_1 = F_2$ If the integration plane in Equation B2 is chosen to be midway between the two transducers and they are separated by the sum of their radii of curvature, then using the Debye approximation (Equation B3) and a substitution $X = \frac{ar}{F}$ it can be shown that Equation B2 becomes

$$p_{rec}(2F, R) = - P_0 e^{i2kF} I \qquad \text{(B8)}$$

where $I = \int_{X=}^{X=}$. (B9)

The integrand and the integral I are plotted as a function of R in Figure B2.

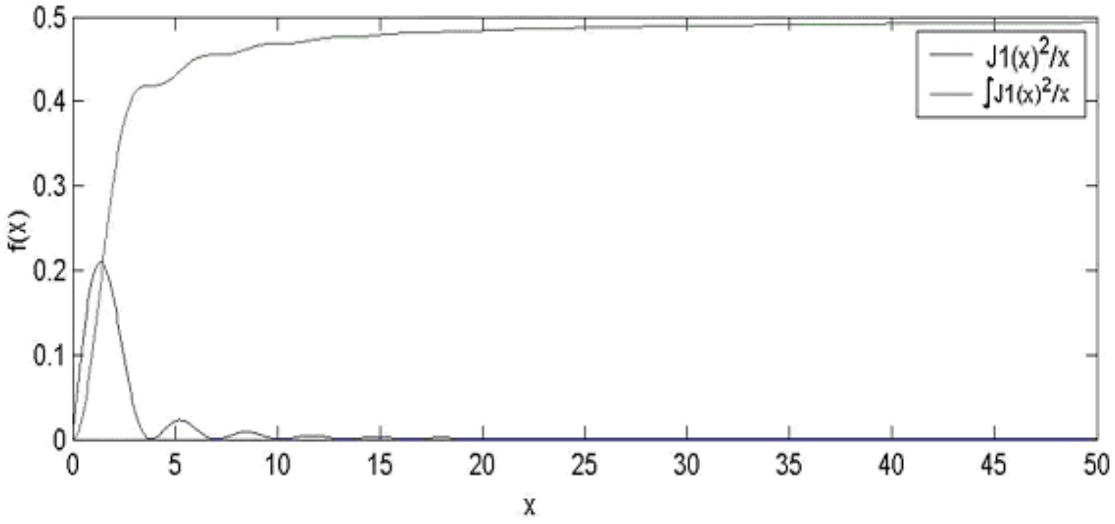

Figure B2. Plot of the functions $\frac{J_1^2(X)}{X}$ and $\int\frac{J_1^2(X)}{X}$ used in the calculation of the receiver response for coaxially aligned transducers (X is dimensionless)

The integral is a monotonically increasing function which reaches a value of 0.5 when integrated over an infinite range. This implies that

$p_{rec}(2F,\infty) = -P_0 e^{i2kF}$

which can be shown by integration of equation B8. However this result neglects the phase term $e^{\frac{ikr^2}{2z}}$.

B2.2 Debye approximation –non-identical transducers

The Debye solution can also be used to consider the case when the transducers are not matched, so $\frac{a_1}{F_1} \neq \frac{a_2}{F_2}$. If the transmitter and receiver have a different geometry but the transducers are still separated by the sum of the two radii of curvature, then the substitution $X = \frac{ar}{F}$ has to be modified to account for the different geometry. If we define $\beta = \frac{F_1 a_2}{F_2 a_1}$ then the substitutions $X = \frac{a_1 r}{F_1}$ and $\beta X = \frac{a_2 r}{F_2}$ can be used to give

$$p_{rex}(F_1+F_2,R) = -2P_0 \frac{a_1}{a_2} e^{ik(F_1+F_2)} \int_{X=0}^{X=R} \frac{J_1(X)J_1(\beta X)}{X} dX. \qquad \text{(B10)}$$

The integral $\int_{X=0}^{X=} \frac{J_1(X)J_1(\beta)}{X} dX$ has a value of $\beta/2$ for $0 < \beta < 1$ and $1/2\beta$ for $\beta > 1$. An example is shown in Figure B3.

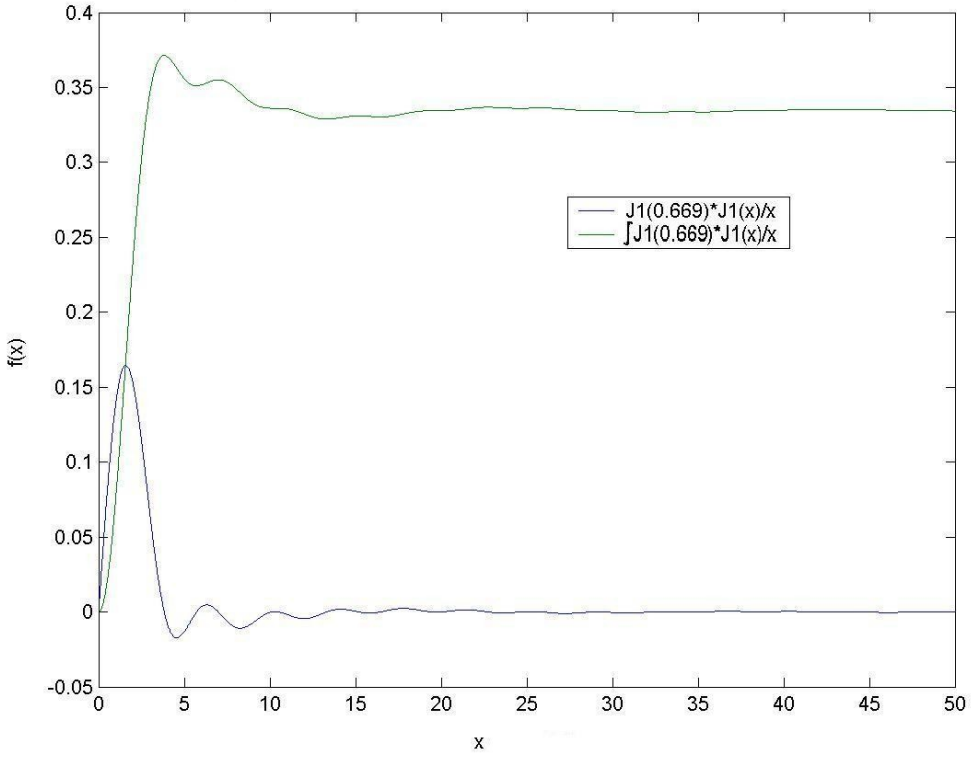

Figure B3. Plot of the functions $\frac{J_1(X)J_1(\beta)}{X}$ and $\int \frac{J_1(X)J_1(\beta)}{X}$ used in the calculation of the receiver response for coaxially aligned transducers with β = 0.669 (X is dimensionless)

It is to be noted that the received signal is less than that for matched transducers, however the received signal approaches the value for infinite R faster than for identical transducers. This comparison between identical and non- identical transducers is illustrated in Figure A4 which shows the radial integration limit R_{lim} for selected ratios of $p_{\text{rec}}(z_T, R) / p_{\text{rec}}(z_T)$, which has no phase variation. Again this result neglects the phase term $e^{\frac{ikr^2}{2z}}$.

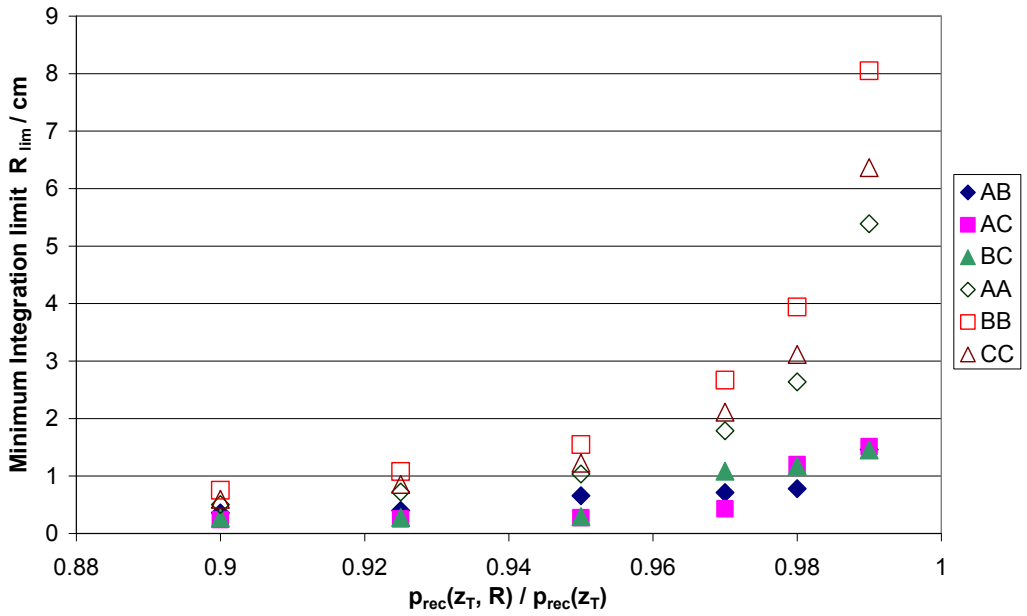

Figure B4. Plot showing the minimum integration limit R_{lim} required for selected ratios of p_{rec} (z_T, R) / p_{rec} (z_T) for matched transducer pairs (AA, BB, CC) and transducer pairs of different geometry (AB, AC and BC) using the Debye approximation (Equation 3)

B2.3 Full expression for identical and non-identical transducers

Figures B5 and B6 show the effect of using the full Lucas and Muir (1982) expression (Equation B4), including the additional transverse phase term, for identical and non-identical transducers respectively. These figures clearly shows that the phase term decreases the minimum integration limit required for the same specified ratio of $|p_{rec}(z_T, R)| / |p_{rec}(z_T)|$. However, the phase term also introduces the possibility that the phase of $p_{rec}(z_T, R) / p_{rec}(z_T)$ is non-zero. Figure B7 shows minimum integration limits required for specified differences in phase between $p_{rec}(z_T, R)$ and $p_{rec}(z_T)$ for paired and unpaired transducers.

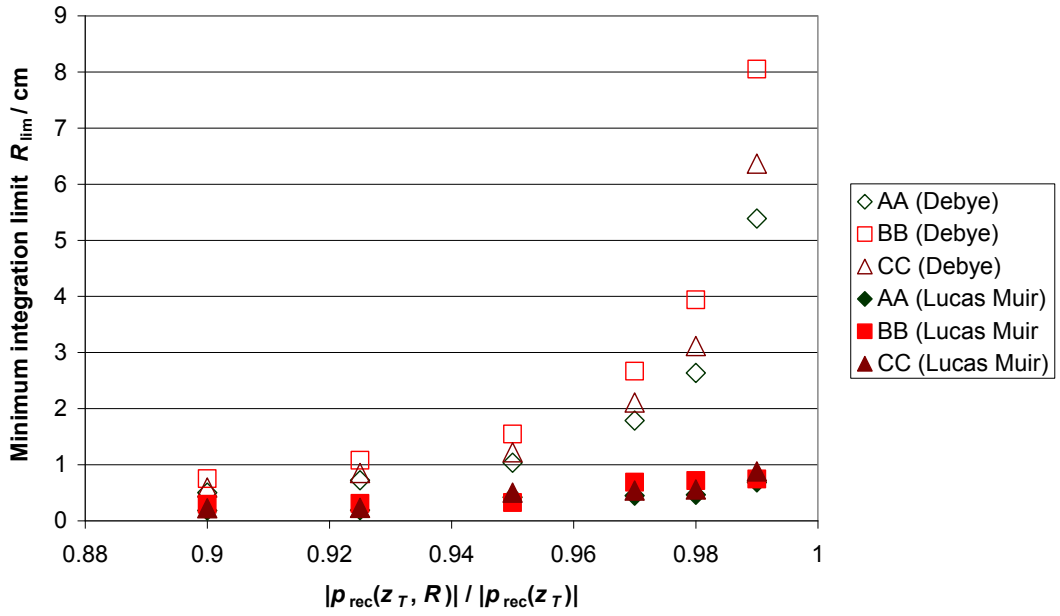

Figure B5. Plot showing the minimum integration limit R_{lim} required for selected ratios of $|p_{rec}(z_T, R)| / |p_{rec}(z_T)|$ for matched transducer pairs (AA, BB, CC) obtained using the Debye approximation (unfilled points, Equation 3) and Lucas and Muir solution (filled points, Equation 4)

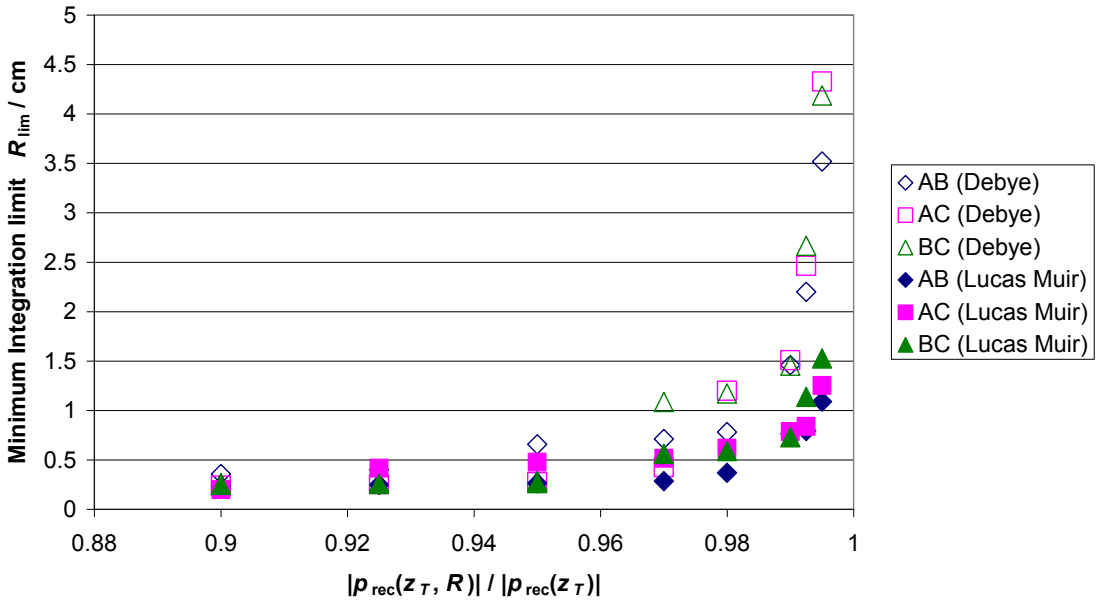

Figure B6. Plot showing the minimum integration limit R_{lim} required for selected ratios of $|p_{rec}(z_T, R)| / |p_{rec}(z_T)|$ for transducer pairs of different geometry (AB, AC, BC) obtained using the Debye approximation (unfilled points, Equation 3) and Lucas and Muir solution (filled points, Equation 4)

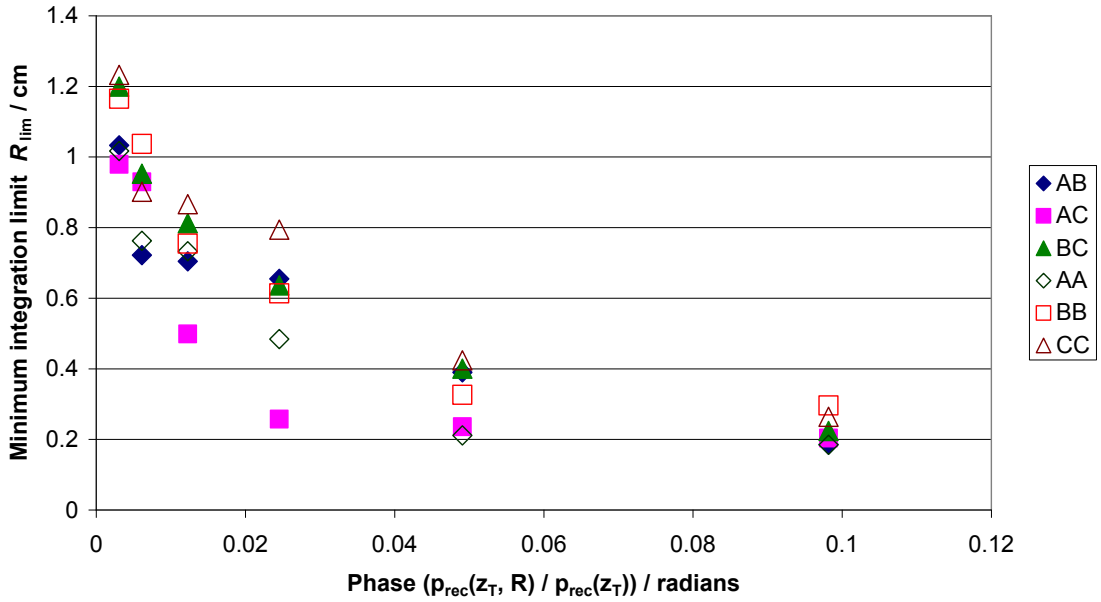

Figure B7. Plot showing the minimum integration limit R_{lim} required for selected phase differences between p_{rec} (z_T, R) and p_{rec} (z_T) for transducer pairs of different geometry (AB, AC, BC) and identical geometry (AA, BB and CC) obtained using the Lucas and Muir solution (filled points, Equation 4)

B2.4 Location of diffraction peak

To reduce the effect of diffraction error on measurements the transducers should be located at a position of diffraction maxima or minima (Bamber, 2004a). This ensures that the diffraction changes caused by the introduction of a medium of different sound speed are minimized when a sample is placed between the transducers. For coaxially aligned strongly focused transducers this has conventionally been accepted as requiring a transducer separation of the sum of the geometric foci (Bamber, 2004a, Penttinen and Luukkala, 1977), as we have considered so far. For weakly focused transducers, however, the location of the diffraction peak is not at a transducers separation of the sum of the geometric foci since the geometric and acoustic foci do not coincide for the individual transducers. Using the model given in Equation B4 the response for different separations can be calculated; example results are shown in Figure B8 for how the integrated response varies with separation for transducers A and C. The sum of the geometric foci is shown as a dotted vertical line on the figure. The transducer separation has to be reduced from the sum of the geometric foci to reach the position of the diffraction maximum. This agrees with measurements of the receiver

output obtained using the coaxial transducers A and C, shown in Figure B9. The sum of geometric foci is indicated at 21 cm and the sum of acoustic foci at 14.5 cm. This demonstrates that the position of the diffraction peak occurs at a positioned between the sum of acoustic foci and the sum of the geometric foci. This effect was seen for all three transducer pairings.

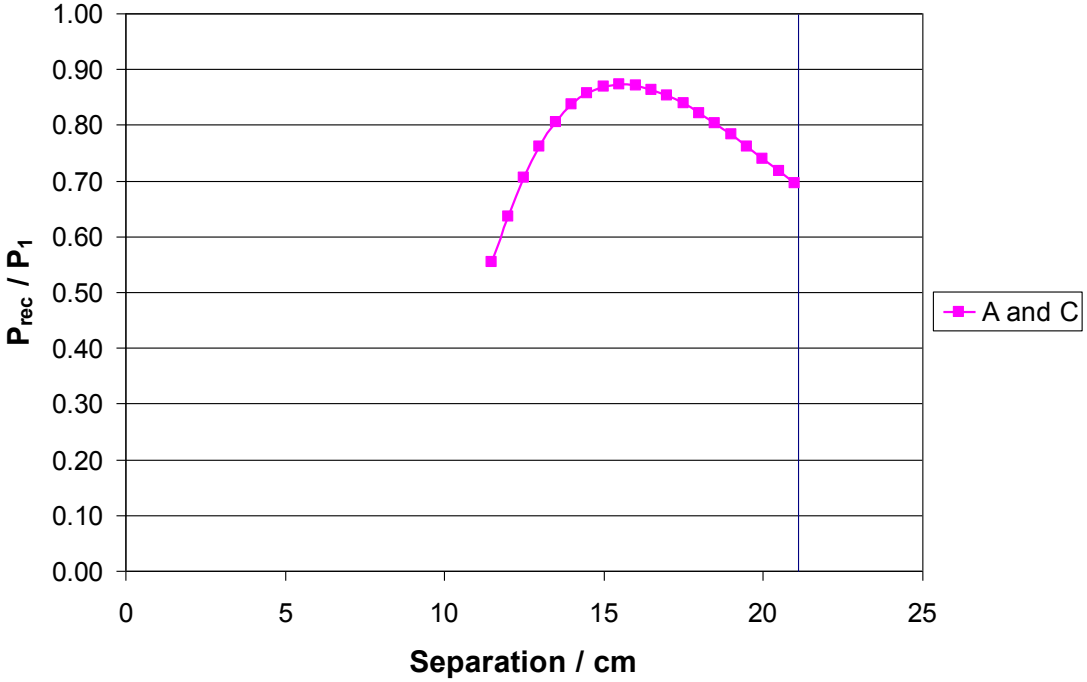

Figure B8. Example of the modelled variation in the received response p_{rec}, normalized to the pressure produced by the transmitting transducer p_1, as a function of the separation between the transducers A and C. The sum of geometric foci is shown at 21 cm separation.

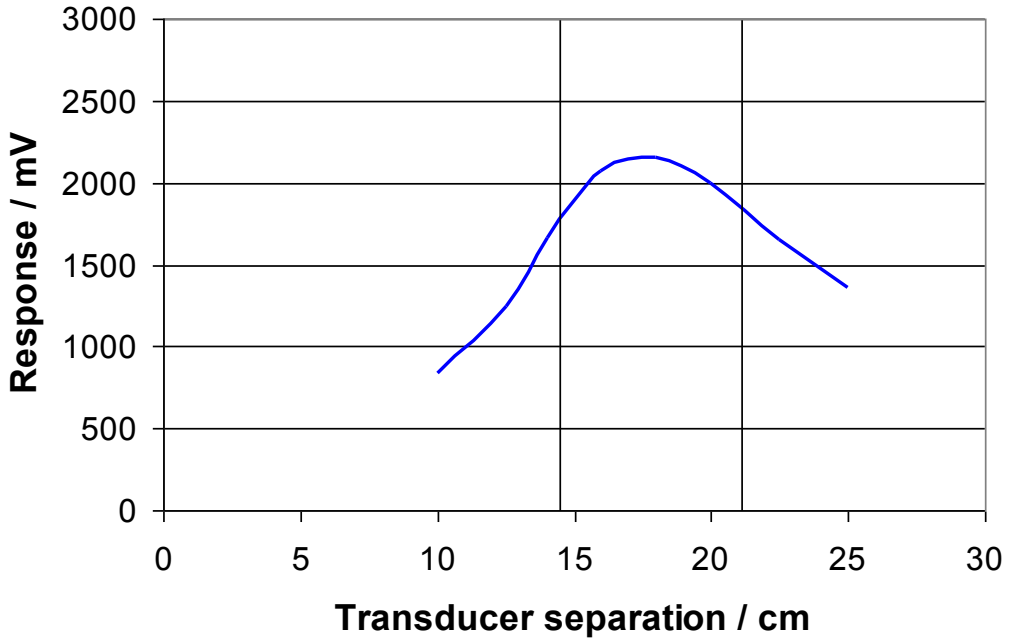

Figure B9. Example of the measured variation in the received response p_{rec}, normalized to the pressure produced by the transmitting transducer, as a function of separation between the transducers A and C. The sum of geometric foci is shown at 21cm and the sum of acoustic foci shown at 14.5cm

B2.5 Effect of choice of integration plane

One of the properties of Equation B1 is that for integration to infinity the average pressure $p_{rec}(z_T)$ (and hence receiver output) is not affected by the integration plane that is chosen. A test of the model was to perform the integration over a number of planes by varying z_1 and z_2 for a fixed separation z_T. Figure B10 shows how magnitude of $p_{rec}(z_T, R)$ varies with R for transducers A and C for different distances of the integration plane from the receiver. When the integration limit is greater than approximately 2.0 cm, the magnitude of $p_{rec}(z_T, R)$ is the same for all integration planes.

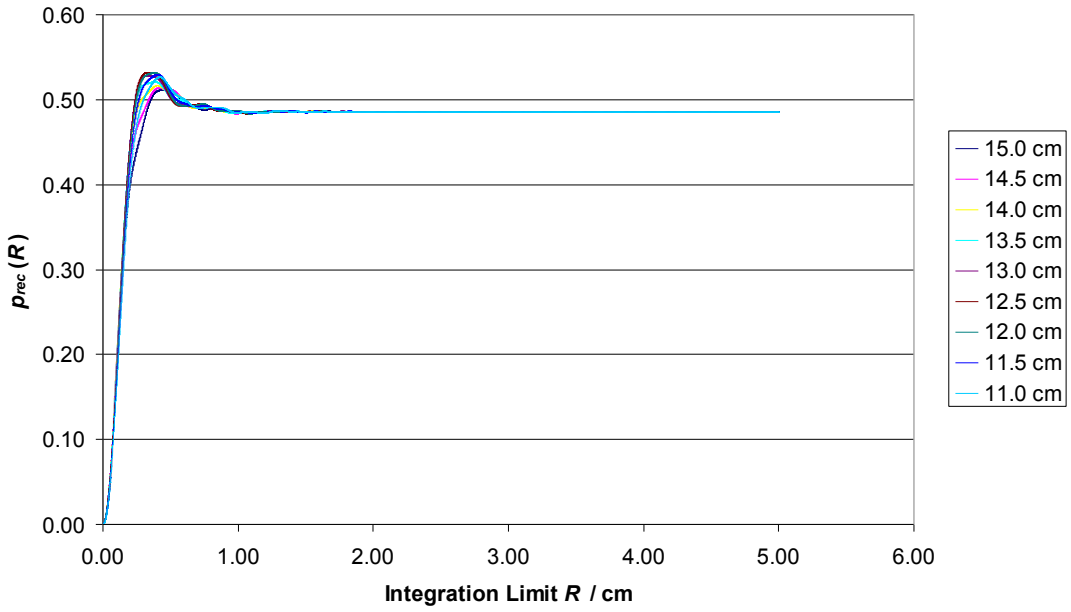

Figure B10. Plot showing the variation in received pressure $p_{rec}(R)$ with integration limit R for different distances of integration plane from the receiving transducer for transducer pairing AC

Figure B11 also demonstrates that there are differences between the integration planes when the integration is performed over a restricted part of the plane. It shows the differences between integration planes for transducers A and C for selected ratios of $|p_{rec}(z_T, R)| / |p_{rec}(z_T)|$. This demonstrates that if $p_{rec}(z_T, R)$ and the infinite value $p_{rec}(z_T)$ differ greatly the required integration limit is relatively small and most integration planes in the range displayed will provide similar results. However, if a more accurate estimation of the value of $p_{rec}(z_T)$ is required, then R_{lim} increases significantly. Across the range of ratios of $|p_{rec}(z_T, R)| / |p_{rec}(z_T)|$ calculated there is no choice of integration plane which will consistently result in a small integration limit R_{lim}. Similar results (not shown) are obtained for the phase difference between $p_{rec}(z_T, R)$ and $p_{rec}(z_T)$.

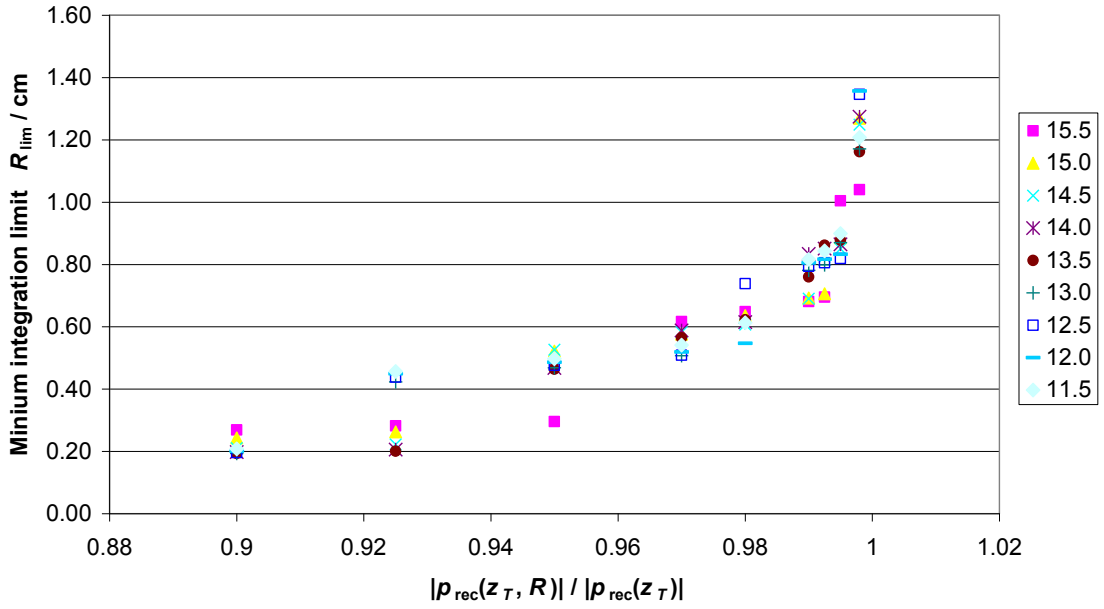

Figure B11. Example of the variation in the minimum integration limit R_{lim} required for selected ratios of $|p_{rec}(z_T, R)| / |p_{rec}(z_T)|$ for different distances of the integration plane from the receiving transducer for transducer pairing AC

Figure B12 demonstrates the effect of the integration radius on the solution at the diffraction peak when the Lucas and Muir Equation, with the additional phase term, is used in the model. It should be noted that there are no longer significant differences between using matched or unmatched transducers. For different ratios of $|p_{rec}(z_T, R)| / |p_{rec}(z_T)|$ there are different transducer combinations which would give the smallest value of R_{lim}. For each transducer separation, the choice of integration plane affects the value of R_{lim}, and the displayed standard deviations quantify the spread obtained if the integration plane is varied over a 4 cm range. Figure B13 shows similar data for the phase difference between the restricted and infinite integration.

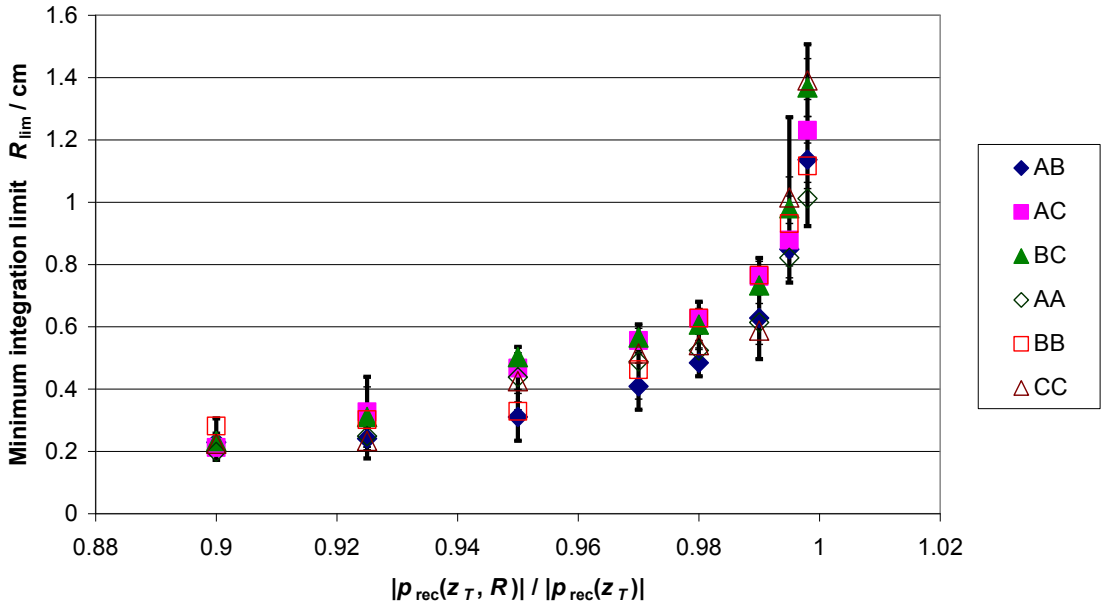

Figure B12. Plot showing the minimum integration limit R_{lim} required for selected ratios of $|p_{rec}(z_T, R)| / |p_{rec}(z_T)|$ for matched transducer pairs (AA, BB, CC) and transducers of different geometry (AB, AC, BC) at the position of diffraction loss peak, calculated using the Lucas and Muir result (Equation 4) for a focused field

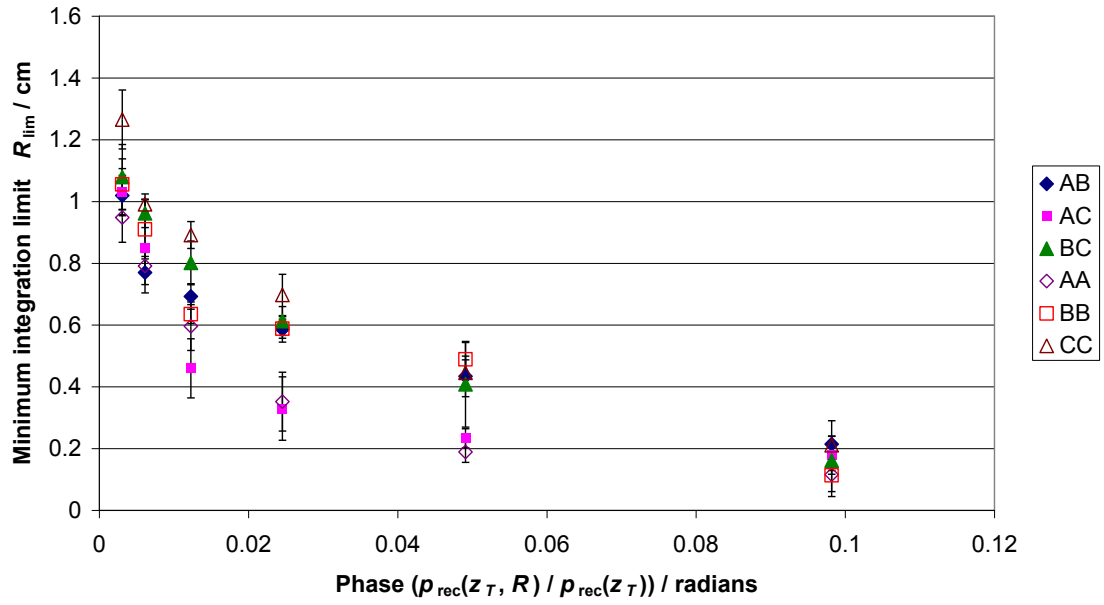

Figure B13. Plot showing the minimum integration limit R_{lim} required for selected phase differences between $p_{rec}(z_T, R)$ and $p_{rec}(z_T)$ for matched transducer pairs (AA, BB, CC) and transducers of different geometry (AB, AC, BC) at the position of diffraction loss peak, calculated using the Lucas and Muir result (Equation 4) for a focused field

B3. Discussion

The results obtained highlight the fact that the Debye solution used by Gavrilov et al. (1988) is an approximation obtained in the geometric optics limit. It agrees with fuller formulations in terms of the focal plane amplitudes but not phases. The results presented here show that is important to include the additional transverse phase term $e^{\frac{ikr^2}{2z}}$ in applications such as this, as the calculation of the receiver response involves an integration of the two transducer complex sound pressure distribution functions over the radial coordinate r. If the phase term is omitted then the calculation, and therefore model, gives inaccurate results. Analysis of the two solutions used in this paper, and comparison with other solutions available, indicates that the phase term reduces the size of the integration limit R_{lim} required to ensure an accurate estimation of p_{rec} by a restricted integration. However, is does introduce a phase difference between the restricted integral $p_{\text{rec}}(z_T, R)$ and the infinite integral $p_{\text{rec}}(z_T)$. However, the phase differences are small and should not significantly affect results (Figure B7, B13).

The difference between the integration results for a limited radius and infinite radius gives an indication of the error that is likely to be obtained by using a coaxial circular sample of a given radius in immersion measurements of acoustic attenuation. Essentially the difference gives an estimate of the likely diffraction magnitude. The results obtained here can be used to estimate the minimum size of sample required to measure a given attenuation to a given precision.

The choice of transducers is affected by the inclusion of the phase term in the full model. Without the transverse phase term included in the model, Figures B2, B3 and B4 imply that geometrically different transducers will have advantages in terms of reducing the required integration limit R_{lim} when compared to geometrically identical transducers. The correct analysis, including the phase term, not only reduces the required integration limit R_{lim} (see Figures B5 and B6) but also removes the significant differences between using identical and geometrically different transducers (Figure A12).

The criteria quoted in the literature (Bamber, 2004a; Penttinen & Luukkala, 1977) to minimize errors in measurement due to diffraction losses is to place opposed

transducers at the diffraction peak. Both the theoretical model and measurements of specific transducers indicate that for the transducers used in this paper, the separation between the transducers should be reduced from the position of the sum of the geometric foci (Figures B8 and B9). This is due to the transducers being weakly focused as opposed to the strongly focused transducers used in the literature (Penttinen & Luukkala, 1977), where the geometric and acoustic foci would coincide. Placing weakly focused transducers at the sum of their geometric foci would tend to lead to increased diffraction errors.

When using coaxially aligned spherically focused transducers to measure ultrasonic attenuation properties of samples the measurement system needs to be designed to minimize any uncertainties in the measurement of the attenuation of the sample. The analysis presented in this paper for the average receiver pressure $p_{\text{rec}}(z_T, R)$ shows that if R is small then $p_{\text{rec}}(z_T, R)$ is not an accurate estimate of $p_{\text{rec}}(z_T)$. To provide an accurate estimate of p_{rec} (small error) the integration must be performed over a large distance ($R > R_{\text{lim}}$).

When measuring ultrasonic attenuation, it has been shown (Challis et. al, 2005; Kalashnikov et. al, 2005) from analysis of noise on signals, that the optimum attenuation for measurement is approximately 1 neper (8.68dB), with a useful range of 0.1 Np to 5 Np (0.9dB to 43dB). The errors introduced by sample size effects as calculated in this paper may have large effects on the measurement of attenuation. Therefore relatively large samples are required, especially for low attenuating samples, to ensure that sample size effects do not contribute a significant error to the sample attenuation measurement. For the transducers used in this paper sample sizes of approximately 0.8cm radius are required to ensure the ratio of $|p_{\text{rec}}(z_T, R)| / |p_{\text{rec}}(z_T)|$ is greater than 0.98 (Figure B12). The actual effect this will have on the estimation of sample transmission is dependent on the transmission properties of the sample itself (see Equation B7). The phase difference between $p_{\text{rec}}(z_T, R)$ and $p_{\text{rec}}(z_T)$ will be negligible with samples of this size.

When the difference between the estimated and actual value of the average receiver pressure is small (ratio $|p_{\text{rec}}(z_T, R)| / |p_{\text{rec}}(z_T)|$ is close to one) there does not seem to be an obvious choice of integration plane to minimize the required sample size (Figure B11). The choice of integration plane is analogous to the physical positioning

of the sample between the two transducers, indicating that for relatively large samples, the axial positioning of the sample is not critical.

B4. Conclusions

Two computation models have been used to calculate the average pressure on the receiver of a pair of coaxial focused transducers. Results for three specific ultrasonic transducers operating at 3.5 MHz have been utilized to analyze the effects of sample size and geometry on the measurement of ultrasonic properties.

A potential source of error in attenuation measurements due to finite sample size has been discussed. This source may introduce significant errors into the measurement of attenuation and should be considered when designing attenuation measurement experiments. For the transducers used in this paper sample sizes of approximately 0.8cm radius are required to ensure an ratio $|p_{rec}(z_T, R)| / |p_{rec}(z_T)|$ is greater than 0.98. This will limit the errors due to sample size effects introduced into attenuation measurements.

Both the theoretical model and measurements of specific transducers indicate that for weakly focused transducers the optimum separation between the transducers should be reduced from the sum of the geometric focal lengths in order to minimise diffraction loss correction.

Appendix C. Matlab code used for data analysis

A number of Matlab codes have been written to aid in the data and image analysis throughout this thesis.

C1. Analysis of text output from oscilloscopes to calculate FFT data of through-transmission measurements

```
function [out] = ni_fft(filename, foldername, T1, T2, n)
%filename is start of the filename under which the stuff is saved.  Foldername is
% the folder in which it is located, T1 is start position, T2 is finish, n is number
% of spaces to do FFT over, usually (T2-T1)/10.  The programme assumes digitization
% frequency is 100MHz.
cd (foldername);
%set timebase
tint = [T1:(T2-T1)/n:T2];
%read in filenames of data and trigger files
filename = [filename,'*.txt'];
s = dir(filename);
s2 = dir('trigger*.txt');
%set up empty matricies
amp = [];
ang = [];
fmax = [];
Posmax = [];
TriggerTime = [];
%read in data
for i = 1:length(s)
   DATA = textread(s(i).name,  '%f', 'headerlines', 1, 'delimiter', '\t');
   Time = (0:10:(length(DATA)-1)*10)';
%perform spline smoothing of data
   intDATAspl = interp1(Time, DATA, tint, 'spline');
   intDATAspl(length(intDATAspl))=[];
   fintDATAspl = fftshift(fft(intDATAspl*10));
%Calculate data
   [C,I] = max(fintDATAspl);
   amp = [amp, abs(fintDATAspl(I))];
   ang = [ang, -angle(fintDATAspl(I))];
   fmax = [fmax, (500*n/(T2-T1))-((I-1)*1000/(T2-T1))];
   [c,i] = max(DATA(1:125));
   Posmax = [Posmax, i];
end
%Calculate position of trigger pulse
for i = 1:length(s2)
   [TrigTime, TrigLevel] = textread(s2(i).name,  '%f %f', 'headerlines', 1, 'delimiter', '\t');
   y = find (0.05<TrigLevel);
   if length (y) >0;
      TriggerTime = [TriggerTime, TrigTime(y(1))];
   else
      TriggerTime = [TriggerTime, 0];
   end
```

```
end

%Save data to file
out = [amp' ang' fmax' Posmax'];
cd('..');
textfile = [foldername,'out2.csv'];

fid = fopen(textfile,'w');
fprintf(fid,'filename,amp,ang,fmax,MaxPos\r');
for i = 1:length(s)
    fprintf(fid, s(i).name);
    fprintf(fid,',');
    fprintf(fid,'%5.5d ,',out(i,1));
    fprintf(fid,'%5.5d ,',out(i,2));
    fprintf(fid,'%3.2d ,',out(i,3));
    fprintf(fid,'%3.2d ,',out(i,4));
    fprintf(fid, s2(i).name);
    fprintf(fid,',');
    fprintf(fid,'%6.5d ,',TriggerTime(i));
    fprintf(fid,'=C');
    fprintf(fid, '%g', i+1);
    fprintf(fid, '/2/PI()/D');
    fprintf(fid, '%g', i+1);
    fprintf(fid, '/1000000 ,');
    fprintf(fid, '=H');
    fprintf(fid, '%g', i+1);
    fprintf(fid, '-G');
    fprintf(fid, '%g', i+1);
    fprintf(fid,'\r');
end
%Automatically write data to calculate in Excel spreadsheet
fprintf(fid,'Average,');
fprintf(fid,'=average(b2:b');
fprintf(fid,'%g',length(s)+1);
fprintf(fid,'),');
fprintf(fid,'=average(c2:c');
fprintf(fid,'%g',length(s)+1);
fprintf(fid,'),');
fprintf(fid,'=average(d2:d');
fprintf(fid,'%g',length(s)+1);
fprintf(fid,'),');
fprintf(fid,'=average(e2:e');
fprintf(fid,'%g',length(s)+1);
fprintf(fid,'),,,,');
fprintf(fid,'=average(i2:i');
fprintf(fid,'%g',length(s)+1);
fprintf(fid,'),');
fprintf(fid,'\r');
fprintf(fid,'Standard Deviation,');
fprintf(fid,'=stdev(b2:b');
fprintf(fid,'%g',length(s)+1);
fprintf(fid,'),');
fprintf(fid,'=stdev(c2:c');
fprintf(fid,'%g',length(s)+1);
fprintf(fid,'),');
fprintf(fid,'=stdev(d2:d');
fprintf(fid,'%g',length(s)+1);
fprintf(fid,'),');
```

```
fprintf(fid,'=stdev(e2:e');
fprintf(fid,'%g',length(s)+1);
fprintf(fid,'),,,,');
fprintf(fid,'=stdev(i2:i');
fprintf(fid,'%g',length(s)+1);
fprintf(fid,'),');
fprintf(fid,'\r');
fprintf(fid,'Min,');
fprintf(fid,'=min(b2:b');
fprintf(fid,'%g',length(s)+1);
fprintf(fid,'),');
fprintf(fid,'=min(c2:c');
fprintf(fid,'%g',length(s)+1);
fprintf(fid,'),');
fprintf(fid,'=min(d2:d');
fprintf(fid,'%g',length(s)+1);
fprintf(fid,'),');
fprintf(fid,'=min(e2:e');
fprintf(fid,'%g',length(s)+1);
fprintf(fid,'),,,,');
fprintf(fid,'=min(i2:i');
fprintf(fid,'%g',length(s)+1);
fprintf(fid,'),');
fprintf(fid,'\r');
fprintf(fid,'Max,');
fprintf(fid,'=max(b2:b');
fprintf(fid,'%g',length(s)+1);
fprintf(fid,'),');
fprintf(fid,'=max(c2:c');
fprintf(fid,'%g',length(s)+1);
fprintf(fid,'),');
fprintf(fid,'=max(d2:d');
fprintf(fid,'%g',length(s)+1);
fprintf(fid,'),');
fprintf(fid,'=max(e2:e');
fprintf(fid,'%g',length(s)+1);
fprintf(fid,'),,,,');
fprintf(fid,'=max(i2:i');
fprintf(fid,'%g',length(s)+1);
fprintf(fid,'),');
fprintf(fid,'\r');fclose(fid);
textfile = [foldername,'summary2.txt'];
fid = fopen(textfile,'w');
fprintf(fid,'\t amp\t ang\t fmax\r MaxPos\r');
fprintf(fid,'Average\t');
fprintf(fid,'%4.4d \t', mean(out(:,1)));
fprintf(fid,'%4.4d \t',mean(out(:,2)));
fprintf(fid,'\t %3.2d \t', mean(out(:,4)));
fprintf(fid,'\r');
fprintf(fid,'Standard Deviation\t');
fprintf(fid,'%4.4d \t', std(out(:,1)));
fprintf(fid,'%4.4d \t',std(out(:,2)));
fprintf(fid,'\r');
fprintf(fid,'Difference\t \t \t');
fprintf(fid,'%3.2d \t',max(out(:,3))-min(out(:,3)));
fprintf(fid,'\r');
fclose(fid);
```

C2. Analysis of text output from oscilloscopes to calculate FFT data of pulse-echo measurements

```
function [out] = AP_MAGIC(filename, L, Tstart, Gain)
%Prepare a matrix
Data = zeros([5000,1]);
%read in data
Data(1:L,1)= textread(filename,  '%f', L, 'headerlines', Tstart+1, 'delimiter', '\t');
% correct for gain setting
Data = Data/10^((Gain-22)/20);
%Filter (smooth) data
Wp = .03; Ws = .015;
Rp = 0.01; Rs = 50;
%[n,Wn] = cheb1ord(Wp,Ws,Rp,Rs);
%[b,a] = cheby1(n,Rp,Wn,'high');
b = [0.76298855416044 -6.10390843328353 21.36367951649235 -42.72735903298469
53.40919879123086 -42.72735903298469 21.36367951649235 -6.10390843328353
0.76298855416044];
a = [1.00000000000000 -7.46133996201130 24.37397611047766 -45.53060622787615
53.19342279833839 -39.79996754731171 18.62394531330514 -4.98312407864198
0.58369362308481];
Data = filter(b,a,Data);
Wp = .1; Ws = .15;
Rp = 0.01; Rs = 50;
%[n,Wn] = cheb1ord(Wp,Ws,Rp,Rs);
%[b,a] = cheby1(n,Rp,Wn);
b = [1.0e-007*0.00258901707202 1.0e-007*0.02589017072016 1.0e-007*0.11650576824073 1.0e-
007*0.31068204864196 1.0e-007*0.54369358512342 1.0e-007*0.65243230214811 1.0e-
007*0.54369358512342 1.0e-007*0.31068204864196 1.0e-007*0.11650576824073 1.0e-
007*0.02589017072016 1.0e-007*0.00258901707202];
a = [1.000000000000 -9.000823400587 36.704814087252 -89.285443487198 143.447967382250 -
159.028253087983 123.185495144657 -65.827701178815 23.222424177719 -4.883254174948
0.464774803074];
Data = filter(b,a,Data);

%Obtain FFT
fData = (fft(Data));

fData(1001:5000,:) = [];

%Plot FFT
freq =  (0:0.02:19.98)';
subplot (2,1,1); plot (freq, abs(fData));
axis([0 10 0 10]);
axis 'auto y';
subplot(2,1,2); plot (Data);
axis([0 2*L 0 10]);
axis 'auto y';
out = [freq abs(fData) angle(fData)];

%Write data to file

[Amplitude, FmaxPos] = max(abs(fData));
Fmax = freq(FmaxPos,1);
Phase = angle(fData(FmaxPos));
Max = max(Data);
Min = min(Data);
```

```
PP = Max-Min;
RMS = norm(Data(1:L)/sqrt(L));
out = [str2double(filename(5:8)), Fmax, Amplitude, Phase, Max, Min, PP, RMS];
```

C3. Data collection of pixel values from image of three thread phantom

```
function [OutPut] = imageanalysis_v6(Pathname,ImageA,X_1,Y_1,X_2,Y_2,X_3,Y_3);
FnameA=ImageA;
close all;
% Read in image
[X,map] = imread([Pathname FnameA]);

%   positions for figures
   bdwidth = 5;
   topbdwidth = 30;
% Ensure root units are pixels and get the size of
% the screen:
   set(0,'Units','pixels')
   scnsize = get(0,'ScreenSize');
%plot figure
    figure('Position',[scnsize(3)/8 scnsize(4)/8 6*scnsize(3)/8 6*scnsize(4)/8])

   image(X(:,:,:));

 icount=0;
         icount=icount+1;
%Take seed position for first thread.
         ycurrent=Y_1;
         xcurrent=X_1;
         temp=0;
         temparea=0;
 %search over a 31 by 21 pixel grid
         for y2=-15:15;
            for x2=-10:10;
               y_=ycurrent+y2;
               x_=xcurrent+x2;
               if X(y_,x_,1) > temp;   %if pixel value is greater than current max store value and
coordinates
                  temp= X(y_,x_,1);
                  xpeak(icount)=x_;
                  ypeak(icount)=y_;
                  zpeak(icount)=temp;
               end

 %calculate average 61 pixel value for region  (5,9,11,11,11,9,5).
               ta=0;
               ta1=0;
               ta2=0;
               ta3=0;
               for kd=-2:2;
                  ta1=(double(X(y_+3,x_+kd,1))+double(X(y_-3,x_+kd,1)));
               end
               for kd=-4:4;
```

```
                ta2=(double(X(y_+2,x_+kd,1))+double(X(y_-2,x_+kd,1)));
            end
            for kd=-5:5;
                ta3=(double(X(y_+1,x_+kd,1))+double(X(y_,x_+kd,1))+double(X(y_-1,x_+kd,1)));
            end
            ta=(ta1+ta2+ta3)/61;
            if ta > temparea; %if average pixel value is greater than current max store value and
coordinates
                temparea= ta;
                xpeakarea(icount)=x_;
                ypeakarea(icount)=y_;
                zpeakarea(icount)=temparea;
            end
        end
    end
 %repeat above for 2nd thread
    icount=icount+1;
    ycurrent=Y_2;
    xcurrent=X_2;
    temp=0;
    temparea=0;

    for y2=-15:15;
        for x2=-10:10;
            y_=ycurrent+y2;
            x_=xcurrent+x2;
            if X(y_,x_,1) > temp;
                temp= X(y_,x_,1);
                xpeak(icount)=x_;
                ypeak(icount)=y_;
                zpeak(icount)=temp;
            end

            ta=0;
            ta1=0;
            ta2=0;
            ta3=0;
            for kd=-2:2;
                ta1=(double(X(y_+3,x_+kd,1))+double(X(y_-3,x_+kd,1)));
            end
            for kd=-4:4;
                ta2=(double(X(y_+2,x_+kd,1))+double(X(y_-2,x_+kd,1)));
            end
            for kd=-5:5;
                ta3=(double(X(y_+1,x_+kd,1))+double(X(y_,x_+kd,1))+double(X(y_-1,x_+kd,1)));
            end
            ta=(ta1+ta2+ta3)/61;
            if ta > temparea;
                temparea= ta;
                xpeakarea(icount)=x_;
                ypeakarea(icount)=y_;
                zpeakarea(icount)=temparea;
            end
        end
    end
%and for third thread
    icount=icount+1;
    ycurrent=Y_3;
```

```
        xcurrent=X_3;
        temp=0;
        temparea=0;
        for y2=-10:10;
           for x2=-10:10;
              y_=ycurrent+y2;
              x_=xcurrent+x2;
              if X(y_,x_,1) > temp;
                 temp= X(y_,x_,1);
                 xpeak(icount)=x_;
                 ypeak(icount)=y_;
                 zpeak(icount)=temp;
              end

              ta=0;
              ta1=0;
              ta2=0;
              ta3=0;
              for kd=-2:2;
                 ta1=(double(X(y_+3,x_+kd,1))+double(X(y_-3,x_+kd,1)));
              end
              for kd=-4:4;
                 ta2=(double(X(y_+2,x_+kd,1))+double(X(y_-2,x_+kd,1)));
              end
              for kd=-5:5;
                 ta3=(double(X(y_+1,x_+kd,1))+double(X(y_,x_+kd,1))+double(X(y_-1,x_+kd,1)));
              end
              ta=(ta1+ta2+ta3)/61;
              if ta > temparea;
                 temparea= ta;
                 xpeakarea(icount)=x_;
                 ypeakarea(icount)=y_;
                 zpeakarea(icount)=temparea;
              end
           end
        end
        %end
        %end

  %plot location of maximum pixel value
  figure('Position',[scnsize(3)/8 scnsize(4)/8 6*scnsize(3)/8 6*scnsize(4)/8])
  image(X(:,:,:));
  hold on
  plot( xpeak,ypeak,'or');

  hold off
  [pathstr,name,ext,versn] = fileparts(ImageA);

  %Produce output for further analysis
  OutPut = [double(zpeak); xpeak; ypeak; zpeakarea; xpeakarea; ypeakarea];

  SaveFile = [Pathname,'Analysed',name,'10by10vA61.csv'];

fid = fopen(SaveFile,'w');
fprintf(fid,'Position ,');
for i = 1:3
   fprintf(fid,'%i ,',i);
end
```

```
fprintf(fid,'\r');
fprintf(fid,'ZPeak ,');
fprintf(fid,'%i ,',(OutPut(1,:)));
fprintf(fid,'\r');
fprintf(fid,'XPeak ,');
fprintf(fid,'%i ,',(OutPut(2,:)));
fprintf(fid,'\r');
fprintf(fid,'YPeak ,');
fprintf(fid,'%i ,',(OutPut(3,:)));
fprintf(fid,'\r');
fprintf(fid,'ZPeakArea ,');
fprintf(fid,'%5.2f ,',(OutPut(4,:)));
fprintf(fid,'\r');
fprintf(fid,'XPeakArea ,');
fprintf(fid,'%i ,',(OutPut(5,:)));
fprintf(fid,'\r');
fprintf(fid,'YPeakArea ,');
fprintf(fid,'%i ,',(OutPut(6,:)));
fprintf(fid,'\r');

fclose(fid);
```

C4. Data collection of pixel values from image of full thread phantom

```
function [OutPut] = imageanalysis_v4(Pathname,ImageA);

FnameA=ImageA;

close all;

% read in image data

[X,map] = imread([Pathname FnameA]);

%   positions for figures
   bdwidth = 5;
   topbdwidth = 30;
% Ensure root units are pixels and get the size of
% the screen:
   set(0,'Units','pixels')
   scnsize = get(0,'ScreenSize');

    figure('Position',[scnsize(3)/8 scnsize(4)/8 6*scnsize(3)/8 6*scnsize(4)/8])

%    figure(1);
   image(X(:,:,:));
%
%       user_entry = input('Enter positon of bottom left thread');
   [x1,y1] = ginput(1);

%    user_entry = input('Enter positon of top right thread');
   [x2,y2] = ginput(1);
```

```
   hold on

%Calculate distaces between threads

   xstep=round((x2-x1)/4.25);
   ystep=round((y2-y1)/3);

   x1=round(x1);
   y1=round(y1);

% Plot seed positions on image

   for i=1:4;
      for j=1:6;

         ycurrent=y1 +(i-1)*ystep;
         xcurrent=x1+(j-1)*xstep- round((i-1)*xstep/4);
         plot( xcurrent,ycurrent,'xr');

      end
   end

 icount=0;

 % For each seed position find the maximum pixel value

 for i=1:4;
      for j=1:6;
         icount=icount+1;
         ycurrent=y1 +(i-1)*ystep;
         xcurrent=x1+(j-1)*xstep- round((i-1)*xstep/4);
         temp=0;
         temparea=0;
         for y2=-10:10;
            for x2=-10:10;
               if X(ycurrent+y2,xcurrent+x2,1) > temp;
                  temp= X(ycurrent+y2,xcurrent+x2,1);
                  xpeak(icount)=xcurrent+x2;
                  ypeak(icount)=ycurrent+y2;
                  zpeak(icount)=temp;
               end

 %calculate average 61 pixel value for region  (5,9,11,11,11,9,5).

                  ta=0;
                  ta1=0;
                  ta2=0;
                  ta3=0;
                  for kd=-2:2;
                     ta1=(double(X(y_+3,x_+kd,1))+double(X(y_-3,x_+kd,1)));
                  end
                  for kd=-4:4;
                     ta2=(double(X(y_+2,x_+kd,1))+double(X(y_-2,x_+kd,1)));
                  end
                  for kd=-5:5;
                     ta3=(double(X(y_+1,x_+kd,1))+double(X(y_,x_+kd,1))+double(X(y_-1,x_+kd,1)));
                  end
                  ta=(ta1+ta2+ta3)/61;
```

```
                if ta > temparea;
                    temparea= ta;
                    xpeakarea(icount)=x_;
                    ypeakarea(icount)=y_;
                    zpeakarea(icount)=temparea;
                end
            end
        end
    end
end

figure('Position',[scnsize(3)/8 scnsize(4)/8 6*scnsize(3)/8 6*scnsize(4)/8])
image(X(:,:,:));
hold on
plot( xpeak,ypeak,'or');

hold off

OutPut = [double(zpeak); xpeak; ypeak; zpeakarea; xpeakarea; ypeakarea];

[pathstr,name,ext,versn] = fileparts(ImageA);

SaveFile = [Pathname,'Analysed',name,'Area.csv'];

%save data

fid = fopen(SaveFile,'w');
fprintf(fid,'Position ,');
for i = 1:24
   fprintf(fid,'%i ,',i);
end
fprintf(fid,'\r');
fprintf(fid,'ZPeak ,');
fprintf(fid,'%i ,',(OutPut(1,:)));
fprintf(fid,'\r');
fprintf(fid,'XPeak ,');
fprintf(fid,'%i ,',(OutPut(2,:)));
fprintf(fid,'\r');
fprintf(fid,'YPeak ,');
fprintf(fid,'%i ,',(OutPut(3,:)));
fprintf(fid,'\r');
fprintf(fid,'ZPeakArea ,');
fprintf(fid,'%5.2f ,',(OutPut(4,:)));
fprintf(fid,'\r');
fprintf(fid,'XPeakArea ,');
fprintf(fid,'%i ,',(OutPut(5,:)));
fprintf(fid,'\r');
fprintf(fid,'YPeakArea ,');
fprintf(fid,'%i ,',(OutPut(6,:)));
fprintf(fid,'\r');

fclose(fid);
```

C5. Data collection of pixel values from image of slab phantom

```
function [OutPut] = slabanalysis3v3(Pathname,ImageA);

FnameA=ImageA;
close all;

% read in image information

[X,map] = imread([Pathname FnameA]);

% initialise variables

icount = 0;
Xd=double(X(:,:,1));

% ultrasound image from 164 to 558 pixels across.  Search over all pixel columns

for i=164:558;
   tempx=0;
   tempy=0;
   tempx3 = 0;
   tempy3 = 0;
   tempx7 = 0;
   tempy7 = 0;
   icount = icount+1;

% interface between 280 and 340 pixel depth.  In each pixel column find maximum pixel value and store
% value and location

   for j=280:340;
      if X(j,i,1) > tempx;
         tempx = X(j,i,1);
         tempy = j;
      end
   end
   xpeak(icount)= tempx;
   ypeak(icount)= tempy;

% in each column find max of 3 pixels and store value and location

   for j=280:340;
      if (Xd(j-1,i)+Xd(j,i)+Xd(j+1,i)) > 3*tempx3;
         tempx3 = (Xd(j-1,i)+Xd(j,i)+Xd(j+1,i))/3;
         tempy3 = j;
      end
   end
   xpeak3(icount)= tempx3;
   ypeak3(icount)= tempy3;

% in each column find max of 7 pixels and store value and location

   for j=280:340;
      if (Xd(j-3,i)+Xd(j-2,i)+Xd(j-1,i)+Xd(j,i)+Xd(j+1,i)+Xd(j+2,i)+Xd(j+3,i)) > 7*tempx7;
         tempx7 = (Xd(j-3,i)+Xd(j-2,i)+Xd(j-1,i)+Xd(j,i)+Xd(j+1,i)+Xd(j+2,i)+Xd(j+3,i))/7;
         tempy7 = j;
      end
```

```
    end
    xpeak7(icount)= tempx7;
    ypeak7(icount)= tempy7;
end

% Save and output data

  OutPut = [double(xpeak); ypeak; xpeak3; ypeak3; xpeak7; ypeak7];

  [pathstr,name,ext,versn] = fileparts(ImageA);

  SaveFile = [Pathname,'Analysed',name,'.csv'];


fid = fopen(SaveFile,'w');
fprintf(fid,'Position,XPeak,YPeak,XPeak3,YPeak3,XPeak7,XPeak7');
fprintf(fid,'\r');
for i = 1:395
    fprintf(fid,'%i ,',i+163);
    fprintf(fid,'%i ,',(OutPut(1,i)));
    fprintf(fid,'%i ,',(OutPut(2,i)));
    fprintf(fid,'%i ,',(OutPut(3,i)));
    fprintf(fid,'%i ,',(OutPut(4,i)));
    fprintf(fid,'%i ,',(OutPut(5,i)));
    fprintf(fid,'%i ,',(OutPut(6,i)));
    fprintf(fid,'\r');
end

fclose(fid);
```

C6. Data collection of pixel values from pulse re-injection system

```
%clear all;
close all;
s=pwd;

%Read in image
FnameA=ImageA;

[X,map] = imread([Pathname FnameA]);

%   positions for figures
    bdwidth = 5;
    topbdwidth = 30;
% Ensure root units are pixels and get the size of
% the screen:
    set(0,'Units','pixels')
    scnsize = get(0,'ScreenSize');

    figure('Position',[scnsize(3)/8 scnsize(4)/8 6*scnsize(3)/8 6*scnsize(4)/8])

    image(X(:,:,:));
    pixval;
```

Appendix C: Matlab code used for data analysis

```
% Set up line for which analysis will be taken - user input could be used to create x1, y1, x2 and y2, or
input
% into file could be used for automated setup.  Rest of routine should still be valid.

   x1 = 370;
   y1 = 160;
   x2 = 370;
   y2 = 490;


   %work out the centre of the line selected
   avex = round ((x1+x2)/2);
   avey = (y1+y2)/2;
   y5 = ((abs(y2-y1))/2)+5;
   y1 = round(avey-y5);
   y2 = round(avey+y5);
   n = y2-y1+1;
%create profiles on the centre of the line selected, and two lines either side
   [cx, cy, c] = improfile(X,[avex avex], [y1 y2],n);
   cminus1 = improfile(X,[avex-1 avex-1], [y1 y2],n);
   cminus2 = improfile(X,[avex-2 avex-2], [y1 y2],n);
   cplus1 = improfile(X,[avex+1 avex+1], [y1 y2],n);
   cplus2 = improfile(X,[avex+2 avex+2], [y1 y2],n);
   c1 = [cminus2(:,:,1) cminus1(:,:,1) c(:,:,1) cplus1(:,:,1) cplus2(:,:,1)];
%display the figure of the line profiles
   figure
   plot(cy,cminus2(:,:,1),cy,cminus1(:,:,1),cy,c(:,:,1),cy,cplus1(:,:,1),cy,cplus2(:,:,1));
%calculate the number of pulses received (to 0.25 resolution) along central line profile, and the number
of pixels
%between each pulse
   len4 = 4*n;
   FFT = fft(c1(:,3),len4);
   Freq = abs(FFT);
   ang = angle(FFT);
   [Max, Number] = max(FFT(6:round(n/2)));
   Number = (Number+4)/4;
   StepLength = n/Number;
   RSL = round(StepLength);
% search for maxima of each pulse, starting at end of profile (beginning may often be lost in noise due to
% lower swept gain)
   [LastMax Pos] = max(c1((n-RSL):n,3));
   LastPos=(n-RSL+Pos-1);
   ValMax = 0;
   PosMax = 0;
   if LastPos+2<n
      for j=1:5
         [C, I]=max(c1(LastPos-3:LastPos+3,j));
         ValMax(j) = C;
         PosMax(j) = LastPos-4+I;
      end
   else
      for j=1:5
         [C, I]=max(c1(LastPos-3:n,j));
         ValMax(j) = C;
         PosMax(j) = LastPos-4+I;
      end
   end
```

```
% look at the end of the spectrum if the position of the max detected earlier indicates there may be a peak
% right at the end
   if Pos<0.18*StepLength
      ValMax = [ValMax; 0 0 0 0 0];
      PosMax = [PosMax; 0 0 0 0 0];
      for j=1:5
         if c1(n,j)<c1(n-1,j)
            ValMax(2,j) = c1(n-1,j);
            PosMax(2,j) = n-1;
         else
            ValMax(2,j) = c1(n,j);
            PosMax(2,j) = n;
         end
      end
   end
% step through the peaks, identifying the peak values
   Pos=(n-RSL+Pos-1);
   for i=1:(fix(Number)-2)
      ValMax = [0 0 0 0 0; ValMax];
      PosMax = [0 0 0 0 0; PosMax];
      for j=1:5
         [C, I]=max(c1((round(Pos-i*StepLength)-3):(round(Pos-i*StepLength)+3),j));
         ValMax(1,j) = C;
         PosMax(1,j) = round(Pos-i*StepLength)-4+I;
      end
   end
%l ook at peak closest to front if possible, if not will be picked up by the next group...
   if round(Pos-(fix(Number)-1)*StepLength)-2 > 1
      ValMax = [0 0 0 0 0; ValMax];
      PosMax = [0 0 0 0 0; PosMax];
      for j=1:5
         [C, I]=max(c1((round(Pos-(fix(Number)-1)*StepLength)-3):(round(Pos-(fix(Number)-
1)*StepLength)+3),j));
         ValMax(1,j) = C;
         PosMax(1,j) = round(Pos-(fix(Number)-1)*StepLength)-4+I;
      end
   else
      if round(Pos-(fix(Number)-1)*StepLength)+3 > 1
         ValMax = [0 0 0 0 0; ValMax];
         PosMax = [0 0 0 0 0; PosMax];
         for j=1:5
            [C, I]=max(c1(1:(round(Pos-(fix(Number)-1)*StepLength)+3),j));
            ValMax(1,j) = C;
            PosMax(1,j) = I;
         end
      end
   end
% check that there is not one more very close to the beginning...
   if abs(PosMax(1,3)-StepLength)<0.18*StepLength
      ValMax = [0 0 0 0 0; ValMax];
      PosMax = [0 0 0 0 0; PosMax];
      for j=1:5
         [C, I]=max(c1(1:round(0.18*StepLength)+1,j));
         ValMax(1,j) = C;
         PosMax(1,j) = I;
      end
   end
% Put the Position of the peaks into actual screen pixel positions...
```

```
    PosMax = PosMax+y1-1;

% Print and save...

  [pathstr,name,ext,versn] = fileparts(ImageA);

  SaveFile = [Pathname,'AnaMax',name,'.csv'];


fid = fopen(SaveFile,'w');
fprintf(fid,'PosMax');
fprintf(fid,'\r');
fprintf(fid,'-2, -1, 0, 1, 2, ,PosAve,ValAve,,PosSD,ValSD');
fprintf(fid,'\r');
for i = 1:size(PosMax,1)
    fprintf(fid,'%i ,',PosMax(i,:));
    fprintf(fid,',=AVERAGE(A');
    fprintf(fid,'%i',i+2);
    fprintf(fid,':E');
    fprintf(fid,'%i',i+2);
    fprintf(fid,')');
    fprintf(fid,',=AVERAGE(A');
    fprintf(fid,'%i',i+size(PosMax,1)+5);
    fprintf(fid,':E');
    fprintf(fid,'%i',i+size(PosMax,1)+5);
    fprintf(fid,')');
    fprintf(fid,', ,=STDEV(A');
    fprintf(fid,'%i',i+2);
    fprintf(fid,':E');
    fprintf(fid,'%i',i+2);
    fprintf(fid,')');
    fprintf(fid,',=STDEV(A');
    fprintf(fid,'%i',i+size(PosMax,1)+5);
    fprintf(fid,':E');
    fprintf(fid,'%i',i+size(PosMax,1)+5);
    fprintf(fid,')');
    fprintf(fid,'\r');
end
fprintf(fid,'\r');
fprintf(fid,'ValMax');
fprintf(fid,'\r');
fprintf(fid,'-2, -1, 0, 1, 2');
fprintf(fid,'\r');
for i = 1:size(ValMax,1)
    fprintf(fid,'%i ,',ValMax(i,:));
    fprintf(fid,',=AVERAGE(A');
    fprintf(fid,'%i',i+size(PosMax,1)+5);
    fprintf(fid,':E');
    fprintf(fid,'%i',i+size(PosMax,1)+5);
    fprintf(fid,')');
    fprintf(fid,'\r');
end
fclose(fid);
```

Appendix C: Matlab code used for data analysis

References

AAPM, 2005. Diode in-vivo dosimetry for patients receiving external beam radiation therapy: Report of Task Group 62 of the Radiation Therapy Committee, Medical Physics Publishing, Madison, WI.

Appleby, A. Christman, E.A. Leghrousz, A., 1987. Imaging of spatial radiation dose distribution in agarose gels using magnetic resonance, *Med. Phys.*, 14, 382-384.

Atkins, T.J. Humphrey, V.F. Duck, F.A. Tooley, M.A., 2010. Investigation of ultrasonic properties of MAGIC gels for pulse-echo gel dosimetry, *J. Phys.: Conf. Ser.*, 250, 012075.

Babic, S. Battista, J. Jordan, K.J., 2008. Three-dimensional dose verification for intensity modulated radiation therapy in the radiological physics centre head-and-neck phantom using optical computed tomography scans of ferrous xylenol-orange gel dosimeters, *Int. J. Radiat. Oncol. Biol. Phys.*, 70, 1281-91.

Baldock, C. De Deene, Y. Doran, S. Ibbott, G. Jirasek, A. Lepage, M. McAuley, K.B. Oldham, M. Schreiner, L.J., 2010. Polymer Gel Dosimetry, *Phys. Med. Biol.*, 55, R1-R63.

Baldock, C. Lepage, M. Back, S.Å.J. Murry, P.J. Jayasekera, P.M. Porter, D. Kron, T., 2001. Dose resolution in radiotherapy polymer gel dosimetry: effect of echo spacing in MRI pulse sequence, *Phys. Med. Biol.*, 46, 449-460.

Bamber, J.C., 2004a. Attenuation and absorption, in Hill CR, Bamber JC, ter Harr GR (eds.), Physical Principles of Medical Ultrasonics, 2nd Edition, J Wiley, Chichester.

Bamber, J.C., 2004b. Speed of sound, in Hill, C.R. Bamber, J.C. ter Harr, G.R. (eds.), Physical Principles of Medical Ultrasonics, 2nd Edition, J Wiley, Chichester.

Bamber, J.C. Bush, N.L. Trapp, J. Partridge, M., 2004. Backscatter ultrasound readout of radiation sensitive gels, *Ultrasound*, 12, 230.

Bayón, A. Gascón, F. Nieves, F.J., 2005. Estimation of dynamic elastic constants from the amplitude and velocity of Rayleigh waves. *J. Acoust. Soc. Am.,* 117, 3469-3477.

Bigg, P.H., 1967. Density of water in SI units over the range 0 – 40 ºC, *British J. Appl. Phys.*, 18, 521-537.

References

Both, S. Aleco, I.M. Stan A.R. Alecu, M. Cuira, A. Hansen, J.M. Alecu, R., 2007, *J.Appl. Clin. Med. Phys.*, 8(2), 1-8.

Boyne, J.A. Williamson, A.G., 1967. Enthalpies of mixture of ethanol and water at 25.degree.C, *J. Chem. & Eng. Data*, 12, 318.

Brindha, S. Venning, A.J. Hill, B. Baldock, C., 2004. Experimental study of attenuation properties of normoxic polymer gel dosimeters, *Phys. Med. Biol.*, 49. N353-N361.

Cancer Research UK, 2013a. *CancerStats report – Cancer Incidence in the UK in 2010*, Cancer Research UK.

Cancer Research UK, 2013b. *CancerStats report – Cancer Mortality in the UK in 2010*, Cancer Research UK.

Challis, R.E. Povey, M.J.W. Mather, M.L. Holmes, A.K., 2005. Ultrasound techniques for characterizing colloidal dispersions, *Reports on Progress in Phys.*, 68, 1541-1637.

Chu, K.C. Jordan, K.J., Battista, J.J. Van Dyk, J. Rutt, B.K., 2000, Polyvinyl alcohol-Fricke hydrogel and cryogel: two new gel dosimetry systems with low Fe^{3+} diffusion, *Phys. Med. Biol.*, 45, 955-969.

Crescenti, R.A., 2009. Backscatter ultrasound readout of radiation-sensitive gels for radiation dosimetry, PhD Thesis, University of London.

Crescenti, R.A. Bamber, J.C. Bush, N.L. Webb, S., 2009. Characterization of dose-dependent Young's modulus for a radiation-sensitive polymer gel, *Phys. Med. Biol.*, 843-857.

Crescenti, R.A. Bamber, J.C. Oberai, A.A. Barbone, P.E. Richter, J.P. Rivas, C. Bush, N.L. Webb, S., 2010, Quantitative Ultrasonic Elastography for Gel Dosimetry, *Ultrason. Med. Biol.*, 36, 268-275.

Crescenti, R.A. Bamber, J.C. Partridge, M. Bush, N.L. Webb, S., 2007. Characterization of the ultrasonic attenuation coefficient and its frequency dependence in a polymer gel dosimeter, *Phys. Med. Biol.*, 52, 6747-6759.

Culjat, M.O. Goldenberg, D. Tewari, P. Singh, R. S., 2010. A Review of Tissue Substitutes for Ultrasound Imaging, *Ultrason. Med. Biol.*, 36, 861–873.

D'Arrigo, G. Paparelli, A., 1988. Sound propagation in water-ethanol mixtures at low temperatures. 1. Ultrasonic velocity, *J. Chem. Phys.*, 88, 405-415.

References

De Deene, Y., 2006. On the accuracy and precision of gel dosimetry, *J. Phys. Conf. Ser.*, 56, 72-85.

De Deene, Y. Hurley, C. Venning, A. Vergote, K. Mather, M. Healy, B.J. Baldock, C., 2002b, A basic study of some normoxic polymer gel dosimeters, *Phys. Med. Biol.*, 47, 3441-3463.

De Deene, Y. Venning, A. Hurley, C. Healy, B.J. Baldock, C., 2002a. Dose-response stability and integrity of the dose distribution of various polymer gel dosimeters, *Phys. Med. Biol.*, 47, 2459-2470.

De Deene, Y. Vergote, K. Claeys, C. De Wagter, C., 2006. The fundamental radiation properties of normoxic polymer gel dosimeters: a comparison between a methacrylic acid based gel and acrylamide based gels, *Phys. Med. Biol.*, 51, 653-673.

De Wagter, C., 2004. The ideal dosimeter for intensity modulated radiation therapy (IMRT): What is required? *J. Phys.: Conf. Ser.*, 3: 4-8.

Debye, P., 1909. Das Verhalten von Lichtewellen in der Nähe eines Brennpunktes oder einer Brennlinie [Composition of light waves in the vicinity of a focal point or focal line], *Ann. Phys.*, 335, 775-776.

Department of Health press release 8 October 2012, http://mediacentre.dh.gov.uk/2012/10/08/eight-thousand-patients-to-benefit-from-advanced-cancer-treatment/ accessed 10 March 2013.

DelGrosso, V.A., 1974. New equation of the speed of sound in natural waters (with comparison to other equations), *J. Acoust. Soc. Am.*, 56, 1084-1091.

Doran S.J. Koerkamp, K.K. Bero, M.A. Jenneson, P. Morton, E.J. Gilboy, W.B., 2001. A CCD-based optical-CT scanner for high-resolution 3D imaging of radiation dose distributions: equipment specifications, optical simulations and preliminary results, *Phys. Med. Biol.*, 46, 3191-3213.

Duck, F.A., 2002. Nonlinear acoustics in diagnostic ultrasound, *Ultrason. Med. Biol.*, 28, 1-18.

Dumas, E.-M. Leclerc, G. Lepage, M., 2006. Effect of container size on the accuracy of polymer gel dosimetry, *J. Phys.: Conf. Ser.*, 56, 239-241.

References

Fricke, H. Morse, S., 1927. The chemical action of roentgen rays on dilute ferrous sulphate solutions as a measure of radiation dose, *Am. J. Roentgenol. Radium Therapy Nucl. Med.*, 18, 430-432.

Fong, P.M. Keil, D.C. Does, M.D. Gore, J.C., 2001. Polymer gels for magnetic resonance imaging of radiation dose distributions at normal room atmosphere, *Phys. Med. Biol.*, 46, 3105-3113.

Gavrilov, L.R. Dmitriev, V.N. Solontsova, L.V., 1988. Use of focused ultrasonic receivers for remote measurements in biological tissues, *J. Acoust. Soc. Am.*, 83, 1167-1179.

Gore, J.C. Kang, Y.S. Schulz, R.J., 1984a, Measurement of radiation dose distributions by nuclear magnetic resonance (NMR) imaging, *Phys. Med. Biol.*, 29, 1189-1197.

Gore, J.C. Kang, Y.S. Schulz, R.J., 1984b. Measurement of radiation dose distribution by nuclear magnetic resonance (NMR) imaging, *Magn. Reson. Imaging*, 2, 244.

Gore, J.C. Ranade, M. Maryanski, M.J. Schulz, R.J., 1996. Radiation dose in three dimensions from tomographic optical density scanning of polymer gels: I. Development of an optical scanner, *Phys. Med. Biol.*, 41, 2695-2704.

Greening, J.R., 1981. Fundamentals of Radiation Dosimetry, Adam Hilger Ltd, Bristol.

Guo, P.Y. Adamovics, J.A. Oldham, M., 2006. Characterisation of a new radiochromic three-dimensional dosimeter, *Med. Phys.,* 33, 1338-45.

Hill, B. Back, S.Å.J. Lepage, M. Simpson, J. Healy, B. Baldock, C., 2002, Investigation and analysis of ferrous sulphate polyvinyl alcohol (PVA) gel dosimeter, *Phys. Med. Biol.*, 47, 4233-4246.

Hill, B. Venning, A. Baldock, C., 2005. The dose response of normoxic polymer gel dosimeters measured using X-ray CT, *Br. J. Radiol.,* 78, 623-630.

IEC TS 61949, 2007. Ultrasonics - Field characterization - In situ exposure estimation in finite-amplitude ultrasonic beams, International Electrotechnical Commission, Geneva.

Izweska, J. and Rajan, G., 2005. Radiation Dosimeters, in Podgorsak, E.B. (ed), Radiation Oncology Physics: A Handbook for Teachers and Students, International Atomic Energy Agency, Vienna.

References

James, H. Beavis, A. Budgell, G. Clark, C. Convery, D. Mott, J. Dearnaley, D. Perry, R. Scrase, C., 2008. Guidance for the Clinical Implementation of Intensity Modulated Radiation Therapy IPEM Report 96, IPEM, York.

Jefferies, S. Taylor, A. & Reznek, R., 2009. Results of a national survey of radiotherapy planning and delivery in the UK in 2007. *Clin. Oncol.*, 21: 204-217.

Kak A.C. Slaney, M., Principles of Computerized Tomographic Imaging, IEEE Press, 1988.

Kalashnikov, A.N. Challis, R.E., 2005. Errors and Uncertainties in the Measurement of Ultrasonic Wave Attenuation and Phase Velocity, *IEEE Trans. Ultrason. Ferroelect. and Freq. Contr.*, 52, 1754-1768.

Kaufman, J.J. Xu, W. Chiabrera, A.E. Siffert, R.S., 1995. Diffraction effects in insertion mode estimation of ultrasonic group velocity, *IEEE Trans. Ultrason. Ferroelect Freq.Cont.*, 42, 232-242.

Kaye, G. W. C. Laby, T. H., 1995. Tables of Physical and Chemical Constants, online edition, v 1.0, http://www.kayelaby.npl.co.uk/.

Kelly, B.G. Jordan, K.J. Battista, J., 1998. Optical CT reconstruction of 3D dose distributions using the ferrous-benzoic-xylenol (FBX) gel dosimeter, *Med. Phys.*, 25, 1741-50.

Kinsler, L.E. Frey, A.R., 1962. Fundamentals of Acoustics (2nd Edition), Wiley and Sons, London.

Kirby, M.C. Glendinning, A.G., 2006, Developments in electronic portal imaging systems, *Br. J. Radiol.*, 79, S50-S65.

Lepage, M. Jayasakera, P.M. Bäck, S.Å.J. Baldock, C., 2001. Dose resolution optimisation of polymer gel dosimeters using different monomers, *Phys. Med. Biol.*, 46, 2665-2680.

Lepage, M. Whittaker, A.K. Rintoul, L. Back, S.A. Baldock, C., 2001b. The relationship between radiation induced chemical processes and transverse relaxation times in polymer gel dosimeters, *Phys. Med. Biol.*, 46, 1061-74.

Liney, G.P. Heathcote, A. Jenner, A. Turnbell, L.W. Beavis, A.W., 2003, Absolute radiation dose verification using magnetic resonance imaging: feasibility study, *J. Radioth. in Practice,* 3, 123-129.

Low, D.A. Harms, W.B, Mutic, S. Purdy, J.A., 1998. A technique for the quantitative evaluation of dose distributions, *Med. Phys.*, 25, 656-661.

Lucas, B.G. Muir, T.G., 1982. The field of a focusing source, *J. Acoust. Soc. Am.*, 72, 1289-1296.

Marczak, W., 1997. Water as a standard in the measurements of speed of sound in liquids, *J. Acoust. Soc. Am.*, 102, 2776-2779.

Maryanski, M.J. Gore, J.C. Kennan, R.P. Schultz, R.J., 1993. NMR relaxation enhancement in gels polymerised and cross-linked by ionising radiation: A new approach to 3D dosimetry by MRI, *Magn. Reson. Imag.*, 11: 253-258.

Maryanski, M.J. Schultz, R.J. Ibbott, G.S. Gatenby, Gatenby, J.C. Xie, J. Horton, D. Gore, J.C., 1994. Magnetic resonance imaging of radiation dose distributions using a polymer-gel dosimeter, *Phys. Med. Biol.*, 39, 1437-1455.

Mather, M.L. Baldock, C., 2003, Ultrasound tomography imaging of radiation dose distributions in polymer gel dosimeters: Preliminary study, *Med. Phys.*, 30, 2140-2148.

Mather, M.L. Charles, P.H. Baldock C., 2003. Measurement of ultrasonic attenuation coefficient in polymer gel dosimeters, *Phys. Med. Biol.*, 48, N269–75.

Mather, M.L. De Deene, Y. Whittaker, A.K. Simon, G.P. Rutgers, R. Baldock, C., 2002. Investigation of ultrasonic properties of PAG and MAGIC polymer gel dosimeters, *Phys. Med. Biol.*, 47, 4397-4409.

Mayles, W.P.M. Cooper, T. Mackay, R. Staffurth, J. Williams, M., 2012. Progress with Intensity-modulated Radiotherapy Implementation in the UK. *Clin. Oncol.*, 24: 543-544.

McCurdy, B.M. Luchka, K., Pistorius, S., 2001, Dosimetric investigation and portal dose image prediction using an amorphous silicon electronic portal imaging device, *Med. Phys.*, 28, 911-924.

McJury, M. Oldham, M. Cosgrove, V.P. Murphy, P.S. Doran, S. Leach, M.O. Webb, S., 2000. Radiation dosimetry using polymer gels: methods and applications, *Br. J. Radiol.*, 73, 919-929.

National Cancer Action Team, 2009. *Intensity Modulated Radiotherapy (IMRT) A guide for Commissioners*, National Cancer Action Team,

http://ncat.nhs.uk/sites/default/files/Commissioner%20paper%20IMRT_0.pdf, download 3rd September 2012.

Nelms, B.E. Simon, J.A., 2007. A survey on planar IMRT QA analysis, *J. Appl. Clin. Med. Phys.*, 8(3), 1-15.

Nightingale, K. Palmeri, M. Nightingale, R. Trahey, G., 2000. Acoustic Remote Palpation: Initial *in vivo* results, *IEEE Ultrasonics symposium*, 1553-1558.

Niroomand-Rad, A. Blackwell, C.R. Coursey, B.M. Gall, K.P. Galvin, J.M. McLaughlin, W.L. Meigooni, A.S. Nath, R. Rodgers, J.E. Soures, C.G., 1998. Radiochromic film dosimetry: Recommendation of AAPM Radiation Therapy Committee Task Group 55, *Med. Phys.*, 25, 2093-2115.

Nutting, C. Dearnaley, D.P. Webb, S., 2000. Intensity modulated radiation therapy: a clinical review. *British J. Radiol.*, 73: 459-469.

Olsson, L.E. Petersson S. Ahlgren, L. Mattsson, S., 1989. Ferrous Sulphate gels for determination of absorbed dose distributions using MRI technique: basic studies, *Phys. Med. Biol.*, 34, 43-52.

O'Neil, H.T., 1949. Theory of focusing radiators, *J. Acoust. Soc. Am.*, 21, 516-526.

Ophir, J. Cespedes, I. Ponnekanti, H. Yazdi, Y. Li, X., 1991, Elastography: a quantitative method for imaging the elasticity of biological tissues, *Ultrasonic Imaging*, 13, 111-134.

Penttinen, A. Luukkala, M., 1977. Diffraction losses associated with curved transducers, *J Phys. D: Appl. Phys.*, 10, 665-669.

Preston, R.C., 1988. The NPL Ultrasound Beam Calibrator, *IEEE Trans. Ultrason. Ferroelect Freq.Cont.*, 35, 122-139.

Sakhalkar, H.S. Adamovics, J.A. Ibbott, G. Oldham, M., 2009. A comprehensive evaluation of the PRESAGE/optical-CT 3D dosimetry system, *Med. Phys.,* 36, 71-82.

Salomons, G.J. Park, Y.S. McAuley, K.B. Schreiner, L.J., 2002. Temperature increases associated with polymerization of irradiated PAG dosimeters, *Phys. Med. Biol.*, 47, 1435-1448.

Saw, C. Loper, A, Komanduri, K. Combine, T, Huq, S. Scicutella, C., 2005, Determination of CT-to-Density conversion relationship for image-based treatment planning systems, *Med. Dosim.,* 30, 145-148.

References

Schulz, R.J. deGuzman, A.F. Nguyen, D.B. Gore, J.C., 1990. Dose-response curves for Fricke-infused agarose gels as obtained by nuclear magnetic resonance, *Phys. Med. Biol.*, 35, 1611-1622.

Seki, H. Grantano, A. Truell, R., 1956. Diffraction effects in the ultrasonic field of a piston source and their importance in the accurate measurement of attenuation, *J. Acoust. Soc. Am.*, 28, 230-238.

Senden, R.J. De Jean, P. McAuley, K.B. Schreiner, L.J., 2006. Polymer gel dosimeters with reduced toxicity: a preliminary investigation of the NMR and optical dose-response using different monomers, *Phys. Med. Biol.*, 51, 3301-3314.

Sigma Aldrich, www.sigmaaldrich.com, Materials Safety Data Sheet Product M7279.

te Nijenhuis, K., 1981. Investigation into the ageing process in gels of gelatine/water systems by the measurement of their dynamic moduli Part 1 – Phenomenology, *Colloid & Polymer Sci.*, 259, 522-535.

Trapp, J.V. Back, S.A.J, Lepage, M. Michael, G. Baldock, C., 2001. An experimental study of the dose response of polymer gel dosimeters imaged with x-ray computed tomography, *Phys. Med. Biol.*, 46, 2939-2951.

UNESCO, 1983. Algorithms for computation of fundamental properties of seawater, *Unesco Tech. Pap. In Mar. Sci.*, 44, 15-24.

UNEP Publications, http://www.inchem.org/documents/sids/sids/79414.pdf.

US EPA, http://www.epa.gov/chemfact/s_acryla.txt.

van Elmpt, W. McDermott, L. Nijsten, S. Wendling, M. Lambin, P. Mijnheer, B., 2008. A literature review of electronic portal imaging for radiotherapy dosimetry, *Radiotherapy & Oncol.,* 88, 289-309.

Varatharaj, C. Moretti, E. Ravikumar, M. Malisan, M.R. Supe S.S. Padovani, R., 2010. Implementation and validation of a commercial portal dosimetry software for intensity-modulated radiation therapy pre-treatment verification. *J. Med. Phys.,* 35 189-196.

Venning A.J. Nitschke, K.N. Keall, P.J. Baldock, C., 2005. Radiological properties of normoxic polymer gel dosimeters, *Med. Phys.*, 32 1047-1053.

Williams, M.V. Cooper, T. Mackay, R. Staffurth, J. Routsis, D. Burnet, N., 2010. The Implementation of Intensity-Modulated Radiotherapy in the UK. *Clin. Oncol.*, 22: 623-628.

References

Wolodzko, J.G. Marsden, C. Appleby, A., 1999. CCD imaging for optical tomography of gel radiation dosimeters, *Med. Phys.*, 26, 2508-2513.

Wong, G.S.K. Zhu, S., 1995. Speed of sound in seawater as a function of salinity, temperature and pressure, *J. Acoust. Soc. Am.*, 97, 1732-1736.

Xu, W. Kaufman, J.J., 1993. Diffraction correction methods for insertion ultrasound attenuation estimation, *IEEE Trans. Biomed. Eng.*, 40, 563-570.

Zequiri, B., 1996. Validation of a diffraction correction model for through-transmission substitution measurements of ultrasonic absorption and phase velocity, *J. Acoust. Soc. Am.*, 99, 996-1001.